Detection of Highly Interrelated Interfacial pH and Polarity for Biologically Relevant Amphiphilic Self-Assemblies Using a Single Optical Probe Molecule

THESIS SUBMITTED FOR THE DEGREE OF

DOCTOR OF PHILOSOPHY (SCIENCE)

By

RINI MAJUMDER

DEPARTMENT OF CHEMISTRY

JADAVPUR UNIVERSITY

KOLKATA -700032

INDIA

June, 2022

JADAVPUR UNIVERSITY

KOLKATA -700032

CERTIFICATE FROM THE SUPERVISOR

This is to certify that the thesis entitled **"Detection of Highly Interrelated Interfacial pH and Polarity for Biologically Relevant Amphiphilic Self-Assemblies Using a Single Optical Probe Molecule"** submitted by **Rini Majumder** who got her registered on 25th May, 2015 for the award of Ph. D. (Science) degree of Jadavpur University, is absolutely based upon her own work under the supervision of **Dr. Partha Pratim Parui** and that neither this thesis nor any part of it has been submitted for any degree/diploma or any other academic award anywhere before.

Date: 30/6/22

Partha Prat. Parui

Dr. PARTHA PRATIM PARUI

(SUPERVISOR)

Dr. Partha Pratim Parui
Professor
Department of Chemistry
Jadavpur University, Kolkata-700032

DECLARATION

I hereby declare that the work embodied in the present thesis entitled **"Detection of Highly Interrelated Interfacial pH and Polarity for Biologically Relevant Amphiphilic Self-Assemblies Using a Single Optical Probe Molecule"** has been carried out by me in the Department of Chemistry, Jadavpur University under direct supervision of **Dr. Partha Pratim Parui**. Neither this thesis nor any part of thereof has been submitted for any degree or whatsoever.

In keeping with the general practice of reporting scientific observations, due acknowledgement has been made whenever the work described is based on the findings of other investigators. Any omission which might have occurred by oversight or error in judgment is regretted.

Date: 30.06.22

Rini Majumder
(RINI MAJUMDER)

Dedicated affectionately

To

My parents and Husband

ACKNOWLEDGEMENT

I would like to express my deep sense of profound gratitude to my esteemed guide ***Dr. Partha Pratim Parui,*** *Professor, Department of Chemistry, Jadavpur University, for his valuable guidance &, constant support. I submit my heartiest indebtedness to him for his sincere & continuous encouragement for completing the work & writing this thesis.*

I would like to express my earnest thanks to Dr. S. K. Bhattacharaya, Head of the Department of Chemistry, Jadavpur University, Dr. Suman Das, Section-In-Charge, Physical Chemistry Section, and all other faculty members of Department of Chemistry. I also sincerely appreciate the selfless service of all the staffs attached to the department.

I gratefully acknowledge Dr. Arup Gayen, Professor, Department of Chemistry, Jadavpur University and Dr. Ambarish Ray, Associate Professor, Taki Gov. College, for their encouraging advice.

Financial assistance received from University Grant Commission, New Delhi is gratefully acknowledged. I am also thankful to the authorities of Jadavpur University for providing the necessary infrastructure and facilities to complete my work.

Cordial cooperation and valuable suggestions rendered by my laboratory colleagues, Sanju Das, Yeasmin Sarkar and Snigdha Roy in every stage of my research work deserve special attention.

I express my deepest gratitude to Saswati Gharami, Nayim Sepai, for all the thoughtful and mind stimulating discussions we had.

I am grateful to Kaushik Bhaumik, Arunavo Chatterjee, M. Sc. project students.

Also, I wish to thank my dear husband for his constant support.

Last but not the least I owe a sense of gratitude to my parents, in-laws and all family members for their patience, encouragement, untiring support and love throughout my research period.

Rini Majumder
30.06.22

(RINI MAJUMDER)
Department of Chemistry
Jadavpur University
Kolkata- 700 032

PREFACE

The work embodied in the present thesis entitled "**Detection of Highly Interrelated Interfacial pH and Polarity for Biologically Relevant Amphiphilic Self-Assemblies Using a Single Optical Probe Molecule**" was initiated in May, 2015 and carried out in the Department of Chemistry, Jadavpur University, Kolkata- 700 032.

This thesis demonstrates a convenient interfacial pH/polarity detection methodology for biologically relevant amphiphilic self-assemblies using optical probe molecule. By employing UV-Vis absorption and fluorescence spectroscopic methods, pH or/and polarity induced interconversion equilibriums between two molecular forms for the probe molecule were evaluated separately at the interface and the bulk phase to estimate interfacial pH/polarity and its deviation from the bulk phase value. We have synthesized interface interacting polarity sensing phenol-based Schiff-base molecular probe to estimate interfacial polarity value. In order to measure interfacial pH and polarity together, a Schiff-base molecule containing two identical phenol-conjugated-imine functional groups was exploited. Polarity induced conversion between non-ionic and zwitterionic forms, while pH induced deprotonation/protonation equilibrium for the probe molecule were evaluated individually to estimate interfacial polarity and pH value, respectively. Since the proton dissociation equilibrium of a pH-probe depends on the local polarity, an accurate estimation of polarity value at the probe localized environment is prerequisite for obtaining the interfacial pH value. However, the value of pH/polarity can alter significantly with a small change in depth at the interfacial cross-section. Thus, estimation of pH and polarity values using two separate probes localized at different interfacial depths can be erroneous. We have synthesized a glucose-pendant porphyrin molecule as a simultaneous interfacial pH and polarity detecting probe molecule. In this thesis, we have identified the interfacial pH/polarity changes during temperature-induced phase transition for anionic lipid membrane. Interfacial pH value for the lipid membrane was found to be more acidic in the gel phase than the liquid-crystalline phase. On the other hand, only a small increase of interfacial polarity value during the gel to liquid-crystalline phase transition was observed.

LIST OF ABREVIATIONS

ACN	….	Acetonitrile
AEP	….	2-(2-aminoethyl)-pyridine
AOT	….	Sodium bis(2-ethylhexyl) sulfosuccinate
BAR	….	BIN-Amphiphysin-Rvs
$CHCl_3$	….	Chloroform
CPCM	….	Conductor polarized continuum model
CTAB	….	Cetyl trimethylammonium bromide
cyt *c*	….	Cytochrome *c*
DAG	….	Diacylglycerol
d_A-GPP	….	Deprotonated, Aggregated Species of GPP
d_M-GPP	….	Deprotonated, Monomer Species of GPP
DAP	….	1,2-diaminopropane
DCTB	….	Trans-2-[3-(4-tert-butylphenyl)-2- methyl-2-propenylidene] malononitrile
DDAB	….	Dimethyl dioctadecyl ammonium
DFT	….	Density functional theory
DLS	….	Dynamic light scattering
DMF	….	Dimethylformamide
DMAP	….	4-Dimethylaminopyridine
DMPC	….	1,2-dimyristoyl-sn-glycero-3-phosphocholine
DMPG	….	Sodium 1,2-dimyristoyl-*sn*-glycero-3- phosphorylglycerol
DMSO	….	Dimethyl sulfoxide
DOPC	….	1,2-Dioleoyl-sn-Glycero-3-Phosphocholine
DOPE	….	1,2-Dioleoyl-sn-Glycero-3-Phosphoethanolamine
DOPG	….	1,2-Dioleoyl-sn-Glycero-3-[Phospho-rac-(1-glycerol]
DSC	….	Differential scanning calorimetry
EtOH	….	Ethanol
GMV	….	Giant multilamellar vesicle
GSIPT	….	Ground state proton-transfer reaction
HD-ESFG	….	Heterodyne-detected electronic sum frequency generation
HHMB	….	2-Hydroxy-3-(hydroxymethyl)-5-methylbenzaldehyde

IGSPT	….	Intramolecular ground state proton transfer
IMM	….	Inner mitochondrial membrane
LUVs	….	Large unilamellar vesicles
MeOH	….	Methanol
MLV	….	Multi-lamellar vesicles
MVV	….	Multi-vesicular vesicles
NMR	….	Nuclear magnetic resonance
PDMA	….	Poly(2-dimethylaminoethyl) methacrylate
PDI	….	Polydispersity index
PE	….	Phosphatidylethanolamine
pH	….	–log of hydrogen ion concentration, $-\log[H^+]$
pH_i/pH(i)/pH(intf)	….	Interfacial pH
ΔpH	….	pH deviation from the bulk to the interface
PI	….	Phosphatidylinositol
PMMA	….	Poly (methyl methacrylate)
p_M-GPP	….	Protonated, Monomer Species of GPP
PMP	….	2-((2-(pyridine-2-yl)ethylimino)methyl)-6-(hydroxymethyl)-4-methylphenol
$PMP^{\pm}$	….	Zwitterionic form of PMP
PMP^0	….	Neutral form of PMP
q-TBP	….	$PDMA^+$-b-PMMA-b-$PDMA^+$, Cationic amine quaternized triblock polymer
SDS	….	Sodium dodecyl sulfate
SM	….	Sphingomyelin
STA	….	Sodium taurocholate
SUV	….	Small unilamellar vesicles
T_m	….	Transition temperature
TBP	….	PDMA-*b*-PMMA-*b*-PDMA, amine-quaternized PDMA, q-PDMA
TD-DFT	….	Time-dependent density functional theory
THF	….	Tetrahydrofuran
TMCL	….	Tetramyristoyl CL
TOCL	….	Tetraoleoyl CL
TX-100	….	Polyethylene glycol tert-octylphenyl ether or titron X-100

a	….	Aggregation number
Δ	….	Apparent pH-shift
ε	….	Extinction coefficient
ϕ_F	….	Fluorescence quantum yield
κ_i	….	Interfacial polarity
τ_c	….	Correlation time/fluorescence anisotropic decay constant
δ	….	Polarity difference between the bulk and interface
Δf	….	Orientation polarizability

CONTENTS

LIST OF PUBLICATIONS (APPENDIX)

Chapter 1

Interfacial physiochemical properties of amphiphilic self-assemblies: background, literature study, scope and objectives

1.1. Amphiphilic self–assemblies

Molecules that can self-assemble into various structures such as vesicles, micelles, tubules, and lamellae in solution are called amphiphilic molecule.[1] Detergents, soaps, block copolymers, and biological phospholipids are familiar examples of amphiphilic molecules.[2,3] Biological membrane comprises phospholipid molecules with a bilayer arrangement.[4] In addition to the various types of phospholipids, biological membrane also contains proteins (membrane protein), sugar, cholesterols, glycolipids, and fatty acids.[5] The self-assembled membrane structures can reshape from one to another form depending on the local pH, temperature, or ionic strength. The function of membrane proteins and peptides is highly corrected with the specific membrane structure and shape.[6,7] Various types of synthesized self-assembled molecules have been extensively investigated to imitate biological systems.[8-11]

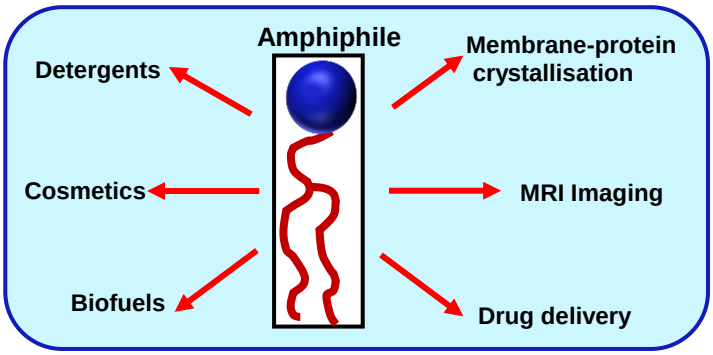

Figure 1. Examples of amphiphile applications.

On the other hand, synthetic self-assembled molecules is of prime importance for various applications including pharmaceutical, food, and cosmetic formulations (Figure 1).[12-14] In addition, self-assembled systems have also drawn considerable attention over many decades because of its wide range of applications in the field of material science, and gene and drug delivery.[15-18] For the development of more hierarchical complex supramolecular self-assembled nanostructures, a verity types of attractive synthetic procedures have been adapted recently.

1.1.1. General characteristics of amphiphilic molecules

Amphiphilic molecule contains two molecular segments with opposite polarity values.[12,19] It consists at least one hydrophilic part and one hydrophobic portion. However, the existence of

several hydrophilic and hydrophobic parts is also possible (Figure 2). The hydrophilic part can be either uncharged or charged. Uncharged groups usually contain alcohol functionality. Common examples of negatively charged groups are phosphates (RPO_4^{2-}), carboxylates (RCO_2^-), sulfonates (RSO_3^-), and sulfate (RSO_4^-). On the other hand, the positively charged groups are mainly based on the quaternary nitrogen (NR_4^+) containing compound. The hydrophobic residues are existed as saturated or unsaturated hydrocarbon chains of variable chain lengths. Amphiphilic molecules may partially dissolve in both aqueous and non-aqueous solvents. Two oppositely polar parts interacts very differently with the solvent molecules due to their amphiphilic character. The combined polar-and-nonpolar nature of amphiphiles causes a strong tendency to reduce the surface tension when the molecules are adsorbing at a specific interface (*i.e.* air-water or oil-water).[20,21] Up to a certain low concentration of amphiphilic molecules, a monolayer at the water-air interface is formed. When the interface becomes saturated with amphiphiles and its concentration goes beyond to a certain critical concentration, the hydrophobic interaction among non-polar segments drives them to form self-assembled molecular aggregation.[22-24]

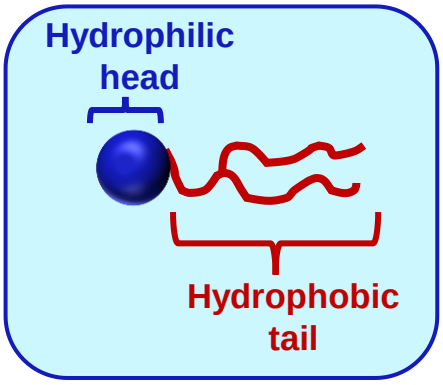

Figure 2. Structure of the amphiphilic molecule.

1.1.2. Classification of amphiphilic molecules

Based on the nature of hydrophilic polar head group, amphiphilic molecules are classified in different categories: a) cationic, b) anionic, c) zwitterionic, d) non-ionic, e) bolaform, f) gemini amphiphilies (Figure 3).

The cationic amphiphiles generally comprise of positively charged quaternary ammonia head groups. Cetyl trimethylammonium bromide (CTAB), dodecyltrimethylammonium bromide

(DTAB), benzethonium chloride (BZT) are common examples of such kind of molecule. Cationic amphiphiles exhibit anti-microbials, anti-fungal activities.[25,26]

The anionic amphiphiles contain a negatively charged head groups such as carboxylate, sulfate, sulphonate, phosphate and positively charged sodium, ammonium ions as counterpart. The common anionic amphiphiles are sodium N-lauroyl-N-methyltaurate, sodium tetradecyl sulfate, and sodium dodecyl sulfate (SDS). Anionic surfactants are used as detergents and soap for cleaning processes.[27]

The zwitterionic amphiphiles contain both anionic and cationic residues in the head group, that eventually convert into a neutral molecule. Zwitterionic amphiphiles behave as anionic or cationic based on pH value of medium. The presence of ionic groups in zwitterionic amphiphiles make highly soluble in water. Zwitterionic surfactants are used in cosmetics, washing products and in chemical enhanced oil recovery (EOR).[28]

For the bola amphiphiles, two head-groups are linked to one alkyl chain. Bola amphiphiles can be divided in two categories: symmetric (with same polar head groups) and asymmetric (consisting different polar head groups). Bola amphiphiles are mainly used in the formation of nanosized spherical structure which is very effective for targeted gene and drug delivery.[29]

The gemini amphiphiles consist of two similar amphiphilic units divided by an organic spacer. The spacer length can be short or long and rigid or flexible. The gemini amphiphiles show usually low critical micelle concentration (cmc) value, low surface tension, and high surface activity.[30]

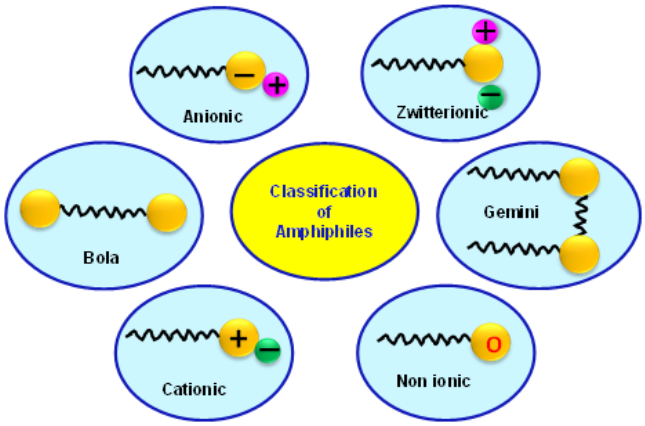

Figure 3. Various types of amphiphiles.

1.1.3. Self-assembly formation

Self-assembly is a process in which the hydrophobic part of the amphiphilic molecules interacts among themselves to form an aggregated structure, while the hydrophilic part faces towards the bulk aqueous phase.[31,32] The large polarity difference between the polar and non-polar segments plays the most important role for the formation of aggregated structure. The hydrophobic tail part of the amphiphilic molecule in solution has a strong tendency to avoid direct contact with water. The unfavorable oil-water interaction can be reduced through aggregation where hydrophilic head groups are located at interface in facing towards the aqueous bulk solvent phase and the hydrophobic tail parts are shielded (Figure 4).[31] In addition, solvation of polar head groups and insertion of the nonpolar tails in the solvent generate additional stability to form aggregated structure.

Usually, the increase of entropy value also plays another significant role to facilitate the self-assembly process.[33,34] When the hydrophobic parts are inserted to the interior region of aggregated structure from the aqueous medium, disruption of 3D-ordered structure of water molecules neighboring the hydrocarbon tail takes place, and such structural changes cause an increase in entropy. The formation of hydrophobic core is also facilitated by the increase of entropy. The hydrophobic tail part of amphiphilic molecules in the nonpolar interior core of the aggregated structure is becoming freer than those in the aqueous environment.[33] This difference of surroundings for the amphiphilic molecule from a single molecular state to the aggregated structure results in the increase of entropy.

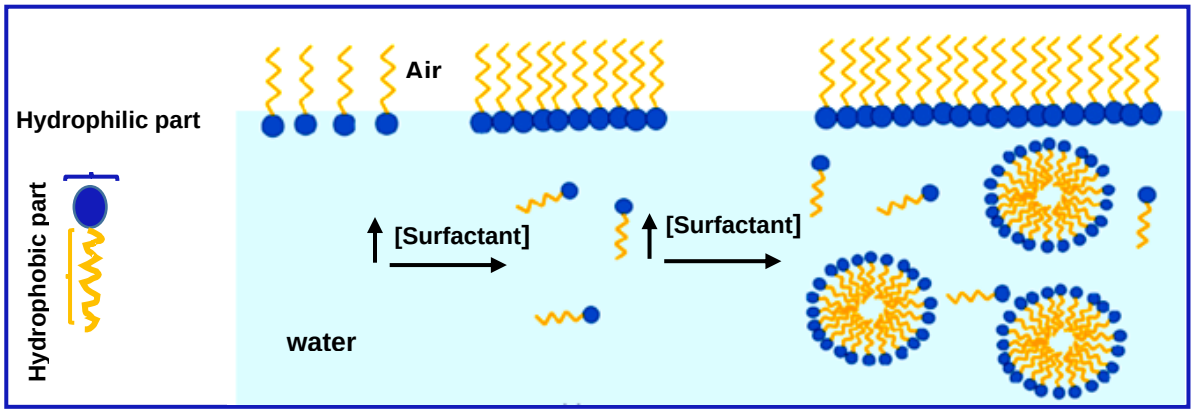

Figure 4. Representation of a surfactant molecule and process of self-assembly formation in aqueous phase.

The self-assembly process involves various kinds of interactions that are mainly non-covalent in nature (Figure 5).[24] The common non-covalent interactions are the Van der Waals forces, hydrogen bonding, dipole-dipole, electrostatic, π-π stacking, and so on.[24,35] The relative interaction strength is shown in table 1.

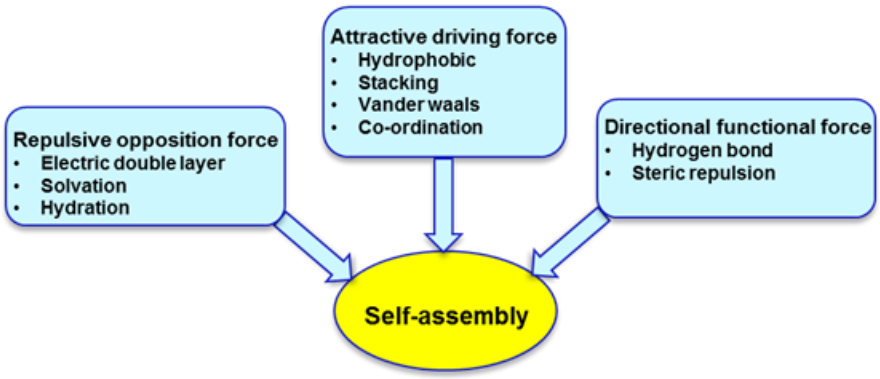

Figure 5. Interactions in self-assembly.

Table 1: Interaction type and their relative strength

Bonding and interaction type	kJ/mol
Hydrogen bond	4–120
Cation-n (π) interaction	5–80
π-π interaction	0–50
Van der Waals interaction	<5
Metal-ligand	0–400

Interaction among aliphatic tails in amphiphiles delivers a vital contribution to the overall non-covalent interactions in self-assembly systems. Van der Waals interaction arises from the variation of the electron distribution of two closely spaced molecules, even though, only a few examples show that the Van der Waals interactions work as a predominant force for the self-assembly process. Hydrogen bonding interaction also plays a significant role for self-assembly of different biomolecules, such as DNA assembly, formation and stabilization of the peptide's secondary structure and protein folding.[31] Richards *et al.* have reported that the aggregated

pyrazinacene nanotubes are stabilized by π-π stacking interactions. Numerous other studies have shown that the intermolecular dipole-dipole interaction also plays very important role for the formation process of supramolecular self-assemblies.[36,37] A variety of elaborate metallo-supramolecules, such as 2D polygons, 3D cages, and polyhedral, have been described based on the coordination-driven self-assembly through metal-ligand interactions.[38-40]

Amphiphilic molecules are self-assembled through a static or dynamic process. The static self-assembly process does not dissipate energy while creating an ordered structure.[41] Common examples of static processes are structured block copolymers, nanoparticles, nanorods, liquid crystals, and hierarchical supramolecular systems. However, in the case of dynamic self-assembly, energy is dissipated during creation of the ordered structure.[41] Formation of micelles, reverse micelles, vesicles are well known examples of dynamic self-assembly process.[42,43] Moreover, the dynamic self-assembly process is observed for different biomolecules, such as phospholipids, proteins, carbohydrates.

1.1.4. Self-assemblies shapes and structures

Amphiphilic molecule generates micelles/reverse micelle or liposomes when dispersed in aqueous/non-aqueous solution (Figure 6).[44] Structural geometry of the aggregated states is mainly influenced by varying physicochemical properties of solutions, such as pH, polarity, temperature, ionic strength.[45] Various aggregated structures are described below:

Micelle: Normally micelles are spherical in shape. Micelle is formed when the concentration of amphiphilic molecule exceeds a certain limiting concentration (CMC) in polar solution. CMC value is affected by ionic strength and pH of the medium.[46] Furthermore, the micelle formation processes are also dependent on a definite solution temperature known as Krafft temperature. For a typical micelle, polar head groups are exposed to the bulk aqueous medium, and the non-polar tail parts form a hydrophobic core region. Micellar sizes and shapes are highly dependent on different physicochemical parameters (pH, ionic strength, temperature) of the solution.[46,47] For a spontaneous micelle formation, the medium temperature must be higher than that of the Kraft temperature. The diameter of spherical micelle can vary within 2 to 20 nm. Shape and sizes of the micelles are guided by the head group functionality and alkyl chain length of amphiphilic molecule. Spherical micelles are formed mainly at low concentration of amphiphilic molecule.[48]

In certain cases, the spherical shapes are converted to an elongated shape such as rod like, cylindrical, bilayers micelles with increasing concentration of amphiphilic molecule. Also, it has been reported that wormlike micelles are turn into a large bilayer micellar structure through hexagonal packing at very high concentration of amphiphilic molecule.

Reverse micelle: In nonpolar medium, amphiphilic molecules aggregates in such a way that the orientation of polar head group lies at the interior, forming structure called reverse micelle.[49] Well known ionic surfactant, bis (2-ethylhexyl) sulfosuccinate sodium salt (AOT), form reverse micelle in non-polar medium. Reverse micelles are able to incorporate polar solvents (*e.g.*, water) and other hydrophilic molecules or water-soluble salts in the hydrophilic cores. Reverse micelles are of prime interest because of their resemblance with biological membrane. Hence it can be used frequently as the model system related to the drug-delivery with the capacity to solubilize bioactive substances.[50] On the other hand, hydrophilic pools of reverse micelles have been considered as perfect microenvironments for hosting polar enzymes owing to large interfacial area.

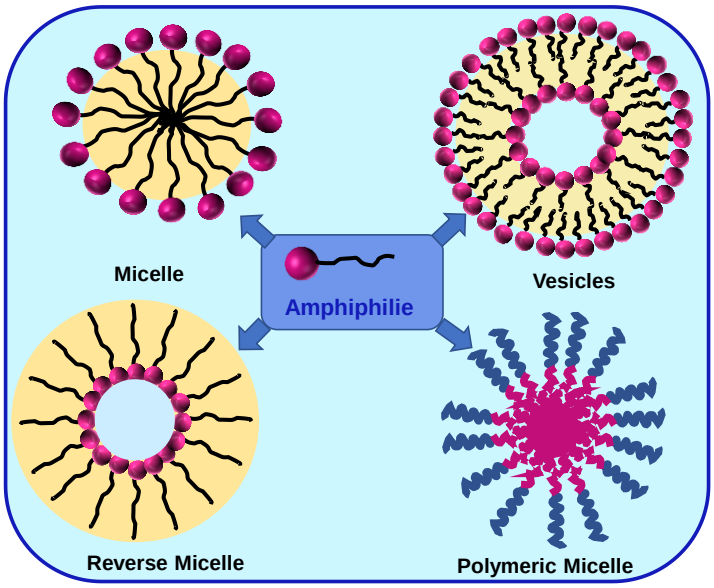

Figure 6. Pictorial representation of different self-assemblies (micelles, reverse micelles, vesicles and polymeric micelle).

Vesicles and Bilayer: In general, amphiphilic molecules containing double-chain tail part are very susceptible to form bilayer structure of vesicle. Different types of phospholipid molecules (anionic, cationic and zwitterionic) are common examples of vesicle forming amphiphilic

molecules.[51] The shape of phospholipid vesicles can be spherical or non-spherical. The physiological cell converts individual phospholipid molecules into the vesicle structure during exocytosis and endocytosis processes. In addition, vesicles can also be produced artificially, known as liposomes.[52] Liposomes are made of a lipid bilayer that separates internal aqueous phase (water-pool) from the bulk aqueous phase. Vesicles play an essential role in many biological processes.[53] The major types of biologically important vesicles are: lysosomes, peroxisomes, extracellular vesicles, transport vesicles, secretory vesicles. Each type of vesicle has a specific function towards different biological processes. Vesicle facilitates the transportation of materials, recycle waste materials, absorb and destroy toxic substances and pathogens to prevent cell damage and infection.

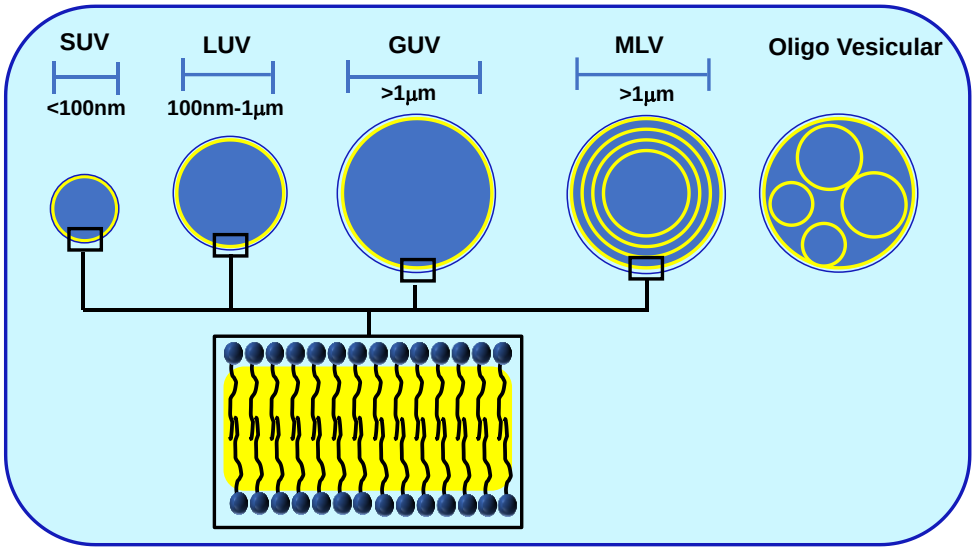

Figure 7. Representation of various structure of vesicle.

Vesicle may compose of a single or more than one bilayer structure. Depending on number of bilayers, vesicles are classified in two major structures: (a) unilamellar vesicles (ULVs) and (b) multilamellar vesicles (MLVs) (Figure 7, 8).

Unilamellar vesicles contain only one bilayer structure. The unilamellar vesicles are categorized based on their size:

(i) Small unilamellar vesicles (SUVs) of diameter below 100 nm.

(ii) Large unilamellar vesicles (LUVs) of diameter in range of 100–500 nm.

(iii) The giant unilamellar vesicles (GUVs) of diameter 0.5–1 µm.

However, MLVs contain multiple concentric bilayers while multi-vesicular vesicles (MVV) have non-concentric vesicles inside a large vesicle. Diameter of MLVs is generally greater than 0.5 μm.

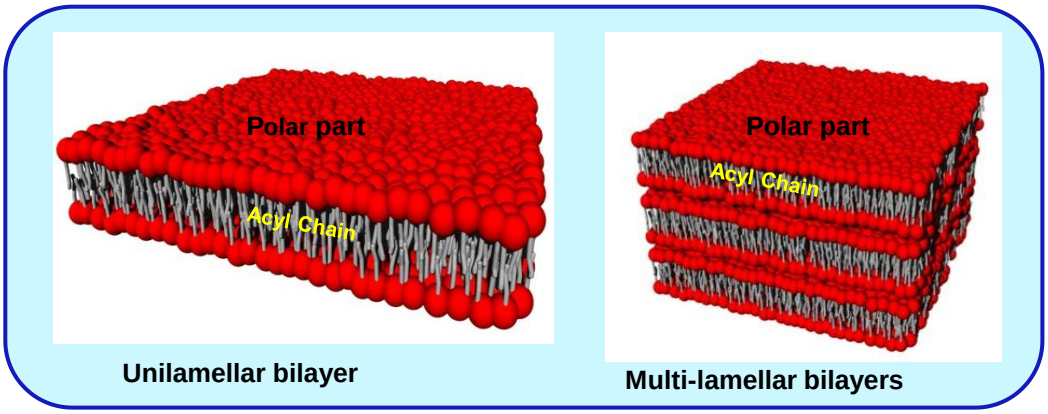

Figure 8. Schematic representation of bilayer sheet structure.

1.2. Correlation of amphiphilic self-assemblies with bio-membrane

Most of bio-membranes show the similar structure as that of lipid bilayer structure. Major lipids present in bio-membranes are phospholipids, glycolipids, cholesterols in which phospholipids are mainly amphiphilic in nature.[54] Phospholipids contain two parts of opposite polarity values; phosphate group as hydrophilic part and double fatty acid chain as hydrophobic part (Figure 9).[55] Different lipid membranes, such as liposomes and bilayers, are developed as models in laboratory using mixture of various phospholipids for the understanding of complex biological membrane properties.[55] In addition to the presence of different proteins, the ratio between different phospholipids may affect the physicochemical properties of lipid membrane.

In cell membranes, phospholipids are distributed asymmetrically between the outer and inner monolayer of cell membranes.[56] Outer monolayer generally contains of choline type lipids, *e.g.*, sphingomyelin (SM) and phosphatidylcholine (PC). On the other hand, the inner monolayer contains amine comprising lipids, such as, phosphatidylethanolamine (PE) and phosphatidylserine (PS). PS, PC and phosphatidylinositol (PI) normally allow ion or water to bind at their head group with resulting the formation of charged or hydrated surface. Conversely, PE lipids provide poorly hydrated surface that hinder protein to bind at surface. Notably, the outer membrane leaflet contains ~70% of PC and SM types in its lipids composition. Vesicles obtained from the lipid

mixture of PC and SM or mixture of PS and PE with various cholesterol mol% (0–50) behave to mimic mammalian cell membrane.[57]

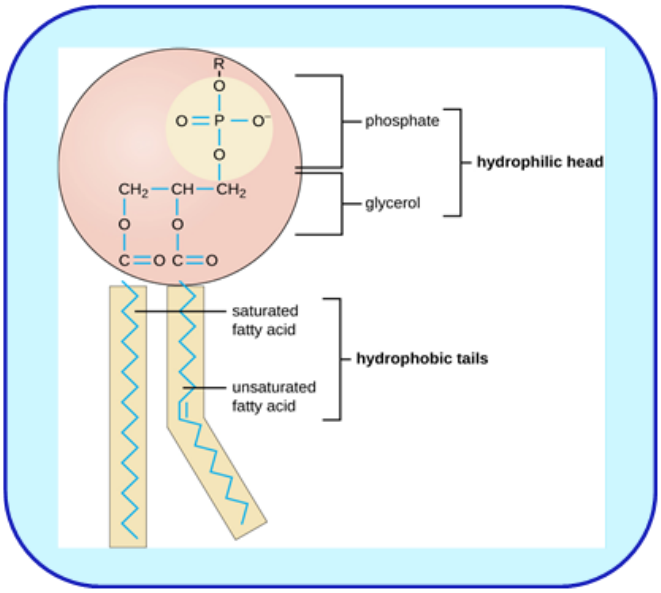

Figure 9. Structure of phospholipid molecule.

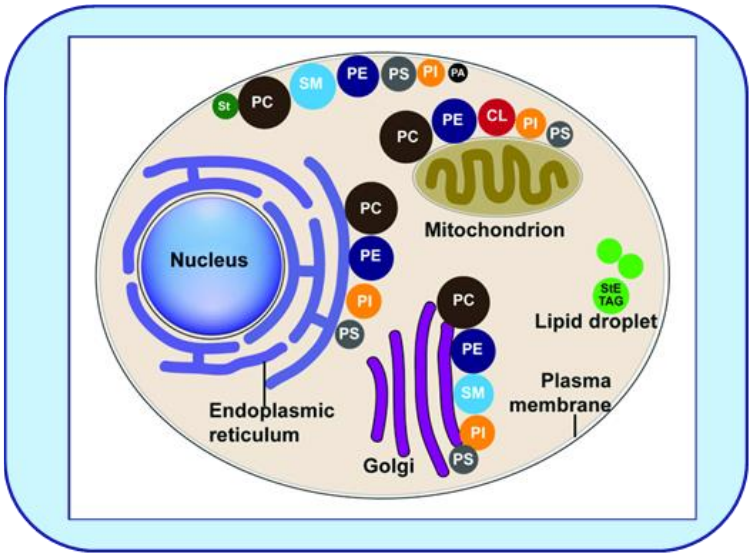

Figure 10. The distribution of major lipids in host organelle membranes. Different colors of circles represent different lipid classes, and the size of circles represent the percentage of one class of lipid to the total phospholipids, as modified from van Meer et al. (2008). CL, cardiolipin; PA, phosphatidic acid; PC, phosphatidylcholine; PE, phosphatidylethanolamine; PS, phosphatidylserine; PI, phosphatidylinositol; SM, sphingomyelin; St, sterol; StE, steryl ester; TAG, triacylglycerol.

In addition to PC, PE types of lipids, bi-anionic phospholipid, cardiolipin (CL) has been found exclusively in the mitochondrial membrane (Figure 10).[58] The lipid composition of mitochondrial membrane is characterized by (i) PC (40%) and PE (30%) and high level of CL (10%–15% of the total lipids composition). Moreover, mitochondrial membrane also contains a low amount of cholesterol and sphingolipids. CL contains a glycerol head group linked with two negatively changed phosphatidyl moieties. CL can be classified based on number of alkyl unsaturation such as, monounsaturated tetraoleoyl cardiolipin (TOCL) and fully saturated tetramyristoyl cardiolipin (TMCL).[59] Vesicles consisting of the lipid composition of DOPC:DOPE:CL:cholesterol = 2.0:1.3:1.0:0.6 molar ratio which is similar to the lipids composition for the mitochondria inner membrane are often used to evaluate the properties of mitochondrial membrane.

Nuclear membrane contains a large fraction of phospholipids (~62% of the total lipid fraction), as well as other neutral biomolecules such as cholesterol, free fatty acids, triglycerides. In their lipid's composition, major phospholipids are PC (55%) and PE (23%), while a small percentage of PI (8%) and PS (6%) types of lipids are also present.[60] Vesicles with lipid composition of DOPC and DOPE with maintaining the similar lipids ratio are generated *in vitro* as a model of the nuclear membrane.

1.3. Interface of amphiphilic self-assemblies and bio-membrane

The interface of the self-assembled system can be defined as the separating region between the bulk aqueous phase and interior hydrophobic core region. The physiochemical properties of the interface are widely different than that of bulk phase or interior hydrophobic phase. The interface of bio-membrane is one of the most crucial locations for many biochemical reactions.[61,62] It has been observed that interface shape and structure of different bio-membrane controls the morphology of organelles and local membrane subdomains.[63-66] Researcher have found that a specific geometry at the membrane interface is required for a particular bio-chemical reactivity.[67,68] Intrinsically, the membranes interface is continually turned over by trafficking intermediates to generate high curvature compartments for all eukaryotic cells.[69] There are five major processes occurred in the biological membrane interface can change the shape and structure of the membrane (Figure 11).[67] Membrane interface can be dynamically modulated because of (i) partitioning of shaped transmembrane domains of integral membrane proteins or domain crowding, (ii)

asymmetry in the lipid composition, (iii) formation of nanoscopic scaffolding by oligomerized hydrophilic protein domains (iv) reversible insertion of hydrophobic protein motifs, and (v) macroscopic scaffolding by the cytoskeleton with forces generated by polymerization and by molecular motors in membranes interface. For example, the shape of the membrane interface is induced by polymerization of the cytoskeleton protein actin.[70] The presence of actin in the cellular membrane plays most essential role for the change in the shape of the membrane interface as well as cell division or cell transfer processes.

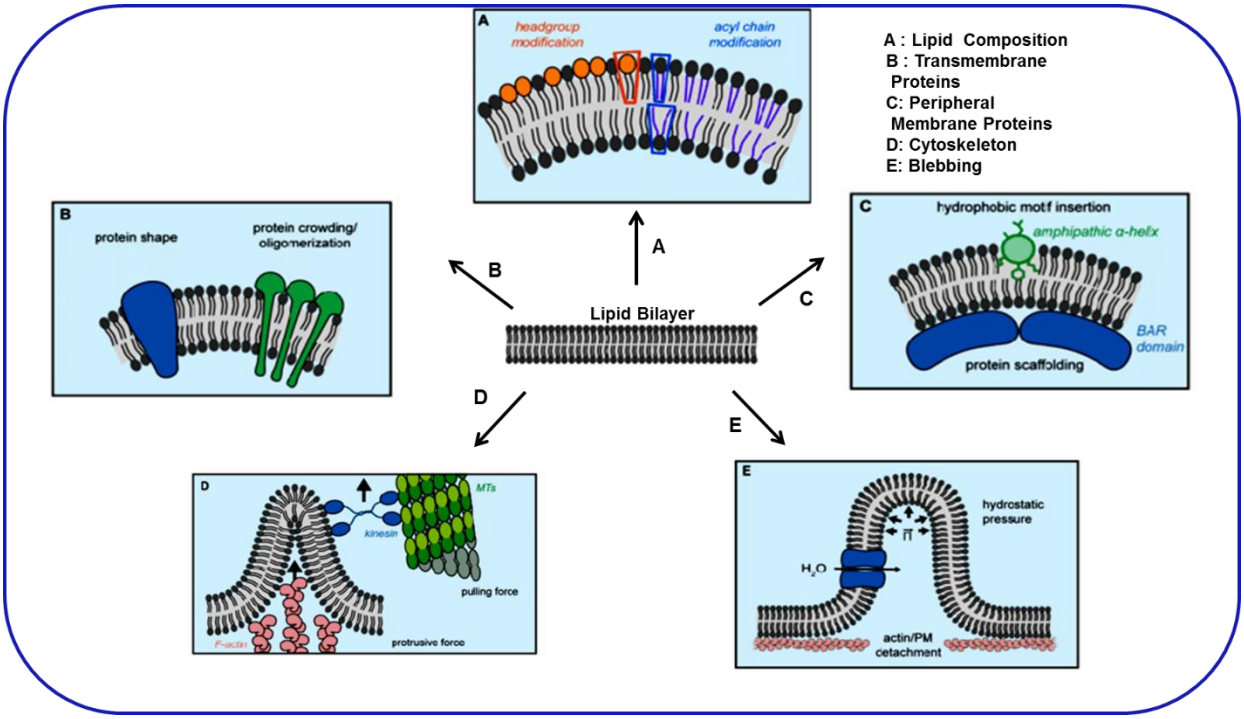

Figure 11. Different structure and shape of interface for lipid bilayer membrane which can be induced by different mechanism.

In general, the membrane curvature is usually attributed to either positive or negative depending on the relative area of the polar head group and the nonpolar acyl chain length of the amphiphilic molecule (Figure 12).[67] However, some lipid molecule such as phosphatidyl choline (PC) and phosphatidyl serine (PS) do not insert any influence on the membrane curvature geometry.[71] These lipids tend to set up a flat monolayer/bilayer with zero curvature, *i.e.* neither bend towards water nor the nonpolar acyl chain region. Amphiphilic molecule with smaller head group than that of PC type of lipid, such as phosphatidylethanolamine (PE) and cardiolipin (CL)

have conical shape that inducts the negatively curved (concave) membrane interface.[72] In this case, interface bends towards nonpolar acyl chain region and experiences less exposure to aqueous medium. On the other hand, lipids containing larger head group like phosphatidylinositol phosphates (PI) or large area ratio of polar head group to nonpolar acyl chain like lysophosphatidyl choline (LPC) acts as conical shaped lipids to generate positive (convex) membrane curvature.[73] For the positive curvature, the interface is tilted towards the water and becomes highly exposed to the water medium. Thus, membrane geometry helps to define local membrane environments holding unique properties through a specific curved configuration (positive/negative or zero).

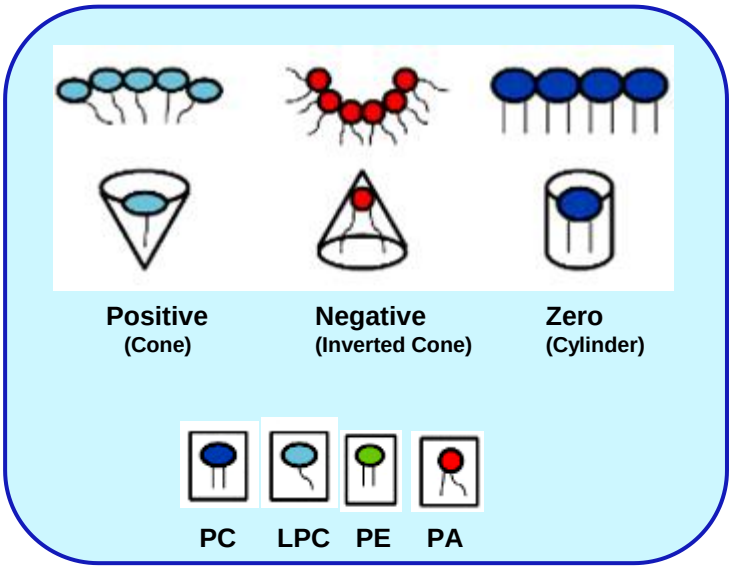

Figure 12. Representation of membrane curvature interface formed by lipid molecule.

1.4. Biochemical reactivity at membrane interface

The bio-membrane plays pivotal role to control many fundamental biochemical processes. It separates the intracellular compartments from the exterior of cell.[74,75] Bio-membranes consists of lipid bilayer and proteins that embedded or bound at the membrane interface.[76] Lipid bilayer creates a hydrophobic semipermeable barrier due to the presence of proteins in the membrane for aqueous solutes. The membrane bound proteins initiate various types of reactions at the membrane surface.[77]

1.4.1. Effect of interface structure and shape

It has been observed that the capacity of bio-membrane interface to curve and adapt their new configurations are crucial for biochemical reactivity at membrane surface, such as, membrane trafficking, membrane fission or fusion, signal transduction, and cell motility.[78] The formation of numerous intracellular membrane interfaces permits the cell to compartmentalize proteins, where protein containing domains or motifs with various curvature are essential for specific interface bio-reactivity.

Bio-membrane interface shape/structure are defined in terms of the geometrical notions of principal curvatures or radii of curvature. The interactions of protein with the membrane interface are preliminary responsible to observe different extent of curved membrane surfaces (Figure 13). Both electrostatic and hydrophobic interaction between lipids and proteins are crucial factors to determine the specific membrane shape. Transmembrane proteins with intrinsic or inverted conical shapes can bend their attached membranes.[79] Asymmetry of extra membrane domains of transmembrane proteins can also lead to bending. Many integral proteins in membrane are oligomerized, either directly between themselves or through attaching with proteins, which effects the native scaffolding at the membrane interface.[67] The BAR (BIN-Amphiphysin-Rvs) and cytochrome *c* (cyt *c*) protein interaction at the membrane interface are highly correlated with specific membrane curvature.[67] The peripheral protein, cyt *c* binds towards the side of the CL-containing membrane which minimizes the bending stress due to the large negative curvature.[80] The enzymatic activity of phosphocholine cytidylyltransferase is occurred under a specific membrane curvature condition. The functions of membrane bound epsin protein are highly dependent of the local membrane curvature. Epsin creates a particular membrane curvature through insertion of an amphipathic domain into the lipid matrix. The ability of epsin to bend membranes is associated to the insertion of its ENTH-domain amphipathic helix into the membrane bilayer.[81] In addition, amphiphycin can also work to create curvature at the interface by inserting its amphipathic helix into lipid monolayer.

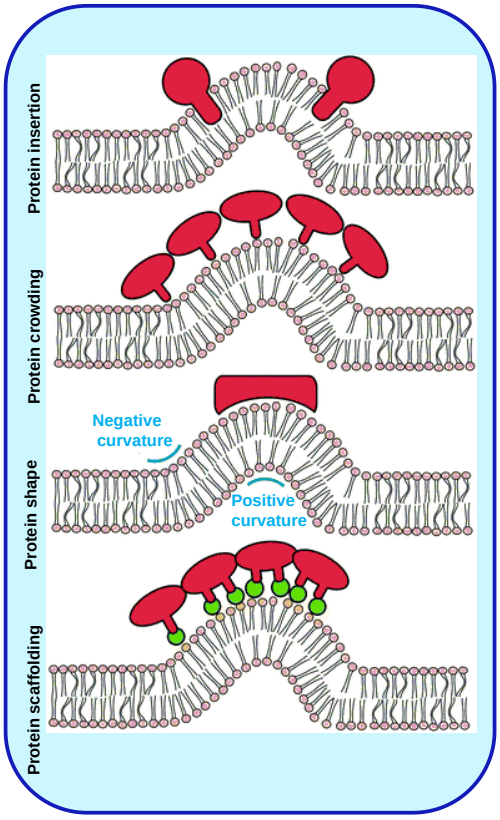

Figure 13. Different mechanisms in order to produce membrane curvature.

1.4.2. Effect of various physiochemical properties

Various physiochemical properties such as pH/polarity, ionic concentration, fluidity and temperature have pronounced effect on various bio-membrane reactivity. The activity of membrane-bound enzyme is affected by the physical state of the lipid bilayer which in turn is affected by temperature.[82] An elevated temperature is highly susceptible to enhance membrane fluidity and permeability *via* modifications in the lipid composition and/or interactions between lipids and proteins.[83]

pH and polarity induced various receptors-based reactions have taken place at the membrane interface. Synthesis of adenosine triphosphate (ATP) *via* oxidative phosphorylation of adenosine diphosphate (ADP) for eukaryotic cell and the activation of inorganic phosphate by the ATPase enzyme for bacteria cells occurs at the inner mitochondrial membrane and plasma membrane respectively (Figure 14).[84,85] A considerable extent of pH difference between exterior and interior of the membrane activates those processes. ATP hydrolysis at inner mitochondrial membrane

makes K^+/Na^+ ionic imbalance between interior and exterior of a cell.[86] Lipid peroxidation to initiate cell apoptosis process is occurred at the cellular membrane interface. The presence of high concentration of polyunsaturated fatty acids at bio-membranes activates the peroxidation process.[87] Peroxidation process causes severe damage to membranes function, lethal effects on the cellular division, enzymatic inactivation and so on.[88] A certain pH/polarity value around membrane surface is prerequisite to generate various oxygen-containing free radicals (*e.g.*, hydrogen peroxide, superoxide, nitric oxide, and hydroxyl radicals) and affects for the oxidation of essential cell components.

Fluidity of the bio-membrane increases with the increase of solution temperature.[83] Higher temperature makes the fatty acid tails of phospholipids less rigid and allows excess movement of proteins and other molecules in and through the membrane. When the fatty acid tails of the phospholipids at bio-membrane are more rigid at low temperature, the reduced fluidity of the bio-membrane affect its permeability with restricting entry of important molecules such as oxygen and glucose into the cell. On the other hand, electrostatic interactions between ions and the lipid membrane plays vital role for lipid phase transitions, membrane fusion, or transport of material across the membrane. It has been observed that bio-membranes are surrounded by Na^+, K^+, Ca^{2+}, Mg^{2+}, or Cl^- ions with quite different concentrations outside and inside of the cell.[90,91] The interactions of divalent cations with charged lipid membrane are usually strong but relatively weak for the zwitterionic lipid membrane.

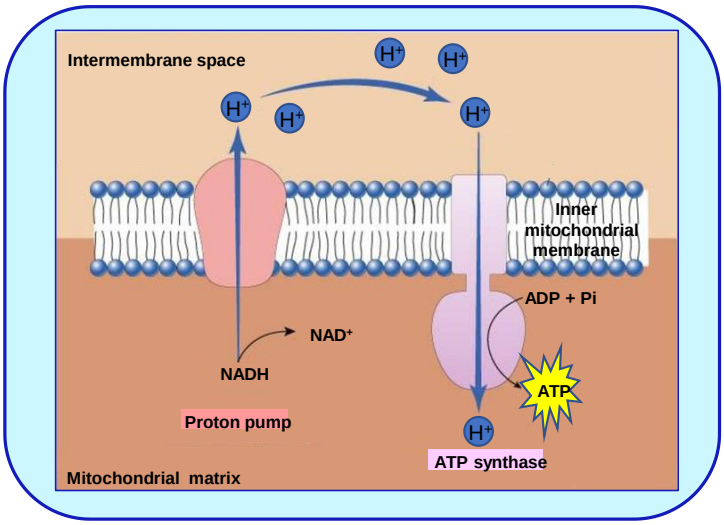

Figure 14. ATP synthesis in the inner membrane of mitochondrion.

1.5. Interfacial pH and polarity values

1.5.1. Why detection of membrane interfacial pH/polarity is important?

Biomolecule acid-base equilibria at cellular membrane interfaces are crucial for many biochemical processes, because most of the biological molecules carry acidic-basic groups that modulate their structure and interactions depending on surrounding pH/polarity.[92,93] Indeed, local pH around the membrane interface affects membrane potential, membrane reactivity, and movement of substances across the membrane surface.[92] The production of ATP by oxidative phosphorylation and ADP-ATP translocation in mitochondria require an optimum proton gradient between the inner and outer mitochondrial membrane.[94,95] Remarkably, some vital membrane functionalities are associated with pH heterogeneities existed at various cellular locations. The protonation/deprotonation equilibrium of phospholipids influences on the optimal membrane curvature to affect the activity of signaling proteins.[96,97] The transportation of amino acids, protein, different chemical species, drugs, inorganic ions occur under a condition of an optimal pH/polarity value at the membrane surface.[92] In addition, the membrane pH plays critical role on various metabolic activation processes, stimulus-response coupling, cell cycle and proliferations.

Water concentration or polarity at the membrane surface is also vital parameter for various polarity-controlled membrane biological processes.[98,99] For example, membrane fusion process is assisted by the elimination of surface-bound water, and the rate of this process is moderated by the change of local polarity or water concentration. Membrane interfacial polarity also plays pivotal role in the substances binding to the lipid membrane bilayer.[98] Binding of protein kinase *c* to the membranes surface is also regulated by the interfacial polarity. Most importantly, the polarity at the lipid membrane interface is a prime indicator for the targeted drug delivery to the cell.[100,101]

Therefore, a precise understanding of the pH/polarity at the lipid membrane interface is essential.

1.5.2. Measurement difficulties

The monitoring of interfacial pH and polarity for self-assemblies are really difficult task due to highly complex micro-heterogeneous compartmentalization with uncertainty of its bulk phase contribution. Researcher have suggested a significant discrepancy in pH and polarity values at the interface than its bulk phase value for different amphiphilic self-assembled systems.[102-106] P.

Mukerjee *et. al.* have shown a difference in H^+ ion concentrations between the bulk and the interface for anionic micelles using pH indicating probe molecule, although the bulk phase uncertainties in the measurement procedure are not thoroughly investigated.[105] C. Graham Knight *et. al.* have assessed a considerable difference in pH between cellular interface and its surrounding bulk phase value by exploiting fluorescence response changes of probe molecule upon its binding with the lipid membrane (phosphatidylethanolamines) interface.[107] By monitoring the polarity induced pK_a changes of a dye molecule, Marta S. Fernandez and Peter Fromherz have shown that the interfacial polarity value for micelle is lower than that of bulk aqueous phase.[108] In another similar study, D. P. Cistola and coworkers have displayed that local dielectric constant of the bilayer lipid surface is lower than that of the bulk by monitoring the apparent pK_a changes of a polarity sensitive optical molecular probe.[109] Even though all those investigations have shown a considerable discrepancy in pH/polarity value between the interface and the bulk, an accurate pH/polarity estimation at a specific interfacial depth have rarely been addressed.

Optical probe method can be experimentally very simple to estimate interfacial pH/polarity for complex self-assembled micelle, polymeric micelle and phospholipid membranes. However, the applicability of this method is to be highly relied on the interface binding properties of the probe molecule.[110,111] A strong binding of probe molecule to the interface is an important criterion to obtain an accurate interfacial pH/polarity value. Moreover, a quantitative separation of the background optical signal due to surrounding bulk phase from the interfacial optical response is also necessary to detect interfacial pH/polarity accurately. Weakly interface binding probes are less effective as its large fraction remains at the bulk phase instead of the interface. To exclude the contribution of the bulk phase, thus a strong interface binding probes are highly recommended. Again, the understanding of probe localized depth within the interface is vital because pH/polarity value can also change significantly with a small alteration of the depth along the interface cross-section. Moreover, since proton dissociation equilibrium of optical pH-probe used in the method are generally dependent on the local polarity, the pH-induced optical responses of probes may contribute to the optical responses resulting from their polar differences.[110-112] Therefor it is very common that optical response of the probe is affected by both local pH and polarity. In order to measure the interfacial pH exclusively, the knowledge of interfacial polarity value is also necessary, and thus simultaneous detection of both pH and polarity in the interface is essential.

1.5.3. Major development

Tahara and coworker have reported a sensitive interfacial pH detection method for various self-assembled systems.[113,114] Heterodyne-detected electronic sum frequency generation (HD-ESFG) spectroscopic method was used to estimate pH values at ionic micelle and lipid/water interface with monitoring acid-base interconversion properties of an indicator molecule adsorbed at the interface. The studies reveals that the pH at the charged lipid/water interfaces is considerably different from the bulk pH. Although the method is intrinsically surface-selective with submonolayer sensitivity, highly complicated instrumental methodology may not be always useful to detect interfacial pH/polarity for complex biological membrane systems.

Recently, Y. Sarkar *et al.* have introduced UV-Vis absorption and fluorescence optical probe method to estimate pH/polarity values at the interface of different self-assembled systems.[110,111] The pH dependent acid/base equilibrium of the probe molecule at the interface was monitored using simple UV-Vis absorption and fluorescence spectroscopic studies to evaluate the interfacial pH value.[115,116] In consistent with previous studies of Tahara group, the pH value at cationic interface is observed to be higher than that of the bulk phase.[113,114] However, the anionic interface for various self-assembled systems is more acidic than the corresponding bulk phase acidity. They argued that interfacial charge character is mainly responsible for the nature of pH deviation between the bulk and the interface. Furthermore, the effect of the curvature (concave/convex) radius on interfacial pH/polarity value for different self-assemblies was monitored. They also evaluated interfacial pH for the membrane interface with the similar lipid composition of inner mitochondrial membrane (IMM). The presence of bi-anionic CL causes much higher pH deviation (~3 pH unit) than that observed (~ 2 pH unit) for the membrane interface containing mono-anionic lipid.[117]

1.6. Relation of interfacial pH/polarity with interface head group properties

The interfacial pH/polarity values are highly dependent on amphiphilic self-assembly head group character.

1.6.1. Interface charge character

It has been reported that the nature of pH deviation at the interface from the bulk phase is dependent on the head group change character.[110,111] For positively charged interface, oppositely charged OH^- ions present in bulk solution is attracted electrostatically to the interface, whereas the interface repels the positively charged H^+/H_3O^+ ions. As a result, the concentration of OH^- ions increase at the interface than that of the bulk phase, while concentration of H^+/H_3O^+ ions become higher in the bulk phase compared to the interface (Figure 15). Thus, the pH value at the interface becomes higher with respect to the pH value of bulk phase. For negatively charged interface, an increase of H^+/H_3O^+ ion concentration with respect to the bulk phase value due to its attractive interaction with the interface causes the interface more acidic compared to the bulk phase acidity. However, the H^+/H_3O^+ or OH^- concentration gradient between the interface and the bulk is expected to be less for non-ionic or zwitterionic head group contained self-assembled systems, and thus the pH deviation is observed to be much lower than that detected for positive or negatively charged interface.[110,111]

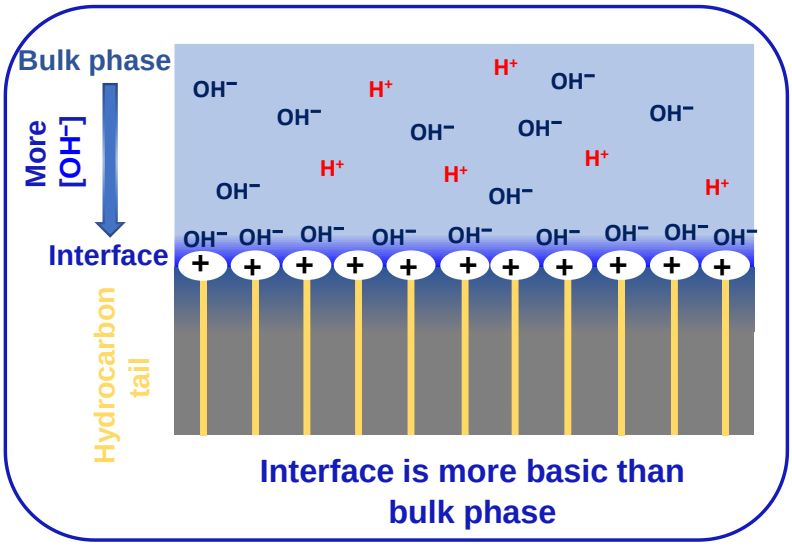

Figure 15. Schematic view of the distribution between H^+ and OH^- ions at the interface for cationic amphiphilic self-assembled systems.

1.6.2. Interface shape and size

Interface shape and size of self-assembled systems are mainly depended upon the properties of head group residue of the amphiphilic molecule.[67] More specifically, the area of the lipid polar

head group relative to that of the hydrophobic tail part should have pronounced role on the relative extent of surface bending or effective curvature radii values. Therefore, the relative head group area plays most critical role to determine the interface shape/structure for various self-assembled systems. Self-assembly molecule with a large area ratio of the polar head groups to the nonpolar acyl chains spontaneously forms positive (convex) curvature radius, while molecule with the opposite ratio value produces negative (concave) curvature radius.[67]

It has been shown that specific curvature radius should have pronounced role on interfacial pH/polarity value.[111,118,119] In case of negatively curved interface, the solvent exposed head group area is smaller compared to that of positively curved interface due to closed head group packing which essentially restricts the electrostatic interaction of solvated H^+/OH^- with the charged head groups. Thus, a significantly lower extent of water and H^+/OH^- penetration into the interface Stern layer from the bulk medium can happen (Figure 16). As a result, pH or polarity deviation from the bulk to the interface value will decrease with the decreasing value of negative curvature radius. Since the head groups for positively curved interface are fairly well exposed to the bulk solvent medium, a further improvement of the interaction between solvated H^+/OH^- with the charged head groups are not possible. As a result, the difference in H^+/OH^- distribution from the bulk to interface is to be remain unchanged with the change in curvature radii of positively curved surface.

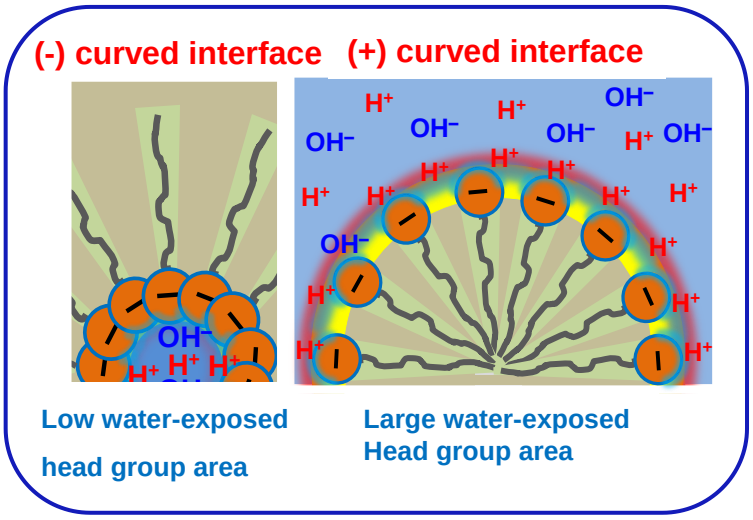

Figure 16. Schematic representation of the curvature-radius-dependent change in pH deviation from the bulk to the interface and interfacial polarity for anionic positively and negatively curved interfaces under the neutral bulk pH condition.

1.6.3. Interfacial depth

Interface is considered to be the separation between the bulk aqueous phase and the self-assembled interior oil phase. The hydrophobic character of the interface is expected to increase with the increase of interfacial depth from water exposed stern layer, because the hydrocarbon chains accumulate in the inner region of self-assembled micelle or vesicle. Therefore, the extent of water concentration is to be decreased gradually with the increase of interfacial depths and as a result the polarity value along the interfacial depth is found to be significantly lower than that of its bulk phase value. On the other hand, since H^+/OH^- ion exists as its water-solvated form, the change of interfacial depth induced penetration of H^+/OH^- ions is also affected to a similar way as that observed for the change in water penetration abilities along the several interfacial depth. Consequently, interfacial pH value should be highly dependent on the interfacial depth.

By exploiting NMR spectroscopy and neutron scattering experiments, researchers have found that the occupation of water molecules at the interface decreases sharply as moving more towards the inner hydrophobic region within the interface.[120-123] Molecular dynamics (MD) simulations also show that the density of water actually decreases with the depth of the interface.[124-126] M. P. Gierula *et. al.* have revealed that the water penetration ability can change significantly with the relative local distributions of polar head group residues within the interface width. When the polar groups of lipids are distributed an up-and-down fashion with maintaining non-uniform distances with respect to bulk water phase, interfacial depth induced a difference in interface water concentration is reported for model lipid membrane systems. It has been shown that most of the water molecules are located in the polar head group localized region where water molecules are attached with the phosphate groups through hydrogen bonding and a small water fraction binds with the carbonyl groups located deep in the lipid bilayer.[124,125] Sobhan Sen and co-worker have investigated depth-dependent change in interfacial polarity or hydration property using polarity sensitive probe molecule containing 4-aminophthalimide moiety. The results are further justified by molecular dynamic simulation.[127] D. C. Crans and coworkers have shown that the extent of ^1H NMR chemical shift of the molecular probe due to change in its location from the bulk to the interface is an important parameter to estimate the interfacial polarity value.[128]

1.7. Thesis overview

This thesis is structured into five leading chapters.

Chapter 1 highlights a brief introduction on the basic concept of self-assembled molecules and their correlation with bio-membrane. The importance of membrane interface along with physicochemical properties at the interface are also amalgamated in this chapter. A concise literature survey on the development and future scope on membrane interfacial pH/polarity measurements have been included in this chapter.

Chapter 2 introduces the materials and methods along with detail instrumentation procedures like UV-Vis absorption and fluorescence spectrometry, fluorescence lifetime and DSC measurements. In this chapter, synthesis of interface interacting different pH and polarity sensing probe molecules and preparation of different amphiphilic self-assembled systems are also described.

Chapter 3 presents a simple UV-Vis absorption method to estimate interfacial polarity by utilizing an interface interacting Schiff-base molecule for different self-assembled systems: anionic SDS and sodium taurocholate, cationic CTAB and tri-block co-polymer (TBP), neutral triton X-100 (TX-100), and anionic 1, 2-dimyristoyl-sn-glycero-3-phosphoryl-glycerol (DMPG) phospholipid. An interface interacting Schiff base probe molecule, 2-((2-(pyridine-2-yl) ethylimino) methyl)-6-(hydroxymethyl)- -methylphenol (PMP) exists in equilibrium between non-ionic and zwitterionic forms and their interconversion is dependent on solvent polarity. The probe localized environmental polarity is estimated by exploiting the interconversion equilibrium from one to another molecular form. The specific interface localization in versatile amphiphilic self-assembled systems have been utilized to monitor their interfacial polarity and its deviation from the bulk phase value by monitoring the shift of acid/base equilibrium value of the probe molecule at the interface than that of the bulk phase value.

Chapter 4 describes the detection of both the interfacial pH and polarity of various amphiphilic self-assembled micelles and vesicles at a similar interface location using an interface interacting Schiff-base molecule. The synthesized Schiff-base molecular probe containing two identical phenol-conjugated-imine functional groups (SBOH-Z-SBOH) exists in equilibrium between non-ionic and zwitterionic forms and their interconversion is dependent on solvent polarity, which is useful to monitor polarity value. Additionally, the solvent pH-dependent equilibrium conversion of both neutral and partially zwitterionic form into the deprotonated di-anionic species is permitted us to monitor the local pH value.

Chapter 5 describes simultaneous assessment of interfacial pH and polarity for amphiphilic self-assemblies. For this, we have synthesized a glucose-pendant porphyrin (GPP) molecule as simultaneous pH and polarity detecting probe. pH-induced protonation equilibrium and polarity-dependent π-π stacking aggregation for GPP are exploited to measure pH and polarity changes at the DMPG membrane interface during DMPG phase transition. An NMR studies have confirmed us that GPP is located at the interface Stern layer of DMPG LUV. Using UV-Vis absorption studies, we have estimated interfacial pH, or its deviation from the bulk phase value (ΔpH), and the interfacial polarity simultaneously using the same UV-Vis absorption spectra. During temperature-induced gel to liquid-crystalline phase transition of DMPG, an increase in both pH-deviation and interfacial dielectric constant were observed.

1.8. References

1. D. Lombardo, M. A. Kiselev, S. Magazù and Pietro Calandra, *Adv. Condens. Matter Phys.*, 2015.
2. Y. Mai and A. Eisenberg, *Chem. Soc. Rev.*, 2012, **41**, 5969.
3. J. Israelachvili, 3rd Ed., Academic Press: London, 2011.
4. V. Villa and R. Hashimb, *Curr. Opin. Colloid Interface Sci.*, 2002, **7**, 395.
5. G. L. Jendrasiak, *J. Nutr. Biochem.*, 1996, **7**, 599.
6. J. A. Hutchinson, S. Burholt and I. W. Hamley, *J. Pept. Sci.*, 2017, **23**, 82.
7. A. Dehsorkhi, V. Castelletto and I.W. Hamley, *J. Pept. Sci.*, 2014, **20**, 453.
8. N. C. Seeman, *Nature*, 2003, **421**, 427.
9. J. Zheng, J. J. Birktoft, Y. Chen, T. Wang, R. Sha, P. E. Constantinou, S. L. Ginell, C. Mao and N. C. Seeman, *Nature*., 2009, **461**, 74.
10. H. W. Gibson, N. Yamaguchi and J. W. Jones, *J. Am. Chem. Soc*., 2003, **125**, 3522.
11. O. J. Plante, E. R. Palmacci and P. H. Seeberger. *Science*. 2001, **291**, 1523.
12. M. Ramanathan, L. K. Shrestha, T. Mori, Q. Ji, J. P. Hill and K. Ariga, *Phys. Chem. Chem. Phys.*, 2013, **15**, 10580.
13. T. F. Tadros, *Wiley-VCH Verlag GmbH & Co. KGaA*, Weinheim, 2005.
14. P. Sar1, A. Ghosh, A. Scarso and Bidyut Saha, *Res. Chem. Intermed.*, 2019, **45**, 6021.
15. T. Fan, X. Yu, B. Shen and L. Sun, *J. Nanomater.*, 2017.

16. Y. Yang, S. Wang, Y. Wang, X. Wang, Q. Wangc and M. Chen, *Biotechnol. Adv.*, 2014, **32**, 1301.
17. H. S. Yoo, J. E. Lee, H. Chung, I. C. Kwon and S. Y. Jeong, *J. Control. Release*, 2005, **103**, 235.
18. Y. Lim, T. Kim, J. W. Lee, S. Kim, H. Kim, K. Kim and J. Park, *Bioconjugate Chem.*, 2002, **13**, 1181.
19. S. Ghosh, A. Ray and N. Pramanik, *Biophys. Chem.*, 2020, **265**, 106429.
20. J. Eastoe and J. S. Dalton. *Adv. Colloid Interface Sci.*, 2000, **85**, 103.
21. K. Holmberg, B. Jonsson, B. Kronberg and B. Lindman, 2nd Ed. *Wiley and Sons Ltd: Chichester*, 2002.
22. M. Z. Elsabeea, R. E. Morsi and A. M. Al-Sabagh, *Colloids Surf. B*, 2009, **74**, 1.
23. C. Tanford, *Krieger: Malabar*, 1991.
24. D. Lombardo, M. A. Kiselev, S. Magazu and P. Calandra, *Adv. Condensed Mat. Phys*., 2015, **2015**, 22.
25. A. Sorrenti, O. Illa and R. M. Ortuño, *Chem. Soc. Rev.*, 2013, **42,** 8200.
26. R. Srinivas, S. Samanta and A. Chaudhuri, *Chem. Soc. Rev*., 2009, **38**, 3326.
27. J. Jesse and Williams, *Handbook for Cleaning/Decontamination of Surfaces*, 2007, **1**, 103.
28. J. Zhao,a Caili Dai, Q. Ding, M. Du, H. Feng, Z. Wei, A. Chenb and M. Zhao, *RSC Adv*., 2015, **5**, 13993.
29. M. Fariya, A. Jain, V. Dhawan, S. Shah and M. S. Nagarsenker, *Adv Pharm Bull*, 2015, **4**, 483.
30. F. M. Menger and J. S. Keiper, *Angew.Chem. Int. Ed.*, 2000, **39**, 1906.
31. J. P. Hill, L. K. Shrestha, S. Ishihara, Q. Ji and K. Ariga, *Molecules*, 2014, **19**, 8589.
32. Y. Mai and A. Eisenberg, *Chem. Soc. Rev.*, 2012, **41**, 5969.
33. G. Liu, Y. Wei, F. Gao, S. Yuan and C. Liua, *Phys.Chem.Chem.Phys*., 2016, **18**, 11357
34. C. Pignet, *Rsc. adv.*, 2010 46: 6209.
35. L. Wang, C. Gong, X. Yuan and G. Wei, *Nanomaterials*, 2019, **9**, 285.
36. C. Kulkarni, K. K. Bejagam, S. P. Senanayak, K. S. Narayan, S. Balasubramanian and S. J. George, *J. Am. Chem. Soc.*, 2015, **137**, 3924.
37. S. Yasuda, K. Miyake, J. Sumaoka, M. Komiyama and H. Shigekawa, *Jpn. J. Appl. Phys.*,1999, **38** ,3888.

38. B. Sun, M. Wang, Z. Lou, M. Huang, C. Xu, X. Li, L. Chen, Y. Yu, G. L. Davis, B. Xu, H. Yang and X. Li, *J. Am. Chem. Soc.*, 2015, **137**, 1556.
39. S. Prusty and Y. Chan, *Chem. Lett*., 2021, **50**, 1202.
40. L. He, S. Wang, L. Lin, J. Cai, L. Li, T. Tu and Y. Chan, *J. Am. Chem. Soc.*, 2020, **142**, 7134.
41. Y. Zhang, Z. Guo and L. Zhang, *Materials Today*, 2019, **25,** 112.
42. P. Schurtenberger, *Curr. Opin. Colloid Interface Sci.*, 1996, **1**, 773.
43. B. A. Grzybowski, K. Fitzner, J. Paczesny and S. Granick, *Chem. Soc. Rev.*, 2017, **46**, 5647.
44. B. V. Amsterdam, *Handbook of Biological Physics. Elsevier Science*, 1995, 97.
45. S. Song, A. Song and J. Hao, *RSC Adv.*, 2014, **4**, 41864.
46. N. Muller, J. Pellerin and W. Chem, *J. Phys. Chem.*, 1972, **76**, 3012.
47. N. A. N. Hanafy, M. El-Kemary and S. Leporatti, *Cancers*, 2018, **10**, 238.
48. O. V. Borisov, E. B. Zhulina, F. A. M. Leermakers and A. H. E. Müller, *Adv. Polym. Sci.*, 2011, **241**, 57.
49. W. D. Van Horn, M. E. Ogilvie and P. F. Flynn, *J. AM. CHEM. SOC.*, 2009, **131,** 8031.
50. M. D. Chatzidaki, K. D. Papavasileiou, M. G. Papadopoulos and A. Xenakis, *Langmuir*, 2017, **33**, 5077.
51. G. Tresset, *PMC Biophys.*, 2009, 2, 3.
52. A. Akbarzadeh1, R. R. Sadabady, S. Davaran1, S. W. Joo, N. Zarghami1, Y. Hanifehpour, M. Samiei, M. Kouhi and K. N. Koshki1, *Nanoscale Res. Lett.*, 2013, **8**, 102.
53. P. B. Devhare and R. B. Ray, *Mol. Asp. Med.*, 2018, **60,** 115.
54. Caforio and A. J.M. Driessen, *Biochim. Biophys. Acta*, 2017, **1862**, 1325.
55. B. Alberts, A. Johnson, J. Lewis, M. Raff, K. Roberts and P. Walter, *Molecular Biology of the Cell*, *4th edition*, Garland Science, 2002.
56. K. B. Battaglia1 and R. J. schimmel, *J. Exp. Biol.*, 1997, **200**, 2927.
57. Q. Lin and E. London, *PLoS one*, 2014, **9.**
58. J. R. Joachim, Krebs, H. Hauser and E. Carafoli, *J. Biolg. Chem*., 1979, **254**, 5308.
59. I. G. Zigoneanu1, Y. J. Yang, A. S. Krois, E. Haque and G. J. Pielak, *Biochim Biophys Acta*. 2012, **1818**, 512.
60. H. Kleinig, *J. cell. Biolg*., 1970, **46**, 396.

61. A. Rosado and E. M. Bayer, *Plant Physio.*, 2021, **185**, 650.
62. M. Faini, R. Beck, F.T. Wieland and J.A. Briggs, *Trends Cell Biol.*, 2013, **23**, 279.
63. K. M. Kim, T. Qin, Y. Jiang, M. Xiong, D. Caetano-Anolles, H. Y. Zhang and G. Anolles, *Structure*, 2012, **20**, 67.
64. A. J. G. Saez and P. Schwille, *Biochim. Biophys. Acta, Biomembr.*, 2010, **1798**, 766.
65. M. Eeman and M. Deleu, *Bio. Technol. Agron. Soc. Environ*. 2010, **14**, 719.
66. D. B. Landry, D. C. Clarke and M. J. Lee, *J. Mol. Biol.*, 2015, **427**, 3416.
67. H. T McMahon and J. L. Gallop, *Nature*, 2005, **438**, 590.
68. Y. Shibata, J. Hu, M. M. Kozlov and T. A. Rapoport, *Annu. Rev. Cell Dev. Biol.*, 2009, **25**, 329.
69. H. T. McMahon and E. Boucrot, *J. Cell Sci.*, 2015, **128**, 1065.
70. C. Simon, V. Caorsi, C. Campillo and C. Sykes, *Phys. Biol.*, 2018, **15**, 065004.
71. R. L. Thurmond, G. Lindblom and M. F. Brown, *Biochem.*, 1993, **32**, 5394.
72. J. Israelachvili, D. J. Mitchell and B.W. Ninham, *J. Chem. Soc., Faraday Trans.*, 1976,**72,** 1525.
73. L. V. Chernomordik and M. M. Kozlov, *Annu. Rev. Biochem.*, 2003, **72**, 175.
74. H. Watson, *Essays Biochem.*, 2015, **59**, 43.
75. J. E. Beyrouthy and E. Freeman**,** *Membrane*s, 2021, **11**, 319.
76. J. L. Robertson, *J. Gen. Physiol*., 2018, **150**, 1472.
77. A. N. Bondar and S. Keller, *J. Membr. Biol.*, 2018, **251**,295.
78. D. B. Landry, D. C. Clarke and M. J. Lee, *J. Mol. Biol.*, 2015, **427**, 3416.
79. S. Aimon, A. C. Jones, A. Berthaud, M. Pinot, G. E. Toombes and P. Bassereau, *Dev. Cell*, 2014, **28**, 212.
80. C. L. Bergstrom, P. A. Beales, Y. Lv, T. K. Vanderlick and J. T. Groves, *PNAS*, 2013, **110**, 6269.
81. C. Steinem and M. Meinecke, *Soft Matter*, 2021, **17**, 233.
82. D. C. Lee and D. Chapman, Symp. Soc. Exp. Biol., 1987, **41**, 35.
83. Y. Niu and Y. Xiang, Front. Plant Sci., 2018, **9**, 915.
84. Y. Wang, R. Branicky, A. Noe and S. Hekimi, *J. Cell Biol.*, 2018, **217**, 1915.
85. W. E.G. Müller, H. C. Schröder and X. Wang, *Chem. Rev.*, 2019, **119**, 12337.
86. A. S. Pivovarov, F. Calahorro and R. J. Walker, *Invert. Neurosci.*, 2019, **19**, 1.

87. A. Catalá, *Curr. Mol. Med.*, 2007, **7**, 638.
88. D. A. Ammendolia, W. M. Bement and J. H. Brumell1, *BMC Biol.*, 2021, **19**, 71.
89. A. Phaniendra, D. B. Jestadi and L. Periyasamy, *Ind. J. Clin.* Biochem., 2015, **30**, 11.
90. R. Friendman, J. M*embr Biol.*, 2018, **251**, 453.
91. R. A. Bockmann, A. Hac, T. Heimburg and H. Grubmuller, *Biophys. J.*, 2003, **85**, 1647.
92. J. R. Casey, S. Grinstein and J. Orlowski, *Nature Rev. Mol. Cell Biol.*, 2009, **11**, 50.
93. M. I. Angelovaa,b, A. F. Bitbolc , M. Seigneuretb , G. Stanevad , A. Kodamae , Y. Sakumae , T. Kawakatsue, M. Imaie and N. Puf, *Biochim. Biophys. Acta Biomembr.*, 2018, **1860**, 2042.
94. W. Kühlbrandt, *BMC Biol.*, 2015, **13**, 89.
95. B. Kadenbach, *Biochim. Biophys. Acta*, 2003, **1604**, 77.
96. R. M. Epand, K. D'Souza, B. Berno and M. Schlame *Biochim. Biophys. Acta Biomembr.*, 2015, **1848**, 220.
97. W. F. Zeno, A. S. Thatte, L. Wang, W. T. Snead, E. M. Lafer and J. C. Stachowiak, *J. Am. Chem. Soc.*, 2019, **141**, 10361.
98. R. M. Epand and R. Kraayenhof, *Chem.Phys.* Lipids, 1999, **101**, 57.
99. Nozomi Watanabe, Keishi Suga and Hiroshi Umakoshi, *J. Chem*., 2019, **2019**.
100. A. Campetelli, D. Bonazzi and N. Minc, *Cytoskeleton*, 2012, **69**, 601.
101. S. Manes, E. Mira, C. Gomez-Mouton, R. A. Lacalle, P. Keller, J. P. Labrador and C. Martınez, *EMBO J*., 1999, **18**, 6211.
102. C. G. Knight and T. Stephens, *Biochem. J*., 1989, **15**, 683.
103. F. R. Beierlein, A. M. Krause, C. M. Jager, P. Fita, E. Vauthey and T. Clark, *Langmuir*, 2013, **29**, 11898.
104. M. A. Voinov, I. A. Kirilyuk and A. I. Smirnov, *J. Phys. Chem. B*, 2009, **113**, 3453.
105. P. Mukerjee and K. Banerjee, *J. Phys. Chem.*, 1964, **68**, 35674.
106. C. J. Drummond, F. Grieser and T. W. Healy, *J. Chem. Soc.*, 1989, **85**, 561.
107. C. G. Knight and T. Stephens, *Biochem. J*., 1989, **258**, 683.
108. M. S. Fernandez and P. Fromherz, *J. Phys. Chem.* 1977, **81**, 1755.
109. D. P. Cistola, D. M. Small, D. Atkinson and J. A. Hamilton, *Biophys. J*, 1985, **47**, 45a.
110. Y. Sarkar, S. Das, A. Ray, S. K. Jewrajka, S. Hirota and P. P. Parui. *Analyst*, 2016, **141**, 2030.

111. Y. Sarkar, R. Majumder, S. Das, A. Ray and P. P. Parui. *Langmuir*, 2018, **34**, 6271.
112. C. Reichardt, *Chem. Rev.*, 1994, **94**, 2319.
113. S. Yamaguchi, K. Bhattacharyya and T. Tahara, *J. Phys. Chem. C*, 2011, **115**, 4168.
114. A. Kundu, S. Yamaguchi and T. Tahara, *J. Phys. Chem. Lett.*, 2014, **5**, 762.
115. U. C. Saha, K. Dhara, B. Chattopadhyay, S. K. Mandal, S. Mondal, S. Sen, M. Mukherjee, S. V. Smaalen and P. Chattopadhyay, *Org. Lett.*, 2011, **13**, 4510.
116. J. T. Miao, C. Fan, X. Y. Shi, R. Sun, Y. J. Xu and J. F. Ge, *Analyst*, 2014, **139**, 6290.
117. P.P. Parui, Y. Sarakar, R. Majumder, S. Das, H. Yang, K. Yasuharab and S. Hirota, *Chem. Sci.*, 2019, **10**, 9140.
118. D. Lombardo, M. A. Kiselev, S. Magazu and P. Calandra, *Adv. Condens. Matter Phys.*, 2015, **2015**, 151683.
119. Barz, T. C. Wang and I. Kosztin, Biochim. *Biophys. Acta, Biomembr*., 2008, **1778**, 945.
120. P. L. Yeagle and R. B. Martin, *Biochem. Biophys. Res. Commun.*, 1976, **69**, 775.
121. J. M. Smaby, A. Hermetter, P. C. Schmid, F. Paltauf and H. L. Brockman, *Biochemistry*, 1983, **22**, 5808.
122. R. E. Jacobs and S. H. White, *Biochemistry*, 1989, **28**, 3421.
123. Z. Zhou, B. G. Sayer, D.W. Hughes, R. E. Stark and R. M. Epand, *Biophys. J.*, 1999, **76**, 387.
124. M. P. Gierula, Y. Takaoka, H. Miyagawa, K. Kitamura and A. Kusumi, *J. Phys. Chem. A*, 1997, **101**, 3677.
125. M. P. Gierula, Y. Takaoka, H. Miyagawa, K. Kitamura and A. Kusumi, *Biophys. J.*, 1999, **76**, 1228.
126. J. Chanda, S. Chakraborty and S. Bandyopadhyay, *J. Phys. Chem. B*, 2006, **110**, 3791.
127. M. Kiran Singh, H. Shweta and S. Sen, *Analysis of Membrane Lipids*, 2020, 161.
128. E. Gaidamauskas, D. P. Cleaver, P. B. Chatterjee and D. C. Crans, *Langmuir*, 2010, **26**, 13153.

Chapter 2

Experimental method and material

General experimental methods

2.1. Chemicals and solvents

Unless otherwise stated all required chemicals and solvents of purest grade were purchased from Sigma-Aldrich Chemicals and were used without further purification. The organic solvents: acetone, methanol (MeOH), ethanol (EtOH), tetrahydrofuran (THF), acetonitrile (ACN), chloroform ($CHCl_3$), were purchased from Spectrochem Pvt. Ltd (India) and were purified by the standard procedure. Deuterated solvent such as DMSO-d_6, MeOD, $CDCl_3$, D_2O, MeCN-d_3 were purchase from Cambridge Isotope Laboratories (USA) for performing NMR studies. The phospholipids, sodium 1,2-dimyristoyl-sn-glycero-3-phosphorylglycerol (DMPG) and 1,2-dimyristoyl-sn-glycero-3-phosphocholine (DMPC), 1,2-Dioleoyl-sn-Glycero-3-Phosphocholine (DOPC), 1,2-Dioleoyl-sn-Glycero-3-(Phospho-rac-(1-glycerol)) (DOPG) and 1,2-Dioleoyl-sn-Glycero-3-Phosphoethanolamine (DOPE), dimethyldioctadecylammonium bromide (DDAB) and sodium taurocholate taurocholate (STA) were purchased from Avanti Polar Lipids (USA). Cetyltrimethylammonium bromide (CTAB), Triton X-100 (TX-100) and sodium dodecyl sulfate (SDS) were dried under vacuum overnight before use.

2.2. Preparation of buffer solutions

Milli-Q water (Millipore) of conductivity 18.2 MΩ cm was used to prepare buffer solution as well as the mixed aqueous buffer for spectroscopic studies. Different 20 mM buffer compositions were used to attain a particular medium pH value within pH 3.4–12.5: citric acid/Na_2HPO_4 buffer for pH 3.4 –7.0, Tris-HCl for pH 7.0–9.0 and carbonate/bicarbonate for pH 9.0–12.5. The pH of the buffer was adjusted by the addition of the required amount of either ~1.0 M NaOH or 1.0 M HCl solution, monitored with a Systronics digital pH meter (Model no. 335). The buffer solution of different concentration (10.0−1.0 mM) was prepared by addition of required amount of Millipore water from 20 mM buffer stock solution. The required amount of pH-probe and amphiphilic molecule were added in buffer solution, with an addition of either 0.1 M NaOH or 0.1 M HCl to adjust the desired pH, if required. The pH of different dielectric constant of organic solvent containing buffer medium were adjusted by addition of 1.0 M NaOH or 1.0 M HCl. The medium dielectric constant and refractive indices for various solvent mixtures were estimated as reported previously.[1-4]

2.3. Synthesis of different polarity/pH sensing probe molecules

2.3.1. Synthesis of PMP molecule

2-hydroxy-3-(hydroxymethyl)-5-methylbenzaldehyde (HHMB) was prepared according to the standard literature by staring with p-cresol.[5] An substantial amount of product yield (62% with respect to p-cresol) was obtained by recrystallizing the crude product from toluene-chloroform mixed solvents (8:2, *v/v*) followed by column chromatography and the purity was checked by NMR measurement. For synthesis of the Schiff base molecule, 2-((2-(pyridine-2-yl)ethylimino)methyl)-6-(hydroxymethyl)-4-methylphenol (PMP), to an methanolic solution of HHMB (0.166 g, 1 mmol), 2-(2-aminoethyl)-pyridine (AEP) (0.122 g, 1 mmol) was added drop-wise at ambient temparature with constant stirring and 2 drops of AcOH were further added to it (scheme 1). The mixture was refluxed for 2 h at 40 °C and then filtered. The filtrate was then evaporated under reduced pressure to get the crude product as gel. It was purified by column chromatography followed by rotary evaporation to obtain the pure product and dried over $CaCl_2$ under vacuum; yield: 85.8% with respect to HHMB. The structural analyses were performed by ESI-MS^+, ^1H and ^{13}C-NMR as well as IR measurements. ^1H NMR ($CDCl_3$, 300MHz): δ = 2.26 (s, 3H, Ar$\underline{CH_3}$), 3.17 (t, J = 6.9 Hz, 2H, $\underline{CH_2}$–CH_2), 4.02 (t, J = 6.9 Hz, 2H, CH_2–$\underline{CH_2}$), 4.7 (s, 2H, $\underline{CH_2}$), 6.92 (s, 1H, $\underline{H}$-3), 7.10-7.18 (4H, Ar$\underline{H}$), 7.26 (due to trace amount of $CHCl_3$ in the solvent $CDCl_3$), 7.57-7.62 (dd, J = 7.6 and 1.7 Hz, $\underline{H}$-1), 8.23 (s, 1H, imine-$\underline{H}$), 8.5 (s, 1H,-O$\underline{H}$) ppm. ^{13}C NMR ($CDCl_3$, 75 MHz): 20.30, 39.38, 58.65, 61.85, 117.90, 121.57, 123.70, 127.21,128.43, 130.56, 132.29,136.49, 149.48, 157.78, 158.95, 165.37 ppm (Figure 1). Selected IR in cm^{-1} (KBr): 3242 (br), 1632 (s), 1592 (s), 1462 (m), 1435 (s). 749(s). ESI-MS^+ for PMP in water: *m/z* Cal for $[PMP+H]^+$: 271.3425; Found: 271.3016 (Figure 2).

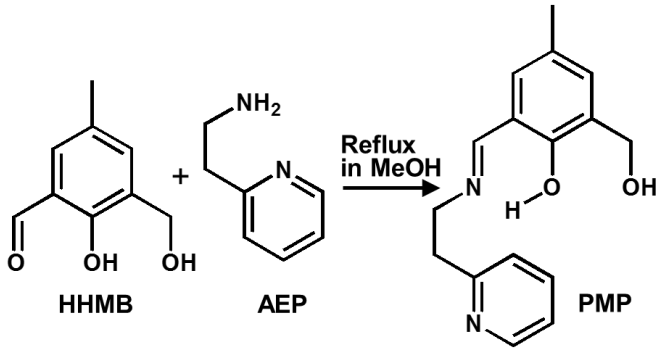

Scheme 1. Synthesis route of the Schiff base molecule (PMP).

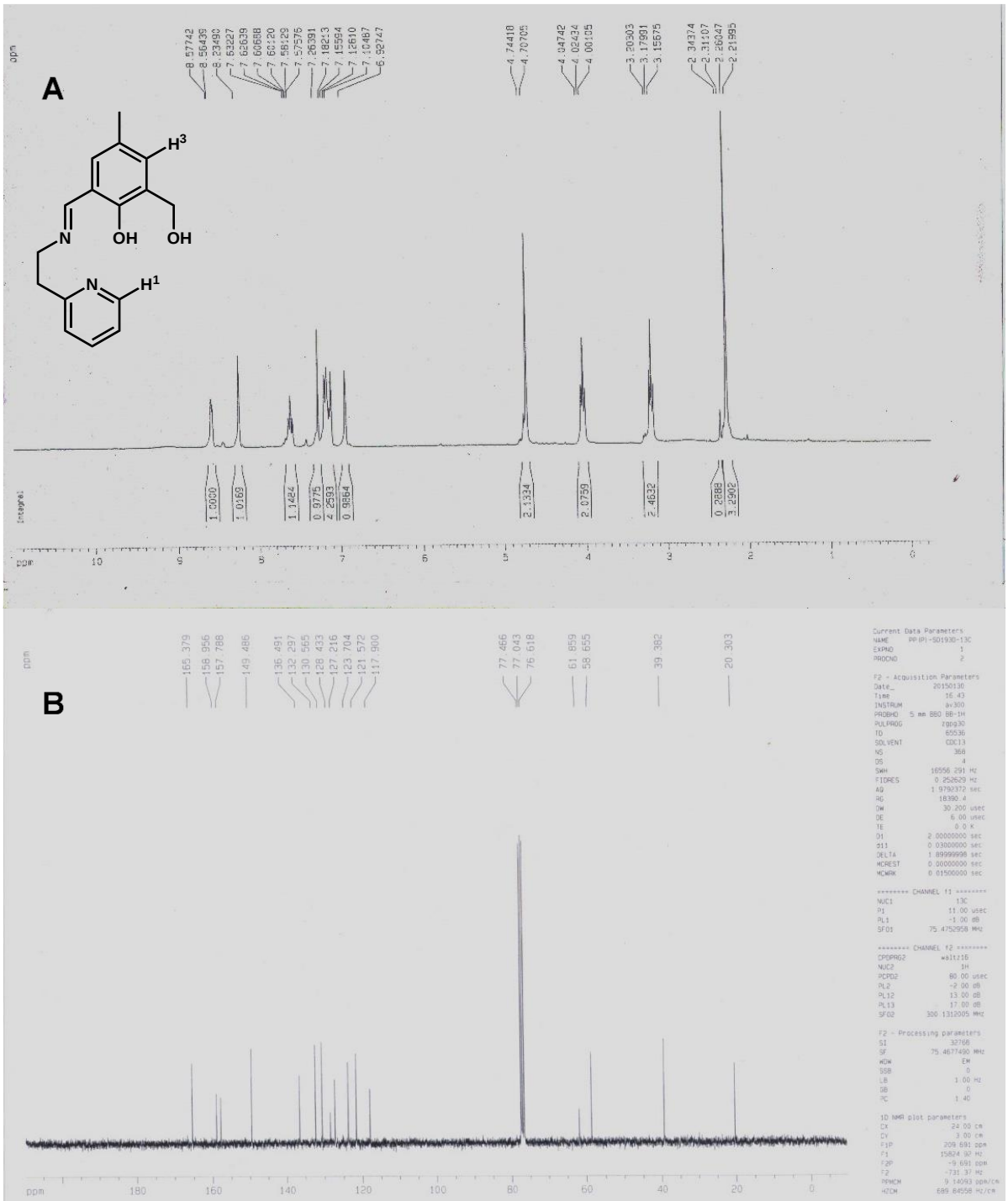

Figure 1. (A) ^{1}H-NMR and (B) ^{13}C-NMR spectra of Schiff base molecule PMP in $CDCl_3$.

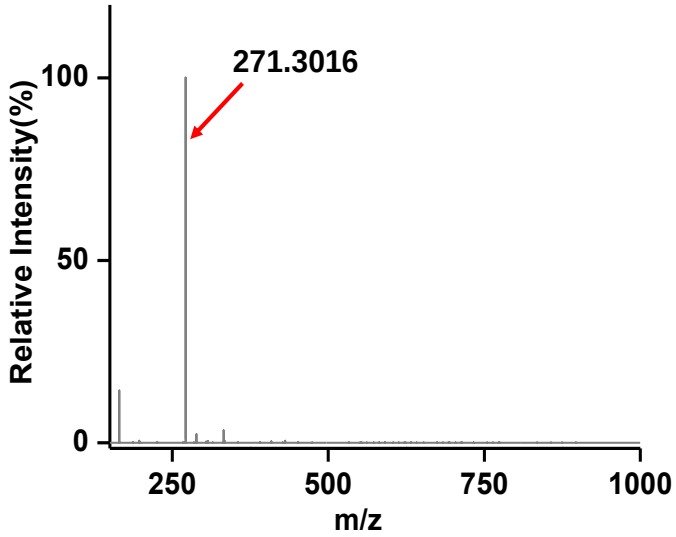

Figure 2. ESI-MS$^+$ of Schiff base molecule PMP (m/z for [PMP+H] $^+$: obs'd – 271.3016 (cal'd – 271.3425)) in water.

2.3.2. Synthesis of the Schiff-base molecule (SBOH-Z-SBOH)

For synthesis of Schiff-base molecular probe, *p*-cresol and 1,2-diaminopropane (DAP) of analytical grade were procured from Sigma-Aldrich (USA) and were used without further purification. The phenolic aldehyde molecule, 2-hydroxy-3-(hydroxymethyl)-5-methylbenzaldehyde (HHMB), was prepared with yield of 62% with respect to *p*-cresol as staring material following standard literature as reported earlier.[5] Pure product was obtained from crude product by column chromatography followed by rotary evaporation and further recrystallized from toluene-chloroform mixed solvents (8:2, *v/v*) resulting light yellow coloured solid HHMB. For the synthesis of Schiff-base molecule (SBOH-Z-SBOH), to an methanolic solution of HHMB (0.322 g, 2.0 mmol), DAP (0.085 mL, 1 mmol) was added drop-wise with constant stirring and few drops of acetic acid were further added to the reaction mixture (scheme 2). The mixture was refluxed for 2 h at 40 °C and then filtered. The filtrate was then evaporated under reduced pressure to get the crude product. It was purified by column chromatography followed by rotary evaporation to obtain the deep yellow solid product and dried over $CaCl_2$ under vacuum. The structural analyses were performed by ESI-MS$^+$ and ^{1}H-NMR measurement. ESI-MS+ in water: m/z Calcd for SBOH-ZSBOH: 371.4485, Found: 371.4112 (Figure 3). ^{1}H NMR ($CDCl_3$, 300MHz): δ = 1.41 (d, J=5.7 Hz, 3H, –$\underline{CH_3}$), 2.26 (s, 6H,2 Ar–$\underline{CH_3}$), 2.33 (s, 1H, N–$\underline{CH}$), 3.66–3.71 (br. d, 1H, N– C$\underline{H_a}$H),

3.84–3.86 (br. d, 1H,N–CH$\underline{H}_b$), 4.72 (d, J=4.2 Hz, 4H, 2$\underline{CH_2}$–OH), 6.87 (s, 1H, Ar–H_f), 6.97 (s, 1H, Ar–H_c), 7.25 (s, 2H, Ar– (H_d, H_d')), 8.27 (s, 1H, imine-$\underline{H}$), 8.31 (s, 1H, imine-$\underline{H}$), 11.18 (s, 2H, 2Ar-O$\underline{H}$) ppm (Figure 4). ^{13}C- NMR (DMSO-d_6, 75 MHz): 20.3, 57.9, 64.2, 65.1, 117.7, 126.8, 129.9, 130.2, 131.5, 155.8, 156.0, 165.7, 167.6 ppm (Figure 4).

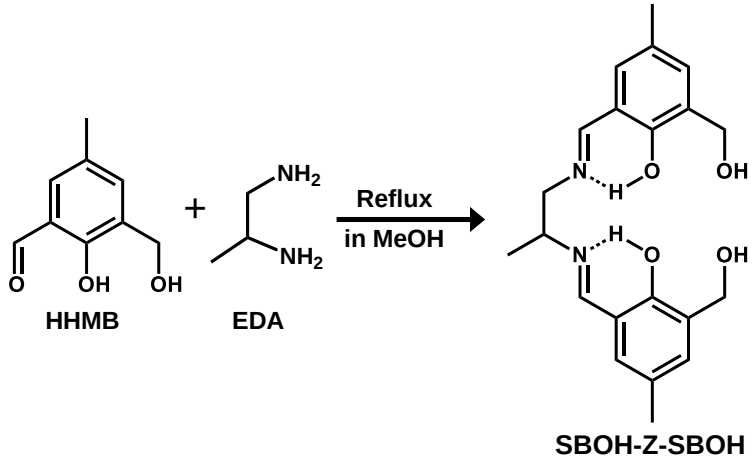

Scheme 2. Synthesis route of the Schiff base molecule (SBOH-Z-SBOH).

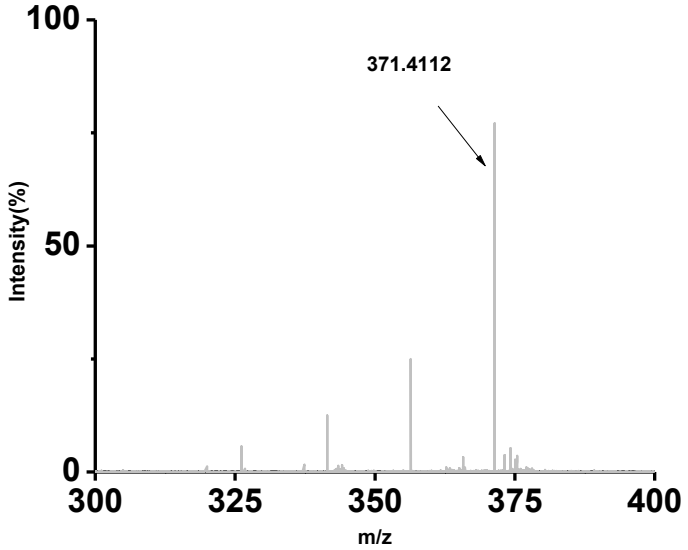

Figure 3. ESI-MS$^+$ spectra of SBOH-Z-SBOH in water: m/z for [SBOH-Z-SBOH+H] $^+$: obs'd – 371.4112, cal'd – 371.44848).

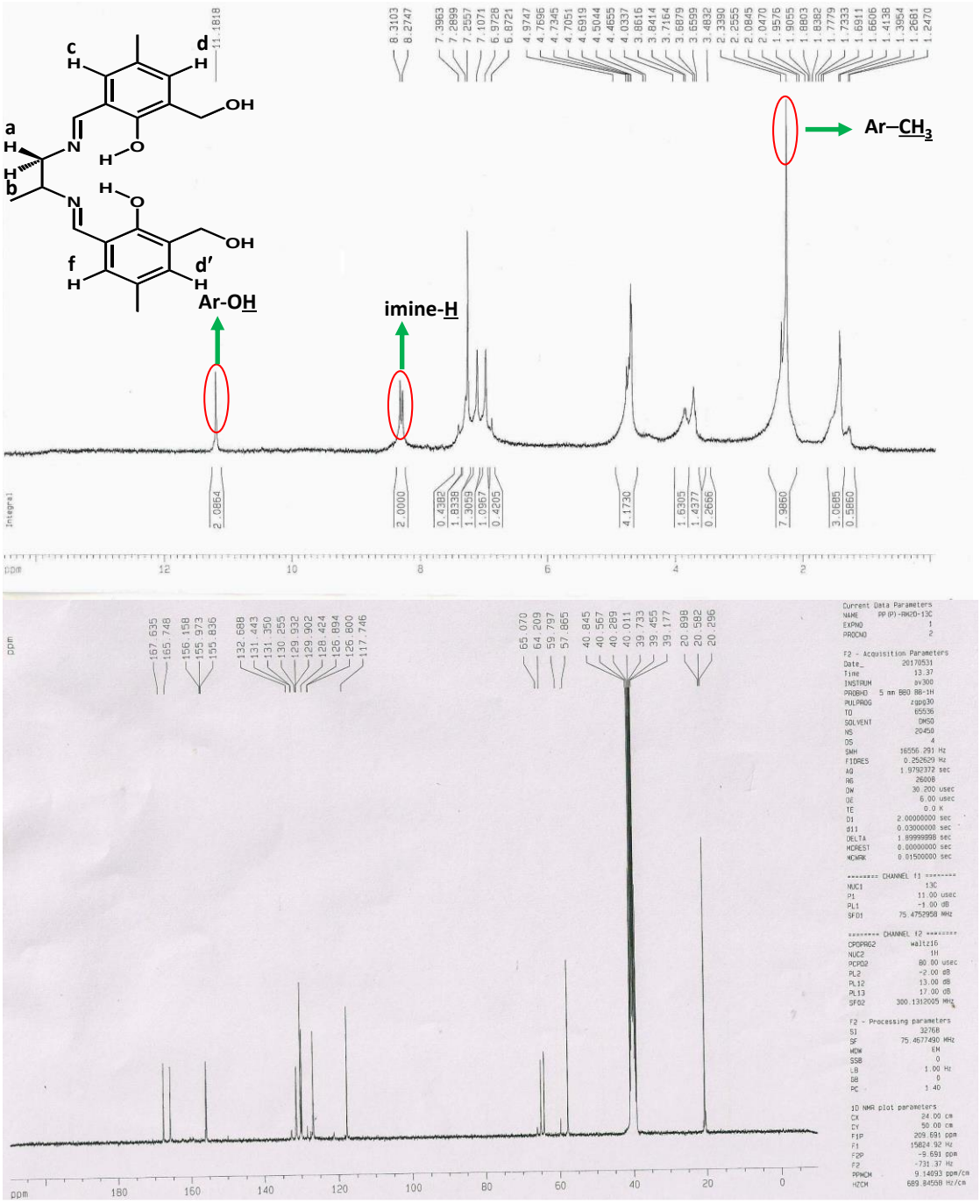

Figure 4. ^{1}H and ^{13}C NMR spectra of SBOH-Z-SBOH in $CDCl_3$ and DMSO-d_6 respectively.

2.3.3. Synthetic protocol of GPP (2)

The synthetic route of GPP (2) is shown in Scheme 3. The complete synthetic direction is described below.

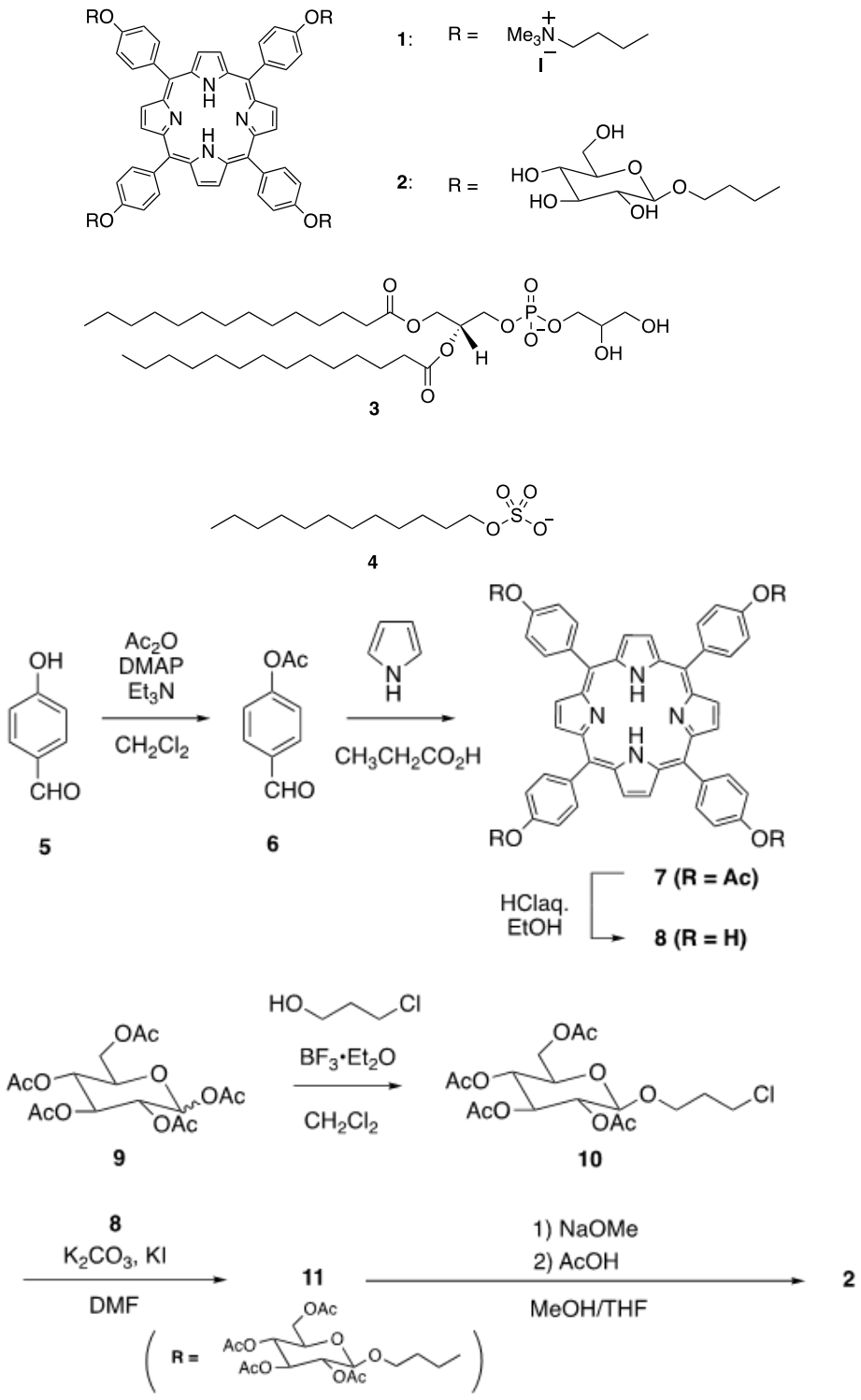

Scheme 3. Synthesis route of the GPP molecule.

Synthesis of 4-aceoxybenzaldehyde (6):

In a 200-mL round-bottom flask, 4-hydroxybenzaldehyde (**5**, 2.44 g, 20 mmol) was suspended in CH_2Cl_2 (50 mL). On the addition of trimethylamine (2.22 g, 22 mmol), the suspension turned into a clear pale-yellow solution. To the solution was added DMAP (0.12 g, 1 mmol) and acetic anhydride (2.64 g, 22 mmol). The solution was stirred at room temperature for 45 min. After the complete of reaction was confirmed by silica TLC (eluent: hexane/AcOEt = 1/1), the solution was diluted with CH_2Cl_2. The solution was washed with water (x 2), 0.1 M HCl (x 2) and 5% $NaHCO_3$ subsequently before dried over Na_2SO_4. The solvent was evaporated to yield **6** as colorless oil (3.3 g, quant). ^{1}H NMR (400 MHz, $CDCl_3$, TMS) δ_H: 9.998 (s, 1H, -C*H*O), 7.927 (dd, AA'BB', 2H, J_{AB} = 8.7, $J_{AA'}$ =4.1 Hz, $J_{AB'}$ = 2.8 Hz, 2,6-phenyl protons), 7.284 (AA'BB', 2H, J_{AB} = 8.7, $J_{AA'}$ = 4.1 Hz, $J_{AB'}$ = 2.8 Hz,3,5-phenyl protons) and 2.370 (s, 3H, -OAc); ^{13}C NMR (100 MHz, $CDCl_3$, TMS) δ_c: 190.74, 168.70. 154.47, 133.68, 130.79. 122.18, 20.98; HR-MS (EI, positive): [M^+] for $C_9H_8O_3$; Calcd. 164.0473; Found 164.0470.

Synthesis of 5,10,15,20-tetrakis(4-acetoxyphenyl) porphyrin (7):

In a 100-mL round-bottom flask equipped with a condenser, compound **6** (0.473 g, 2.88 mmol) was suspended in propionic acid (15 mL). Pyrrole (0.193 g, 2.88 mmol, 200 μL) was added at 80 ˚C, and the solution was refluxed for 30 min with avoiding light. After the resultant deep purple solution was cooled to room temperature, porphyrin deposited from the solution was collected by suction. The purple solid was rinsed with cold MeOH till washing solution became colorless. After the solid was rinsed with hexane, the solid was dried *in vacuo* to yield **7** as purple powder (0.128 g, 21% yield). ^{1}H NMR (400 MHz, $CDCl_3$, TMS) δ_H: 8.879 (s, 8H, β-protons), 8.215 (d, 8H, J = 8.5 Hz, 2,6-phenyl protons), 2.510 (s, 3H, -OAc) and –2.838 (br, 2H, inner-NH); ^{13}C NMR (100 MHz, $CDCl_3$, TMS) δ_c: 169.68, 150.79, 139.65, 135.29, 120.34, 119.08, 21.21 (α- and β-Carbons in pyrrole rings were not detected under the measurement conditions); HR-MS (MALDI; matrix: DCTB, positive): [M^+] for $C_{52}H_{38}N_4O_8$; Calcd. 846.2684; Found 846.2685.

Synthesis of 5,10,15,20-tetrakis(4-hydroxyphenyl) porphyrin (8):

In a 100-mL round-bottom flask equipped with a condenser, compound **7** was suspended in a mixed solvent of H_2O (3 mL) and EtOH (1 mL). The addition of conc. HCl (1 mL) made a green

suspension. The suspended solution was refluxed for 1.5 h. After the residual of the starting material was confirmed on a silica TLC plate (eluent: $CHCl_3$/MeOH = 5/1), H_2O (3 mL), EtOH (1 mL) and conc. HCl (1 mL) were further added. After refluxed for 2 h, the green suspension was cooled to room temperature. The reaction mixture was diluted with water and neutralized with 2 M NaOH to adjust pH = 8 (checked by pH test paper). During this procedure, the suspension turned to be purple in color. The solution was stirred for 30 min in the dark, and AcOEt (50 mL) was added. The mixed solution was vigorously stirred for 30 min and transferred into a separatory funnel. The organic phase (purple in color) was separated and dried over Na_2SO_4. After the solvent was evaporated, the formed purple solid was suspended in CH_2Cl_2 and collected by suction. The solid was subsequently rinsed with CH_2Cl_2 and hexane to yield porphyrin **8** as purple solid (90 mg, 88% yield). ^{1}H NMR (400 MHz, DMSO-d_6, TMS) δ_H : 9.971 (s, 4H, phenol-OH), 8.855 (s, 8H, β-protons), 7.988 (d, 8H, J = 8.0 Hz, 2,6-phenyl protons), 7.206 (d, 8H, J = 8.0 Hz, 3,5-phenyl protons), –2.907 (br, 2H, inner-NH); ^{13}C NMR (100 MHz, $CDCl_3$, TMS) δ_C : 157.16, 135.96, 131.51, 119.64, 114.13 (α- and β-Carbons in pyrrole rings were not detected under the measurement conditions); HR-MS (MALDI; matrix: DCTB, positive): [M^+] for $C_{44}H_{30}N_4O_4$; Calcd. 678.2267; Found 678.2262.

Synthesis of 2,3,4,6-tetra-O-acetyl-1-O-(3-chloropropyl)-β-D-glucopyranoside (10):

In a 200-mL three-neck flask with a dropping funnel, 1,2,3,4,6-penta-*O*-acetyl-D-glucopyranoside (**9**, 3.90 g, 10 mmol) and 3-chloropropanol (1.88 g, 20 mmol) were dissolved in dry CH_2Cl_2 (25 mL) under a N_2 atmosphere. The solution was cooled with an ice bath (below 5 ˚C). To the solution was added BF_3•Et_2O (7.1 mL, *ca*. 5 equiv.) dropwise. The solution was stirred in the ice bath for 1 h and at room temperature for 12 h. After neutralized by trimethylamine (5.05 g, 50 mmol) slowly, the solution was concentrated and AcOEt (100 mL) was added. The solution was washed with water (x 3), 5% $NaHCO_3$ (x 2) and brine. The organic phase was dried over Na_2SO_4. The solvent was evaporated and the residue was subjected to a silica gel chromatography with elution of hexane/AcOEt = 1/1. The product was detected on a TLC plate stained in Von's reagent. After evaporation of solvent, compound **10** was obtained as colorless viscous oil (1.90 g, 45% yield). ^{1}H NMR (400 MHz, $CDCl_3$, TMS) δ_H : 5.227 (dd, J = 9.5 Hz, 9.5 Hz, 1H, sugar-H3), 5.097 (dd, J = 9.5 Hz, 9.5 Hz, 1H, sugar-H4), 5.002 (dd, J = 9.5 Hz, 8.0 Hz, 1H, sugar-H2), 4.522

(d, *J* = 8.0 Hz, 1H, sugar-H1), 4.283 (dd, *J* = 4.8 Hz, 14.5 Hz, 1H, sugar-6H_a), 4.153 (dd, *J* = 2.6 Hz, 12.5 Hz, 1H, sugar-6H_b), 4.010 (ddd, *J* = 5.1 Hz, 5.0 Hz, 9.5 Hz, 1H, sugar-5H), 3.716 (m, 2H, -OC$\underline{H}_2$CH$_2$CH$_2$Cl), 3.618 (dd, *J* = 5.1 Hz, 6.8 Hz, 2H, -OCH$_2$C$\underline{H}_2$Cl), 2.104 (s, 3H, -OAc), 2.074 (s, 3H, -OAc), 2.040 (s, 3H, -OAc), 2.024 (s, 3H, -OAc,), 1.980 (m, 2H, -OCH$_2$C$\underline{H}_2$CH$_2$Cl); ^{13}C NMR (100 MHz, CDCl$_3$, TMS) δ_C : 171.39, 171.03, 169.94, 101.75, 73.38, 72.48, 71.91, 69.03, 67.08, 62.57, 42.02, 32.83, 21.44. 21.34. 21.31. 21.30; HR-MS (MALDI; matrix: DCTB, positive): [M+Na$^+$] for $C_{17}H_{25}ClO_{10}Na$; Calcd. 447.1028; Found 447.1024.

Synthesis of tetraacetylglucose-pendant porphyrin 11:

In a 100-mL two-neck flask with a condenser and a CaCl$_2$-tube, porphyrin **8** (0.25 g, 0.45 mmol) was dissolved in dry DMF (20 mL) under a N_2 atmosphere. To the solution were added glucose derivative **10** (1.26 g, 3.0 mmol), KI (0.743 g, 4.48 mmol) and K_2CO_3 (1.86 g, 13.5 mmol). The reaction mixture was stirred at 60 ˚C for 13 h. The product formation was confirmed by TLC (elution: CHCl$_3$/MeOH = 10/1). Insoluble materials were removed by filtration and rinsed with CH_2Cl_2 on a filter paper. The mother liquor was concentrated using a rotary evaporator (65 ˚C, 35 mbar). Water was added the residue and filtered. The resultant purple gummy material was dissolved in AcOEt. The solution was washed with brine and dried over Na_2SO_4. After removal of the salt, silica gel (5 g) was added to the solution, and the solvent was slowly evaporated to have porphyrin pre-absorb onto silica. The porphyrin-absorbed silica was load onto a silica gel equilibrated with hexane/AcOEt = 1/1 (column volume (CV) = 65 mL). The porphyrin component was washed on silica with hexane/AcOEt = 1/1 (2CV) to remove excess the glucose derivative. After that the porphyrin was eluted with hexane/AcOEt = 1/4. Purple fraction was collected and the solvent was evaporated. Porphyrin **11** was obtained by addition of hexane as purple solid (0.62 g, 61% yield). ^{1}H NMR (600 MHz, CDCl$_3$, TMS) δ_H : 8.843 (s, 8H, β-protons), 8.115 (d, *J* = 8.8 Hz, 8H, 2,6-phenyl protons), 7.273 (d, *J* = 8.8 Hz, 8H, 3,5-phenyl protons), 5.275 (dd, *J* = 9.5 Hz, 9.5 Hz, 4H, sugar-H3), 5.153 (dd, *J* = 9.5 Hz, 9.5 Hz, 4H, sugar-H4), 5.098 (dd, *J* = 9.5 Hz, 8.0 Hz, 4H, sugar-H2), 4.650 (d, *J* = 8.0 Hz, 4H, sugar-H1), 4.320 (m, 12H, -OCH$_2$CH$_2$C$\underline{H}_2$OPh and sugar-6H_a), 4.206 (m, 8H, -OC$\underline{H}_a$CH$_2$CH$_2$OPh and sugar-6H_b), 3.919 (m, 4H, -OC$\underline{H}_b$CH$_2$CH$_2$OPh), 4.010 (ddd, *J* = 9.5 Hz, 4.4 Hz, 2.2 Hz, 4H, sugar-5H), 2.262 (m, 2H, -OCH$_2$C$\underline{H}_2$CH$_2$OPh), 2.130 (s, 3H, -OAc), 2.079 (s, 3H, -OAc), 2.053 (s, 3H, -OAc), 2.038 (s, 3H,

-OAc,), –2.271 (br, 2H, -inner-NH); ^{13}C NMR (150 MHz, $CDCl_3$, TMS) δ_c : 170.77, 170.36, 169.47, 169.41, 158.68, 135.63, 134.68, 119.70, 112.65, 101,10, 72.82, 71.87, 71.37, 68.40, 66.79, 64.34, 61.95, 29.59, 20.82, 20.72, 20.66, 20.64 (α- and β-Carbons in pyrrole rings were not detected under the measurement conditions). After confirmation of NMR spectral information, this material was used for next reaction as is.

Synthesis of glucose-pendant porphyrin (GPP) 2:

In a 100-mL round-bottom flask equipped with a $CaCl_2$-tube, tetraacetyl glucose-pendant porphyrin **11** was dissolved in mixed solvent of MeOH (30 mL) and THF (7 mL). To the solution was added 28% NaOMe in MeOH (0.3 mL), and the solution was stirred at room temperature for 12 h. After neutralized by AcOH (checked pH by wet pH test paper), the solvent was evaporated. The residue was dissolved in pyridine and passed through a Sephadex LH-20 gel column with elution of pyridine/MeOH = 1/3. Purple band was collected and the solvent was evaporated. Addition of toluene afforded purple solid. The solid was collected by suction and suspended in toluene. After the suspension was stirred for 1 h, residual pyridine was removed by azeotrope with toluene three times. The solid was rinsed with CH_2Cl_2 and dried *in vacuo*. Porphyrin **2** was obtained as purple powder (320 mg, 74% yield). ^{1}H NMR (600 MHz, DMSO-d_6, residual protons in solvent) δ_H : 8.854 (s, 8H, β–protons), 8.095 (d, J = 8.3 Hz, 8H, 2,6-phenyl protons), 7.362 (d, J = 8.8 Hz, 8H, 3,5-phenyl protons), 5.139 (d, J = 4.8 Hz, 4H, -OH at sugar-H2), 5.000 (d, J = 4.8 Hz, 4H, -OH at sugar-H3), 4.957 (d, J = 4.8 Hz, 4H, -OH at sugar-H4), 4.563 (t, J = 6.0 Hz, 4H, -OH at sugar-H6), 4.361 (t, J = 5.4 Hz, 8H, -OCH$_2$CH$_2$C$\underline{H}_2$OPh), 4.248 (d, J = 7.6 Hz, 4H, sugar-H1), 4.069 (dt, J = 6.6 Hz, 7.8 Hz, 4H, -OC$\underline{H}_a$CH$_2$CH$_2$OPh), 3.771 (dt, J = 6.6 Hz, 7.8 Hz, 4H, -OC$\underline{H}_b$CH$_2$CH$_2$OPh), 3.714 (dd, J = 5.4 Hz, 1.2 Hz, 4H, sugar-H6$_a$), 3.489 (dd, J = 6.0 Hz, 12 Hz, 4H, sugar-H6$_b$), 3.169 (m, 8H, sugar-H3 and sugar-H5), 3.097 (m, 4H, sugar-H4), 3.031 (ddd, 4H, J = 4.8 Hz, 7.6 Hz, 7.9 Hz, sugar-H2), 2.167 (m, 8H, -OCH$_2$C$\underline{H}_2$CH$_2$OPh), –2.905 (br, 2H, inner-NH) (Figure 5); ^{13}C NMR (150 MHz, DMSO-d_6, solvent) δ_c : 158.73, 149.65, 135.43, 133.45, 119.80, 113.05, 103.80, 76.98, 76.77, 73.60, 70.12, 65.54, 64.91, 61.14, 29.46 (α- and β-Carbons in pyrrole rings were not detected under the measurement conditions) (Figure 6); HR-MS (MALDI; matrix: DCTB, positive): [M$^+$] for $C_{80}H_{94}N_4O_{28}$; Calcd. 1558.6049; Found 1558.6049.

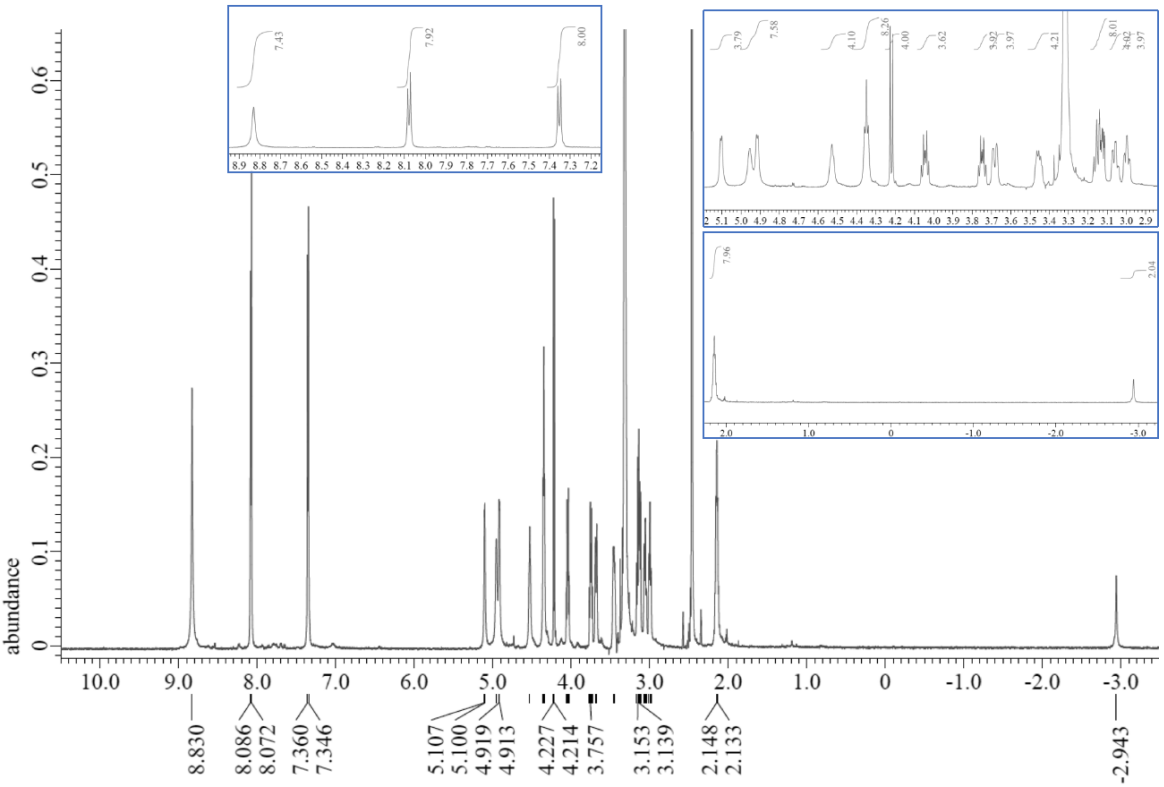

Figure 5. 600 MHz-^{1}H NMR spectrum of GPP (2).

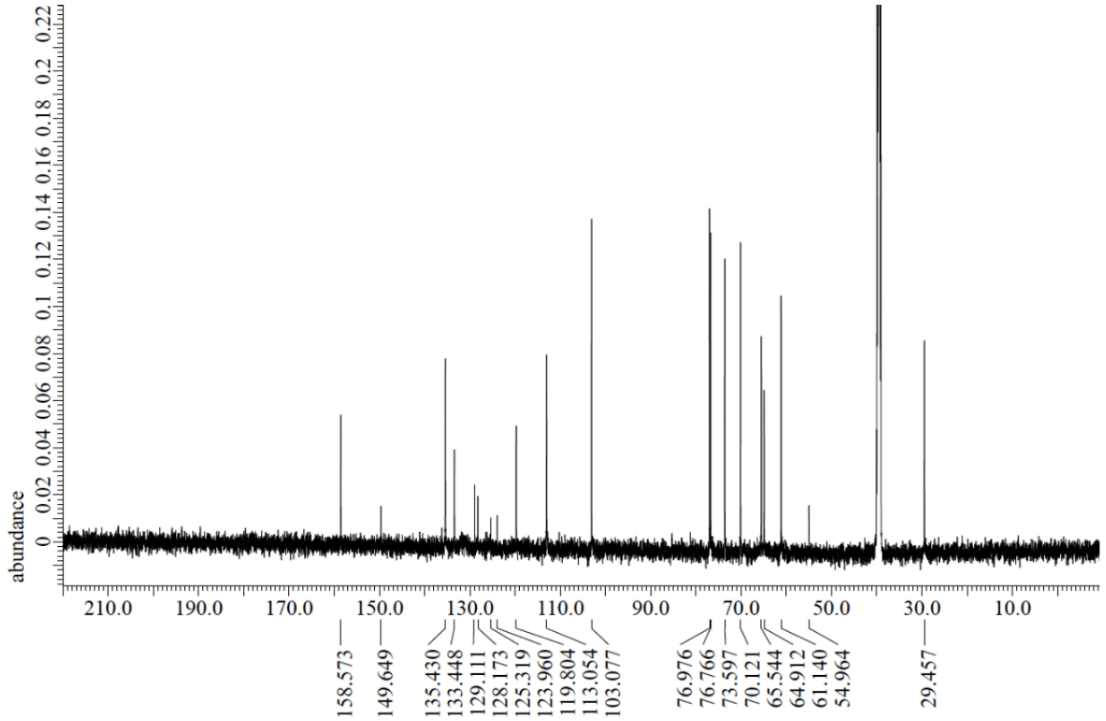

Figure 6. 150 MHz-^{13}C NMR spectrum of GPP (2).

2.3.4. Synthesis of neutral and quaternized QPDMA-b-PMMA-b-QPDMA block co-polymer (TBP and q-TBP)

The triblock copolymer containing central poly (methyl methacrylate) block (PMMA) and poly (2-dimethyl aminoethyl) methacrylate end block (PDMA) with molecular weight (M_n) ~ 28 kD and a polydispersity index (PDI) ~1.20 was synthesized by two step atom transfer radical polymerization.[6,7] A bi-functional Br–PMMA–Br was synthesized at 35 °C using CuCl/bpy as the catalyst and 1,2-bis(bromoisobutyryloxy)ethane as the initiator with the following recipe: MMA (7.0 g, 0.07 mol), acetone (4.2 mL), CuCl (0.1 g, 0.00094 mol), bpy (0.3 g, 0.0019 mol) and 1,2-bis(bromoisobutyryloxy)ethane (0.34 g, 0.00094 mol). After 12 h, the conversion was 80% and the M_n and PDI values were 6300 g/mol and 1.30 respectively. In the next step, the dried and purified Cl–PMMA–Cl macroinitiator was used to polymerize DMA. The recipe was as follows: DMA (4.66 g, 0.03 mol), acetone (4.2 mL), CuCl (0.016 g, 0.00016 mol), bpy (0.05 g, 0.00032 mol) and Cl–PMMA–Cl (1.1 g, 0.00017 mol) (M_n = 6300 and PDI = 1.30). After 12 h incubation of reaction mixture, the conversion was found to be ~78%.[6] The polymer was purified by passing its solution through a silica gel column using toluene as an eluent. The copper free solution was concentrated by rotary evaporator and precipitated in petroleum ether. The polymer was dissolved in acetone and precipitated in petroleum ether again. The precipitated mass was dried in air for 12 h and then in vacuum oven at 60 °C for 48 h. The structural analyses were performed by ^{1}H NMR measurement (Figure 7).

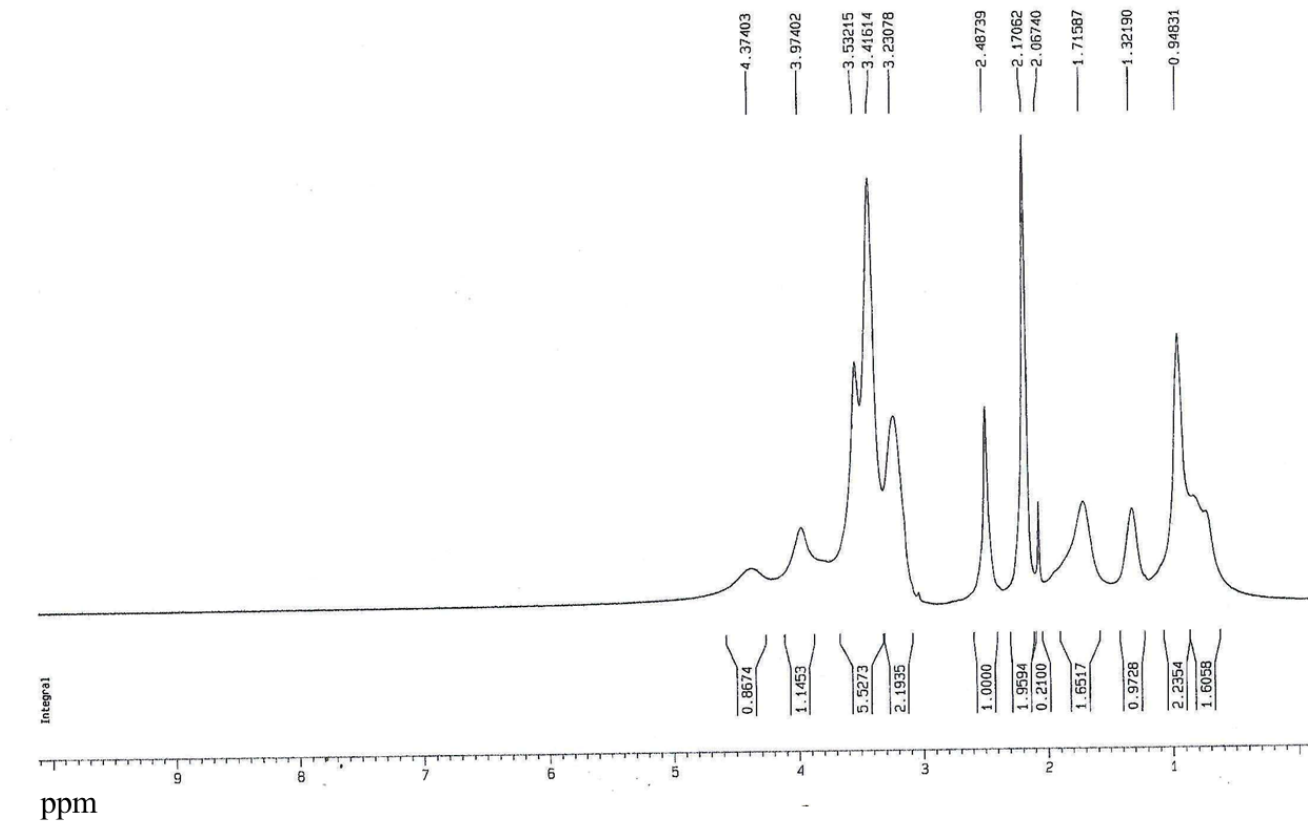

Figure 7. ^{1}H-NMR spectra of TBP in DMSO-d_6 solvent.

The tertiary amino groups in the PDMA were quaternized by butyl bromide to obtained corresponding cationic polymer (q-TBP). For quaternization, PDMA-PMMA-PDMA copolymer (1.0 g) was dissolved in DMF (10 mL). Excess n-butyl bromide (1.0 g) was added into the copolymer solution. Next, the mixture was stirred at 50 °C for 24 h. The DMF was removed by rotary evaporator, and the polymer was dissolved in THF and precipitated in hexane. This process was repeated twice to remove any unreacted butyl bromide. The structural analyses were performed by ^{1}H measurements, where about complete quaternization was confirmed by the ^{1}H NMR spectrum. ^{1}H NMR (DMSO-d_6, 300 MHz): δ = 3.33 (s, 8H, $^{+}$N $(CH_3)_2$, nBu), 3.98 (broad, 4H, $–CH_2–N^{+}–CH_2$), 3.54 (s, 3H, –O-$COCH_3$ of PMMA) and broad 4.37 (2H, $–COOCH_2–$) for quaternized PDMA unit (Figure 8).

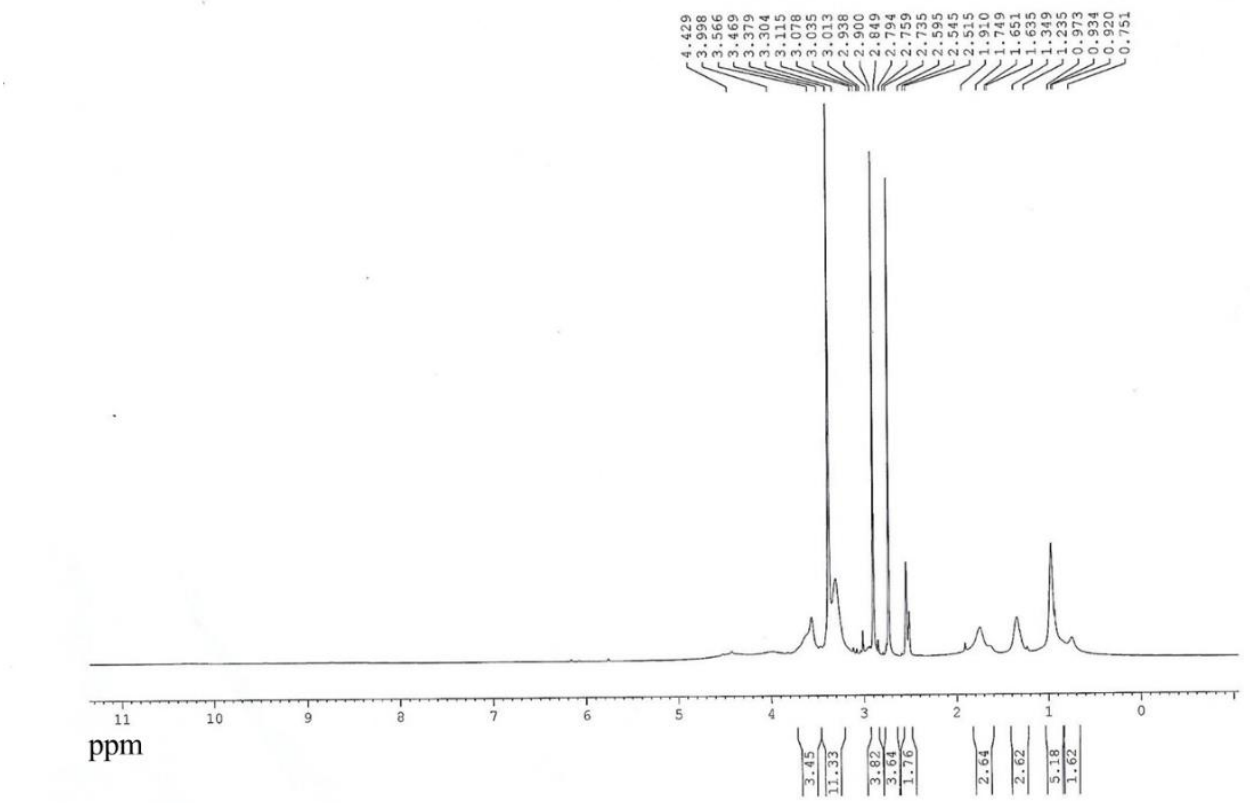

Figure 8. ^{1}H-NMR spectra of q-TBP in DMSO-d_6 solvent.

2.4. Preparation of different amphiphilic self-assembled system

2.4.1. Micellar solution

An appropriate amount of micelle forming molecules (CTAB, DDAB, SDS, and TX-100) are dissolved in millipore water to prepare a 50 mM stock solution. The concentrated solutions are properly diluted in buffer medium to prepare an exact necessitate concentration.

2.4.2. Unilamellar vesicle (ULV) preparation

The required amount of dimethyldioctadecyl ammonium bromide (DDAB) or 1,2-dioleoyl-sn-glycero-3-phosphocholine (DOPC) was dissolved in 1.0 mL of chloroform. The chloroform was removed with a rotary evaporator at room temperature to acquire a thin lipid film on the wall of a round-bottom flask. Any residual chloroform in the thin lipid film was completely removed in vacuo for 3 h. The appropriate 20 mM buffer solution was added to the lipid film at 40 °C for hydration of the film. The solution was vortexed for 2 min to complete dissolution of the lipids.

Seven cycles of freeze-and-thaw were performed between −196 and 50 °C to produce giant multilamellar vesicles. To obtain large unilamellar vesicles (ULVs), the liposome dispersion was extruded 15 times through two stacked polycarbonate membrane filters (Whatman) of pore size 100 nm equipped in a Liposo Fast mini extruder (Avanti, USA). For spectroscopic measurements, the resultant ULV solution was diluted with an appropriate amount of buffer to a definite lipid concentration. Pictorial representation of liposome preparation is given below (Scheme 4).

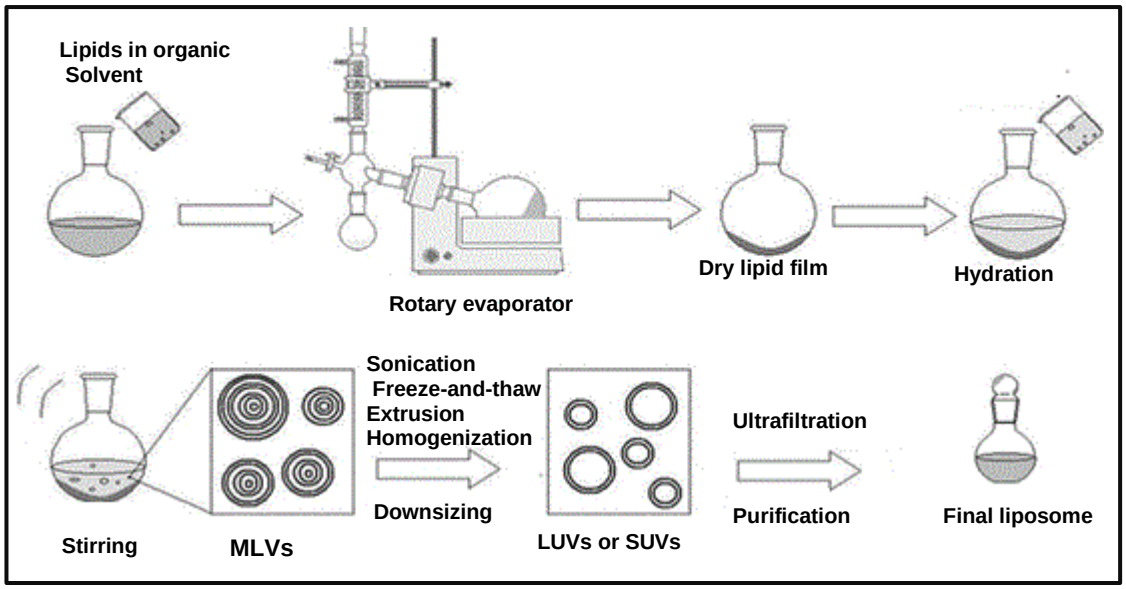

Scheme 4. Representation of liposome preparation by lipid hydration followed by vortex or manual stirring.

2.4.3. Preparation of polymer micelle solution

PDMA-b-PMMA-b-PDMA (TBP) or its amine-quaternized analogue (q-TBP) (50 mg) was dissolved in DMF (1.5 mL), and the solution added drop wise in 10 mL water under constant stirring. The resulting mixture was dialyzed (MW cut-off ~1000 Da) against water for 48 h. The water was exchanged after 6 h interval.

2.4.4. Preparation of DMPG LUV

DMPG was dissolved in 1.0 mL chloroform/methanol (5:1) mixed solvent in a 5 mL round bottom flask. The organic solvents were removed using a rotary evaporator at 35 °C to prepare thin lipid film. Any residual amount of organic solvent was completely removed *in vacuo* for 3 h.

For hydration of prepared thin film, appropriate buffer solution at desired pH was added at 45 °C. The solution was vortexed for 2.0 min for complete dissolution of the lipids to form multilamellar vesicles. Seven cycles of freeze-and-thaw were performed between −196 and 50 °C to produce giant multilamellar vesicles. To obtain unilamellar vesicles (LUVs) of diameter ∼100 nm, the liposome dispersion was extruded 15 times through two stacked polycarbonate membrane filters (Whatman) of 100 nm pore sizes equipped in a Mini-Extruder system (Avanti Polar Lipid, USA). The temperature throughout the LUV preparation process before and after lipid film hydration was maintained above 30 °C.

2.5. UV-Vis absorption and fluorescence studies

UV-Vis optical absorption and fluorescence spectra were recorded with Shimadzu UV-2550/UV-2450 double beam spectrophotometer and a Perkin Elmer LS-55 spectro-fluorimeter (Perkin Elmer, USA), respectively. Quartz cells with 1 cm path-lengths were used for the absorption and fluorescence measurements, respectively. All fluorescence spectra were corrected for the instrumental response. A spectro-fluorimeter equipped with an excitation and emission automatic polarizer was used for fluorescence anisotropic measurements.

UV-Vis absorption spectra and steady state fluorescence spectra of the Schiff-base molecule PMP (5 μM) were performed at different dielectric constants (κ) (7.4–78.5) in water/THF mixed medium. UV-Vis absorption spectra of Schiff base molecule PMP (5 μM) in the presence of intensity-saturated concentrations of different amphiphilic molecules (SDS: 15.0, CTAB: 7.0, TX-100: 9.0, STA: 10.0, TBP: 0.5 and DMPG: 5.0 mM) at 20 mM HEPES buffer, pH 7.3 were recorded. Normalization of molar extinction coefficients at 420 nm ($\varepsilon^{X}{}_{420}$) is done by dividing the molar extinction coefficient at 420 nm for the κ = 7.4 of THF ($\varepsilon^{7.4}{}_{420}$).

UV-Vis absorption spectra of SBOH-Z-SBOH (5.0 μM) at different dielectric constants (κ) (8.0–78.5) in buffer/THF mixed medium at pH 7.0 were recorded. The pH dependent UV-Vis absorption spectra and steady state fluorescence spectra of SBOH-Z-SBOH (5.0 μM) were performed at different pH range (5.5-12). UV-Vis absorption spectra of SBOH-Z-SBOH (5.0 μM) in the presence of intensity-saturated concentrations of different amphiphilic molecules (CTAB: 5.0 mM, DDAB: 3.0 mM, TX-100: 5.0mM and DOPC: 4.0 mM) at 20 mM HEPES buffer, pH 7.3 were measured.

UV-Vis absorption spectra of GPP-2 (2.5 μM) in 10.0mM sodium citrate/sodium phosphate buffer containing various amounts of acetone % (*w/w*), pH 6.0 at different temperature were measured. pH-dependent UV−Vis spectra of GPP-2 (2.5 μM) in the pure buffer and buffer containing 31% (*w/w*) acetone were recorded at various temperature. pH-dependent UV−Vis spectra of GPP-2 (2.5 μM) in 10 mM sodium citrate/sodium phosphate buffer containing DMPG LUV (lipid, 1.1 mM) and SDS (8 mM) were measured at various temperature.

2.5.1. Time resolved emission and transient fluorescence anisotropy measurements

Fluorescence lifetimes were determined from time-resolved intensity decay by the method of time-correlated single-photon counting using different picosecond diode laser (nano-LED; IBH, U.K) as exciting light source and the emissions monitored as corresponding steady-state emission wavelengths. The signal was detected at the magic angle (54.7) polarization using a Hamamatsu MCP PMT (3809U). The time resolution achievable with the present setup following deconvolution analysis of the fluorescence decays was 100 ps. The solutions for analysis were passed through a 0.22 mm filter (Millex, Millipore) before the measurements. The data stored in a multichannel analyzer was routinely transferred to IBH DAS-6 decay analysis software. For all the lifetime measurements the fluorescence decay curves were analyzed by mono-exponential and bi-exponential iterative fitting program provided by IBHDAS6 at Data Station v2.3 through exponential fitting to yield the corresponding excited-state lifetimes of probes.

The time resolved emission decay spectra at different pH values was recorded for SBOH-Z-SBOH (5.0 μM) molecule with excitation and emission wavelengths at 450/530 nm, respectively at different pH values (7.0–12.0). The transient fluorescence anisotropy measurements for PMP/SBOH-Z-SBOH (5.0 μM) in absence and presence of different self-assemble systems were performed to identify the precise probe location within the micellar interface. Fluorescence anisotropy values for PMP molecule were recorded with certain concentration of different amphiphilic systems (CTAB, polymer TBP) in buffer, pH 7.3. Excitation and emission wavelength were 440 and 500 nm, respectively. Fluorescence anisotropic decay curves of SBOH-Z-SBOH (5.0 μM) in absence and presence of deviation saturated concentration of different self-assembled

systems at pH 10.5: CTAB (5.0 mM), DDAB (3.0 mM), TX-100 (6.0 mM) and DOPC (4.0mM) were measured.

2.5.2. Determination of fluorescence quantum yield

The fluorescence quantum yields were determined for different probes (PMP and SBOH-Z-SBOH) in the presence of different lipid compositions by adapting the procedure described previously.[8] In brief, 9,10-diphenylanthracene in ethanol was used as the reference fluorophore with fluorescence quantum yield (ϕ_r) = 0.95. The fluorescence quantum yield of PMP and SBOH-Z-SBOH (ϕ_s) in the presence of LUV was measured by using the following equation:

$$\phi_s = (A_r.F_s.n_s/A_s.F_r.n_r)\times\phi_s \qquad (1)$$

Where, A is the absorbance at the excitation wavelength, F represents the integrated emission area, and n is the refraction index of the solvent used. The subscripts refer to the reference (r) or sample (s) compound. By using the above eqn (1), the fluorescence quantum yield values for SBOH-Z-SBOH in the presence and absence of amphiphilic systems were estimated as follows: ~0.002 at pH 7.0 and 0.11 at pH 11.5 without amphiphilic molecules; ~0.25 at pH 10.0 in the presence of CTAB/DDAB; ~0.21–0.24 at pH 12.5 in the presence of TX-100/DOPC.

2.5.3. Binding studies

To measure the binding affinity of the probes towards different phospholipid, binding study was performed. The ULVs of DDAB or DOPC lipids (3.0 or 4.0 mM, final concentration) in 20 mM buffer solution was incubated for 30 min in presence of probe SBOH-Z-SBOH with 5.0 mM concentration. A 100 K MW cut-off centrifugal mini-filter (Amicon Ultra-0.5 mL Centrifugal Filters, Millipore) was used to collect the unbound SBOH-Z-SBOH in the bulk phase. Around 200 μL of the filtrate was collected from the initial 400 μL lipid solution after centrifugation for about 2 min at 5000 g. The amount of residual probe in the filtrate was estimated by UV-Vis absorption spectra, and the amount of unbound probe was calculated.

2.6. NMR and Mass Spectrum

The ^{1}H NMR spectra of PMP/SBOH-Z-SBOH were acquired with a Bruker 300 MHz NMR spectrophotometer using tetramethylsilane ($\delta = 0$) as an internal standard. However, the ^{13}C NMR

spectra were acquired in DMSO-d_6 and recorded on the same instrument operating at 75 MHz. The ESI-MS^+ experiment was performed on a Waters Qtof Micro YA263 mass spectrometer in positive mode.

^1H NMR spectra of GPP (2) were collected using JEOL NM-ECA600 or JNM-ECX400 spectrometers. Electron ionization mass (EI-MS) measurements were conducted using a JEOL JMS-700 mass spectrophotometer. Matrix-assisted laser desorption ionization mass (MALDI-TOF-MS) spectra were measured using a JEOL JMS-S3000 mass spectrophotometer, where trans-2-[3-(4-tert-butylphenyl)-2- methyl-2-propenylidene] malononitrile (DCTB) was used as a matrix reagent.

2.7. DLS measurements

The average particle size for lipid vesicles was evaluated by dynamic light scattering (DLS) measurement with Malvern Instruments, DLS-nano ZS, Zetasizer, Nanoseries. For DLS measurement, DMPG LUV (lipids, 50 μM) is taken at different pH value 4.0 and 7.0. Each of these spectra is an average of 48 scan.

2.8. DSC measurements

Differential scanning calorimetry (DSC) measurements were carried out using a Malvern MicroCal VP-DSC calorimeter at a scan rate of 1 °C/min. DMPG is known to exhibit weakly energetic pretransition peaks at low temperatures (∼11−15 °C) and highly cooperative strongly energetic gel to liquid-crystalline phase transitions (∼23−25 °C). The phase transition temperatures (T_m) of DMPG in its LUV were measured by DSC in 10 mM citrate/phosphate buffer solution at various pH 4.5−5.5.

2.9. Cryo-TEM study

Cryo-transmitted electron microscopy (TEM) experiments were performed with an FEI Tecnai F20 electron microscope equipped with Gatan K2 summit direct detection device. About 4.0 μL aqueous sample solution of DMPG lipid LUV (1.0 mg/mL) is applied to into a glow-discharged electron microscopy (EM) grid, coated with a holey carbon film. Then extra solution is removed by filter paper, preparing a thin film of the solution covering the holes of the carbon

film on the EM grid. The vitrification of the thin film is completed by rapid falling off the grid into liquid ethane held just above its freezing point. Finally, the vitrified specimen is preserved below 108 K during storage before examination, transfer to the microscope and investigation was carried out.

2.10. Theoretical calculations

Density functional theory (DFT) and time-dependent DFT (TD-DFT) calculations were performed using the Gaussian 09 program.[9] Geometry optimization based on the most probable structure for various molecular forms of PMP and SBOH-Z-SBOH was performed using the B3LYP exchange–correlation function. The 6-31G++ (d,p) basis set was used for the atoms and the geometries were optimized in the gas phase. The global minima of all the species were confirmed by the positive vibrational frequencies. To investigate the electronic properties of the singlet excited state in water, TD-DFT calculations were applied using the optimized geometries of the ground states (S_0) for the respective species in aqueous solution by adapting the conductor polarized continuum model (CPCM). The excitation energies, respective oscillator strengths (f_{cal}) and extension coefficients (ε) of the optical absorption for the respective species were evaluated.

2.11. References

1. G. Akerlof, *J. Am. Chem. Soc.*, 1932, **54**, 4125.
2. F. E. Critchfield, J. A. Gibson and J. L. Hall, *J. Am. Chem. Soc.*, 1953, **75**, 6044.
3. A. Awe, A. Blanco, A. Soto and I. Vidal, *J. Chem. Eng.*, 1993, **38**, 336.
4. M. Iglesias, B. Orge and J. Tojo, *Fluid Phase Equilib.* 1996, **126**, 203.
5. E. Lambert, B. Chabut, S. C. Noblat, A. Deronzier, G. Chottard, A. Bousseksou, J. P.Tuchagues, J. Laugier, M. Bardet and J. M. Latour, *J. Am. Chem. Soc.*, 1997, **119**, 9424.
6. U. Chatterjee, S. K. Jewrajka and B. Mandal, *Polymer*, 2005, **46**, 1575.
7. R. Majumder, Y. Sarkar, S. Das, S. K. Jewrajka, A. Ray and P. P. Parui, *Analyst*, 2016, **141**, 3246.
8. J. V. Morris, M. A. Mahaney and J. R. Huber, *J. Phys. Chem.*, 1976, **80**, 969.
9. M. J. Frisch, et al., *Gaussian 09 Rev. A.1, Gaussian Inc., Wallingford, CT*, 2009.

Chapter 3

Detection of interfacial polarity for various amphiphilic self-assemblies using Schiff base molecular probe

Detection of interfacial polarity for various amphiphilic self-assemblies using Schiff base molecular probe

Abstract

A newly synthesised Schiff base molecule (PMP) existing in equilibrium between non-ionic and zwitterionic forms displays solvent polarity induced ratiometric interconversion from one to another, such novelty being useful to detect medium polarity. The specific interface localization of PMP in versatile amphiphilic self-assemblied systems has been exploited to monitor their interfacial polarity by evaluating such interconversion equilibrium with simple UV-Vis absorption spectroscopy. Inspite of large differences in pH and/or viscosity between the bulk and interface, the unchanged equlibrium between the two molecular forms on medium pH or viscosity provide a huge advantage for the exclusive detection of interfacial polarity.

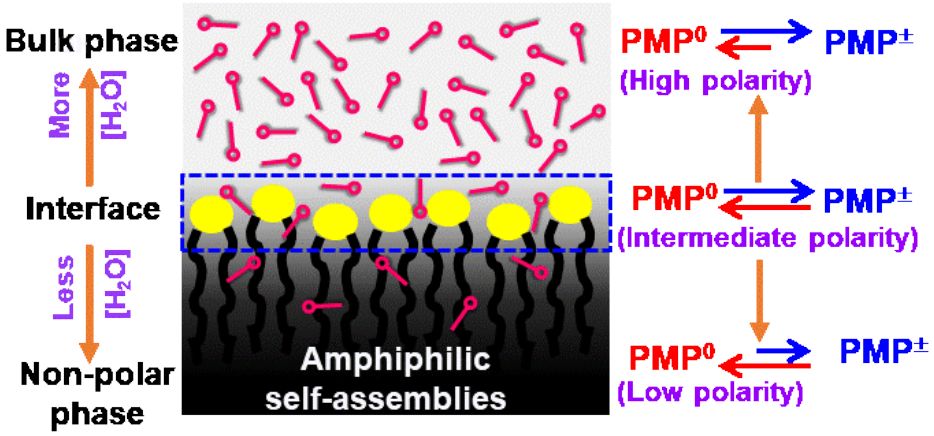

3.1. Introduction

The interfacial physicochemical properties, mainly the surface charge density, pH, polarity, viscosity etc. for self-aggregated assembly of amphiphilic molecules are of prime importance in a variety of fields, extending from material science[1-4] to catalysis[5-8] and controlled drug delivery.[9-15] As the interface is considered as the separation between bulk aqueous and self-assembled interior oil phase, interfacial polarity is expected to be less polar than that of bulk water. It has been reported that the local polarity across the membrane interface plays critical role for controlling different biochemical processes like membrane transport,[16] ion transport across the membrane interface,[17-19] insertion of protein/molecules into membranes and their translocation across the membrane.[15,20,21] On the other hand, the dramatic change of interfacial polarity for drug-loaded polymeric micelle during its interaction with cellular membrane plays the ultimate role for targeted drug release.[9,22-24] Therefore, the detection of interfacial polarity is indispensable to understand those interface selective biological processes that are controlled by its local polarity.

The polarity induced change in the electronic transition energy parameter (E_T) for small organic chromophoric systems has commonly been utilized to detect medium polarity.[25-27] However, the similar approach to evaluate the interfacial polarity for different self-assembled systems has yet to be addressed, although numerous studies have indicated a large difference in the polarities between the interface and bulk.[28-31] The detection of interfacial polarity with optical probe is challenging mainly due to micro-heterogeneous compartmentalization and the uncertainty about its bulk phase contribution. Moreover, the optical signal originated from the interface is often caused by multiple interfacial parameters,[26-32] such as the optical response due to the pH difference between interface and bulk phase may contributes in the optical responses originated due to the difference in their polarities.[32]

3.2. Work Analysis

Recently, a simple UV-Vis absorption spectrometry to evaluate the interfacial pH for cationic micelle and vesicle interfaces by utilizing an interface interacting Schiff-base molecule has been reported by P. Parui and co-workers.[32] The simplicity of such detection methodology encourages us to show it as a simple and powerful technique for monitoring various interfacial physicochemical properties. Herein, for the first time, detection of interfacial polarity for versatile

self-assemblies, such as lipid vesicles and micelles with variable interfacial charge characters and aggregation numbers, is reported. The newly synthesized interface interacting Schiff base molecule which mainly exists as a non-ionic species in non-polar medium, gradually converts into a zwitterionic form via the ground state intra-molecular proton transfer (GSIPT) process with increasing medium polarity (Scheme 1). UV-Vis absorption spectroscopy has been utilized to evaluate the interfacial polarity for vesicles and micelles by estimating the equilibrium between the two molecular forms at the interface.

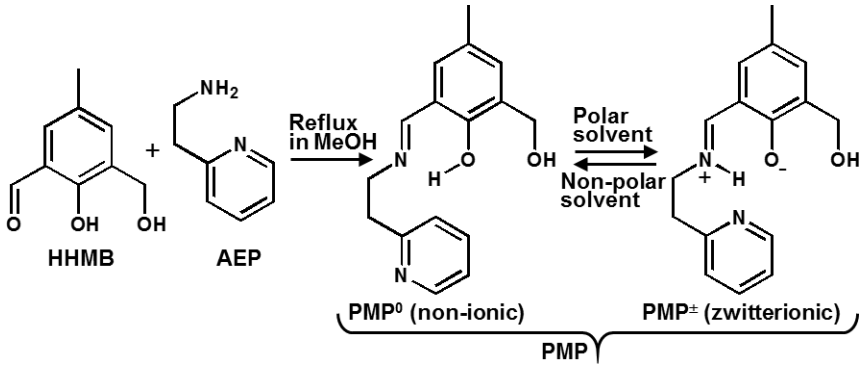

Scheme 1. Synthesis and solvent polarity dependent equilibrium between two molecular forms of the schiff base molecule (PMP).

3.3. Results and discussions

Several phenolic moieties containing Schiff base molecules with multiple polar O- and N-centres is highly prone to locate at the water/oil interface of self-assemblies.[32] To anchor the Schiff base molecule to the micro-heterogeneous charged interface electrostatically, 2-((2-(pyridine-2-yl) ethylimino) methyl)-6-(hydroxymethyl)-4-methylphenol (PMP) was synthesized, containing multiple polar O- and N-centers (Scheme 1).

3.3.1. Polarity dependent UV-Vis absorption studies of PMP

PMP shows excellent solvent polarity dependent changes in UV-Vis absorption responses. On increasing solvent polarity by increasing the amount of water fraction in the mixed THF/water medium, the 330 nm band intensity representing the phenol-conjugated-imine function gradually decreased with concomitant increase of a visible band centered at ~ 420 nm with a 360 nm isosbestic point[32,33] (Figure 1A). Identical spectral changeover was also detected for the comparable variation of medium polarity by using acetone or ethanol as a co-solvent in a mixed

medium with water (Figure 2). The results suggest that PMP exists as an equilibrium between the two molecular species and the polarity of the medium preliminary governs their relative concentrations.

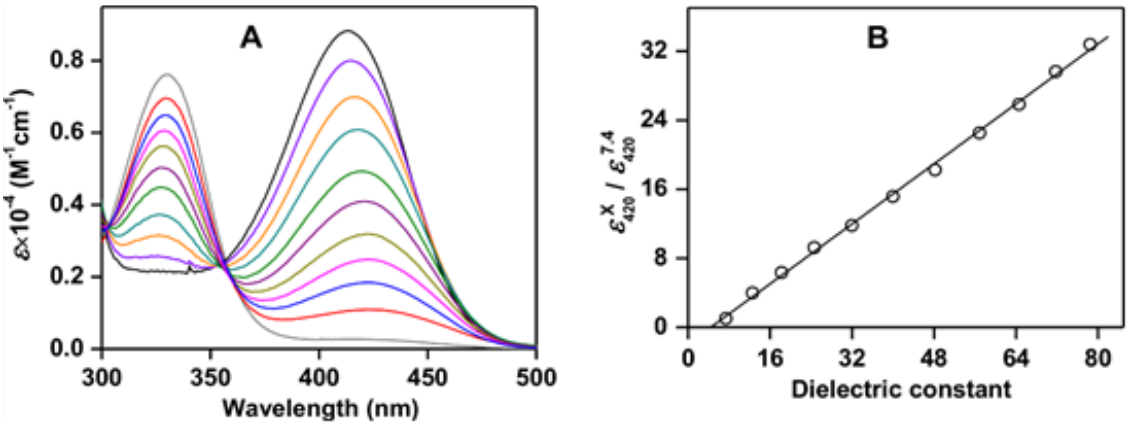

Figure 1. (A) UV-Vis absorption spectra of Schiff-base molecule PMP (5 µM) at different dielectric constants (κ) (7.4–78.5) in water/THF mixed medium at 25°C (*wt* % of THF in the mixtures are depicted in bracket): gray, 7.4 (1.0); red, 12.6 (0.9); blue, 18.3 (0.8); pink, 24.6 (0.7); dark yellow, 32.0 (0.6); purple, 40.0 (0.5); green, 48.2 (0.4); cyan, 56.6 (0.3); orange, 64.6 (0.2); violet, 71.7 (0.1) and black, 78.5 (0.0). (B) Normalized molar extinction coefficients at 420 nm (ε^{X}_{420}) (normalized by dividing molar extinction coefficient at 420 nm for the κ = 7.4 of THF ($\varepsilon^{7.4}_{420}$)) are plotted with κ.

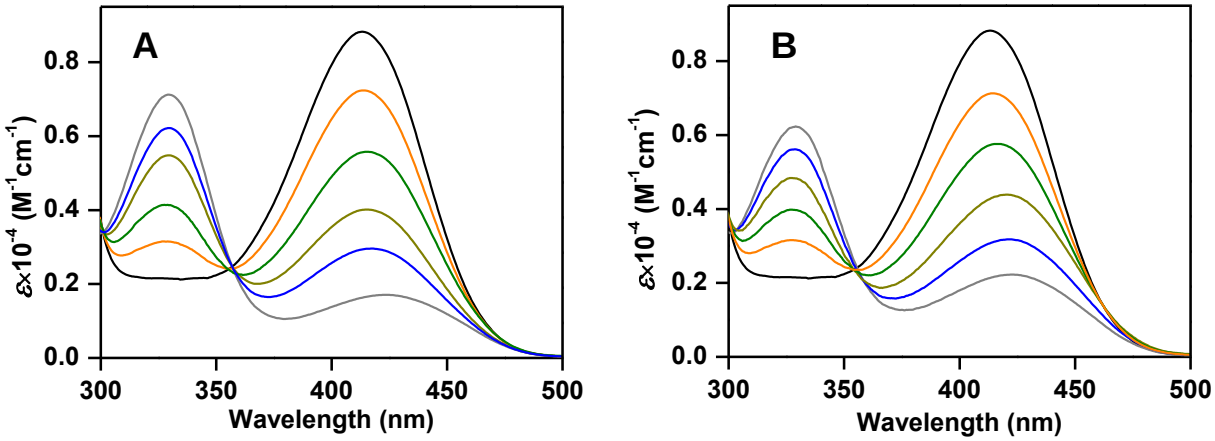

Figure 2. UV-Vis absorption spectra of PMP (5 µM) in (A) acetone/water and (B) ethanol/ water mixed medium at different dielectric constants (wt % of acetone or ethanol in the mixtures are depicted in bracket): (A) gray, 19.1 (1.0); blue, 29.6 (0.8); dark yellow, 41.8 (0.6); green, 54.6 (0.4); orange, 67.0 (0.2); and black, 78.5 (0.0): (B) gray, 24.3 (1.0); blue, 32.9 (0.8); dark yellow, 43.5 (0.6); green, 55.1 (0.4); orange, 67.3.0 (0.2); and black, 78.5 (0.0).

As the interaction between the solvent and chromophore affects the energy difference between the ground and electronically excited states, medium polarity/refractive index dependent absorption wavelength shift is often observed owing to the change in the dipole moment during electronic excitation. However, the relatively small slope values for the Stokes shift ($\nu_A - \nu_F$) *vs* orientation polarizability (Δf) linear plot according to the Lippert equation[34] for different solvent mixtures indicates a negligible change of dipole moment during excitation, and thus the influence of the solvent polarization on the large absorption shift (~ 85 nm or 6200 cm^{-1}) can be ignored (Figure 3).

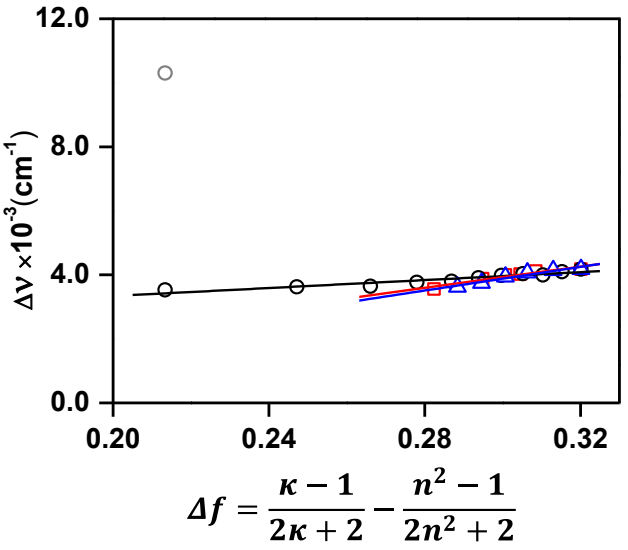

Figure 3. Lippert plot for PMP in (black) THF/water, (red) acetone/water and (blue) ethanol/water mixtures: Δν, stokes' shift for ~ 500 nm fluorescence intensity; Δ*f*, orientation polarizability containing dielectric constant (*κ*) and refractive index (*n*). The energy difference (cm^{-1}) between the absorption intensity maxima around 330 nm and the fluorescence intensity maxima around 500 nm for PMP in THF medium is depicted by gray point for comparison.

Since the absorbance changes with increasing solvent polarity was similar to that of previously observed base induced conversion of phenol (neutral) to phenolate (anion) form,[32,33] the 420 nm intensity may be originated for the formation of phenolate moiety. However, the unperturbed 420 nm intensity with decreasing the pH of the buffer medium from 11.0 to 6.0 indicates that the medium pH is not responsible for the phenol-to-phenolate interconversion (Figure 4A), since the pK_a for such phenolic-OH is close to 8.7.[32] Moreover, in 1:1 THF/H_2O medium, the identical absorbances without any increase of the 420 nm intensity for the phenolate between the pH higher and lower than 8.7 in 6.0–11.0 was observed possibly due to the increasing pK_a with decreasing

solvent polarity[35] (Figure 4B). Also, the unaltered absorption spectra on changing the solvent composition without changing its polarity, such as changing non-protonic acetonitrile (ACN) to protonic water containing THF/water mixture with same polarity (Figure 4C), shows that the H-bonding property of the solvent does not affect the interconversion between the two molecular forms of PMP. All these results support exclusive solvent polarity induced phenol-to-phenolate interconversion at pH 6.0–11.0. A zwitterionic species ($PMP^{\pm}$) containing the phenolate moiety with an absorption maximum at ~420 nm is observed presumably by gradual transfer of proton from the phenolic-OH to the imine-N through the GSIPT reaction with increasing the medium polarity resulting in an enhanced solvent-solute electrostatic stabilization (Scheme 1).

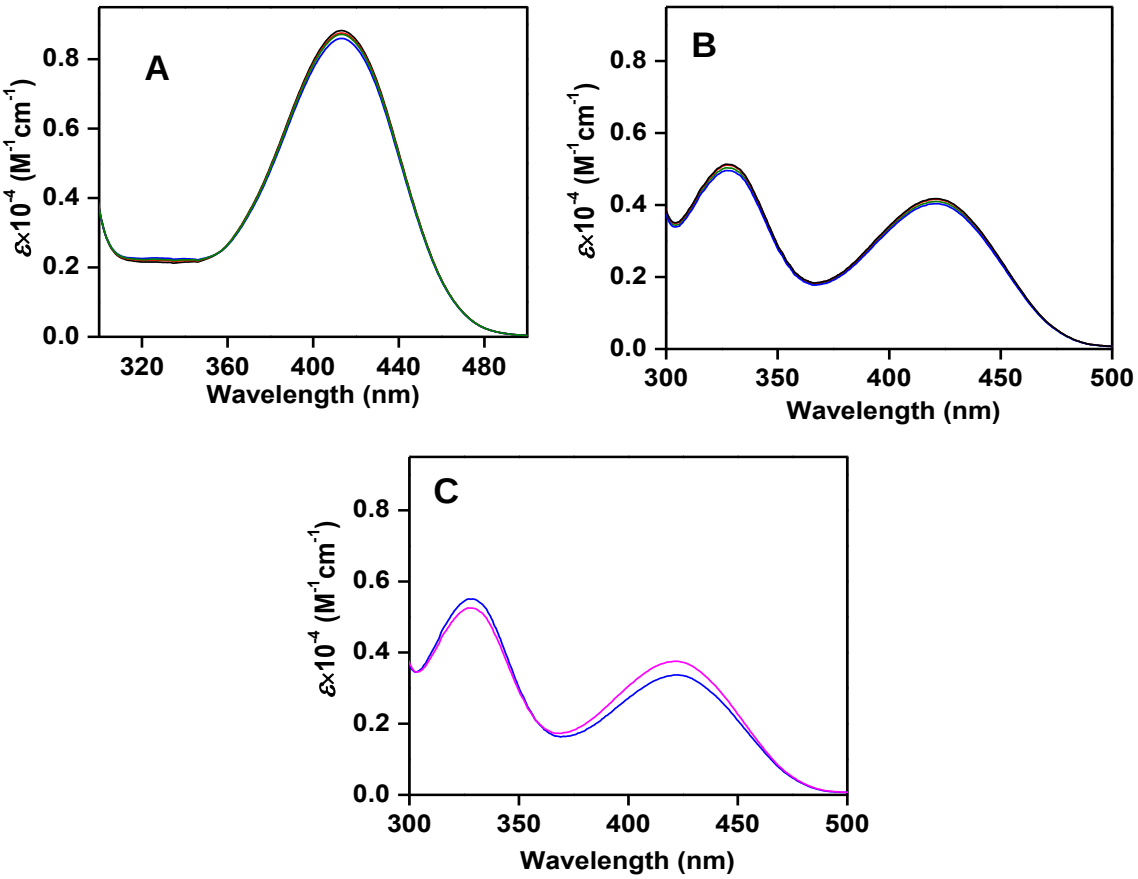

Figure 4. (A) UV-Vis absorption spectra of Schiff base molecule PMP (5 μM) in buffer at different pH: black, 6.0; red, 7.0; blue, 9.0; green, 11.0. (B) 1:1 THF/buffer solution at different pH: black, 6.0; red, 7.0; blue, 9.0; green, 11.0. (C) Solvent variation at identical dielectric constant (37.5): pink, THF/water mixture (52.5% (*w/w*) THF in the mixture); blue, ACN.

3.3.2. UV-Vis absorption studies of PMP in the presence of self-assembled systems

A series of amphiphilic self-assembled systems of different structural and interfacial charge characters from one to another, such as anionic sodium dodecyl sulphate (SDS) and sodium taurocholate (STA), cationic cetrimonium bromide (CTAB) and tri-block co-polymer (TBP) [36], neutral triton X-100 (TX-100), and anionic 1,2-dimyristoyl-sn-glycero-3-phosphoryl-glycerol (DMPG) phospholipid have been included to investigate the interaction at interface using UV-Vis absorption spectra (Figure 5,6). All amphiphilic molecules generate micelle in aqueous medium, whereas DMPG produces vesicle containing bilayer membrane structure.

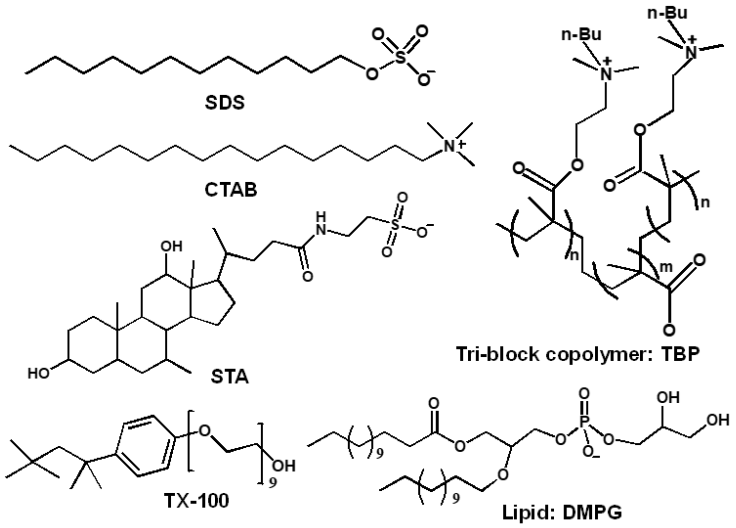

Figure 5. Structure of different amphiphilic molecules.

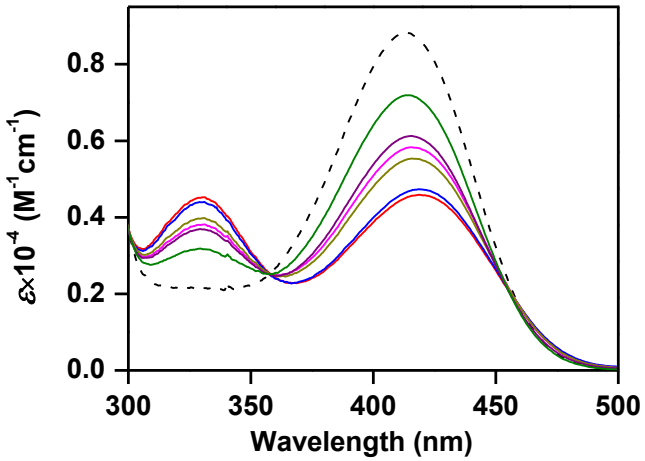

Figure 6. UV-Vis absorption spectra of Schiff base PMP (5 μM) in the presence of intensity-saturated concentrations of different amphiphilic molecules in 20 mM HEPES buffer, pH 7.3, 25°C: red, SDS (15.0 mM); blue, CTAB (7.0 mM); pink, TX-100 (9.0 mM); green, STA (10.0 mM); purple, TBP (0.5 mM); dark yellow, DMPG (5.0 mM). The spectrum in absence of any amphiphilic molecule is depicted by black.

In the UV-Vis absorption spectra, irrespective to the self-assemblies, a gradual decrease in intensity at 420 nm with concomitant increase at 330 nm was detected for PMP (5.0 µM) when increasing the concentration of any amphiphilic molecule until a saturation was observed at a particular concentration (SDS: 15.0, CTAB: 7.0, TX-100: 9.0, STA: 10.0, TBP: 0.5 and DMPG: 5.0 mM) (Figure 6,7). Such gradual change of intensities with increasing concentration of amphiphilic molecule indicates that increasing amount of PMP (PMP^0 and $PMP^{\pm}$) is located at the interface and the intensity saturation justifies the absence of any residual PMP in the bulk medium.

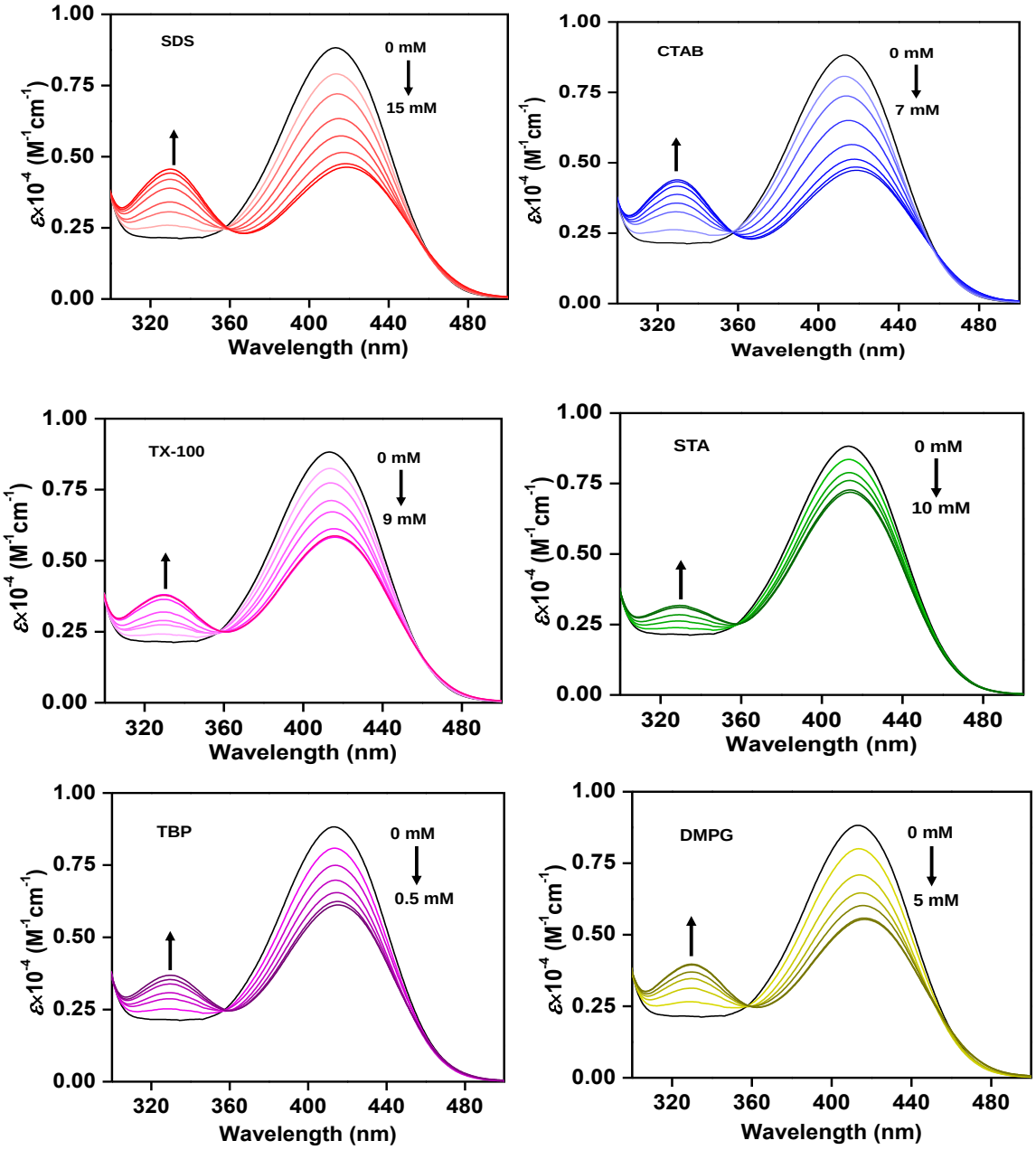

Figure 7. UV-Vis absorption spectra of PMP (5 μM) in presence of increasing concentration of different self-assembled systems in 20 mM HEPES-NaOH, pH 7.3.

3.3.3. DFT-based theoretical calculation

For explanations of the experimental absorption parameters, the TD-DFT calculations on the DFT-optimized geometries in various dielectric mediums were performed.[37] Most probable DFT-optimized geometry is considered for PMP molecule with the intra-molecular H-bonding between pyridine-N and proton in the imine-N (Scheme 2). The calculated vertical electronic transition wavelength both for neutral (PMP^0) (~ 320 nm) and $PMP^{\pm}$ (~ 390 nm) were close to the observed absorption maxima ~ 330 and 420 nm for the respective species without showing any significant solvation polarizability induced spectral shift (Table 1). The results strongly support the hypothesis on not only the formation of $PMP^{\pm}$, but also the negligible effect of the solvent polarity on the observed large spectral shift.

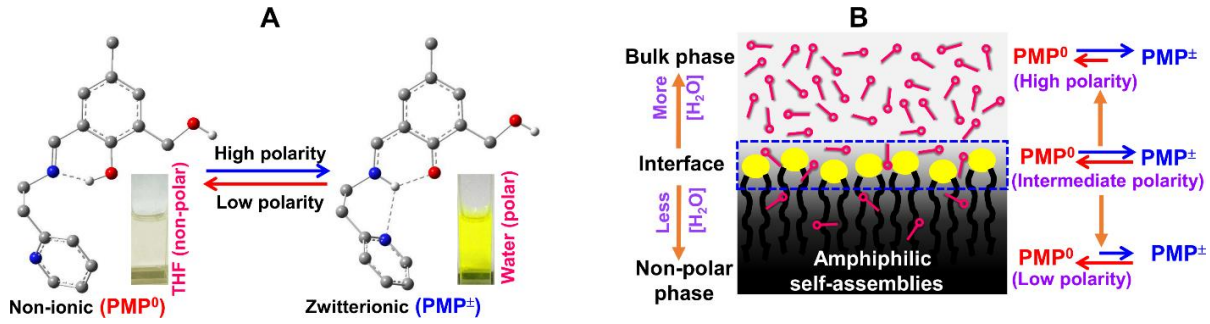

Scheme 2. (A) The equilibrium between two molecular forms of PMP (PMP^0 and $PMP^{\pm}$) with visible colorimetric response (PMP ~ 30 μM). In the DFT-optimized structure, all H's except bonded with N (blue) and O (red) are removed for clarity (single broken lines denote H-bond). (B) Schematic representation for the distribution of water (pink) in presence of amphiphilic self-assemblies. The equilibrium between two forms of PMP at various micro-environments are indicated in the right.

3.3.4 Dielectric constant dependent fluorescence studies of PMP

PMP (5.0 μM) molecule exhibits emission band at 500 nm upon excitation of ~440 nm in water/THF mixed medium at different dielectric constants (Figure 8). Although there is no correlation in relative interconversion between fluorescent $PMP^{\pm}$ and non-fluorescent PMP^0 with solvent polarity i.e., the dielectric constant (κ) was identified. In the fluorometric studies, a gradual increase in the steady state fluorescence anisotropy values for the 500 nm band of $PMP^{\pm}$ was observed by increasing the concentration of an amphiphilic molecule until a saturation was observed, at which an identical concentration was obtained for the absorption intensity saturation,

suggesting also that almost all PMP molecules were located at the interface (Figure 9 (A, B)). Probably, electrostatic interaction of self-assembled systems possessing variable interfacial charge (positive or negative) characters with $PMP^{\pm}$ possessing the opposite polarity site existed in a considerable amount, which resulted the interface location of PMP. On the other hand, the multiple O and N polar-centres containing relatively non-ionic PMP^{0} is also intent to stay at the interface with intermediate polarity rather than the highly polar bulk or highly non-polar interior phase (Scheme 2A). Although, the precise depth for probe (PMP) localization within the interface is not entirely clear.

Table 1: Electronic excitation wavelength (nm), oscillator strengths (f_{cal}) and extinction coefficient (ε) of non-ionic (PMP^{0}) and zwitterionic ($PMP^{\pm}$) forms obtained by the TD-DFT/B3LYP/6-31G++(d,p) calculation on ground state geometries with CPCM different dielectric solvation. The experimentally obtained UV-Vis absorption (Obs/Abs) parameters for PMP are depicted for comparison.

	Form	Solvent (κ)	λ (nm)	f_{cal}	$\varepsilon \times 10^{-4}$ (M^{-1} cm^{-1})
TD-DFT	PMP^{0}	Heptane (1.9)	324.63	0.109	0.46
		THF (7.4)	322.50	0.109	0.45
		MeOH (33.0)	321.45	0.104	0.43
		Water (78.5)	321.36	0.104	0.43
	$PMP^{\pm}$	Heptane (1.9)	393.08	0.169	0.66
		THF (7.4)	390.52	0.170	0.69
		MeOH (33.0)	388.52	0.164	0.66
		Water (78.5)	388.42	0.165	0.68
Obs/Abs	PMP	THF (7.4)	330.00	-	0.76
			425.80		0.03
		MeOH (33.0)	329.00	-	0.56
			423.25		0.32
		Water (78.5)	328.00	-	0.21
			413.60		0.88

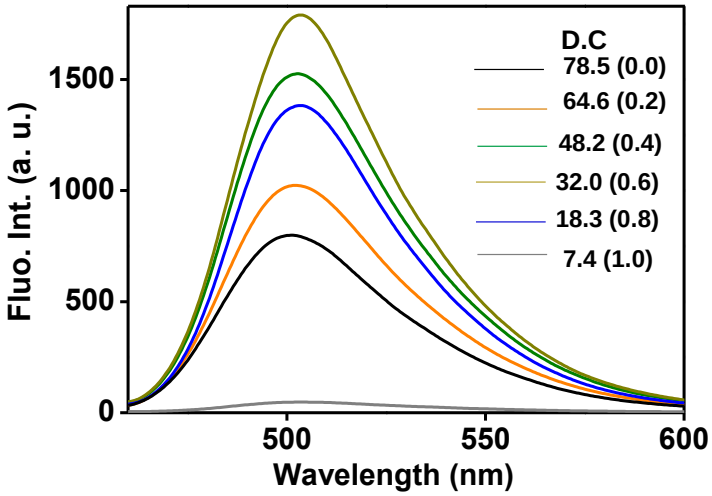

Figure 8. Fluorescence spectra of PMP (5 μM) in water/THF mixed medium at different dielectric constants (D.C).

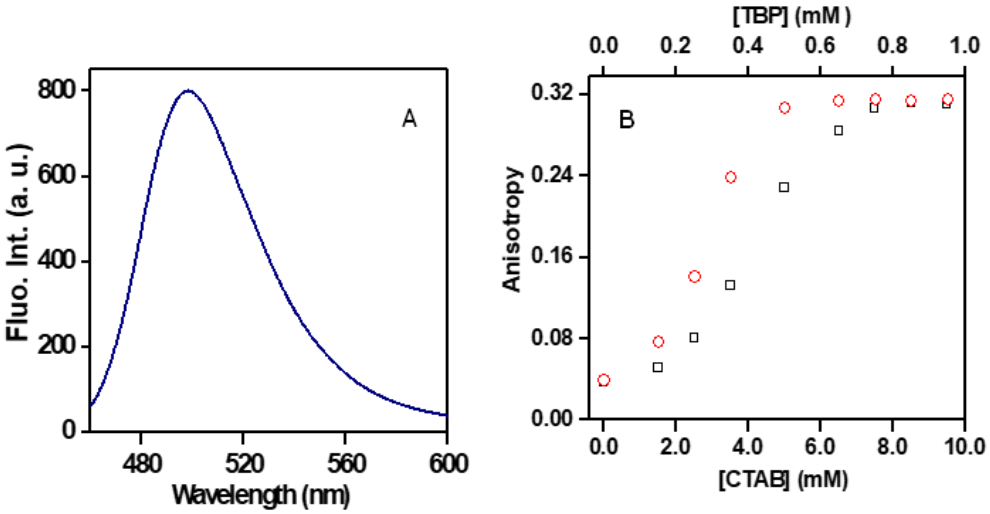

Figure 9. (A) Steady state fluorescence spectra of PMP (5.0 μM) in buffer, pH 7.3. (B) Change in fluorescence anisotropy values with concentration of different amphiphilic systems in buffer, pH 7.3: (squire) CTAB (lower x-axis), (circle) polymer TBP (upper x-axis). (A, B) Excitation and (B) emission wavelength was 440 and 500 nm, respectively.

3.3.5. Determination of interfacial polarity

As the relative concentration between non-ionic PMP^0 and zwitterionic $PMP^{\pm}$ was found to remain unchanged with the change of solvent viscosity or the pH 6.0 – 11.0 without changing the polarity (Figure 10), the solvent polarity, i.e., dielectric constant (κ) can be estimated from the

normalized 420 nm extinction coefficient ($\varepsilon^{X}_{420}/\varepsilon^{7.4}_{420}$) vs κ ratiometric linear correlation according to Fig. 1B as follows.

$$\kappa = 0.44 \times (\varepsilon^{X}_{420}/\varepsilon^{7.4}_{420}) \qquad (1)$$

Where, the extinction coefficient of measuring solution (ε^{X}_{420}) is normalized by the 420 nm ε for solvent THF ($\varepsilon^{7.4}_{420}$) and 0.44 represent the slope value of the linear plot.

The identical absorbance in pure methanol (κ ~ 33.0) to that in same κ achieved by increasing the κ value from 33.0 to 55.0 and subsequently reversing back to 33.0 by consecutive addition of water and THF, respectively, suggests the polarity induced reversible interconversion between PMP^0 and $PMP^{\pm}$. The generation of the visible absorption intensity at ~ 420 nm due to conversion from PMP^0 to $PMP^{\pm}$ and subsequent change of color from colorless to bright yellow with increasing polarity is also useful for estimating the medium polarity calorimetrically (Scheme 2A). All these observations suggest that the PMP can be utilized as a novel polarity indicator.

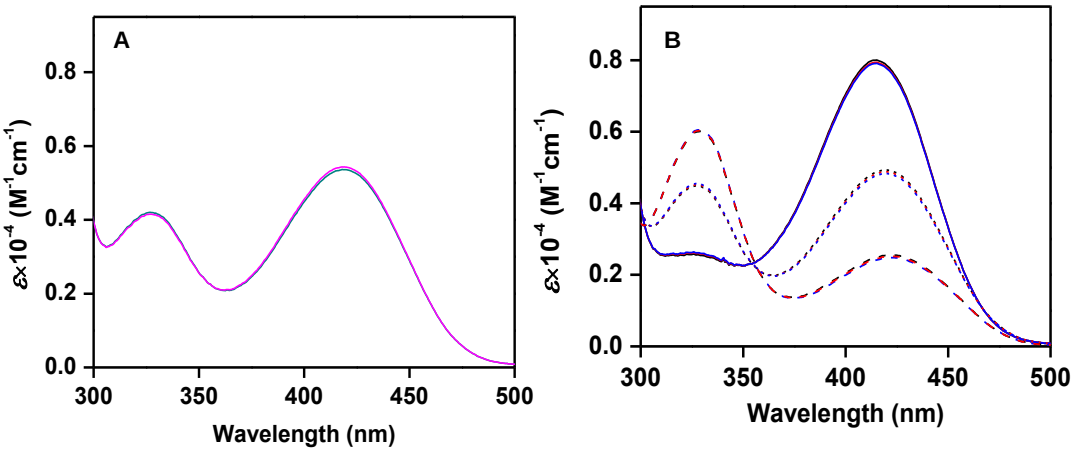

Figure 10. (A) UV-Vis absorption spectra of PMP (5 μM) at different medium viscosity under identical dielectric constant (51.0): pink, water/THF mixed medium (37.5% (*w/w*) THF in the mixture); cyan, water/glycerol mixed medium (80% (*w/w*) glycerol in the mixture). (B) In buffer of different pH (6.0, black; 7.0, red; 8.0, blue) and dielectric constants (solid, 72.0; short dash, 48.0; broken, 25.0) of the medium.

As any absorption intensity changes due to variation of $[PMP^{\pm}]$ or $[PMP^0]$ are only dictated by the medium polarity, the difference in pH or viscosity between the interface and bulk as reported previously[32,38] may not contribute in the self-assembly induced absorbance changes. Therefore, the change of normalized ε_{420} owing to the relocation of PMP from bulk to interface can be directly

correlated with the interfacial polarity. The κ value corresponding with the deviation-saturated normalized ε_{420} according to eqn. 1 represents the interfacial κ (Figure 1.B, 6 and Table 2). It is noteworthy to mention that the bulk polarity remains same as that of pure buffer in presence of self-assemblies, since the overall volume occupied by the interface is extremely smaller compared to the total effective volume occupied by the bulk phase. A highly reduced interfacial κ compared to that of bulk aqueous phase were detected for both SDS and CTAB micelles, where the interfacial κ for the anionic SDS micelle ~ 43.5 is close to the cationic CTAB micelle ~ 44.5 (Table 2). It suggests that the interfacial polarity does not depend on interfacial charge property. As the interface is the separation between highly polar aqueous phase and nonpolar micellar core, a considerable decrease of water concentration at the interface compared to the bulk phase may be responsible for such observed similar intermediate polarity between micellar core and bulk water (Scheme 2B).

Table 2: The saturation deviated normalised ε^{X}_{420} ($\varepsilon^{X}_{420}/\varepsilon^{7.4}_{420}$) for PMP in the presence of different self-assemblies in 20 mM HEPES buffer, pH 7.3, 25 °C. The interfacial dielectric constants (κ) are deduced from eqn. (1).

Amphiphilic molecule	$\varepsilon^{X}_{420}/\varepsilon^{7.4}_{420}$	κ
Buffer[a]	32.3	78.7
SDS	16.9	43.5
CTAB	17.3	44.5
TX-100	21.5	53.8
STA	26.3	65.0
TBP	22.5	56.0
DMPG	20.3	51.2

[a] Pure aqueous buffer medium without any amphiphilic molecule.

However, a significant increase in polarity was detected for TX-100 micellar interface (~ 53.8) compared to the polarity of SDS or CTAB micellar interface (Scheme 2B, Table 2). It indicates that the presence of polymeric oxo-ethylene residue in TX-100 induces greater extent of water

penetration by H-bonding interaction directed towards the hydrophobic core resulting an increase of water concentration at the interface (Scheme 2B, Figure 6). Also, the presence of multiple polar residues besides ionic residues in both tri-block copolymer (TBP) and lipid DMPG may be responsible for relatively higher κ ~ 56.0 and 51.2 for respective self-assemblies, similar to that of TX-100 micelle (Figure 6, Table 2). Although both SDS and STA contain a same anionic sulphate moiety, a large increase of interfacial polarity was identified for the STA micelle ~ 65.0, (Figure 6, Table 2), presumably due to the interface of the STA micelle with low aggregation number (a) ~ 4–5 was more hydrated and solvent exposed compared to that of the SDS micelle with high a ~ 80.

3.4. Conclusions

In conclusion, a highly interface selective Schiff base molecule (PMP) showing polarity dependent interconversion from its non-ionic (PMP^0) to zwitterionic ($PMP^{\pm}$) form has been synthesized to evaluate the interfacial polarity for versatile self-assembled systems of different structural and interfacial change characters from one to another. The GSIPT leading to switchover from PMP^0 to $PMP^{\pm}$ as evident in the UV-Vis absorption studies and DFT-based theoretical calculations follows a linear correlation with κ of the medium. Although interfacial pH or viscosity is appreciably different from that of bulk, the unchanged [$PMP^{\pm}$] or [PMP^0] with change of pH 6.0–11.0 and/or viscosity is highly useful for detection of interfacial κ (SDS: 43.5, CTAB: 44.5, TX-100: 53.8, STA: 65.0, tri-block-polymer TBP: 56.0 and lipid DMPG: 51.2) by utilizing the linear relation between normalized ε_{420} (or [$PMP^{\pm}$]) and κ.

3.5. References

1. V. Uskokovic and M. Drofenik, *Surf. Rev. Lett.*, 2005, **12**, 239.
2. M. V. Tirrell and A. Katz, *MRS BULLETIN*, 2005, **30**, 700.
3. M. F. Ottaviani, A. Moscatelli, D. Desplantier-Giscard, F. Di Renzo, P. J. Kooyman, B. Alonso and A. Galarneau, *J. Phys. Chem. B.*, 2004, **108**, 12123.
4. S. Forster and M. Antonietti, *Adv. Mater.*, 1998, **10**, 195.
5. G. L. Sorella, G. Strukul and A. Scarso, *Green Chem.*, 2015, **17**, 644.
6. Z. Nairoukh, D. Avnir and J. Blum, *ChemSusChem.*, 2013, **6**, 430.
7. G. Stavber, M. Zupan and S. Stavber, *Synlett.*, 2009, **4**, 589.

8. D. R. M. Arenas, C. A. M. Bonilla and V. V. Kouznetsov, *Org. Biomol. Chem.*, 2013, **11**, 3655.
9. C. J. F. Rijcken, O. Soga, W. E. Hennink and C. F. V. Nostrum, *J. Control. Release*, 2007, **120**, 131.
10. N. Nishiyama, Y. Kato, Y. Sugiyama and K. Kataoka, *Pharm. Res.*, 2001, **18**, 1035.
11. P. Couvreur, F. Puisieux and N. Ano, *Adv. Drug Delivery Rev.*, 1995, **10**, 141.
12. D. D. Lasic, *Nature*, 1996, **380**, 561.
13. A. Krishnadas, I. Rubinstein and H. Onyuksel, *Pharm. Res., 2003,* **20**, 297.
14. M. Yokoyama and M. Novel, *Biorelated Polymers and Gels, San Diego, CA: Academic Press*, 1998, 193.
15. J. Cladera and P. Oshea, *Biophys. J.*, 1998, **74**, 2434.
16. G. Apodaca, L. I. Gallo and D. M. Bryant, *Nat Cell Biol.*, 2012, **14**, 1235.
17. S. Kim, K. No and S. Hong, *Chem. Commun.*, 2016, **52**, 831.
18. J. Kim, J. H. Jeon, H. J. Kim, H. Lim and I. K. Oh, *ACS Nano*, 2014, **8**, 2986.
19. S. Liu, Y. Liu, H. Cebeci, R. G. Villoria, J. H. Lin, B. L. Wardle and Q. M. Zhang, *Adv. Funct. Mater*., 2010, **20**, 3266.
20. M. Barberon, G. Dubeaux, C. Kolb, E. Isono, E. Zelazny and G. Vert, *Proc. Natl. Acad. Sci*., 2014, **111**, 8293.
21. L. Voglino, T. J. McIntosh and S.A. Simon, *Biochemistry*, 1998, **37**, 12241.
22. D. Neradovic, W. L. J. Hinrichs, J. J. K. Bosch, C. F. V. Nostrum and W. E. Hennink, *Macromol. Rapid Commun.*, 1999, **20**, 577.
23. D. Neradovic, C. F. V. Nostrum and W. E. Hennink, *Macromolecules*, 2001, **34**, 7589.
24. O. Soga, C. F. V. Nostrum, A. Ramzi, T. Visser, F. Soulimani, P. M. Frederik, P. H. H. Bomans and W. E. Hennink, *Langmuir*, 2004, **20**, 9388.
25. M. S. Tunuli, M. A. Rauf and Farhataziz, *J. Photochem*., 1984, **24**, 411.
26. C. Reichardt, *Chem. Rev.*, 1994, **94**, 2319.
27. P. Jose, C. Carrasco, D. Jacquemin, C. Laurence, A. Planchat, C. Reichardt and K. Sraidi, *J. Phys. Org. Chem.*, 2014, **27**, 512.
28. S. Marta, FernBndez and P. Fromherz, *J. Phys. Chem.*, 1997, **81**, 1755.
29. R. Epand and R. Kraayenhof, *Chem. Phys. Lipids*, 1999, **101**, 57.
30. P. L. Novaki and O. A. E. Seoud, *Langmuir* 2000, **16**, 35.

31. A. S. Klymchenko, Y. Mely, A. P. Demchenko and Guy Duportail, *Biochimic et Biophysica Acta*, 2004, **1665**, 6.
32. Y. Sarkar, S. Das, A. Ray, S. K. Jewrajka, S. Hirota and P. P. Parui, *Analyst*, 2016, **141**, 2030.
33. S. Das, S. Biswas, S. Mukherjee, J. Bandyopadhyay, S. Samanta, I. Bhowmick, D. K. Hazra, A. Ray and P. P. Parui, *RSC Adv.*, 2014, **4**, 9656.
34. J. R. Lakowicz, in *Principles of Fluorescence Spectroscopy*, Springer, 3rd edn, 2006, ch. 6.
35. A. Kütt, I. Leito, I. Kaljurand, L. Sooväli, V. M. Vlasov, L. M. Yagupolskii and I. A. Koppel, *J. Org. Chem.*, 2006, **71**, 2829.
36. U. Chatterjee, S. K. Jewrajka and B. Mandal, *Polymer*, 2005, **46**, 1575.
37. D. Robinson, N. A. Besley, P. O'Shea and J. D. Hirst, *J. Phys. Chem. B*, 2011, **115**, 4160.
38. S. Yamaguchi, K. Bhattacharyya and T. Tahara, *J. Phys. Chem. C*, 2011, **115**, 4168.

Chapter 4

Detection of interfacial pH and polarity for amphiphilic self-assemblies using a single Schiff-base molecule

Detection of interfacial pH and polarity for amphiphilic self-assemblies using a single Schiff-base molecule

Abstract

The interfacial pH and polarity are two highly interrelated parameters in amphiphilic self-assembled systems. The hydronium ion (H_3O^+) concentration and/or the pH value near the water/oil separating interface may change significantly due to large polarity gradients between water- and oil-exposed surfaces within the interface. Therefore, for precise detection of these two properties (pH and polarity) at a specific interfacial depth, a similar interfacial location of the same probe is a prerequisite. In this regard, we have synthesized a new interface-interacting Schiff-base (SBOH-Z-SBOH) molecule to detect both the interfacial pH and polarity of various amphiphilic self-assembled micelles and vesicles at a similar interfacial location. SBOH-Z-SBOH, existing mostly as a non-ionic species ($SBOH^0$-Z-$SBOH^0$) in nonpolar solvents, exhibits an exclusive solvent polarity-dependent linear interconversion equilibrium with its partially charge separated zwitterionic form $SBOH^0$-Z-$SBOH^{\pm}$ as the polarity of the medium increases, which makes it useful to detect the polarity. Additionally, the solvent pH-dependent conversion of both $SBOH^0$-Z-$SBOH^0$ and $SBOH^0$-Z-$SBOH^{\pm}$ into the deprotonated di-anionic species (SBO^--Z-SBO^-) allows it to monitor the pH. We found that the interfacial dielectric constant (~ 44.0–54.0) differs substantially from that of the bulk aqueous medium depending on the amphiphilic system. On the other hand, unlike the neutral interface of titron X-100 (TX-100) micelles or 1,2-dioleoyl-sn-glycero-3- phosphocholine (DOPC) unilamellar vesicles (ULVs), a large positive pH-deviation of ~1.8 and 2.2 units from the bulk to the interface was identified for cationic cetrimonium bromide (CTAB) micelles and dimethyldioctadecylammonium bromide (DDAB) ULVs, respectively. The present study provides a unique and simple Schiff-base molecule to monitor the pH and polarity at similar interfacial depths for amphiphilic self-assembled systems.

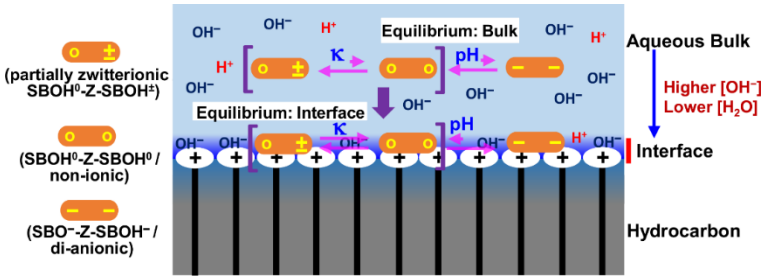

4.1. Introduction

The cellular membrane interface organizes enormous number of complex biological reactions which plays various essential roles in our life processes. Most of these biochemical reactions at the membrane interface, such as membrane transport,[1] ion transport across the membrane,[2-4] insertion of protein/molecules into membrane and their translocation across the membrane,[5,6] is highly interrelated with the membrane subdomain structural identity. However, in most of the cases, the mechanisms for the membrane's structure dependent reactivities are not completely understood. The major difficulties appear primarily for the highly complicated structure of cellular membrane interface. Such structural complicacy is often generated due to the micro-heterogeneous distribution of different kind of lipids and protein molecules.[7-10] Nevertheless, it has also been identified that these membrane reactivities are profusely affected by the changes in intercellular physiochemical parameters, such as, pH and polarity.[11-15] In this context, we strongly believe that distinct membrane reactivities originated from the membrane structure dependent manipulation of the interfacial pH and polarity values. Therefore, accurate detection of the interfacial pH as well as polarity is really essential to identify various biochemical events controlled by the interfacial pH and/or polarity of the cellular membranes.

It has frequently been observed that the amphiphilic self-assembled micelle and bilayer lipid vesicle are exploited as the model of a cellular membrane to explain various interfacial biological processes.[16-19] However, the monitoring of interfacial properties themselves for self-assemblies is extremely difficult due to highly complex micro-heterogeneous compartmentalization including the uncertainty about its bulk phase contribution. A number of studies have indicated a discrepancy in interfacial properties from the bulk value in amphiphilic self-assembled systems,[20-22] although their precise estimation has rarely been addressed. Recently, Tahara and co-workers designed a heterodyne-detected electronic sum frequency generation spectroscopic method to estimate the acid/base interconversion properties at ionic micelles and vesicles, and monitored the interfacial pH values.[23,24] The studies showed that the interfacial pH differs adequately from the bulk pH.

4.2. Work Analysis

The strategically designed Schiff-base molecule due to its enormous applicability[25-28] could be utilized to evaluate interfacial pH/polarity for amphiphilic self-assembled systems. P. parui and

co-worker have recently introduced a new interfacial pH/polarity monitoring method for biologically important micelles and vesicles by utilizing interface interacting Schiff-base molecular probes.[29, 30]They have shown that the pH/polarity substantially changes at the interface from that of the bulk phase. The inherent simplicity of this detection technique may be highly effective for complicated biological interfaces.

However, the pH and polarity are two highly interrelated physiochemical parameters at the interface. A minute change of interfacial polarity may affect the pH value to a considerable extent probably due to difference in the H^+ ion conducting ability as H_3O^+ ion.[31-34] As the interface separates hydrocarbon (hydrophobic) from the polar aqueous medium, the interfacial polarity may be expected to change substantially with a small alteration of the depth along the interfacial cross-section.[35,36] Therefore, the detection of pH and polarity at a similar interfacial depth is essential. To eliminate the discrepancies arising due to the difference in probe location depth for pH and polarity, we propose a single optical probe for dual detection purpose. Herein, a simple interface interacting Schiff-base molecule containing two identical phenol-conjugated-imine functions is synthesized for the detection of interfacial pH and polarity (scheme 1). The deviation in the pH/polarity-induced interconversion equilibrium among various molecular forms of the Schiff-base molecule from the bulk to interface is exploited to monitor the interfacial pH and polarity for various self-assembled micelles and vesicles. Under acidic-to-neutral bulk pH conditions, the polarity dependent interconversion equilibrium between the non-ionic and the zwitterionic forms for the probe molecule can be utilized to estimate the interfacial polarity. On the other hand, the interfacial pH value and its deviation from the bulk pH value are detected from the pH dependent interconversion from the non-ionic/zwitterionic species to deprotonated anionic species for the probe molecule.

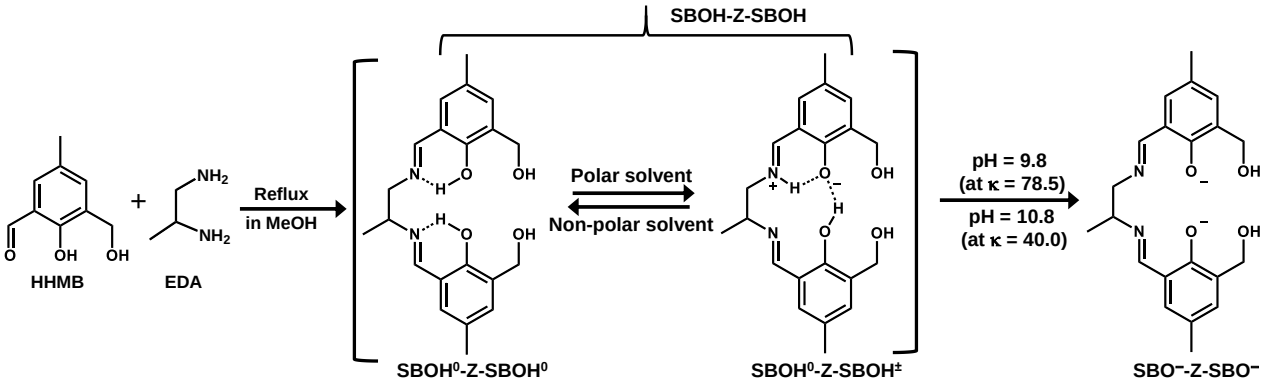

Scheme 1. Synthesis and solvent polarity/pH-dependent different molecular forms of the Schiff base molecule (SBOH-Z-SBOH).

4.3. Results and discussions

4.3.1. SBOH-Z-SBOH acid/base equilibrium in buffer to measure pH

UV-Vis absorption studies: The SBOH-Z-SBOH acid/base equilibrium was utilized to measure the pH. The phenolic-OH deprotonation reaction for the newly synthesized Schiff-base molecule (SBOH-Z-SBOH) containing two identical phenol-conjugated-imine moieties was investigated by pH-metric titration (Scheme 1). Recently, we have observed that the 320 nm UV-Vis absorption band for a similar phenol-conjugated-imine moiety gradually depletes with increasing pH of the medium to generate 400 nm intensity due to deprotonation of the phenol moiety (pK_a ~ 8.7).[29] Although SBOH-Z-SBOH contains two closely related phenol moieties, the co-existence of ~ 420- and 320 nm absorption intensities even at an acidic pH ~ 5.5 indicates a substantial fraction of both the phenol and phenolate moieties (Figure 1A). However, the unchanged 420- to 320 intensity ratio within pH 5.5 to 8.0 also shows that the phenol-to-phenolate ratio did not vary in this pH range (Figure 1). The result suggests that any one between two closely related phenol moieties in SBOH-Z-SBOH is probably susceptible to conversion into its phenolate form to generate 420 nm absorbances in the pH ~ 5.5–8.0 (Scheme 1). According to our DFT-based theoretical calculation (*vide infra*), it has been proposed that large polarity of the aqueous medium induces intramolecular ground state proton transfer reaction (IGSPT) from the phenolic-OH to its adjacent imine-N in in the SBOH-Z-SBOH. However, the other –SBOH moiety exists as its protonated form to produce partially charge separated zwitterionic species ($SBOH^0$-Z-$SBOH^{\pm}$) (Scheme 1). Most probably, such partial zwitterion formation in aqueous medium predominates as a result of large solute-solvent electrostatic stabilization effect.[30]

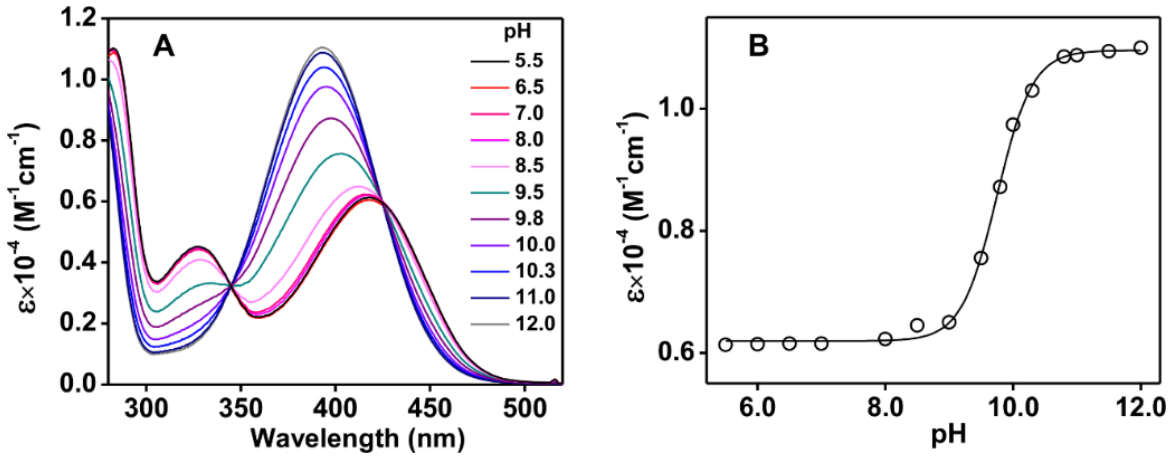

Figure 1. (A) UV-Vis absorption spectra of Schiff-base molecule SBOH-Z-SBOH (5.0 μM) at different pH (5.5–12.0) values in different 20 mM buffers: sodium citrate/sodium phosphate, pH 5.5–7.5; Tris-HCl, pH 8.0–9.0 and sodium carbonate/bi-carbonate, pH 9.0–12.0. (B) Molar extinction coefficient at the absorption intensity maxima (395–420 nm) (ε) at different pH values.

On further increasing the buffer pH (> 8.5), the 420 nm absorption band was gradually blue shifted maximally up to 395 nm with an increase in its intensity and subsequent depilation of the 320 nm band, until the intensity saturation observed at pH ~ 11.0 (Figure 1A). The absorption changeover with two different isosbestic points ~ 345 and 425 nm indicates that the di-anionic (SBO^{-}-Z-SBO^{-}) species with two identical anionic phenolate-conjugated-imine moieties (-SBO^{-}) was generated due to simultaneous deprotonation reaction from both the non-ionic -$SBOH^{0}$ and zwitterionic -$SBOH^{\pm}$ moieties in the SBOH-Z-$SBOH^{\pm}$ (Figure 1A, Scheme 1). Unlike phenolic-OH deprotonation from a single phenol-conjugated-imine moiety containing similar Schiff-base molecule,[29] the multiple proton dissociation reactions from $SBOH^{0}$-Z-$SBOH^{\pm}$ to form SBO^{-}-Z-SBO^{-} require more basic pH (pK_a ~ 9.7)[42,43] (Figure 1B). Nevertheless, the identical absorption spectra at pH ~ 8.5 to that at the same pH achieved by decreasing the SBOH-Z-SBOH (5.0 μM) containing buffer pH from 12.0 to 8.5 by addition of dilute HCl, suggests a medium pH-induced reversible interconversion between the $SBOH^{0}$-Z-$SBOH^{\pm}$ and the SBO^{-}-Z-SBO^{-} species.

Fluorescence studies: The fluorometric pH-titration for the SBOH-Z-SBOH was also performed in buffer medium (Figure 2). The weak fluorescence intensity at ~ 500 nm (ϕ_F ~ 0.002) due to excitation of the zwitterionic moiety (-$SBOH^{\pm}$) by 420 nm light remains invariant with a change in buffer pH from 5.5 to 8.0. Meanwhile, the non-ionic -$SBOH^{0}$ moiety is non-emissive in nature (ϕ_F ~ 0.0), since not even a trace amount of fluorescence intensity was identified with the

320 nm excitation (Figure 2A). However, the generation of SBO^{-}-Z-SBO^{-} at highly basic pH of ~ 11.0 results in a large increase in intensity (ϕ_F ~ 0.11). In the fluorescence transient decay studies, the excited state fluorescence lifetime (τ_F) value of ~ 0.5 ns for the -$SBOH^{\pm}$ moiety at low pH ~ 7.0 was enhanced by an order of magnitude to ~ 4.8 ns due to its conversion into -SBO^{-} moiety at pH ~ 11.0 (Figure 2B, Table 1). On the other hand, the bi-exponential transient decay nature at a pH close to the acid/base interconversion pK_a ~ 9.7 suggests the co-existence of both the $SBOH^{0}$-Z-$SBOH^{\pm}$ and the SBO^{-}-Z-SBO^{-} species. The fluorescence studies also suggest that the SBOH-Z-SBOH molecules mostly exists as $SBOH^{0}$-Z-$SBOH^{\pm}$ at pH 5.5–8.0, and convert gradually into the SBO^{-}-Z-SBO^{-} species with increasing pH of the medium.

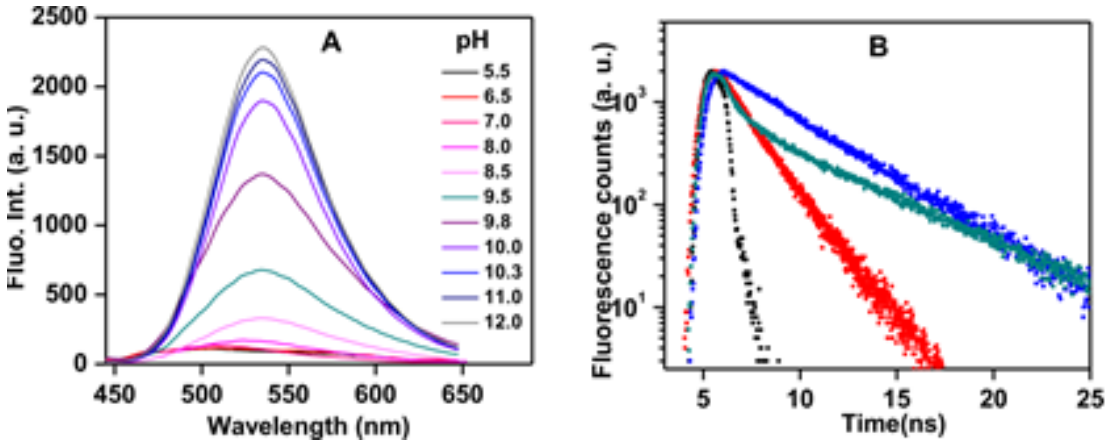

Figure 2. (A) Steady state fluorescence spectra of SBOH-Z-SBOH (5.0 µM) at different pH (5.5–12.0) values for 400 nm excitation. (B) Time resolved emission decay curves at different pH values: pH, 7.0 (red); pH, 9.8 (dark cyan); pH, 11.0 (blue). Excitation and emission wavelengths were 450 and 530 nm respectively. Scattering profile is represented in black.

As fluorescence properties are highly influenced by different environmentally controlled physicochemical parameters (polarity, viscosity),[44,45] the pH-dependent interconversion equilibrium among various molecular forms of SBOH-Z-SBOH was monitored by UV-Vis absorption spectroscopy to determine the pH (Figure 1B). However, to estimate the interfacial pH for different amphiphilic self-assembled systems, the measurement of interfacial polarity and subsequently the change in acid/base interconversion pK_a for the SBOH-Z-SBOH due to the difference in polarity from the bulk to interface is essential. To estimate the polarity/dielectric constant at a similar interfacial location/depth to that of the pH sensing molecule (SBOH-Z-

SBOH), the investigations were performed by utilizing the same probe molecule (SBOH-Z-SBOH).

Table 1: Fluorescence transient decay parameters of SBOH-Z-SBOH (5.0 μM) with residual of fitting (χ^2) in aqueous buffer solution at different pH values. Excitation and emission wavelengths were 450 and 500/530 nm respectively.

pH	Life time (ns)	χ^2
7.0	0.47 –	1.02
9.8	0.51 4.31	1.05
11.0	4.79 –	1.01

4.3.2. Polarity-dependent different molecular forms of SBOH-Z-SBOH: estimation of dielectric constant

The dielectric constant (κ) or polarity can be estimated from the solvent polarity dependent changes in the absorption profile of the SBOH-Z-SBOH in mixed THF/buffer medium at pH 5.5–8.0. The 420 nm UV-Vis absorption intensity for the zwitterionic moiety (-$SBOH^{\pm}$) in $SBOH^0$-Z-$SBOH^{\pm}$ was found to decrease gradually with increasing solvent κ. The equivalent increase in the 320 nm intensity while maintaining 365 nm isosbestic absorption suggests the conversion from -$SBOH^{\pm}$ to -$SBOH^0$ form (Figure 3A). Most probably, an inadequate solute-solvent electrostatic stabilization is responsible for converting -$SBOH^{\pm}$ into its non-ionic -$SBOH^0$ *via* reverse-IGSPT reaction to form $SBOH^0$-Z-$SBOH^0$ species at a decreased medium polarity. In the fluorometric studies, the 500 nm fluorescence band for the -$SBOH^{\pm}$ moiety in $SBOH^0$-Z-$SBOH^{\pm}$ was also observed to decrease gradually with the decrease of the solvent κ (Figure 4). The result supports the proposed formation of $SBOH^0$-Z-$SBOH^0$ containing two non-fluorescent -$SBOH^0$ moieties.

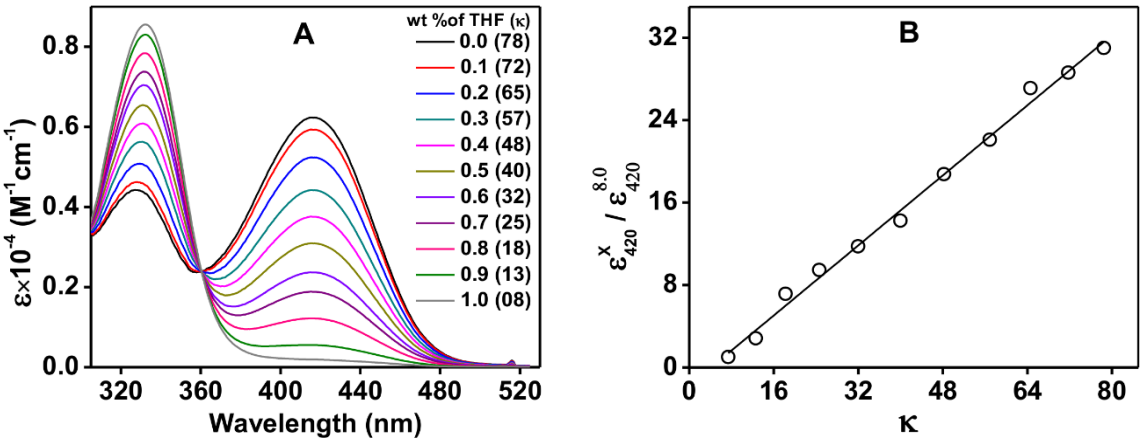

Figure 3. (A) UV-Vis absorption spectra of Schiff-base molecule SBOH-Z-SBOH (5.0 µM) at different dielectric constants (κ) (8.0–78.5) in buffer/THF mixed medium, pH 7.0. (B) Normalized molar extinction coefficients at 420 nm (ε^{X}_{420}) (normalized by dividing molar extinction coefficient at 420 nm for the κ of THF ($\varepsilon^{8.0}_{420}$)) are plotted against κ.

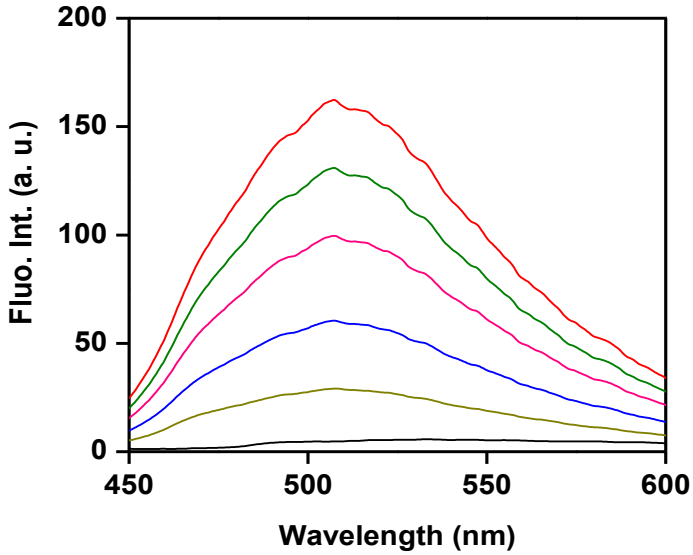

Figure 4. Fluorescence spectra of SBOH-Z-SBOH (5.0 µM) in buffer/THF mixed medium at different dielectric constants (wt % of THF in the mixtures are depicted in bracket): black, 8.0 (1.0); dark yellow, 18.3 (0.8); blue, 32.0 (0.6); pink, 48.2 (0.4); green, 64.6 (0.2); and red, 78.5 (0.0).

Noteworthy to mention, the extent of spectral changeover at a particular THF/buffer ratio in the mixed medium did not depend on the medium pH in the range 5.5–8.0 (Figure 5). Moreover, the relative 420 to 320 nm band intensity did not vary by the change of solvent composition or H-

bonding character or viscosity without varying the κ value (Figure 6). Also, the unchanged UV-Vis spectra in methanol solvent (κ ~ 33.0) to that in same κ achieved by increasing κ value from 33.0 to 55.0 and subsequently reversing it back to 33.0 by consecutive addition of water and THF, respectively, also suggests the polarity induced reversible interconversion between the $SBOH^0$-Z-$SBOH^{\pm}$ and the $SBOH^0$-Z-$SBOH^0$. All these results strongly suggest that the interconversion equilibrium between the $SBOH^0$-Z-$SBOH^0$ and the SBOH-Z-$SBOH^{\pm}$ depends exclusively on polarity of the medium. Therefore, the probe (SBOH-Z-SBOH) is highly effective for the detection of interfacial polarity for various amphiphilic self-assembled systems, in spite of large differences in pH and/or viscosity between the bulk and interface. Importantly, we identified a linear correlation between the normalized ε at 420 nm (ε_{420}) and the medium κ (Figure 3B).

$$\varepsilon^{X}_{420}/\varepsilon^{8.0}_{420} = 0.42\times\kappa - 1.8 \quad (1)$$

Where, the extinction coefficient of measuring solution (ε^{X}_{420}) is normalized by the 420 nm ε for the solvent THF ($\varepsilon^{8.0}_{420}$). The 0.42 and −1.8 represent the slope and intercept, respectively, for the linear plot. The unknown κ can be estimated using such linear correlation according to equation (1).

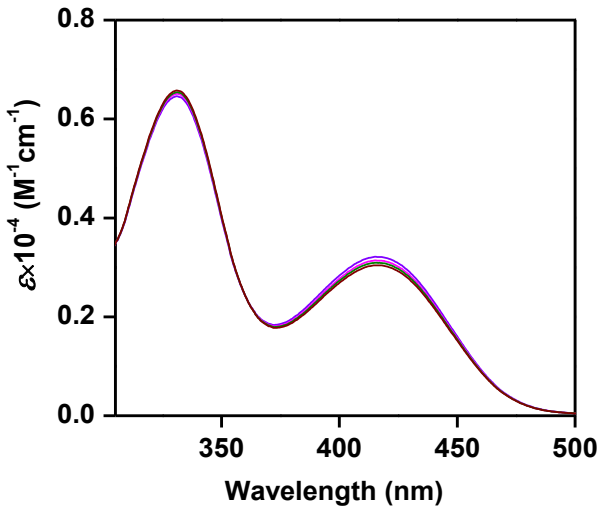

Figure 5. UV-Vis absorption spectra of SBOH-Z-SBOH (5.0 μM) in 1:1 THF/buffer solution at different pH: violet, 5.5; brown, 7.0; pink, 8.0; green, 10.0.

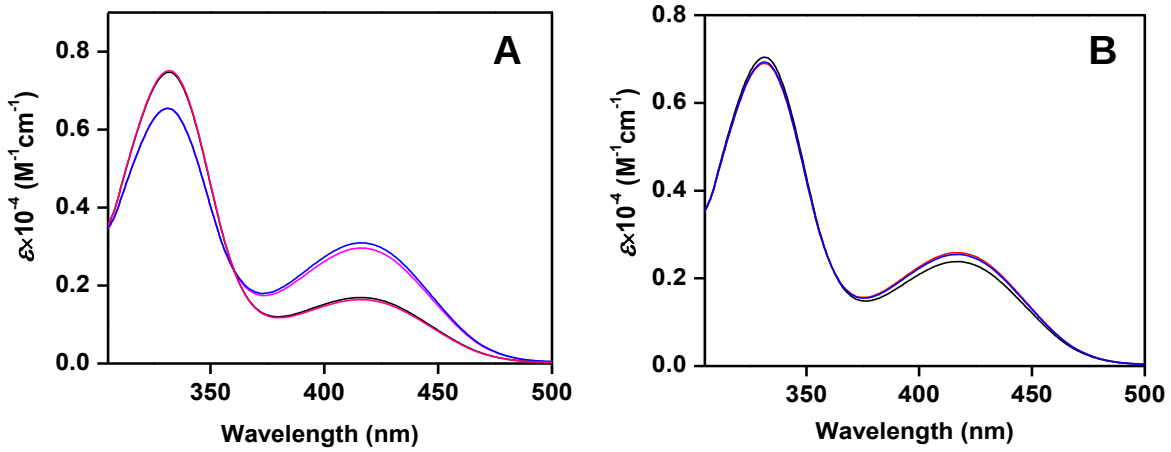

Figure 6. (A) Solvent composition dependent UV-Vis absorption spectra of SBOH-Z-SBOH (5.0 μM): pink, acetonitrile (κ ~ 37.5); blue, THF/water mixture (52.5% (*w/w*) THF in the mixture, κ ~ 37.5); red, THF/water mixture (70% (*w/w*) THF in the mixture, κ ~ 24.5); black, EtOH (κ ~ 24.5). (B) Solvent variation at under identical κ (~ 37.5) at pH 8.0: red, buffer/EtOH mixed medium (75% (*w/w*) EtOH in the mixture); blue, acetonitrile; black, buffer/glycerol mixed medium (80% (*w/w*) glycerol in the mixture).

4.3.3. DFT-based theoretical calculation

The structural elucidation for different molecular forms of the Schiff-base molecule (SBOH-Z-SBOH) identified in the spectroscopic studies were performed by the DFT-based theoretical calculation with the Gaussian 09.[41] The most probable ground state geometries for the non-ionic ($SBOH^0$-Z-$SBOH^0$), partially zwitterionic ($SBOH^0$-Z-$SBOH^{\pm}$) and di-anionic (SBO^--Z-SBO^-) species were optimized (Figure 7). The TD-DFT calculation of the optimized geometry for each species was performed to obtain different UV-Vis absorption parameters due to ground singlet (S_0) to excited singlet (S_1) state electronic transition. The excitation energies, oscillator strengths (*f*), calculated molar extinction coefficient (ε_C) for different molecular species are shown in Table 2. On changing $SBOH^0$-Z-$SBOH^0$ to $SBOH^0$-Z-$SBOH^{\pm}$ structure, the calculated ε ($\varepsilon_C = 9.5\times10^3$ $M^{-1}cm^{-1}$) for the 315 nm vertical electronic transition was decreased to about 40% (~ 5.8×10^3 $M^{-1}cm^{-1}$) along with the appearance of a new low energy transition at ~ 385 nm (ε_C ~ 6.6×10^3 $M^{-1}cm^{-1}$). Such spectral changeover is nicely correlated with the experimental 420 nm intensity generation by reducing the 330 nm band intensity (~ 50%) due to change of solvent polarity from highly polar aqueous to non-polar THF medium (Figure 8 and Table 2). The results justify our proposed structural assignment for $SBOH^0$-Z-$SBOH^0$ and $SBOH^0$-Z-$SBOH^{\pm}$ molecular forms of the SBOH-Z-SBOH (*vide supra*).

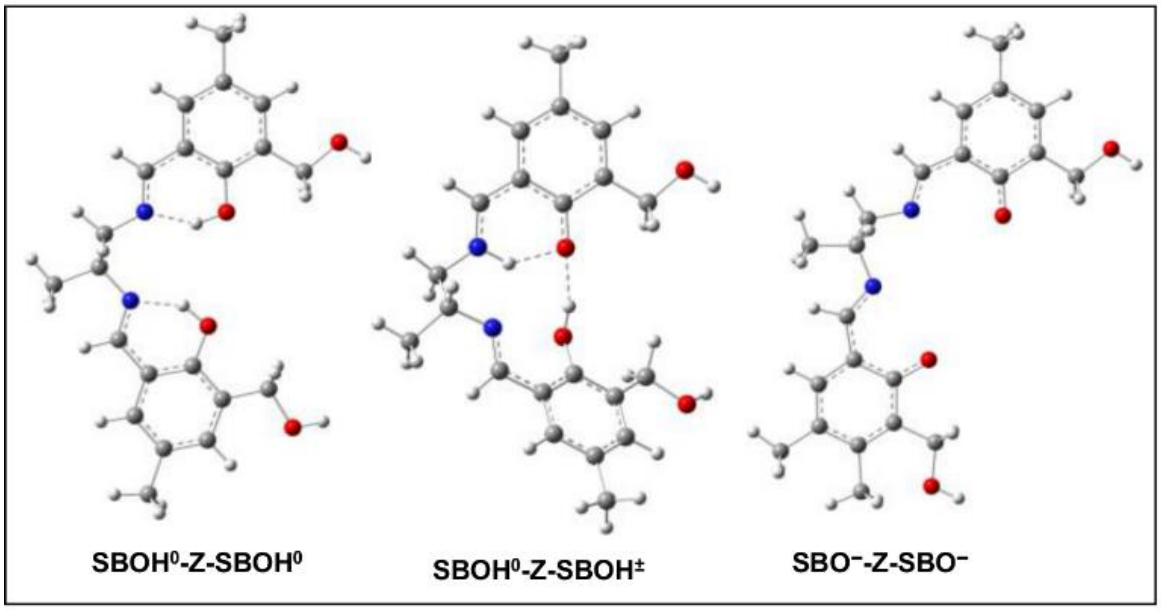

Figure 7. Optimized geometries for different molecular forms of Schiff-base molecule ($SBOH^0$-Z-$SBOH^0$, $SBOH^0$-Z-$SBOH^{\pm}$ and SBO^--Z-SBO^-) obtained from DFT calculations (color code: white, H; gray, C; blue, N and red, O). The H-bonding is detonated by single broken line.

Table 2: Electronic excitation wavelength (nm), oscillator strengths (f_{cal}), absorption maxiam (λ_{max}) and extinction coefficient (ε) of non-ionic ($SBOH^0$-Z-$SBOH^0$), partially zwitterionic ($SBOH^0$-Z-$SBOH^{\pm}$), di-anionic (SBO^--Z-SBO^-) forms obtained by the TD-DFT/B3LYP/6-31G++(d,p) calculation on ground state geometries in various solvent with CPCM dielectric solvation model. The experimentally obtained UV-Vis absorption (Obs/Abs) parameters for SBOH-Z-SBOH are depicted for comparison.

	Form	Solvent	λ_{max} (nm)	f_{cal}	$\varepsilon\times10^{-4}$ ($M^{-1}cm^{-1}$)
TD-DFT	$SBOH^0$-Z-$SBOH^0$	THF	315	0.160	0.887
	$SBOH^0$-Z-$SBOH^{\pm}$	Water	385 315	0.132 0.098	0.657 0.582
	SBO^--Z-SBO^-	Water	390	0.203	1.205
Obs/Abs	SBOH-Z-SBOH	THF	330		1.005
		Buffer, pH 7.0	420 330	-	0.629 0.454
		Buffer, pH 11.0	395		1.103

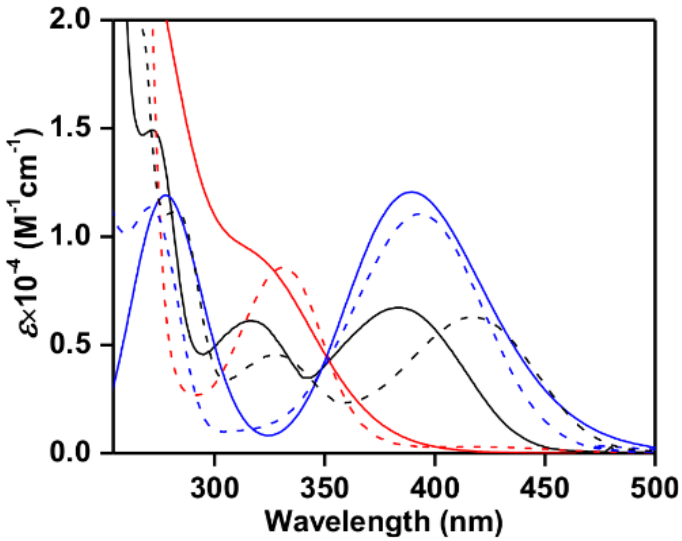

Figure 8. Theoretically calculated UV–Vis absorption spectra for different molecular species of Schiff-base (SBOH-Z-SBOH): $SBOH^0$-Z-$SBOH^0$, red; $SBOH^0$-Z-$SBOH^{\pm}$, black; SBO^--Z-SBO^-, blue. The pH/polarity dependent experimental UV-Vis spectra (broken) are depicted for comparison: red, in THF solvent; black, pH 9.8 and blue, pH 12.0.

On the other hand, the experimental UV-Vis spectral shift from 420 to 395 nm by increasing the aqueous buffer pH from 8.0 to 11.0 was also nicely correlated with the calculated imine-deprotonation induced ~ 20 nm blue shift (390 to 370-nm) for the phenolate moiety from $SBOH^0$-Z-$SBOH^{\pm}$ to SBO^--Z-SBO^- species (Figure 8). As similar with the pH-metric studies, about twice the calculated ε_C enlargement is observed for the 370-nm transition of $SBOH^0$-Z-$SBOH^{\pm}$ compared to the 390 nm intensity for SBO^--Z-SBO^- , which indicates similar magnitude of the ε_C value between -$SBOH^{\pm}$ and -SBO^- moiety (Table 2). All those results support our structural consideration of various molecular forms of SBOH-Z-SBOH.

4.3.4. Interaction of SBOH-Z-SBOH with amphiphilic self-assemblies

The UV-Vis absorption spectroscopic method was utilized to monitor the interaction of SBOH-Z-SBOH with various amphiphilic micelles (CTAB, SDS, TX-100) and unilamellar vesicles (ULVs) (DDAB, DOPC) containing various interfacial charges in aqueous buffer medium (Figure 9). The 420 nm absorption intensity of the SBOH-Z-SBOH decreases gradually with concomitant increase in the 320 nm intensity following the addition of increasing concentration of different amphiphilic systems at pH 7.0 until saturation of the intensity was identified (CTAB: 5.0, DDAB: 3.0, TX-100: 5.0 and DOPC: 4.0 mM) (Figure 10). For different amphiphilic molecules,

the identical 365 nm isosbestic wavelength indicates that the partially zwitterionic $SBOH^0$-Z-$SBOH^{\pm}$ form changes into corresponding non-ionic $SBOH^0$-Z-$SBOH^0$ form with the change of the probe location from the bulk to interface (Figure 10). The intensity saturation in presence of definite concentration of amphiphilic molecule justify that almost all SBOH-Z-SBOH molecules are involved in interaction with the self-assembled system.[29,30]

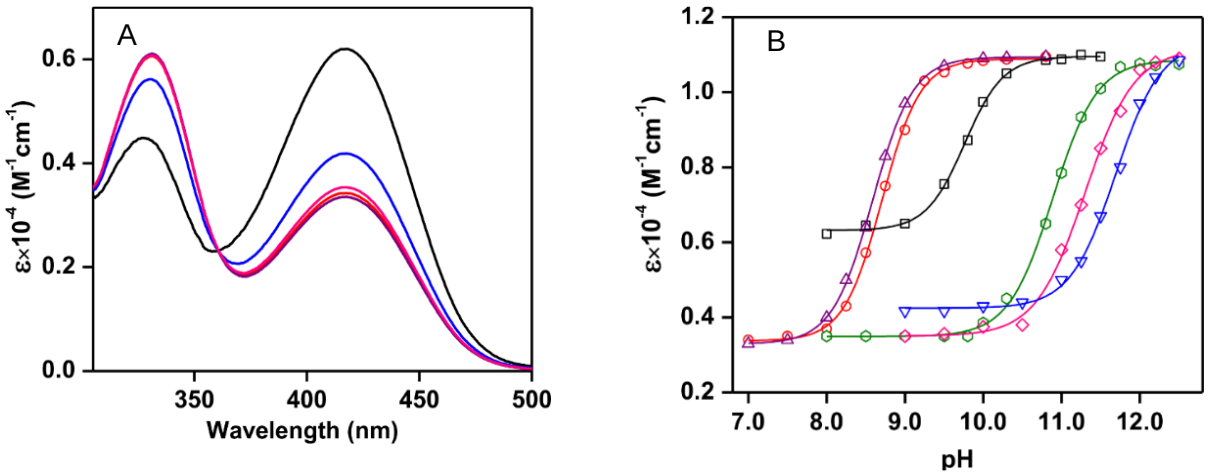

Figure 9. (A) UV-Vis absorption spectra of Schiff base SBOH-Z-SBOH (5 μM) in the presence of intensity-saturated concentrations of different amphiphilic molecules in 20 mM buffer, pH 7.0: blue, TX-100 (6.0 mM); pink, DOPC (4.0 mM); red, CTAB (5.0 mM); purple, DDAB (3.0 mM). The spectrum in absence of any amphiphilic molecule is depicted by black. (B) Plots of molar extinction coefficient (ε) at the absorption intensity maxima (395–420 nm) against the bulk pH in the presence of saturated concentrations of different self-assembled molecules in 20 mM buffer: black, buffer solution without any amphiphilic molecule; purple, DDAB (3.0 mM); red, CTAB (5.0 mM); green, 53% (*w/w*) ethanol containing buffer; pink, DOPC (4.0 mM); blue, TX-100 (5.0 mM).

To identify the precise probe location environment within the w/o interface, the time-dependent fluorescence anisotropic measurement was performed (Figure 11).[46,47] The cationic CTAB micelle or DDAB ULV induced a large increase in the correlation time (τ_c) from ~ 0.5 to 2.0 ns at pH 10.5, which suggests that the SBOH-Z-SBOH localizes in the ULV/micellar environment with restricted molecular motion (Table 3). Presumably, the SBOH-Z-SBOH in its ionic molecular form interacted strongly with cationic polar head-group of the amphiphilic systems to locate at the interfacial Stern layer. However, neutral TX-100/DOPC self-assembled system induced a comparatively small increase of τ_c value from ~ 0.5 to 1.0 ns. Most probably, the probe is involved in weak electrostatic interaction with the non-ionic micellar/ULV interfaces (Table 3). In fact, the binding of SBOH-Z-SBOH with DDAB vesicles were investigated by determining the residual SBOH-Z-SBOH fraction in the bulk phase in presence of vesicles. About 90–95% of the

SBOH-Z-SBOH molecules were attached to the ULVs in the solution containing 5.0 µM SBOH-Z-SBOH and 3.0 mM DDAB or DOPC ULVs (Figure 12). These results suggest that most of the SBOH-Z-SBOH molecules were bounded/located specifically at the Stern layer for different self-assembled systems.

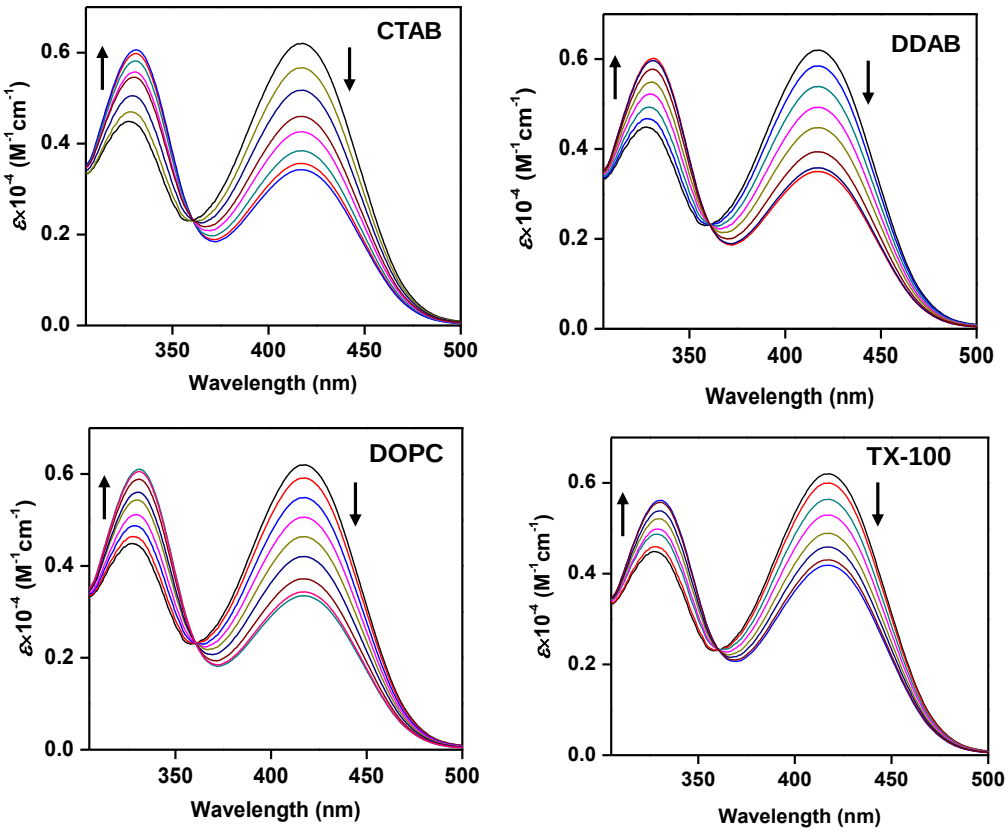

Figure 10. UV-Vis absorption spectra of SBOH-Z-SBOH (5.0 µM) in presence of increasing concentration of different self-assembled systems in 20 buffer, pH 7.0: CTAB (0–5.0 mM), DDAB (0–3.0 mM), TX-100 (0–6.0 mM) and DOPC (0–4.0 mM).

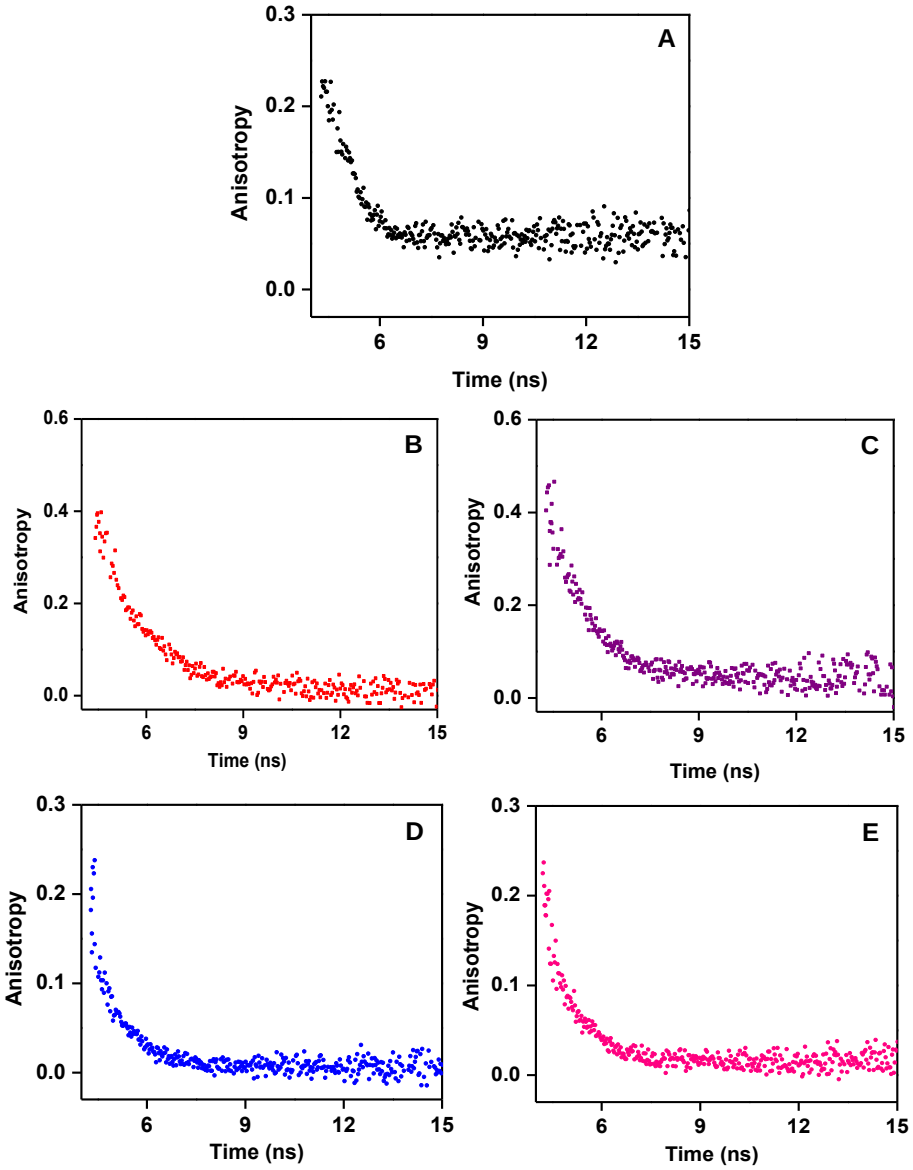

Figure 11. Fluorescence anisotropic decay curves of SBOH-Z-SBOH (5.0 μM) in (A) absence and (B–E) presence of deviation saturated concentration of different self-assembled systems at pH 10.5: (B), CTAB (5.0 mM); (C), DDAB (3.0 mM); (D), TX-100 (6.0 mM) and (E) DOPC (4.0 mM).

To observe the effect of interfacial SBOH-Z-SBOH binding on its pH induced proton dissociation interconversion equilibrium, the pH-metric titration with SBOH-Z-SBOH (5.0 μM) was performed in the presence of absorption saturated concentration of different self-assembled systems. The CTAB/DDAB induced intensity change from 320- and 420 nm to 390 nm show that more amount of -SBO^{-}-Z-SBO^{-} is formed by the simultaneous deprotonation from -$SBOH^{\pm}$ and –$SBOH^{0}$ moieties in $SBOH^{0}$-Z-$SBOH^{\pm}$ and/or $SBOH^{0}$-Z-$SBOH^{0}$ (pK_a ~ 8.9 for CTAB and ~ 8.6

for DDAB) (Figure 9B). On the other hand, in comparison with buffer solution, a relatively higher interconversion pK_a (~ 11.5) was detected for neutral TX-100/DOPC (Figure 9B). However, the similar studies with anionic self-assembled systems (SDS micelle) exhibits an unchanged absorption spectrum for almost entire pH region (5.5–12.0), except a small change at pH 12.5 (Figure 13). All the results clearly suggest that interfacial charge character plays the essential role in the SBOH-Z-SBOH proton dissociation equilibrium.

Table 3: The correlation time (τ_c) with residual of single exponential fitting (χ^2) for SBOH-Z-SBOH (5.0 μM) obtained from fluorescence anisotropic decays in presence of different self-assembled systems at pH 10.5.

System	τ_c (ns)	χ^2
Buffer	0.63	1.02
CTAB	1.90	1.03
DDAB	2.01	0.98
TX-100	1.02	1.09
DOPC	1.11	1.03

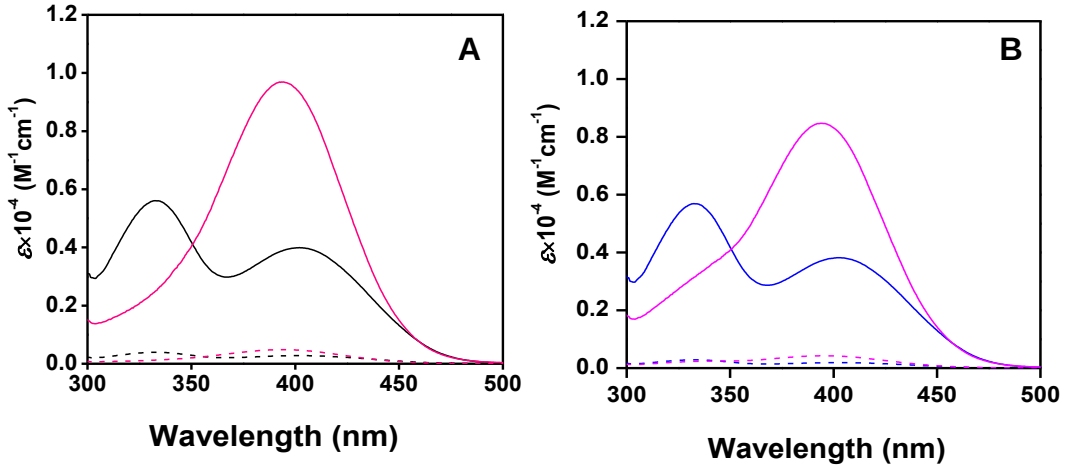

Figure 12. UV-Vis absorption spectra of SBOH-Z-SBOH (5.0 μM) in presence (solid) of different deviation-saturated concentration of ULVs, and (broken) its filtrated solution: (A) DDAB: red, pH 9.0; black, pH 8.0. (B) DOPC: pink, pH 11.5; blue, pH 10.5. The filtrated solution was obtained using a 100K MW cut-off filter.

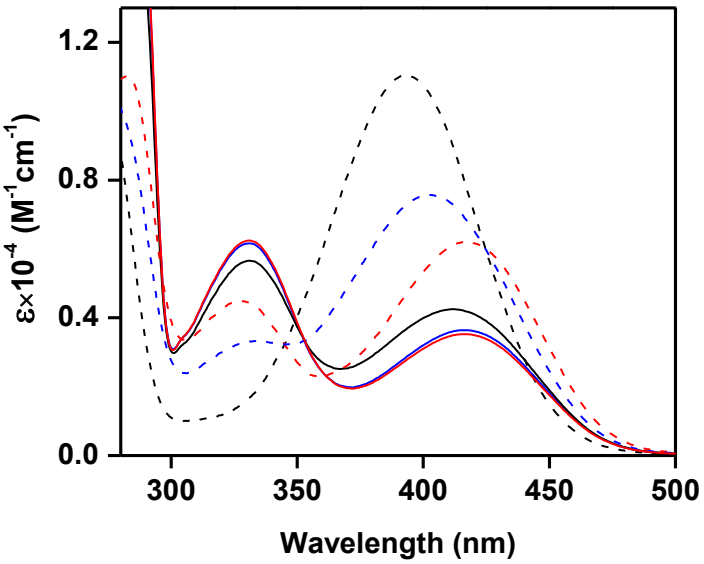

Figure 13. UV-Vis absorption spectra of SBOH-Z-SBOH (5.0 μM) in the absence (dash) and in presence of SDS (solid) in different pH: black, pH 12.5; blue, pH 9.5; red, pH 7.0.

4.3.5. Determination of the interfacial pH and polarity at similar interfacial depths for different self-assembled systems

Our studies have revealed that the SBOH-Z-SBOH exists mostly in the partially zwitterionic ($SBOH^0$-Z-$SBOH^{\pm}$) forms in aqueous medium (pH 5.5–8.0), but gradually converts into the non-ionic $SBOH^0$-Z-$SBOH^0$ by maintaining a linearity with a decrease in solvent polarity or an increase in the ratio of nonpolar solvent in mixed aqueous medium (Figure 3A). Notably, the highest pH value to observe such solvent polarity dependent exclusive $SBOH^0$-Z-$SBOH^{\pm}$ to $SBOH^0$-Z-$SBOH^0$ equilibrium increases from ~ 8.0 to 9.5 with decrease in solvent κ from 78.5 (aqueous medium) to ~ 40.0 (ethanol/water mixture) (Figure 14). With a further increase in pH from the above value, the di-anionic SBO^--Z-SBO^- was produced gradually by the deprotonation from $SBOH^0$-Z-$SBOH^0$ and/or $SBOH^0$-Z-$SBOH^{\pm}$ (Figure 1A, 14 and 15). The unaffected ε value and isosbestic wavelengths for the various molecular forms of SBOH-Z-SBOH between the presence and absence of self-assembled system indicates that there is no structural deformation due to change in the SBOH-Z-SBOH location between the bulk and interface (Figure 1A, 3A and 10). Therefore, the deviation of interfacial pH/κ from the bulk value can be directly correlated with the self-assembled system induced change in interconversion equilibria.

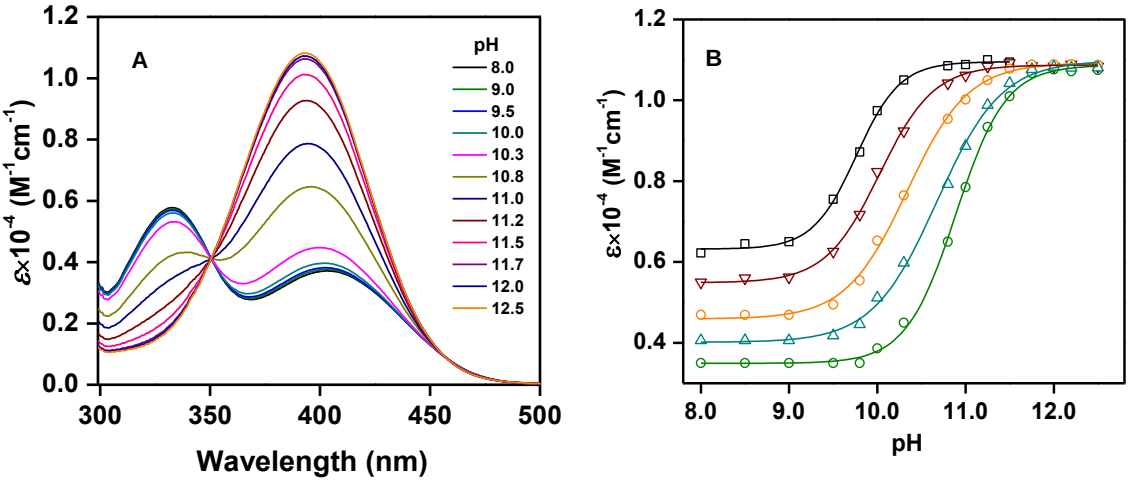

Figure 14. (A) pH dependent UV-Vis absorption spectra of SBOH-Z-SBOH (5.0 µM) in 53% (*w/w*) ethanol containing buffer medium. (B) Molar extinction coefficient (ε) at the absorption intensity maxima (395–420 nm) at different pH under different solvent polarity (κ) of ethanol/buffer mixed: black, 78.5; brown, 70.0; orange, 60.0; cyan, 50.0; green, 43.0.

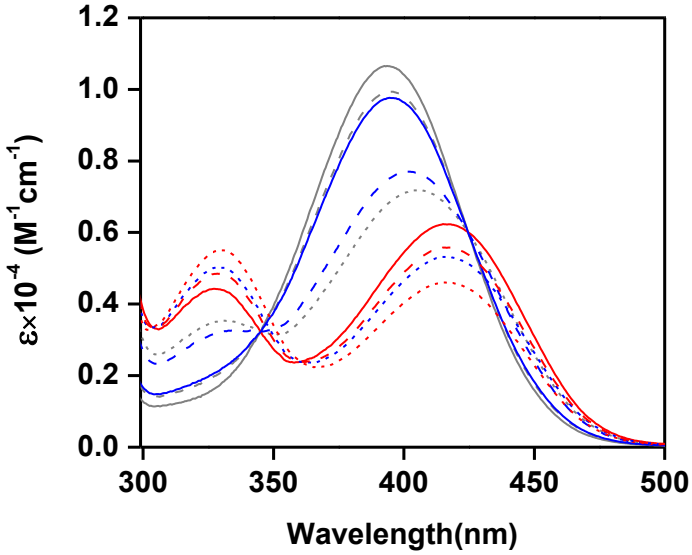

Figure 15. UV-Vis absorption spectra of SBOH-Z-SBOH (5.0 µM) in buffer of different pH (10.8, gray; 10.0, blue; 8.0, red) and κ (solid, 72.0; short dash, 48.0; broken, 25.0) of the medium.

To obtain the interfacial κ for different self-assembled systems, the exclusive $SBOH^0$-Z-$SBOH^0$ to $SBOH^0$-Z-$SBOH^{\pm}$ equilibrium in presence of absorption saturated concentration of self-assembled systems is evaluated by monitoring the relative intensity between 320- and 420 nm bands at a bulk pH ~ 7.0. The self-assembled system induced a gradual intensity changeover from

420- to 320 nm without changing 420 nm intensity maxima (λ_{max}) at the bulk pH ~ 7.0, which confirms that the observed intensity changes occur due to the generation of $SBOH^0$-Z-$SBOH^0$ from $SBOH^0$-Z-$SBOH^{\pm}$ species following the change in the probe location from the bulk to interface (Figure 9). The interfacial κ is evaluated from the linear $\varepsilon_{420}/\varepsilon^{8.0}_{420}$ *vs* κ relation according to eqn. 1 (Figure 3B). Irrespective of different amphiphilic systems and their interfacial charge characters, a highly reduced interfacial κ ~ 44.0–54.0 compared to that of the bulk aqueous phase were identified (Table 4). As the interface of a self-assembled system of amphiphilic molecule is the separation between highly polar aqueous phase and nonpolar hydrocarbon phase, a considerable decrease in water concentration plays pertinent role for the decrease of κ(i) compared to its value in the bulk phase (Scheme 2). It has also been reported that the extensive H-bonding network identified in the bulk water structure is greatly distressed as the molecule move towards the interface from bulk water, which may also contributes to the lower interfacial polarity than the aqueous bulk phase value.[48,49] Most likely, interfacial water concentration is not affected by the difference in self-assembly charge character, and thereby the interfacial κ does not differ widely among various self-assembled systems with different interfacial charge characters.

Table 4: The pH deviation from the bulk to interface (ΔpH) and interfacial κ for various self-assembled systems.

Amphiphilic molecule	ΔpH	κ
Buffer[a]	-	78.7
CTAB	1.84	43.5
DDAB	2.20	44.5
TX-100	–0.21	53.8
DOPC	–0.32	45.0

[a] Pure aqueous buffer medium without any amphiphilic molecules.

On the other hand, the pH deviation from the bulk to interface is highly interrelated with the interfacial charge character for amphiphilic self-assemblies.[29] It has been suggested that the distribution between H^+/H_3O^+ and OH^- ions around the charged interface at any bulk pH value can vary from their bulk phase distribution. For the cationic interface of CTAB/DDAB self-assembled

system, its attractive electrostatic interaction with oppositely charged OH^- ions and simultaneously the repulsive interaction with H^+/H_3O^+ ions may result higher OH^- ion concentration at the interface compare to the bulk phase (Scheme 2). Therefore, the pH at the interface is expected to be higher with respect to the bulk phase pH at any bulk pH value. However, the H^+/OH^- ions distribution within the bulk solvent and the corresponding the bulk phase pH value are not affected by interfacial charge in the H^+/OH^- ion distribution, since the overall volume occupied by the interface is extremely small compared to the total effective volume occupied by the bulk phase. To determine the interfacial pH and its deviation from the bulk for different amphiphilic system, the deprotonation equilibrium from $SBOH^0$-Z-$SBOH^0$ and/or $SBOH^0$-Z-$SBOH^{\pm}$ to SBO^--Z-SBO^- at different bulk pH was estimated in presence of absorption intensity saturated concentration of self-assembled systems (Figure 9). The cationic amphiphilic system induced greater deprotonation amount (pK_a: CTAB ~ 8.9; DDAB ~ 8.6) with respect to the bulk phase value (pK_a ~ 9.7), which suggests that the cationic interfaces are more basic than the bulk pH (Figure 9, Scheme 2). To estimate precise interfacial pH-deviation between the bulk and interface, the change in the proton dissociation pK_a due to difference in κ from the bulk aqueous to the medium with identical κ to that of interface is essential. The pH-metric titration with SBOH-Z-SBOH in ethanol/buffer mixed medium by maintaining an identical κ (42.0–54.0) to the interfacial κ has identified ~ 0.9–1.0 unit increase in pK_a with respect to its value in pure buffer medium (Figure 9 and 14). For the correlation between the pH deviation from the bulk to interface with the self-assembled system induced change in pK_a (ΔpK_a), the difference in pK_a owing to the polarity difference between the bulk and interface (δ) needs to be added to the obtained ΔpK_a. The interfacial pH would be greater than ΔpK_a by δ unit, by considering the increase of the deprotonated SBO^--Z-SBO^- fraction due to the decrease in the interfacial κ compared to the aqueous bulk value. Therefore, the difference between interfacial and bulk pH may be expressed as follows:

$$pH_{intf} - pH_{bulk} = \Delta pK_a + \delta \qquad (2)$$

$$pH_{intf} = pH_{bulk} + \Delta pK_a + \delta \qquad (3)$$

By using eq. 2 or 3, the interfacial pH for CTAB micelle and DDAB ULVs are more basic by 1.8 and 2.2 units, respectively, compared to that of the corresponding bulk phase pH (Table 4). Notably, the estimated pH-deviation from the bulk to interface for those cationic self-assembled systems are nearly same as the values reported previously.[23,29] However, the polarity factor (δ ~

0.9–1.0) contributed most to the self-assembled system induced increased value of ΔpK_a ~ 1.1 and 1.3 for the neutral TX-100 micelles and DOPC vesicles, respectively. According to eqn. 1 or 2, the interface is slightly more acidic by an amount of –0.2 and –0.3 units than the corresponding bulk pH value for TX-100 and DOPC systems, respectively (Table 4).

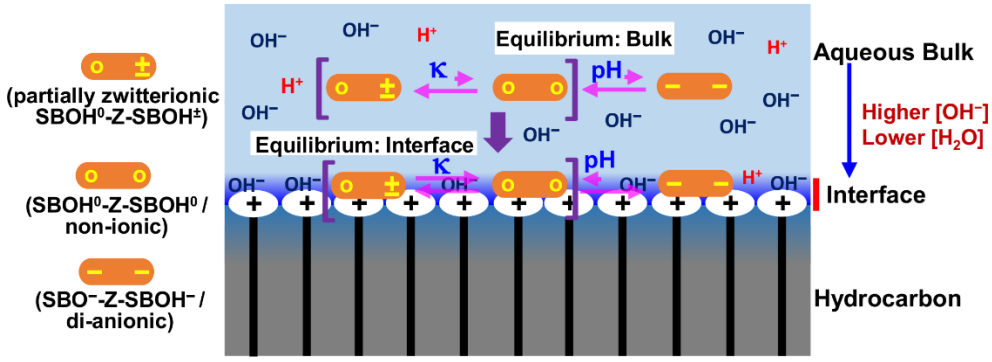

Scheme 2. Schematic view of distribution between H^+/H_3O^+ and OH^- ions at interface for cationic amphiphilic self-assembled systems. The pictorial representation of different molecular forms is indicated in the left. The change in various interconversion equilibrium (pink) from the bulk to interface among those molecular forms of SBOH-Z-SBOH are also depicted.

4.4. Conclusions

A new interface interacting Schiff-base molecule (SBOH-Z-SBOH) with two similar phenol-conjugated-imine moieties was synthesized for detection of pH and polarity at a similar depth in the water/oil separating interface for various self-assembled micelles and unilamellar vesicles. To detect the interfacial dielectric constant, the difference in the polarity dependent interconversion equilibrium from non-ionic ($SBOH^0$-Z-$SBOH^0$) to the partially zwitterionic ($SBOH^0$-Z-$SBOH^{\pm}$) form of the probe (SBOH-Z-SBOH) between the interface and bulk phase was investigated. On the other hand, the self-assembled system induced change in deprotonation equilibrium from $SBOH^0$-Z-$SBOH^0$ and/or $SBOH^0$-Z-$SBOH^{\pm}$ to anionic species (SBO^--Z-SBO^-) is evaluated to obtain the interfacial pH at a similar interfacial depth. In compare with the small negative pH-deviation ~ –0.2 or –0.3 unit from the bulk to interface for the neutral micelle/vesicle, a large positive pH-deviation ~ 1.8–2.2 is identified for the cationic micelle/vesicle. It is our proposition that the interfacial cationic charge properties are primarily responsible for the greater interfacial pH compared to the corresponding bulk pH value. On the other hand, almost similar interfacial dielectric constant (44.0–53.0) irrespective of different interfacial charge also indicates that the interfacial polarity does not depends on its specific charge properties.

4.5. References

1. G. Apodaca, L. I. Gallo and D. M. Bryant, *Nat Cell Biol.*, 2012, **14**, 1235.
2. S. Kim, K. No and S. Hong, *Chem. Commun.*, 2016, **52**, 831.
3. J. Kim, J. H. Jeon, H. J. Kim, H. Lim and I. K. Oh, *ACS Nano*, 2014, **8**, 2986.
4. S. Liu, Y. Liu, H. Cebeci, R. G. Villoria, J. H. Lin, B. L. Wardle and Q. M. Zhang, *Adv. Funct. Mate.*, 2010, **20**, 3266.
5. M. Barberon, G. Dubeaux, C. Kolb, E. Isono, E. Zelazny and G. Vert, *Proc. Natl. Acad. Sci.*, 2014, **111**, 8293.
6. L. Voglino, T. J. McIntosh and S. A. Simon, *Biochemistry*, 1998, **37**, 12241.
7. A. Spector and M. A. Yorek, *J. Lipid Res.*, 1985, **26**, 1015.
8. M. P. Sarria, J. Soares, M. N. Vieira, L. F. C. Castro, M.M. Santos and N.M. Monteiro, *Chemosphere*, 2011, **85**, 1543.
9. M. G. Swetha, V. Sriram, K. S. Krishnan, V. M. J. Oorschot, C. T. Brink, J. Klumperman and S. Mayor, *Traffic*, 2011, **12**, 1037.
10. D. Lee, J. R. Brender, M. F. M. Sciacca, J. Krishnamoorthy, C. Yu and A. Ramamoorthy, *Biochemistry*, 2013, **52**, 3254.
11. A. Mugs, J. M. Gonzalez-ManasllII, J. H. Lakeyll, F. Pattusy and W. K. Surewicz, *J. Biol. Chem.*, 1993, **268**, 1553.
12. A. D. Petelska and Z. A. Figaszewski, *Biophys. J.*, 2000, **78**, 812.
13. D. Marsh, *Proc. Natl. Acad. Sci. U.S.A.*, 2001, **98**, 7777.
14. M. Naumowicz and Z. A. Figaszewski, *J. Membr. Biol.*, 2014, **247**, 361.
15. M. K. Singh, H. Shweta, M. F. Khan and S. Sen, *Phys. Chem. Chem. Phys.*, 2016, **18**, 24185.
16. S. J. Singer and G.L. Nicolson, *Science*, 1972, **175**, 720.
17. Y. M. Chan and S. G. Boxer, *Curr. Opin. Chem. Biol.*, 2007, **11**, 581.
18. G.J. Hardya, R. Nayaka and S. Zauschera, *Curr. Opin. Colloid Interface Sci.*, 2013, **18**, 448.
19. F. M. Goni, *Biochim. Biophys. Acta*, 2014, **1838**, 1467.
20. C. G. Knight and T. Stephens, *Biochem. J.*, 1989, **15**, 683.
21. F. R. Beierlein, A. M. Krause, C. M. Jager, P. Fita, E. Vauthey and T. Clark, *Langmuir*, 2013, **29**, 11898.
22. M. A. Voinov, I. A. Kirilyuk and A. I. Smirnov, *J. Phys. Chem. B*, 2009, **113**, 3453.
23. S. Yamaguchi, K. Bhattacharyya and T. Tahara, *J. Phys. Chem. C*, 2011, **115**, 4168.

24. A. Kundu, S. Yamaguchi and T. Tahara, *J. Phys. Chem. Lett.*, 2014, **5**, 762.
25. M. F. Yin, T. F. Jiao and M. H. Liu, *Chinese Chemical Letters*, 2007, **18**, 30.
26. T. Jiao, X. Li, Q. Zhang, P. Duan, L. Zhang, M. Liu, X. Luo, Q. Li and F. Gao, *Colloids and Surfaces A: Physicochem. Eng. Aspects*, 2012, **407**, 108.
27. X. Zhao, K. Ma, T. Jiao, R. Xing, X. Ma, J. Hu, H. Huang, L. Zhang and X. Yan, *Scientific Reports*, 2017, **7**, 44076.
28. J. T. Feng, L. X. Hui, Z. Q. Rui, L. Q. Rong, Z. J. Xin and G. F. Ming, *Science China Technological Sciences*, 2013, **56**, 20.
29. Y. Sarkar, S. Das, A. Ray, S. K. Jewrajka, S. Hirota and P. P. Parui, *Analyst*, 2016, **141**, 2030.
30. R. Majumder, Y. Sarkar, S. Das, S. K. Jewrajka, A. Ray and P. P. Parui, Analyst, 2016, **141**, 3246.
31. K. Naa, K. H. Leea and Y. H. Baea, *J. Controlled Release*, 2004, **97**, 513.
32. E. S. Lee, K. T. Oh, D. Kim, Y. S. Youn and Y. H. Bae, *J. Controlled Release*, 2007, **123**, 19.
33. D. M. Mitchell, J. P. Shapleigh, A. M. Archer, J. O. Alben and R. B. Gennis, *Biochemistry*, 1996, **35**, 9446.
34. W. Chen, D. A. Tomalia and J. L. Thomas, *Macromolecules*, 2000, **33**, 9169.
35. E. Gaidamauskas, D. P. Cleaver, P. B. Chatterjee and D. C. Crans, *Langmuir*, 2010, **26**, 13153.
36. B. B. Lorenz, D. C. Crans and M. D. Johnson, *Eur. J. Inorg. Chem.*, 2014, 4537.
37. G. Akerlof, J. Am. Chem. Soc., 1932, **54**, 4125.
38. F. E. Critchfield, J. A. Gibson and J. L. Hall, *J. Am. Chem. Soc.*, 1953, **75**, 6044.
39. E. Lambert, B. Chabut, S. C. Noblat, A. Deronzier, G. Chottard, A. Bousseksou, J. P. Tuchagues, J. Laugier, M. Bardet and J. M. Latour, *J. Am. Chem. Soc.*, 1997, **119**, 9424.
40. J. V. Morris, M. A. Mahaney and J. R. Huber, *J. Phys. Chem.*, 1976, **80**, 969.
41. M. J. Frisch, et al., Gaussian 09 Rev. A.1, Gaussian Inc., Wallingford CT, 2009.
42. I. D. Cunningham and M. Woolfall, *J. Org. Chem.*, 2005, **70**, 9248.
43. R. Álvarez-Diduk, M. T. Ramírez-Silva, A. Galano and A. MerkoçI, *J. Phys. Chem. B*, 2013, **117**, 12347.
44. S. Y. Kim, A. N. Semyonov, R. J. Twieg, A. L. Horwich, J. Frydman and W. E. Moerner, J. Phys Chem B., 2005, **109**, 24517.
45. J. Hu, H. Zhu, Y. Li, X. Wang, R. Ma, Q. Guo and A. Xi, *Phys. Chem. Chem. Phys.*, 2016, **18**, 18750.

46. J. R. Lakowicz, in Principles of Fluorescence Spectroscopy, Springer, 3rd edn, 2006, ch. 11.
47. Sonu, S. Kumari and S. K. Saha, *Phys. Chem. Chem. Phys.*, 2016, **18** 1551.
48. D. E. Moilanen, E. E. Fenn, D. Wong and D. M. Fayer, *J. Chem. Phys.*, 2009, **131**, 014704.
49. N. Nandi, K. Bhattacharyya and B. Bagchi, *Chem. Rev.*, 2000, **100**, 2013.

Chapter 5

Simultaneous detection of interfacial acidity and polarity during lipid phase transition of vesicle using a porphyrin-based probe

Simultaneous detection of interfacial acidity and polarity during lipid phase transition of vesicle using a porphyrin-based probe

Abstract

Biochemical activities at a membrane interface are affected by local pH/polarity related to membrane lipid properties including lipid dynamics. pH and polarity at the interface are two highly interdependent parameters, depending on various locations from the water-exposed outer-surface to the less-polar inner-surface. The optical response of common pH or polarity probes is affected by both the local pH and polarity; therefore, estimation of these values using two separate probes localized at different interfacial depths can be erroneous. To estimate interfacial pH and polarity at an identical interfacial depth, we synthesized a glucose-pendant porphyrin (GPP) molecule for simultaneous pH and polarity detection by a single optical probe. pH-induced protonation equilibrium and polarity-dependent π–π stacking aggregation for GPP are exploited to measure pH and polarity changes at the 1,2-dimyristoyl-sn-glycero-3-phospho-(1'-rac-glycerol) (DMPG) membrane interface during DMPG phase transition. An NMR study confirmed that GPP is located at the interfacial Stern layer of DMPG large unilamellar vesicle (LUV). Using UV-Vis absorption studies with an adapted analysis protocol, we estimated interfacial pH, or its deviation from the bulk phase value (ΔpH), and the interfacial polarity simultaneously using the same spectra for sodium dodecyl sulfate (SDS) micelle and DMPG LUV. During temperature dependent gel to liquid-crystalline phase transition of DMPG, there was ~0.5 unit increase in ΔpH from approximately –0.6 to –1.1, with a small increase in interfacial dielectric constant from ~60 to 63. A series of spectroscopic data indicate the utility of GPP for evaluation of local pH/polarity change during lipid phase transition of vesicles.

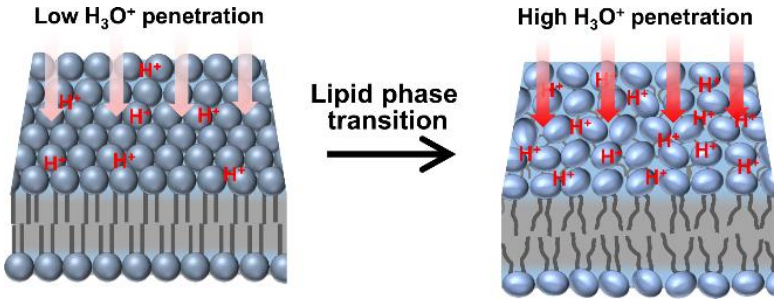

5.1. Introduction

Cellular events at phospholipid membrane interfaces are associated with the structural dynamics of the membrane, *e.g*., the lipid phase transition from tightly-packed gel to flexible liquid-crystalline state at room temperature.[1,2] Because the membrane becomes softer in the liquid-crystalline state, endocytosis and exocytosis reactivity are accelerated above the lipid melting temperature.[3,4] Mechanical signal propagation phenomenon such as nerve pulses transmittance is strongly associated with lipids phase transition.[5] However, several other independent investigations have revealed that those membrane biochemical activities are highly sensitive to local pH and polarity surrounding the membrane.[6-8] In this context, we believe that any changes in these physicochemical properties at the membrane interface during lipids phase transition may have profound roles to affect aforementioned membrane reactivity.

Self-assembly occurs at the interface whereby charged/uncharged polar head groups separates from nonpolar (lipid/surfactant acryl chain) phase and assemble at the polar (aqueous) phases. Thus, pH and polarity at the interface are different from that of the bulk medium. We have recently developed a new interfacial pH and polarity monitoring method for micelles and vesicles using two *separate* pH and polarity sensitive chromophore probes that interact with the interface.[9,10] However, interfacial pH and polarity are highly interrelated physicochemical parameters along various interfacial locations. For example, a decrease of polarity with increasing interfacial depth towards the hydrophobic phase may decrease interfacial acidity because of a lack of H_3O^+ conduction ability.[11] pH-induced optical changes for a pH probe are frequently affected by solvent polarity[9,10] and *vice versa*. Thus, the precise measurement of pH and polarity using two separate probes localized at different interfacial depths can be problematic. The simultaneous detection of pH and polarity at an identical interfacial depth using a single optical probe is proposed here to evaluate either of these two parameters. This is particularly useful for temperature-dependent studies because polarity is intrinsically related to temperature.

5.2. Work Analysis

Porphyrin derivatives have characteristic absorption bands around 400 nm (Soret band) and 550 nm (Q band). A large extinction coefficient (~10^4–10^5 $M^{-1}cm^{-1}$) at the Soret band is useful as an indicator reagent.[12] Porphyrin derivatives work as pH indicators because of the significant UV-Vis spectral changes during protonation at inner nitrogen atoms in the ring. For example, Liu and

co-workers reported that tetraphenylporphyrin (TPP)-type compound **1** (Scheme 1) works as a pH indicator in the range of pH 4–5, where the electron-donating phenoxy moiety is a key structural factor of pH detection in this range.[13] Furthermore, deprotonated porphyrin compounds (*i.e.* non-protonated state at the inner nitrogen atoms) readily form molecular aggregation states (known as *J*-aggregation or *H*-aggregation) through intermolecular hydrophobic π-stacking under polar environments, whereas the porphyrin compounds exist as a monomer state in non-polar solvents.[14,15] The aggregation behavior is also reflected in the shape of UV-Vis spectra of porphyrins. Therefore, the UV-Vis spectra of porphyrin derivatives reflect both environmental pH and polarity. According to these characteristics, we expected that TPP-type porphyrins are suitable for simultaneously elucidating the local pH and polarity at a membrane interface.

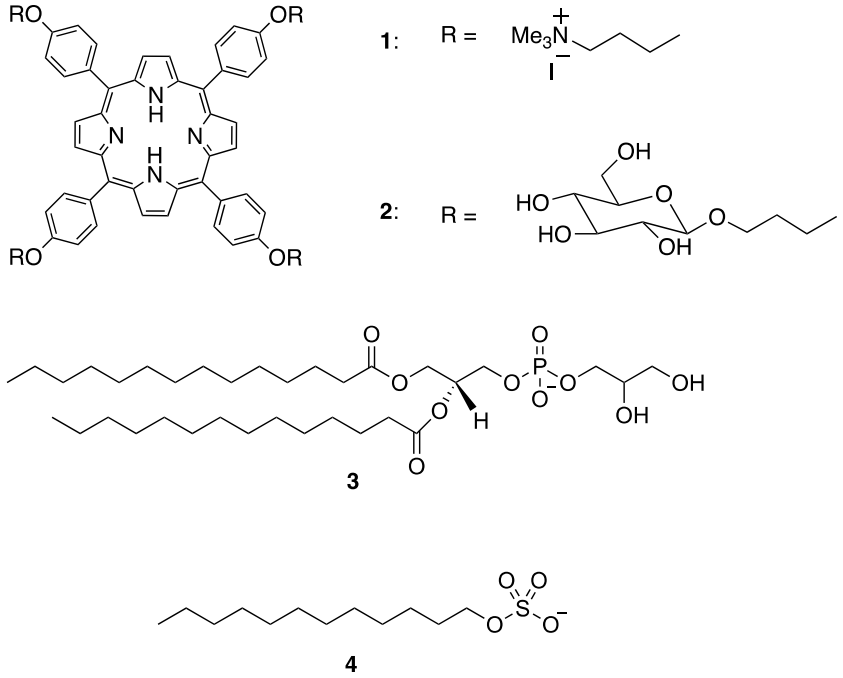

Scheme 1. Chemical structures of TPP-type porphyrins and lipid surfactants.

In this study, we demonstrate the utility of moderately water-soluble glucose-pendant porphyrin GPP (2) for monitoring pH and polarity simultaneously at the membrane inter-face. GPP (2) adopts both a neutrally charged (basic form) and cationic forms (acidic form) depending upon the surrounding pH. This assures: (1) binding of GPP (2) to the Stern layer of the anionic interface assisted by the cationic charge in the acidic-form porphyrin unit and/or by the dual characteristics

of GPP (2) with the polar glucose residues and the nonpolar basic-form porphyrin unit; and (2) polarity-induced aggregation behaviour of GPP (2) without affecting the intrinsic protonation property at the porphyrin core. Firstly, we demonstrate the protocol for synchronized evaluation of pH and polarity in homogeneous solvents. Next, we applied this protocol for the simultaneous evaluation of local pH and polarity at the interface of self-assembled sodium dodecyl sulfate (SDS) (3) micelles and 1,2-dimyristoyl-sn-glycero-3-phospho-(1'-rac-glycerol) sodium salt (DMPG) (4) vesicles. In addition, we succeeded in the quantitative measurement of interfacial pH and polarity changes during temperature-induced DMPG phase transition in vesicles.

5.3. Results and discussions

5.3.1. GPP monomer/aggregate equilibrium: estimation of polarity

At first, we attempted to evaluate medium polarity [dielectric constant (κ)] by the observation of UV-Vis spectral changes in buffer/acetone mixed medium (Figure 1). In buffer (pH > 6.0) at 25 °C, GPP (2, 2.5 μM) exhibited broad absorbances consisting of weak overlapping intensities spreading from ~400 to 440 nm (Figure 1A). This spectrum shape is often observed for *H*-type aggregated porphyrins with a small contribution of *J*-type aggregation in aqueous media,[14] where the inner nitrogen atoms in GPP (2) are deprotonated.

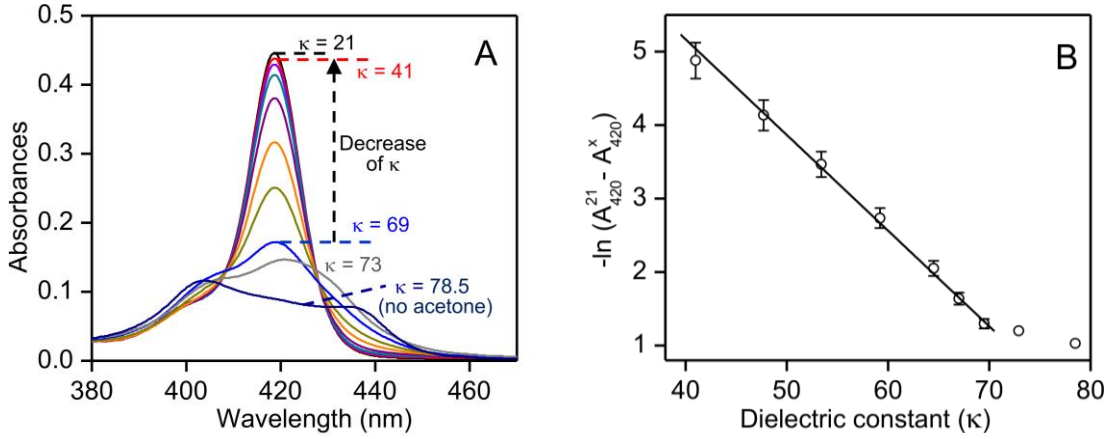

Figure 1. (A) UV-Vis absorption spectra of GPP (2; 2.5 μM) in 10.0 mM sodium citrate/sodium phosphate buffer containing various amounts of acetone% (*w/w*), pH 6.0 at 25 °C: red, 60% (κ = 41.5); violet, 51% (κ = 47.7); dark cyan, 42% (κ = 53.4); purple, 33% (κ = 59.2); orange, 24% (κ = 64.5); light green, 20% (κ = 67.0); blue, 16% (κ = 69.5) and gray, 73% (κ = 72.9). The spectra in pure buffer (κ = 78.5) and acetone (κ = 21.0) medium are shown by dark blue and black, respectively. The change in dielectric constant (κ) is depicted by the arrow. (B) The negative logarithmic values of

intensity difference at 420 nm from pure acetone with κ ~21 (A_{420}^{21}) of other various acetone/buffer mixed mediums with κ ~41.5–69.5 (A_{420}^{x}) are plotted against k. The values of dielectric constants were quoted from a previous paper.[17]

With an increasing amount of acetone in the buffer, a sharp absorption band around 420 nm appeared with concomitant depletion of those broad bands (Figure 1A). The absorption band around 420 nm is a typical feature of TPP-type porphyrins observed in organic solvents.[20] Although the absorbance changes were not systematic up to 10% (*w*/*w*) of acetone with dielectric constant (κ) ~73 (due to change in aggregation fashion[14,21] (Figure 2), the absorbance increased from ~0.17 to 0.44 upon the addition of acetone from ~16% to 60% (*w*/*w*) with maintaining isosbestic points at ~407 and 430 nm (Figure 1A). The quantity of intensity changes at ~420 nm was very similar in other organic solvents than acetone (*e.g.* methanol and ethanol, protic solvents) (Figure 1A and 2); suggesting that the observed UV-Vis spectral change is interpretable as not specific solvent effect but as polarity effect in the range of solvent κ from approximately 41 to 69. The series of observed spectral changes indicate that the deprotonated GPP undergoes an interconversion equilibrium between the aggregated form (denoted as d_A-GPP) and the monomer form (d_M-GPP), where "d", "A" and "M" stand for "deprotonated", "aggregated", and "monomer", respectively.

In contrast to GPP (**2**), porphyrin **1** showed a distinct absorption band at ~420 nm in aqueous medium with comparable intensity to that observed for GPP (**2**) in the presence of organic solvents (Figure 3). The absorption pattern and intensity increased a little (< 10%) in the presence of methanol or acetone in buffer at pH 7.0. These results demonstrate that the UV-Vis spectra of porphyrin **1** are less sensitive on solvent polarity compared to GPP (**2**). The spectral changes indicate that porphyrin **1** predominantly exists as a monomer form in the buffer solution because of cationic ammonium moieties. Therefore, GPP (**2**) is superior to **1** as a polarity indicator.

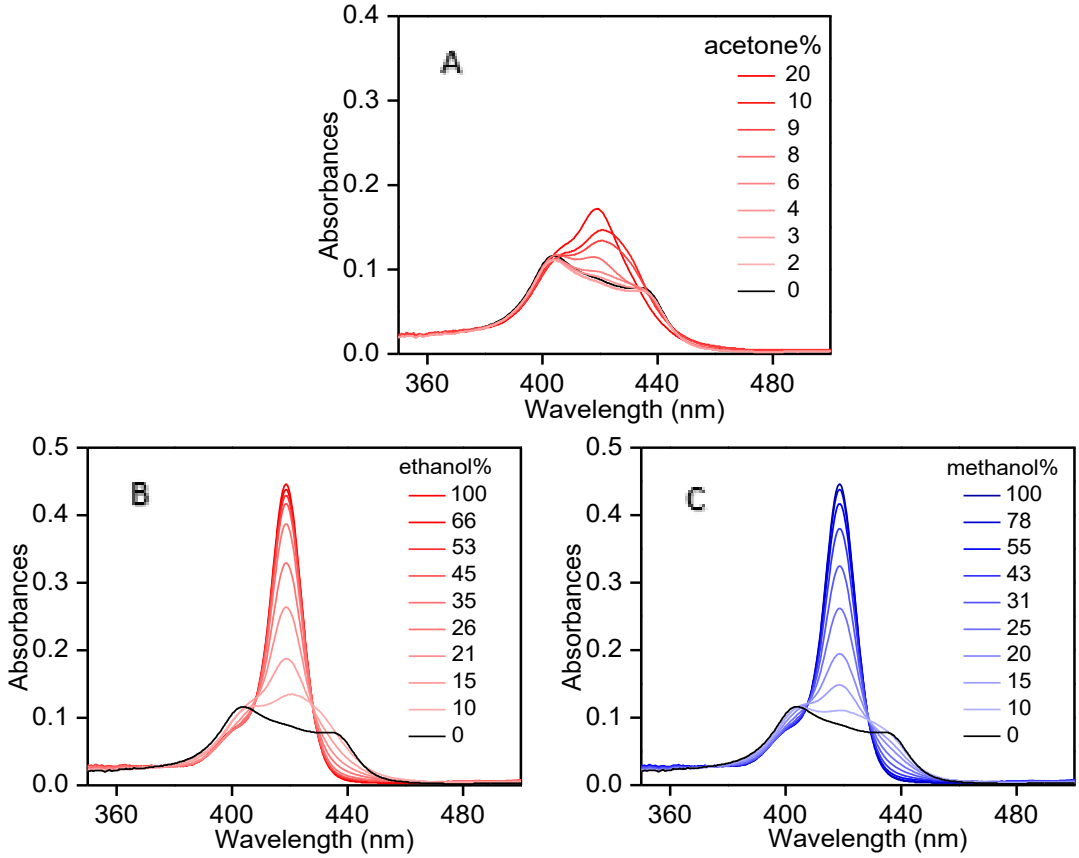

Figure 2. UV-Vis absorption spectra of GPP (2) (2.5 μM) in 10 mM citrate/phosphate buffer containing different (A) acetone% (*w*/*w*), (B) ethanol%(*w*/*w*) and (C) methanol% (*w*/*w*) at pH 6.0 at 25 °C.

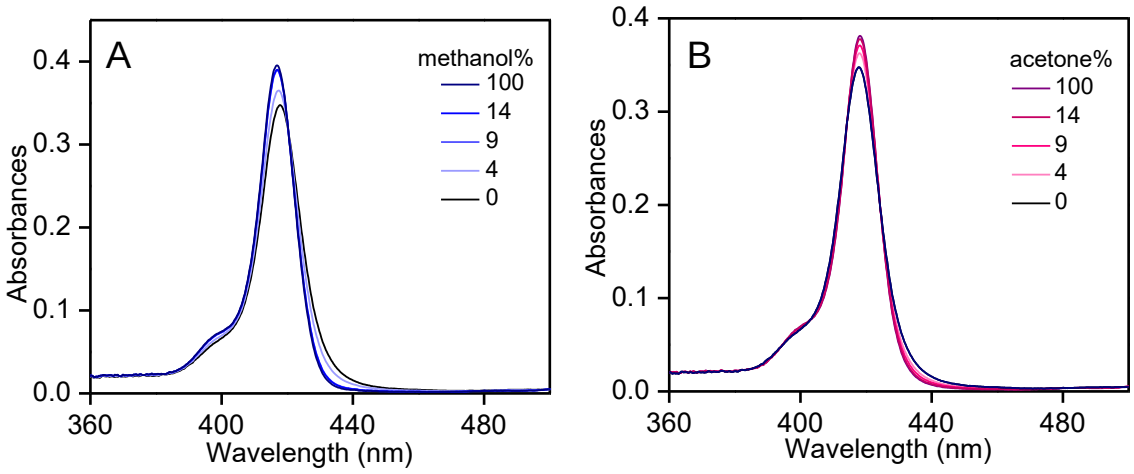

Figure 3. UV-Vis absorption spectra of cationic porphyrin (1) (2.5 μM) in buffer containing various amount of (A) methanol% and (B) acetone% (*w*/*w*) at pH 7.0 at 25 °C. The spectra in the absence of acetone are depicted by black.

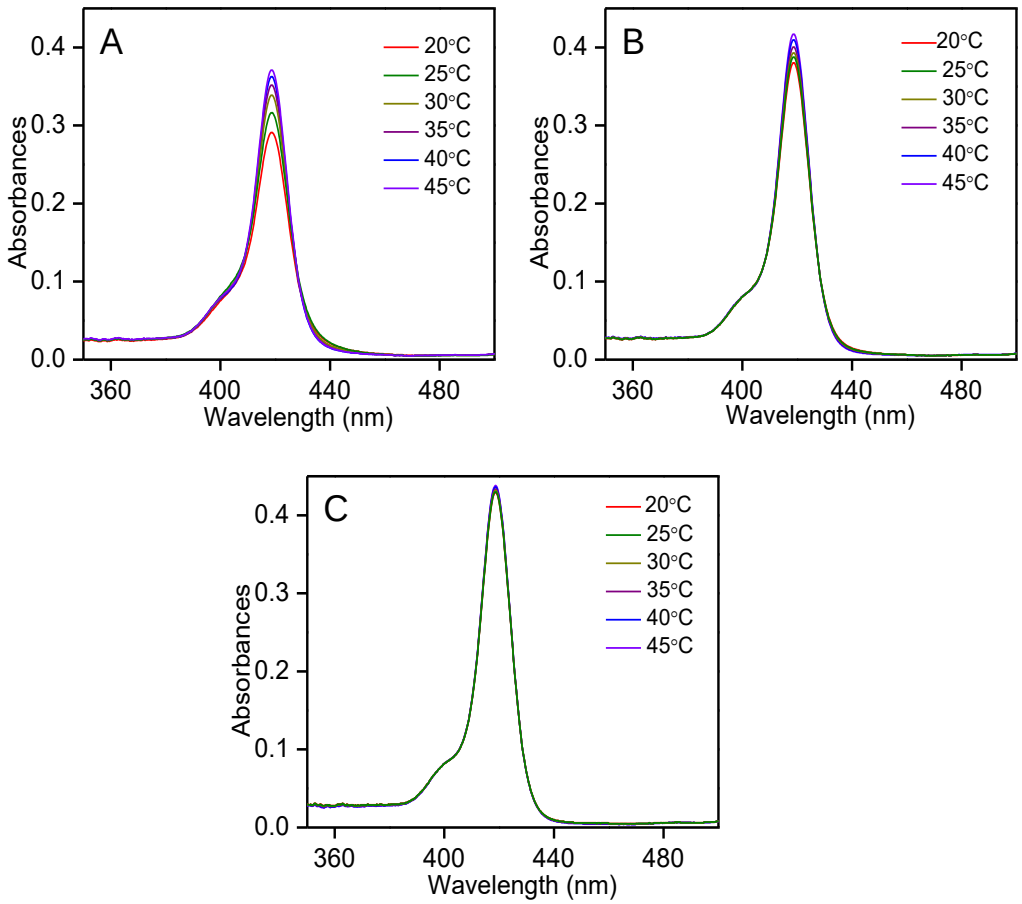

Figure 4. Temperature-dependent UV-Vis absorption spectra of GPP (2) (2.5 μM) in 10 mM citrate/phosphate buffer containing various amount of acetone% (*w/w*) at pH 6.0: A, 24%; B, 33%; and C, 50%.

The d_A-GPP to d_M-GPP interconversion equilibrium was found to depend on medium temperature as well. For the mixed medium containing different acetone ratios (24–50%) in buffer, the intensity at ~420 nm for GPP (**2**; 2.5 μM) increased gradually with rising temperature from 20 °C to 45 °C (Figure 4). Both the increase in temperature and in acetone ratio displayed a similar decrease in solvent κ ~5.5–6.0 units (Figure 1A and 4).[17] Namely, the temperature-induced absorbance change at ~420 nm is regarded as the temperature affected change in medium κ.[17] Therefore, κ of GPP (**2**) localized environment can be estimated by monitoring d_A-GPP to d_M-GPP interconversion based on the absorbance change at ~420 nm. Accordingly, we empirically correlate the absorbance change at ~420 nm and medium κ. The negative logarithmic value for the amount of intensity decreases at ~420 nm from the saturated intensity at $\kappa < 35$ under complete conversion

to d_M-GPP exhibited a linear correlation with solvent κ in the range from κ ~40 to 70 (Figure 1B), and thus κ can be estimated by using the eq. (1):

$$-\ln (A_{420}^{21} - A_{420}^{x}) = -0.13 \times \kappa + 10.3 \quad (40 \leq \kappa \leq 70) \quad (1)$$

where A_{420}^{21} and A_{420}^{x} represent the absorbance value at ~420 nm in acetone medium (κ = 21) and the observed absorbance for a solution at unknown polarity (*i.e.* an observation target), respectively. The intercept and slope values are represented by 10.3 and –0.13, respectively.

5.3.2. GPP acid/base equilibrium: estimation of pH

Next, we attempted to develop the protocol for evaluation of medium pH in pure buffer and subsequently in acetone/buffer medium of various polarities based on the UV-Vis spectra of GPP (2). In pH-dependent UV-Vis absorption studies for GPP (2.5 μM) in a buffer solution, a new absorption band at ~446 nm appeared with the decrease in the broad band of d_A-GPP on decreasing pH from 5.2 (Figure 5A). The spectral change is due to the protonation at inner nitrogen atoms in the porphyrin ring. The absorbance increase saturated at pH below 3.5, sug-gesting a complete protonation at inner nitrogen atoms in GPP.[12] A much sharper Soret band of the protonated GPP compared to d_A-GPP (Figure 5A) indicates that the protonated GPP exists in the monomeric state. Namely, the pro-tonated GPP is denoted as "p_M-GPP", where "p" stands for "protonated" form. In the presence of buffer containing different acetone ratios, the single isosbestic point in the pH-dependent spectral changes indicate the apparent one-step interconversion of two deprotonated forms (d_A-GPP and d_M-GPP) (at high pH, λ_{abs} ~ 420 nm) into protonated p_M-GPP (at low pH, λ_{abs} ~ 450 nm and 685 nm) (Figure 5B and 6). The whole porphyrin interconversion reflected in Figures 5A and 5B are summarized in Scheme 2.

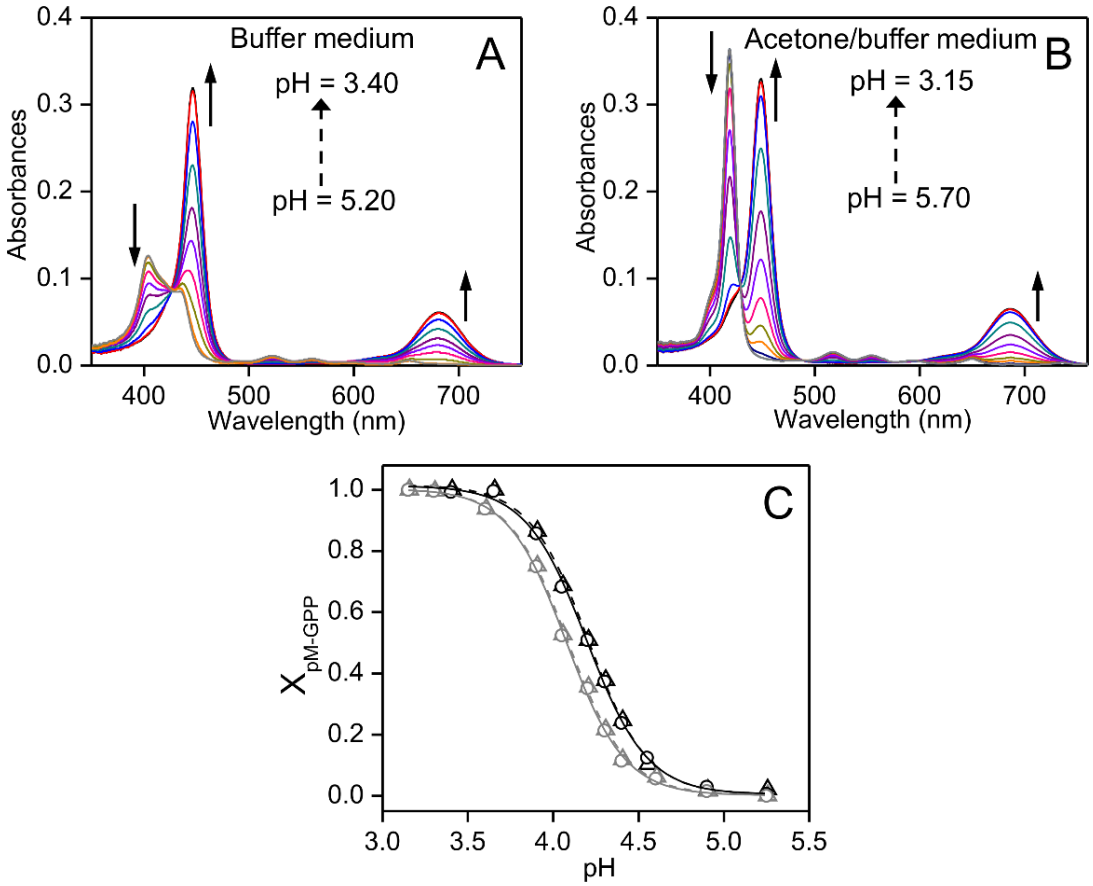

Figure 5. pH-dependent UV-Vis analyses of GPP (2; 2.5 µM) at 25 °C; (A) Spectral changes observed in 10 mM sodium citrate/sodium phosphate buffer, pH 3.40, 3.70, 3.90, 4.05, 4.20, 4.30, 4.40, 4.55, 4.90, and 5.20; (B) Spectral changes observed in the buffer containing 31%(*w/w*) acetone, pH 3.15, 3.40, 3.60, 3.90, 4.05, 4.20, 4.30, 4.40, 4.60, 4.90, 5.25, and 5.7. The change in intensities with decreasing pH is shown in arrows. (C) pM-GPP mole-ratio (XpM-GPP) analyzed from the intensity at ~450 nm (circle, solid lines) and ~685 nm (triangle, broken lines) is plotted against pH: black, 10 mM sodium citrate/sodium phosphate buffer; gray, 31% (*w*/*w*) acetone containing buffer.

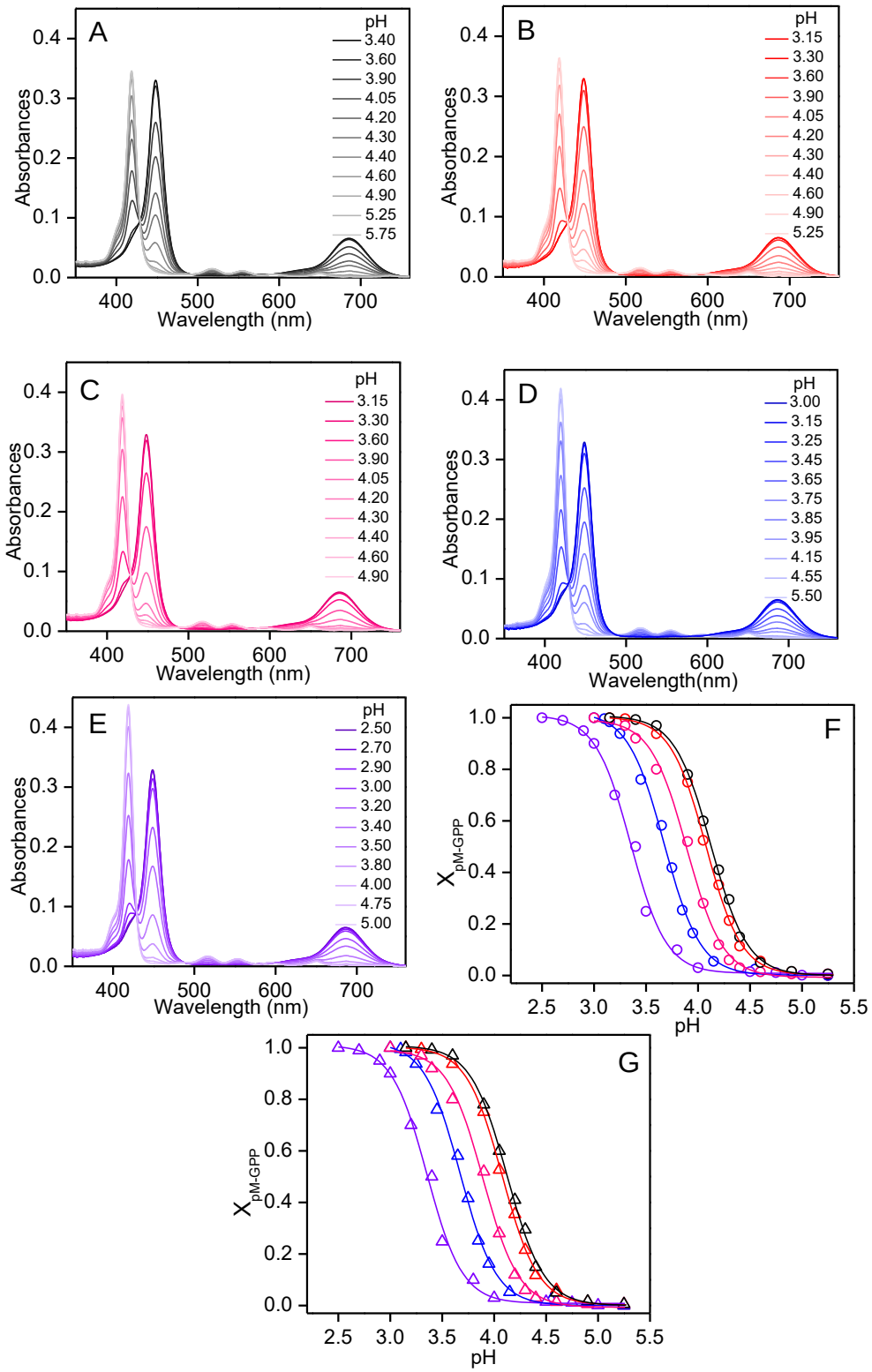

Figure 6. pH-dependent UV-Vis absorption spectra of GPP (2) (2.5 μM) in 10 mM sodium citrate/sodium phosphate buffer containing various amount of acetone% (*w*/*w*) at 25 °C: A, 28% (dielectric constant: 62.0); B, 31% (dielectric constant: 60.5); C, 37% (dielectric constant: 56.4); D),

42.5% (dielectric constant: 53.0) and E, 60% (dielectric constant: 42.0). (F, G) p_M-GPP mole-ratio ($X_{pM\text{-}GPP}$) analyzed from the intensity at ~450 nm (graph F) and ~685 nm (graph G) vs. pH in the buffer containing different wt% of acetone (Black: 28%; Red: 31%; Pink: 37%; Blue: 42.5% and Violet: 60%).

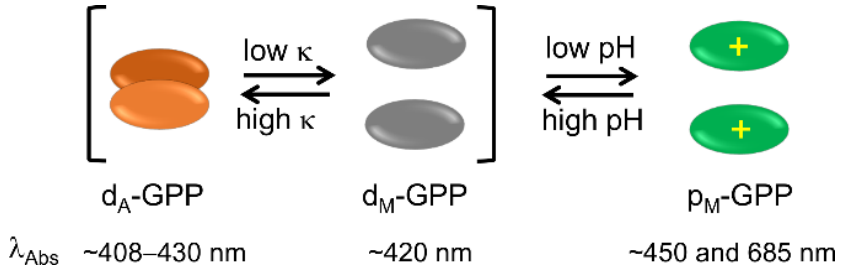

Scheme 2. pH and dielectric constant (κ) dependent interconversion equilibrium among aggregated-deprotonated (d_A-GPP), monomeric-deprotonated (d_M-GPP) and monomeric-protonated (p_M-GPP) forms of GPP.

Electrostatic repulsion between positively-charged porphyrins with protonated inner nitrogen atoms may prevent the hydrophobic π-stacking interaction to exist as monomeric state even in pure aqueous buffer. By following a similar trend, another relatively weak absorption intensity at ~685 nm was also increased systematically with decreasing pH, suggesting that both intensities at ~446 and ~685 nm are associated to the p_M-GPP form (Figure 5A). Therefore, the equilibrium mole-ratio of p_M-GPP ($X_{pM\text{-}GPP}$) can be determined by analyzing the absorption intensities at ~446 nm and ~685 nm as follows:

$$X_{pM\text{-}GPP} = (A_\lambda^{pH} - A_\lambda^{6.0})/ (A_\lambda^{3.5} - A_\lambda^{6.0}) \qquad (2)$$

where A_λ^{pH} and $A_\lambda^{3.5}$ represent the pH-dependent absorbance and the saturated intensities below pH 3.5 at wavelength (λ) ~446 or ~685 nm, respectively. $A_\lambda^{6.0}$ denotes the absorption intensity at ~446 nm or ~685 nm when GPP exists as deprotonated state (d_M-GPP and/or d_A-GPP) at pH above 6.0. The mole-ratios of p_M-GPP ($X_{pM\text{-}GPP}$) were plotted with pH (Figure 5C), and the acid/base pK_a for GPP was estimated to be ~4.2 by fitting data points with a sigmoidal-Boltzmann equation (the data of first raw in Table 1). The unknown pH of an aqueous medium can be estimated from the pH vs. p_M-GPP mole-ratio calibration curve.

The pH vs. p_M-GPP mole-ratio calibration curve in acetone/buffer solutions shifted to the direction of lower pH compared to the pure buffer solution (cf. black and gray lines in Figure 5C). The deviation reflects the polarity effect on the protonation/deprotonation equilibrium. This

indicates that the contributions of solvent κ and pH should be separated in the observed UV-Vis spectral changes in order to develop the protocol to estimate pH under variable po-larity conditions.

Table 1: Acid/base pK_a values for GPP (2) at various temperature (T) and bulk dielectric constant (κ(b)) of buffer in the presence and absence of acetone.

		T (°C)	pK_a [a]		κ(b)[b]
			450 nm	685 nm	
Acetone% (*w*/*w*) in buffer	0	25	4.20 ± 0.02	4.20 ± 0.03	78.5
	28.0	25	4.10 ± 0.02	4.10 ± 0.03	62.0
	31.0	25	4.07 ± 0.02	4.07 ± 0.03	60.6
	31.0	35	3.94 ± 0.02	3.93 ± 0.03	58.1
	31.0	40	3.88 ± 0.02	3.90 ± 0.03	56.7
	37.0	25	3.90 ± 0.02	3.85 ± 0.02	56.4
	42.5	25	3.68 ± 0.02	3.67 ± 0.03	53.0
	60.0	25	3.35 ± 0.02	3.34 ± 0.03	42.0

[a] pK_a values were estimated from the absorption intensities at ~450 nm and ~685 nm for GPP. [b] ref. 17

Accordingly, we performed the pH-metric titration of GPP under various polarity conditions to monitor the inter-conversion from d_A-GPP and/or d_M-GPP to p_M-GPP (Figures 6 (A–E)). Similar to the spectral change observed in buffer solutions, a sharp band around ~450 nm for p_M-GPP form gradually appeared with decreasing pH from 6.0 to 2.5. The apparent acid/base pK_a decreased from ~4.10 to 3.35 with decreasing solvent κ from ~62.0 to ~42.0 at 25 °C (Table 1, Figure 6). The lack in solvation of cationic p_M-GPP at low results in the decrease in apparent pK_a. Because the magnitude of $A_\lambda^{6.0}$ (in eq. 2) is independent of medium polarity (κ ≤ 70), the pH dependent p_M-GPP/GPP ratio (X_{pM}-GPP) can be estimated independently without knowing the κ of mixed solvents.

For the acetone/buffer mixed medium, temperature dependent pK_a values are estimated and listed in Table 1. Interestingly, a certain decrease in solvent κ by either an increase in acetone ratio or increase in temperature in the buffer/acetone mixed medium exhibited a similar extent in acid/base pK_a shift (Table 1, Figures 6 and 7). These results suggest that the temperature-dependent pK_a shift for GPP is mostly associated with the variation of solvent κ (Figures 6 and 7). Therefore,

maintaining an identical temperature condition of the measuring and calibrating solutions is a prerequisite to determine the GPP environmental pH by utilizing pH-metric titration curves.

5.3.3. Simultaneous estimation of pH and polarity in homogeneous soutions with GPP

Under complete protonation of GPP, the identical absorption intensity at various solvent κ (Figure 5 for buffer solutions, Figure 6 for acetone-containing buffer solutions, and in Figure 7 for solutions at different temperatures) indicates molar extinction coefficients (ε) at all wavelengths does not depend upon mediumκ. However, when GPP becomes partially protonated, the intensity changes at ~420 nm is to be affected not only by the κ-induced change in d_A-GPP to d_M-GPP ratio for deprotonated GPP, but also their protonation to form p_M-GPP. By evaluating $X_{pM\text{-}GPP}$ from eq. (2), the intensity because of the p_M-GPP form at ~420 nm is calculated as $A^p_{420} \times X_{pM\text{-}GPP}$, where A^p_{420} denotes the intensity for the fully protonated GPP ($X_{pM\text{-}GPP} = 1$). Therefore, the actual intensity of deprotonated GPP (d_A-GPP and/or d_M-GPP) at ~420 nm can be obtained by subtracting $A^p_{420} \times X_{pM\text{-}GPP}$ from the observed intensity (A_{420}^{obs}). Furthermore, ($A_{420}^{obs} - A^p_{420} \times X_{pM\text{-}GPP}$) was normalized by dividing it with the mole-ratio of deprotonated GPP ($1 - X_{pM\text{-}GPP}$) to use eq. (1) for the estimation of κ:

$$A_{420}^{N} = A_{420}^{x} = (A_{420}^{obs} - A^p_{420} \times X_{pM\text{-}GPP}) / (1 - X_{pM\text{-}GPP}) \qquad (3)$$

$$-\ln (A_{420}^{21} - A_{420}^{x})$$

$$= -\ln [A_{420}^{21} - (A_{420}^{obs} - A^p_{420} \times X_{pM\text{-}GPP}) / (1 - X_{pM\text{-}GPP})]$$

$$= -0.13 \times \kappa + 10.3 \qquad (4)$$

Using eq. 4, an unknown κ can be estimated by evaluating X_{pM}-GPP and A_{420}^{N} from the intensities at ~450 or 685 nm and 420 nm, respectively. Notably, the more general eq. 4 than eq. 1 can be used to estimate κ under the conditions of various extent of GPP protonation in a wide range of bulk pHs. Once the medium κ is known, pH of the medium can also be simultaneously estimated from the same ab-sorption spectrum by correlating X_{pM}-GPP with the pH-metric calibration curve obtained under same medium κ. A series of demonstrated procedure above indicates that GPP (**2**) is a highly effective for simultaneous detection of environmental pH and κ using a single absorption spectrum.

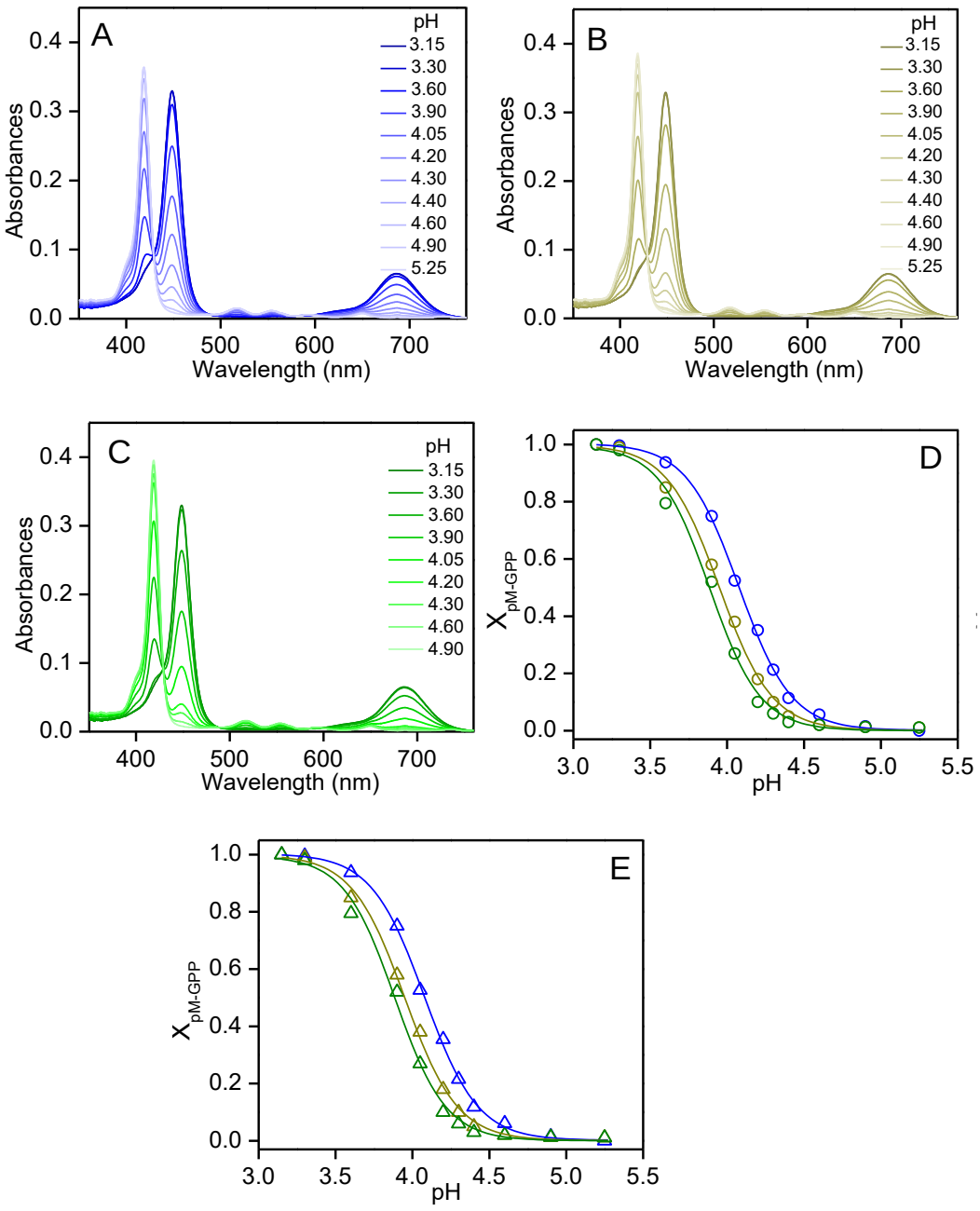

Figure 7. pH-dependent UV-Vis absorption spectra of GPP (2) (2.5 μM) in 31% (*w*/*w*) acetone/buffer medium at various temperature: A, 25 °C; B, 35 °C and C, 40 °C. (D, E) p_M-GPP mole-ratio ($X_{pM\text{-}GPP}$) analyzed from the intensity at ~450 nm (graph D) or ~685 nm (graph E) vs. pH in the mixed medium (Blue: 25 °C; Dark yellow: 35 °C; Green: 40 °C).

5.3.4. Interaction of GPP with self-assembly interfaces

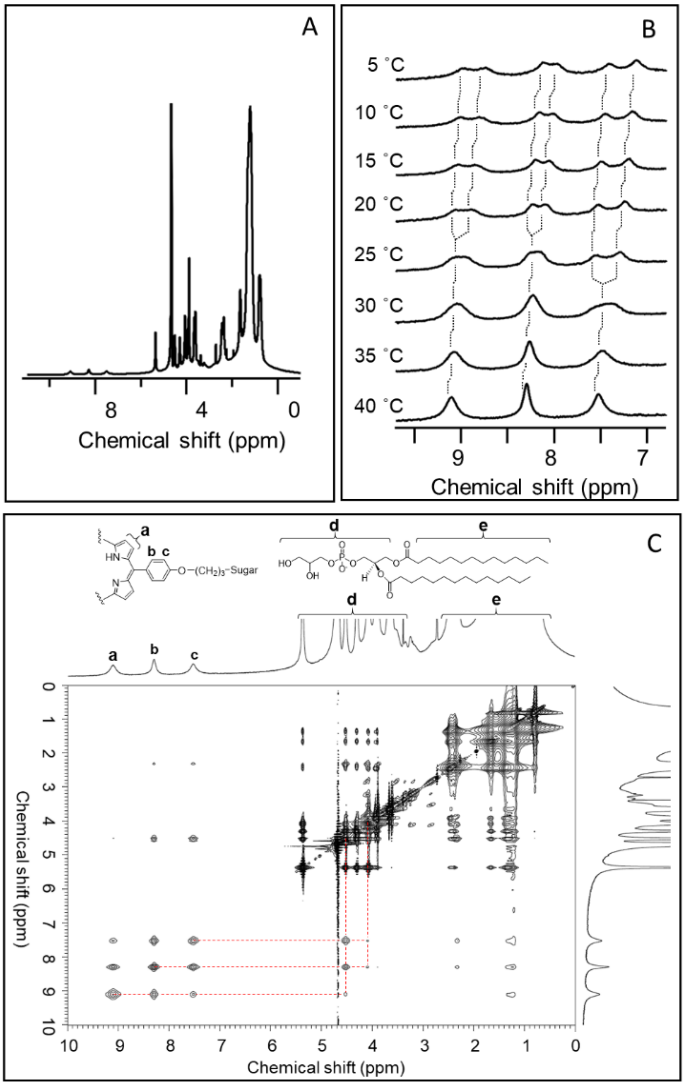

Figure 8. 600 MHz-1H NMR spectroscopic analysis for the mixture of GPP (2) and DMPG LUV; (A) Whole 1D NMR spectrum at 40 °C; (B) 1D NMR spectra at various temperatures in the range from 7.0 ppm to 10.0 ppm; (C) NOESY spectrum at 40 °C; Conditions: [2] = 1 mM, [DMPG LUV (*d* ~100 nm)] = 8 mM in D_2O containing DMSO-d_6 (5% v/v)) The dotted lines marked in Figure 8 (B) indicate the signal shifts of the protons during change in temperature. Red broken lines in Figure 8 (C) indicate the correlations between the protons in GPP (2) and those in the head moiety of DMPG.

Encouraged by the proved utility of GPP (**2**) for simultaneous determination of the local polarity and pH around the molecule, we investigated the availability of GPP (**2**) for probing the local environment at the interface of lipid emulsions. At first, we attempted to elucidate interaction fashions between GPP (**2**) and DMPG LUV by ^{1}H NMR spectroscopy. The full 1D ^{1}H NMR spectrum of the mixture of GPP (**2**) and DMPG LUV observed at 40°C is shown in Figure 8A.

Figure 8B shows the temperature dependency on 1D ^{1}H NMR spectrum in the range from 7.0 ppm to 10.0 ppm. The diameter of DMPG LUV at ~100 nm was controlled by the lipid extrusion method and the size distribution and morphology were confirmed by Dynamic Light Scattering (DLS) and cryo-Transmission Electron Microscopy (TEM), respectively (Figures 9 and 10).

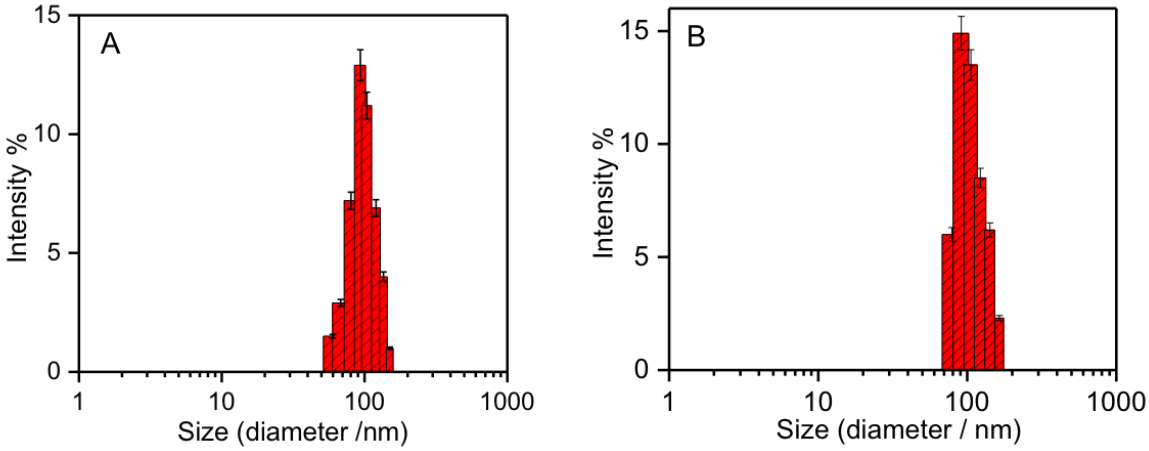

Figure 9. DLS measurement showing particle size distribution profile of DMPG LUV (lipids, 50 µM) at different pH: (A) pH 4.0 and (B) pH 7.0. Each of these spectra is an average of 48 scan. Standard deviations for measurements taken from five independent experiments are depicted by error bars.

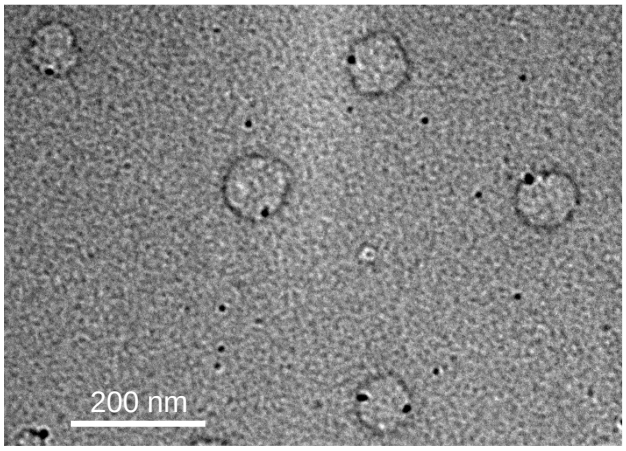

Figure 10. Cryo-transmission electron microscope (TEM) image of DMPG LUV.

The signals at 7.5 ppm, 8.3 ppm, and 9.1 ppm are assigned as protons of m-phenyl, o-phenyl and porphyrin β-positions, respectively. The signal broadening is wholly because of the existence of LUV macro-molecular substance. At lower temperatures, each signal tends to split into two

peaks (Figure 8B). The splitting occurs around 25–30 °C, which is close to the phase transition temperature of DMPG LUV (vide infra).[22,23] Consequently, this finding indicates that GPP (2) interacts with DMPG LUV. The signal splitting at low temperatures is caused by the decrease in exchange rate between several interaction fashions. We also collected the NOESY spectrum of the mixture of GPP (2) and DMPG LUV at 40 °C in order to address the location of GPP (**2**) in DMPG LUV (Figure 8C). The proton signals at 7.5 ppm, 8.3 ppm and 9.1 ppm of **2** displayed correlation signals with proton peaks at 4.1 ppm and 4.5 ppm, corresponding to the protons at the head moiety of DMPG. Similar cross peaks were also observed in the measurement at 20 °C (Figure 11). The results of 2D NMR spectral analysis strongly indicate that GPP (**2**) locates on the interfacial Stern layer of DMPG LUV regardless of temperature change. Therefore, GPP (**2**) is suitable to measure pH and polarity at a similar Stern layer location for DMPG LUV during the temperature-induced lipid phase transition.

Next, we measured UV-Vis spectra of GPP in the presence of amphiphilic systems. The absorbances at ~450 nm or ~685 nm for GPP (2.5 μM) in 10 mM citrate/phosphate buffer (pH 4.2) increased gradually with increasing concentration of SDS micelles or DMPG LUV (Figure 12). This is indicative of the interaction between GPP and the interface of those self-assemblies. The increase in absorbances shown in Figure 12 is very similar to the spectral change observed for the pH titration in a buffer solution (Figure 5), suggesting GPP in the amphiphilic systems undergoes the acid/base equilibrium to generate p_M-GPP form. No significant changes in LUV morphology are confirmed by the observation of almost identical distribution in DMPG LUV diameter (Figure 9). The intensities saturated in the presence of 8 mM SDS or 1.1 mM DMPG, and the intensity saturation justifies that all the GPP molecules interacted with the interface. The red-shift of absorption band from ~446 to 450 nm for p_M-GPP form in the self-assembled system suggests that GPP interacted with the self-assembly interface with κ lower than the bulk phase. Therefore, we performed further measurement under these micelle or LUV-interacting intensity saturation conditions to monitor d_A-GPP and/or d_M-GPP to p_M-GPP interconversion for GPP at the self-assembly interfaces.

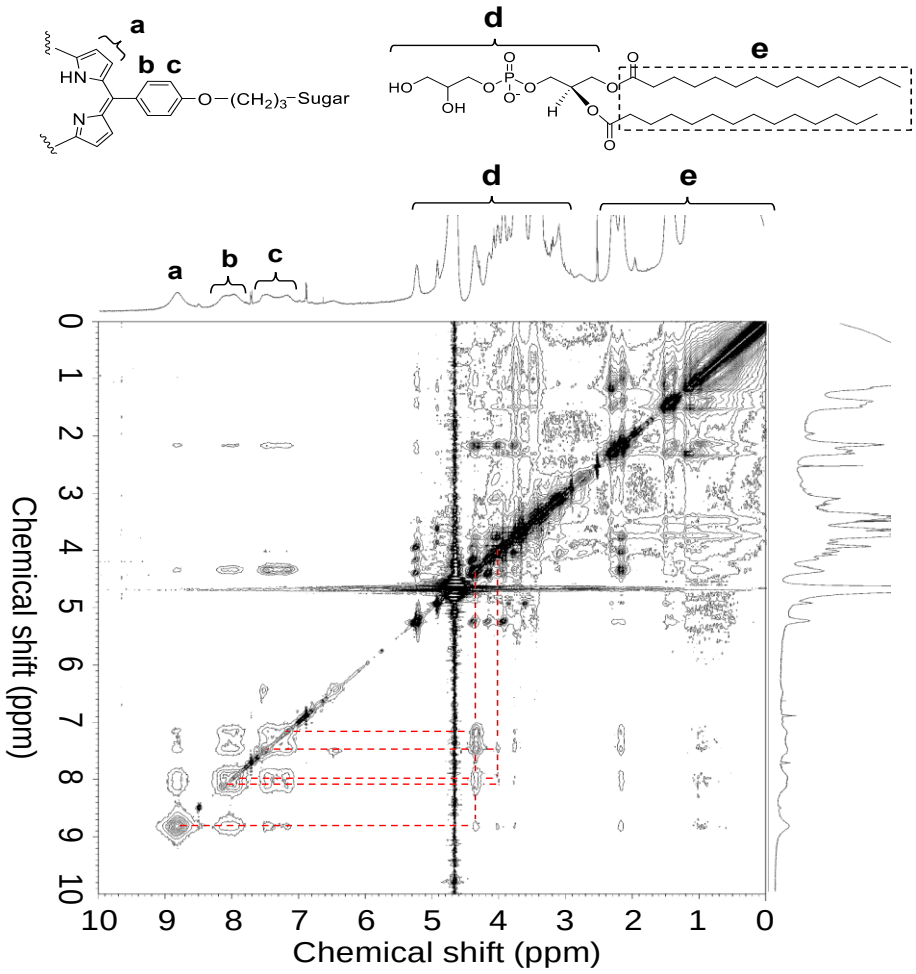

Figure 11. NOESY spectrum of the mixture of GPP (2) and DMPG LUV at 20 °C; Conditions: [2] = 1 mM, [DMPG LUV (d = 100 nm)] = 8 mM in D_2O containing DMSO-d_6 (5% *v*/*v*)). The correlations between the protons of *m*-phenyl, *o*-phenyl and porphyrin *p*-positions with those of the head moiety of DMPG are shown by broken red lines.

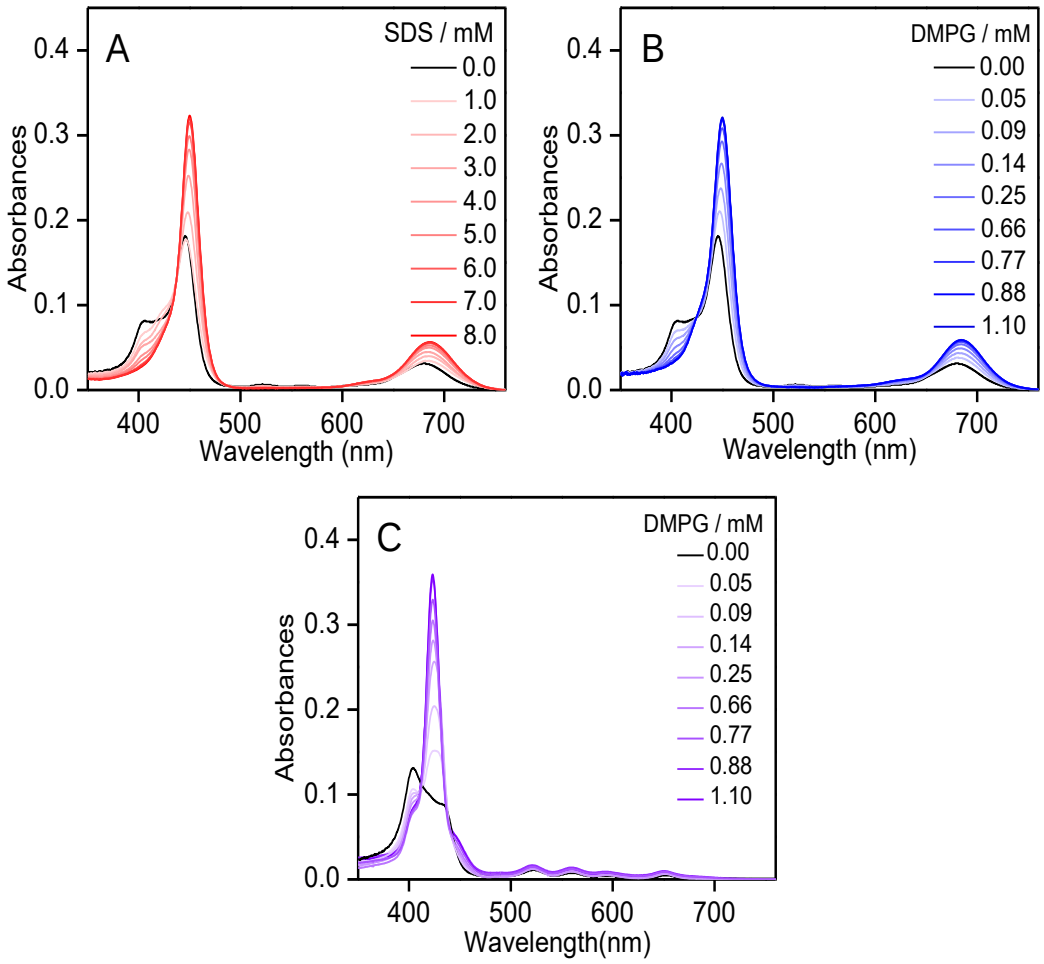

Figure 12. UV-Vis absorption spectra of GPP (2) (2.5 μM) in presence of different concentration of amphiphilic molecule in 10 mM sodium citrate/sodium phosphate buffer at different pH: A, SDS micelle (pH 4.2); B, DMPG LUV (pH 4.2) and C, DMPG LUV (pH 6.2).

5.3.4.1. Simultaneous estimation of pH and polarity at self-assembly interfaces

pH-metric titrations for GPP(2) were performed with a interaction saturated high concentration of DMPG LUV (lipid, 1.1 mM, Figure 13A) and SDS micelles (8 mM, Figure 14B) at 25 ˚C. As described above, the extinction coefficient of pM-GPP form does not depends on κ. The pH-dependent equilibrium p_M-GPP mole-ratio (X_{pM}-GPP) at the DMPG LUV interface was estimated by monitoring absorption intensity at ~450 nm or ~685 nm at the full interaction of GPP with self-assembled systems according to eq. (2). On the other hand, for the determination of X_{pM}-GPP value at the SDS micelle interface, only absorbance change at ~685 nm can be used for the analysis. The higher energy absorption band around 450 nm tended to gradually blue-shift with

decreas-ing pH from 5.3 to 4.3 and overlapped considerably with that of d_A-GPP and/or d_M-GPP (Figure S14B). When using X_{pM}-GPP under different bulk pH conditions, the interfacial κ was estimated by calculating the corresponding A_{419}^N from the observed intensity at ~420 nm according to eq. 3 and 4. The interfacial κ were determined to be similar at ~61.5 and 60.5 for SDS micelle and DMPG LUV, respectively, at 25 °C using eqs. 3 and 4 (Table 2).

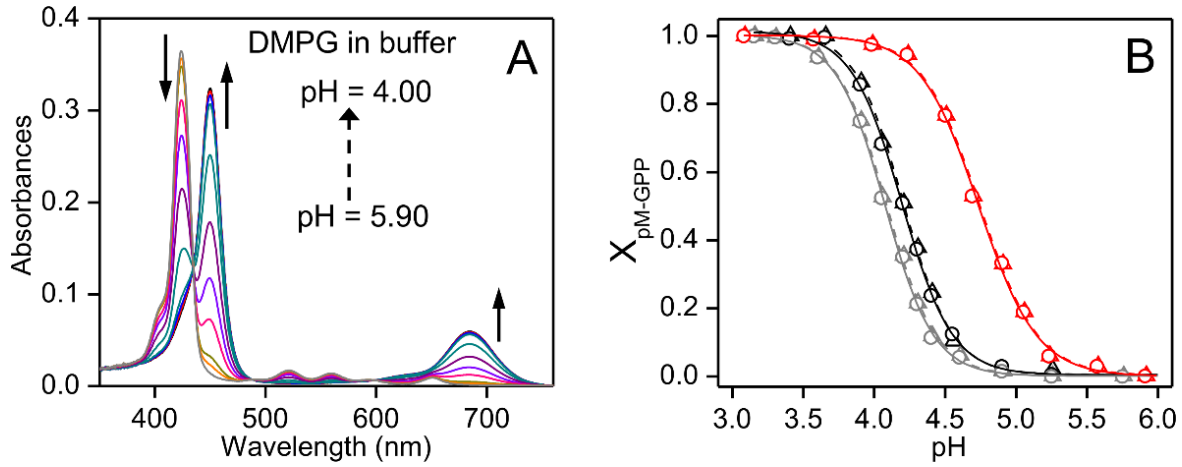

Figure 13. pH-dependent UV-Vis analysis of GPP (2; 2.5 μM) at 25 °C in 10 mM sodium citrate/sodium phosphate buffer containing DMPG LUV (lipid, 1.1 mM); (A) Spectra measured at pH 4.0, 4.25, 4.50, 4.70, 4.90, 5.05, 5.25, 5.55, 5.90. The change in intensities with decreasing pH are shown in arrows; (B) p_M-GPP mole-ratio (X_{pM-GPP}) analyzed from the intensity at ~450 nm (circle, solid lines) and ~685 nm (triangle, broken lines) is plotted against bulk pH (red). The plots for pure buffer solutions (black) and buffer containing 31% (*w*/*w*) acetone (gray) in Figure 5 are shown for comparison.

The interfacial pH can be evaluated by monitoring the bulk pH-dependent p_M-GPP mole-ratio between the interface and the bulk. The increase in the amount of p_M-GPP mole-ratios observed in self-assembled systems indicate that the interfaces of these self-assemblies provide more acidic environments than the bulk phase does (DMPG LUV: Figure 13; SDS: Figure 14B). For quantitative measurement of pH at the interface, the p_M-GPP mole-ratio in the absence and presence of interaction saturated high concentration of SDS or DMPG LUV is compared with that of bulk pH (Figures 13B and 14E). The apparent pH shift between the interface and the bulk pH (Δ) can be estimated from the difference in p_M-GPP ratio between the interface and the bulk at 25 °C, where Δ should be negative because the interface is more acidic compared to the bulk. Irrespective of a different bulk pH, the Δ value was estimated to be approximately –0.54 and –0.59

for DMPG LUV and SDS micelles, respectively (Figures 13 and 14). Because the pH-induced interconversion between p_M-GPP and d_A-GPP and/or d_M-GPP is also affected by medium κ, Δ can also be affected by the difference in κ between the interface and the bulk. The polarity contribution (δ) to Δ is estimated by the apparent pH shift caused by the difference in κ between the interface and the bulk. The pH deviation (ΔpH) from the bulk to the interfacial pH (pH_{inf}), and subsequently pH_{inf} is obtained from the bulk pH (pH_{bulk}), Δ, and δ:

$$\Delta pH = \Delta - \delta \qquad (5)$$

$$pH_{inf} = pH_{bulk} + \Delta - \delta \qquad (6)$$

Δ is the function of combined interfacial pH and κ, whereas δ is related to interfacial κ. Conventionally, two separate pH and polarity responsive probe molecules are used to evaluate Δ and δ, respectively.[9, 10] However, the change in the locations of these pH and polarity probes at various interfacial depths makes the determination of δ erroneous because the interfacial polarity can decrease drastically with increasing interfacial depth from the water-exposed outer-surface. In contrast, the simultaneous estimation of Δ and δ parameters using a single GPP probe at an identical interfacial depth not only enables us to compute the correct value of δ for measuring interfacial pH, but also provides simultaneous values of interfacial pH and κ.

The value of κ in acetone/buffer mixed solution was adjusted same as the interfacial κ for SDS micelles and DMPG LUV at 25 °C (Table 2), and δ was found to be ~0.11 for SDS micelles and ~0.13 DMPG LUV, respectively, under different pH conditions at 25 °C (Figure 6 (B, F and G)). With the variation of bulk pH, the estimated pH deviation from the bulk to the interface (ΔpH) for SDS micelles and DMPG LUV were found to be similar ~0.70 and ~0.67, respectively, at 25°C (Table 2, Figures 13B, and 6 (B, F and G)). For anionic self-assemblies, the negatively charged head group at the interface may involve attractive electrostatic interaction with H^+, but it repels OH^-. In comparison to the bulk phase, $[H^+]$ and $[OH^-]$ may increase and decrease, respectively, at the interface. However, $[H^+]$ and $[OH^-]$ remain unchanged in the bulk owing to the larger volume of the bulk phase than the interface. Therefore, higher $[H^+]$ at the anionic SDS micelle or DMPG LUV interface than the corresponding bulk phase makes the interface more acidic compared to the bulk pH.

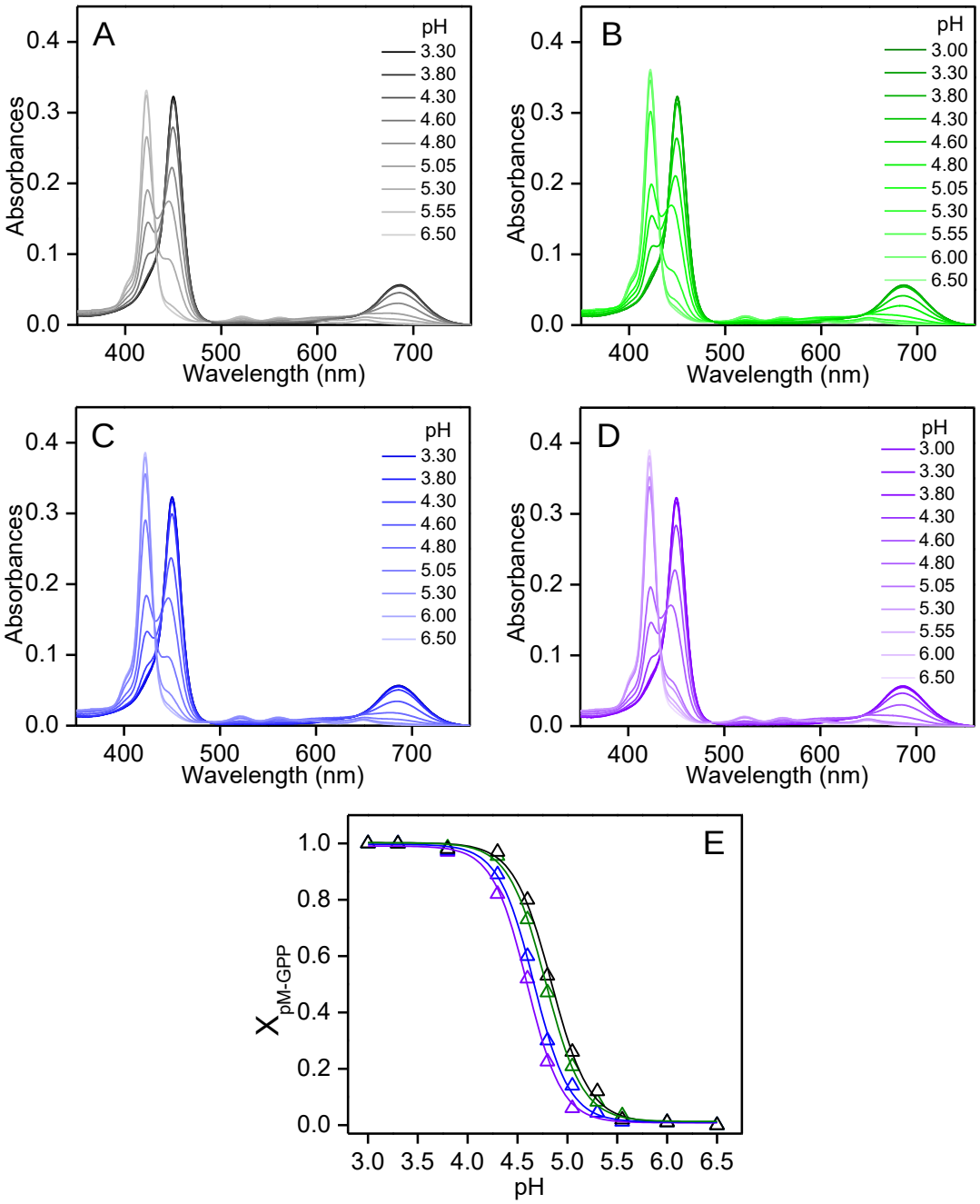

Figure 14. pH-dependent UV-Vis absorption spectra of GPP (2) (2.5 μM) in 10 mM sodium citrate/sodium phosphate buffer containing SDS micelle (8 mM) at various temperatures: A, 20 °C; B, 25 °C; C, 35 °C and D, 40 °C. (E) p_M-GPP mole-ratio ($X_{pM\text{-}GPP}$) analyzed from the intensity at ~685 nm vs. pH (Black: 20 °C; Green: 25 °C; Blue: 35 °C and Violet: 40 °C).

Table 2: Temperature and bulk pH-dependent pH deviation from the bulk to the interfacial (ΔpH), interfacial dielectric constant (κ(i)) for SDS micelle and DMPG LUV

	T (°C)	Bulk pH	Interfacial κ	ΔpH
SDS micelle	20	4.3–5.3	63.0 ± 0.2	–0.72 ± 0.03
	25	4.3–5.3	61.5 ± 0.2	–0.70 ± 0.03
	35	4.2–5.2	59.4 ± 0.2	–0.69 ± 0.03
	40	4.1–5.1	57.6 ± 0.2	–0.67 ± 0.03
DMPG LUV	20	4.5	61.6 ± 0.4	–0.62 ± 0.03
		4.9–5.3	61.5 ± 0.2	–0.62 ± 0.03
	25	4.5	60.6 ± 0.4	–0.67 ± 0.03
		4.9–5.3	60.3 ± 0.2	–0.67 ± 0.03
	30	4.5	59.6 ± 0.4	–0.85 ± 0.03
		4.9–5.3	61.9 ± 0.2	–1.01 ± 0.03
	35	4.5	62.1 ± 0.4	–1.05 ± 0.03
		4.9–5.6	63.0 ± 0.2	–1.09 ± 0.03
	40	4.5	62.6 ± 0.4	–1.10 ± 0.03
		4.9–5.6	61.4 ± 0.2	–1.11 ± 0.03

5.3.4.2. Temperature effect on SDS micelle interfacial pH and polarity

The general temperature effect on interfacial pH and κ were examined for SDS micelle. Upon increasing the temperature from 20 °C to 40 °C, the acid/base pK_a at the SDS micelle interface decreased from ~4.8 to 4.6 (Table 3 and Figure 14). At first, the dependency of interfacial κ on temperature was estimated by analyzing the intensity contribution of d_M-GPP from absorption spectra under various pH conditions according to eq. 1 (for complete deprotonation of GPP, pH > 7.0) or eq. 4 (for a mixture of protonated and deprotonated GPP, pH < 7.0). Irrespective of different bulk pH, the observed intensity (for pH ≥ 7.0) or normalized intensity (A_{420}^N for pH < 7.0) at 420 nm increased from ~0.34 to 0.39 with an increase of temperature from 25 °C to 40 °C (Figure 14), which corresponds to a decrease of interfacial κ from ~61.5 to 57.6 (Table 2 and Figure 6). Interestingly, the identical decrease of κ from 25 °C to 40 °C was observed for 31% acetone-containing buffer medium (Table 1, Figures 4 and 6), suggesting that the typical temperature vs. κ correlations are also maintained at the SDS micelles interface. In addition, a similar amount of pK_a

decrease ~0.2 for GPP between SDS micelle and acetone/buffer medium with κ similar to that of the SDS interface was detected by the increase of temperature from 25 °C to 40 °C (Tables 1 and 3, Figures 7 and 14). The results show that the interfacial pH for SDS micelle remains unchanged and the acid/base pK_a change for GPP is caused by the temperature induced variation of interfacial κ.

Table 3: Acid/base pK_a values for GPP (2) at various temperature (T) in the presence amphiphilic self-assembled systems.

		T (°C)	pK_a [a]		κ(b) [b]
			450 nm	685 nm	
Self assembly	SDS	20	–	4.83 ± 0.03	80.4
		25	–	4.79 ± 0.03	78.5
		35	–	4.66 ± 0.03	76.8
		40	–	4.58 ± 0.03	73.1
	DMPG	20	4.70 ± 0.02	4.71 ± 0.03	80.4
		25	4.74 ± 0.02	4.74 ± 0.03	78.5
		30	4.87 ± 0.02	4.88 ± 0.03	76.8
		35	4.98 ± 0.02	4.99 ± 0.03	75.0
		40	5.02 ± 0.02	5.03 ± 0.03	73.1

[a] pK_a values were estimated from the absorption intensities at ~450 nm and ~685 nm for GPP. [b] ref.17

5.3.4.3. Interfacial pH/polarity changes during temperature induced phase transition for DMPG LUV

The gel to liquid-crystalline phase transitions process of lipids in LUV membrane is not only affected by temperature, but also dependent on environmental pH conditions.[24] DMPG is known to exhibit weakly energetic pre-transitions peaks at low temperatures (~11–15 °C) and highly cooperative strongly energetic gel to liquid-crystalline phase transitions (~23–25 °C).[25] The phase transition temperatures (T_m) of DMPG in its LUV were measured by differential scanning calorimetry (DSC) in 10 mM citrate/phosphate buffer solution at various pH 4.5–5.5 (Figure 15). The weak pre-transition peak at ~16 and 21 °C were observed at pH 5.5 and 5.0, respectively,

although no such peak appeared at pH 4.5. However, the main phase transition temperature T_m,[26] was found to increase from 28.0 to 32.3 °C by decreasing pH from 4.9 to 4.5, whereas T_m increased to a relatively lower extent from 26.6 to 28.0 °C with increasing pH to 5.5.

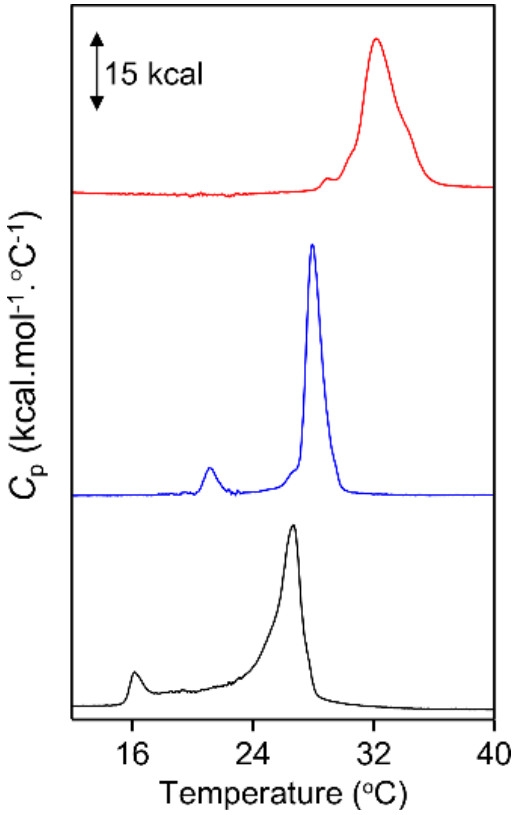

Figure 15. Differential scanning calorimetry (DSC) thermograms of DMPG LUV (lipids, 1 mM) in 10 mM citrate-phosphate buffer, pH 4.5 (red), pH 4.9 (blue), and pH 5.5 (black).

Temperature- and pH-dependent acid/base equilibrium for GPP (2.5 µM) were monitored at the DMPG LUV interface to monitor the effect of phase transition from DMPG gel state to its liquid-crystalline state on the interfacial pH and κ (Figure 16). In contrast to SDS micelles, an increase in absorption intensity at ~450 nm and ~685 nm was observed for DMPG LUV by increasing temperature from 20 °C to 40 °C (Figure 16 and 17) under a different, but constant pH. However, major increases in absorption intensity at ~450 nm from ~0.12 to 0.21 and at ~685 nm (from ~0.02 to 0.04) were detected between 25°C and 35 °C at bulk pH 4.9. No further intensity increase was observed at above 35 °C (Figure 17 and Table 2). Under a decreased bulk pH condition of 4.5, a major increase in intensity was noticed at above 30 °C up to 40 °C (Figure 17B).

The increase in T_m for DMPG LUV from 28.0 °C to 32.3 °C with decreasing pH from 4.9 to 4.5 also clearly correlates with the increasing temperature required to obtain the major increase in p_M-GPP mole-ratio from 4.9 to 4.5 (Figure 17). The temperature induced increase in p_M-GPP mole-ratio indicating an increase in interfacial acidity can be correlated with the phase transitions process of DMPG gel state to liquid-crystalline state (Figure 17 and Table 2).

According to our analysis protocol, we first estimated interfacial κ by normalizing each spectrum in Figure 16 and 17. For example, normalized spectra at pH 4.9 and 4.5 according to eq. 3 are represented in inset of Figure 17. Interfacial κ for DMPG LUV at different temperatures and pH values were determined from the value of normalized intensity (A_{420}^N) using eq. 4 (Figures 16, 17 and Table 2). When DMPG involves a phase transition process from ~25 °C to 35 °C at pH 4.9 and ~30 °C to 40 °C at pH 4.5, the interfacial κ increased from 60.3 to 63.0 and 59.6 to 62.6, respectively (Figures 15, 17 and Table 2). For other temperatures when DMPG did not involve a phase transition significantly according to DSC measurements (Figure 15), a decrease in interfacial κ with increasing temperature was also observed in similar to SDS micelles (Figure 14, and Table 2). Because the acid/base equilibrium for GPP is affected substantially by environmental κ (Figure 6 and Table 1), various polarity correction factors (δ ~0.09–0.13 depending on different interfacial κ ~60.3–63.0) are considered to estimate interfacial pH and its deviation from the bulk pH (ΔpH) using eq. 5 and 6. Bulk pH and temperature-dependent interfacial pH and ΔpH are listed in Table 2. A similar increase of ΔpH ~ –0.5 was mostly observed upon increasing temperature from 20 °C to 40 °C at bulk pH 4.9 and 4.4, respectively, although the major increase of ΔpH was observed around the DMPG phase transition temperature (Figures 15 and 17, Table 2). As we observed that pH at typical self-assembly interface (SDS micelle) does not depend on temperature, the temperature dependent increase of Stern layer interfacial acidity for DMPG LUV should be associated with the DMPG gel to liquid-crystalline phase transition.

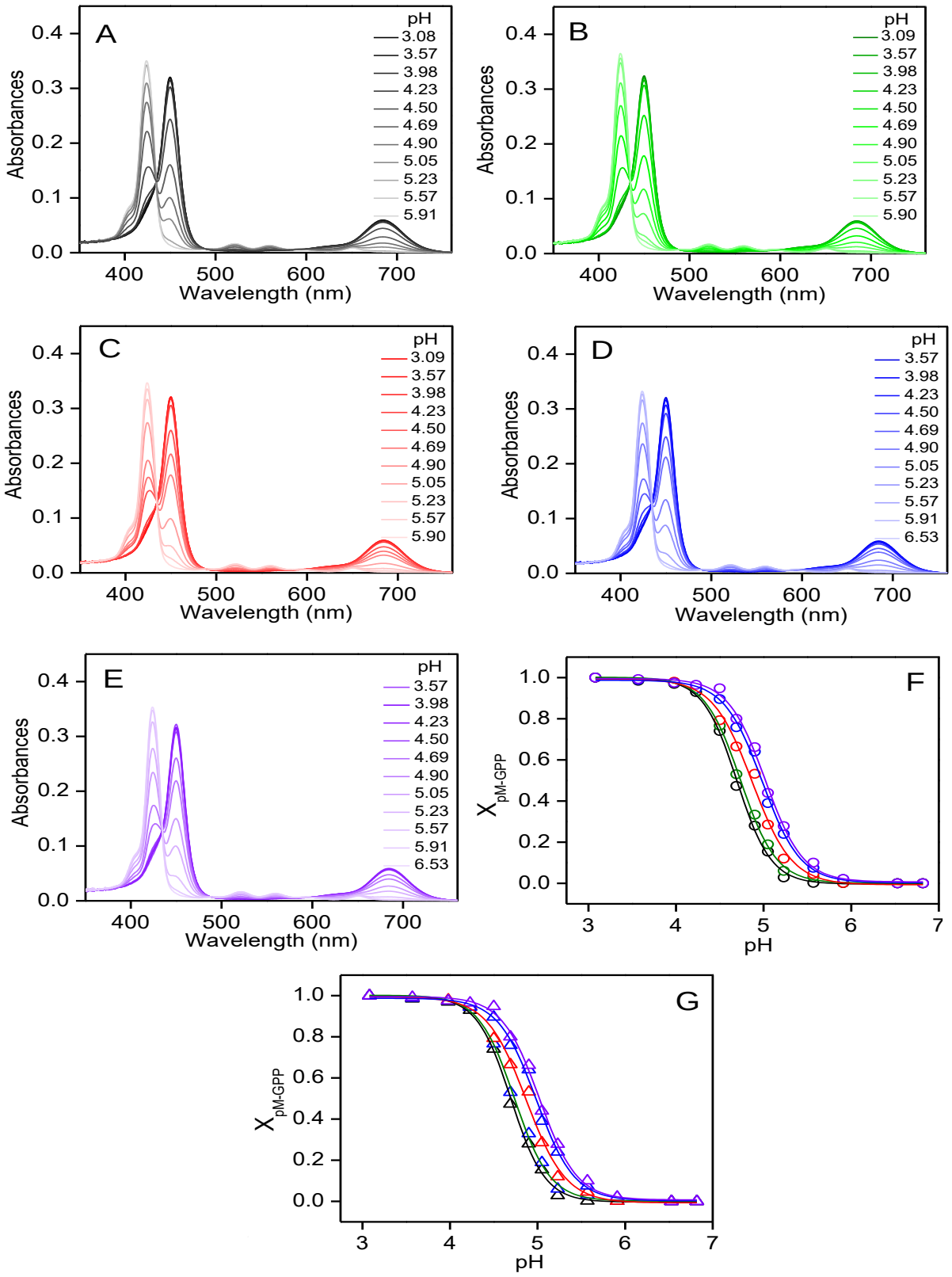
A
pH
3.08
3.57
3.98
4.23
4.50
4.69
4.90
5.05
5.23
5.57
5.91
Absorbances
Wavelength (nm)
B
pH
3.09
3.57
3.98
4.23
4.50
4.69
4.90
5.05
5.23
5.57
5.90
C
pH
3.09
3.57
3.98
4.23
4.50
4.69
4.90
5.05
5.23
5.57
5.90
D
pH
3.57
3.98
4.23
4.50
4.69
4.90
5.05
5.23
5.57
5.91
6.53
E
pH
3.57
3.98
4.23
4.50
4.69
4.90
5.05
5.23
5.57
5.91
6.53
F
X pM-GPP
pH
G
X pM-GPP
pH

Figure 16. pH-dependent UV-Vis absorption spectra of GPP (2) (2.5 μM) in 10 mM sodium citrate/sodium phosphate buffer containing DMPG LUV (1.1 mM) at various temperatures; (A): 20 °C; (B): 25 °C; (C): 30 °C; (D): 35 °C; (E): 40 °C; (F,G) p_M-GPP mole-ratio ($X_{pM\text{-}GPP}$) analyzed from the intensity at ~450 nm (graph F) or ~685 nm (graph G) vs. pH at various temperatures (Black: 20 °C; Green: 25 °C; Red: 30 °C; Blue: 35 °C; Violet: 40 °C).

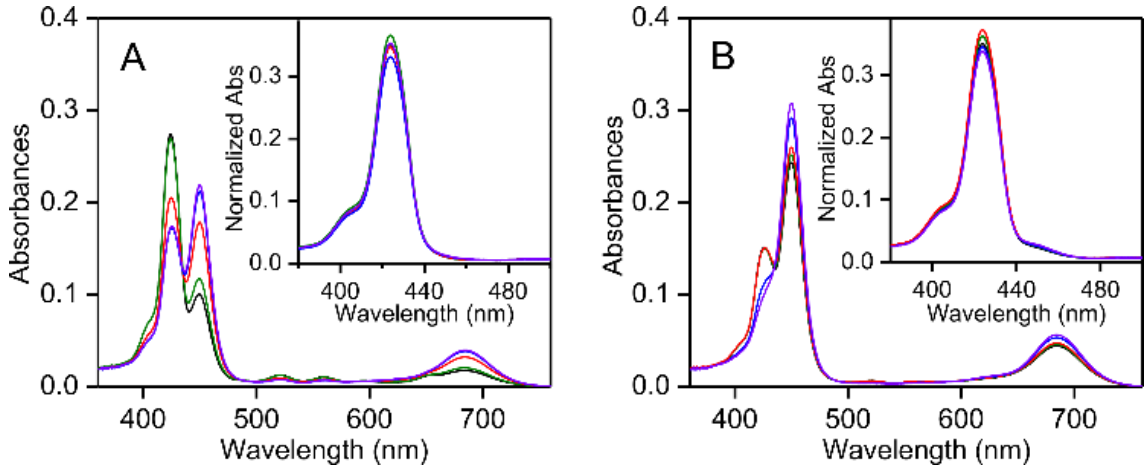

Figure 17. Temperature dependent UV-Vis absorption spectra of GPP (2; 2.5 μM) and (inset) corresponding normalized absorption spectrum in 10 mM sodium citrate/sodium phosphate buffer containing DMPG LUV (1.1 mM) at (A) pH 4.9 and (B) pH 4.5: black, 20 °C; green, 25 °C; red, 30 °C; blue, 35 °C and violet, 40 °C. Each spectrum in inset is normalized according to the similar procedure to obtain normalized intensity (A_{420}^N) using eq. (3).

It has been reported that interfacial pH and κ for a charged amphiphilic self-assembled system are highly controlled by the packing arrangement of ionic headgroups at the interfacial Stern layer.[9,27] A tight headgroup packing arrangement with their low solvent accessible surface area restricts the electrostatic penetration of H_3O^+ (for an anionic headgroup) or OH^- (for a cationic headgroup) and H_2O (for solvation) into the interfacial stern layer.[9] However, the penetrating ability are gradually improved with increasing inter-headgroup separation distance (loose headgroups packing) during gel to liquid-crystalline phase transition. The packing flexibility may allow the anionic headgroup to have more access to the bulk water phase for solvation and penetration of H_3O^+ into the interface (Scheme 3).

The higher H_3O^+ penetration at the DMPG LUV interface makes the interface more acidic by ~0.5 pH unit for liquid-crystalline phase compared to the gel phase. Notably, no significant change of pH at the SDS micelle interface was observed in the range of 20–40 °C (Table 2), which surely

eliminates any role of intrinsic temperature induced pH change at LUV interface. On the other hand, only a small increase of interfacial κ from ~60 to 63 was detected for the transition from gel to liquid-crystalline phase (*inset* of Figure 17 and Table 2). Presumably, the lipid phase transition-induced increase of interfacial κ may be partially compensated by increasing temperature-dependent decrease in κ (Table 2), resulting in the affection to the small change of interfacial κ.

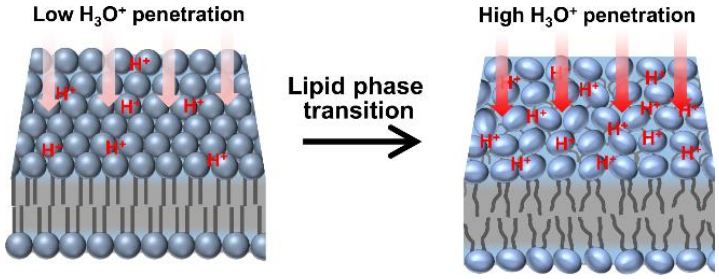

Scheme 3. Schematic representation of lipid headgroup packing arrangement in DMPG LUV in gel (left) and liquid-crystalline (right) phases.

5.4. Conclusion

A series of UV-Vis spectral changes shown by GPP (2) prove the utility of GPP (2) as a probe for the simultaneous evaluation of interfacial pH and polarity for amphiphilic self-assemblies. Throughout the UV-Vis spectral changes during the protonation/deprotonation at inner nitrogen atoms in the porphyrin ring and aggregation character, GPP (2) is able to reflect the local pH and polarity in media around GPP (2). Furthermore, the delicately balanced structure composed of a porphyrin moiety (hydrophobic deprotonated or cationic protonated) and hydrophilic glucose parts in GPP (2) enables the compound to stay at the Stern layer of anionic phospholipid self-assemblies. The evaluation of physicochemical properties based on the spectral changes of GPP (2) in the presence of DMPG LUV is possible during the phase transition of the lipid self-assembly. The difference in pK_a between the bulk and the lipid membrane surface is interpretable in terms of a structural dynamics of phospholipid self-assemblies that affects the interface ion penetration abilities. Designed chromophore probes, such as GPP (2), will be useful to understand chemical events on membrane surface.

5.5. References

1. T. Heimburg, *Thermal biophysics of membranes*, Wiley-VCH Verlag GmbH & Co. KGaA: Weinheim, 2007.
2. T. Heimburg and A. D. Jackson, *Proc. Natl. Acad. Sci. U.S.A.*, 2005, **102**, 9790.
3. N. Ben-Dov and R. Korenstein, *Biochim. Biophys. Acta*, 2013, **1828**, 2672.
4. R. Nambiar, R. E. McConnell and M. J. Tyska, *Proc. Natl. Acad. Sci. U.S.A.*, 2009, **106**, 11972.
5. M. I. Pérez-Camacho and J. C. Ruiz-Suárez, *Soft Matter* , 2017, **13**, 6555.
6. S. D. Freedman, H. F. Kern and G. A. Scheele, *Eur. J. Cell Biol*., 1998, **75**, 153.
7. Z. Zhang, K. T. Nguyen, E. F. Barrett and G. David, *Neuron*, 2010, **68**, 1097.
8. S. Neuhoff, A-L. Ungell, I. Zamora and P. Artursson, *Eur. J. Pharm. Sci.*, 2005, **25**, 211.
9. Y. Sarkar, R. Majumder, S. Das, A. Ray and P. P. Parui, *Langmuir*, 2018, **34**, 6271.
10. P. P. Parui, Y. Sarakar,R. Majumder, S. Das, H. Yang, K. Yasuhara and S. Hirota, *Chem. Sci.*, 2019, **10**, 9140.
11. M. K. Singh, H. Shweta and M. F. Khan and S. Sen, *Phys. Chem. Chem. Phys.*, 2016, **18**, 24185.
12. A. B. Rudine, B. D. DelFatti and C. C. Wamser, *J. Org. Chem.*, 2013, **78**, 6040.
13. Y. Y. Liu, M. Wu, L. N. Zhu, X. Z. Feng and D. M. Kong, *Chem. Asian J.*, 2015, **10**, 1304.
14. V. Villari, P. Mineo, E. Scamporrino and N. Micali, *RSC Adv.*, 2012, **2**, 12989.
15. S. Verma, A. Ghosh, A. Das and H. N. Ghosh, *J. Phys. Chem. B*, 2010, **114**, 8327.
16. A. Meister, S. Finger, G. Hause and A. Blume, *Eur. J. Lipid Sci.Technol.*, 2014, **116**, 1228.
17. G. Akerlof, *J. Am. Chem. Soc.*, 1932, **54**, 4125.
18. A. D. Adler, F. R. Longo, J. D. Finarelli, J. Goldmacher, J. Assour and L. Korsakoff, *J. Org. Chem.*, 1967, **32**, 476.
19. J. S. Lindsey, I. C. Schreiman, H. C. Hsu, P. C. Kearney and A. M. Marguerettaz, *J.Org. Chem.*, 1987, **52**, 827.
20. S. Matile, N. Berova, K. Nakanishi, J. Fleischhauer and R. W. Woody, *J. Am. Chem. Soc.*, 1996, **118**, 5198.
21. N. C. Maiti, S. Mazumdar and N. Periasamy, *J. Phys. Chem. B*, 1998, **102**, 1528.
22. K. A. Riske, L. Q. Amaral and M. T. Lamy-Freund, *Biochim. Biophys. Acta, Biomembr.*, 2001, **1511**, 297.
23. K. A. Riske, R. M. Fernandez, O. R. Nascimento, B. L. Bales and M. T. Lamy-Freund, *Chem. Phys. Lipids*, 2003, **124**, 69.

24. G. Cevc, A. Watts and D. Marsh, *Biochemistry*, 1981, **20**, 4955.

25. M. T. Lamy-Freund and K. A. Riske, *Chem. Phys. Lipids*, 2003, **122**, 19.

26. A. Watts, K. Harlos, W. Maschke and D. Marsh, *Biochim. Biophys. Acta*, 1978, **510**, 63.

27. R. Nagarajan, *Langmuir*, 2002, **18**, 31.

LIST OF PUBLICATIONS

1. **R. Majumder**, Y. Sarkar, S. Das, S. Jewraika, A. Ray and P. P. Parui, *Analyst*, 2016, **141**, 3246.
2. **R. Majumder**, Y. Sarkar, S. Das, A. Ray and P. P. Parui, *New J. Chem.*, 2017, **41**, 8536.
3. **R. Majumder**, S. Roy, K. Okamoto, S. Nagao, T. Matsuo and P. P. Parui, *Langmuir*, 2020, **36**, 426.
4. S. Das, Y. Sarkar, **R. Majumder**, S. Mukherjee, J. Bandyopadhyay, A. Ray and P. P. Parui. *New J. Chem*., 2017**, 41**, 1488.
5. Y. Sarkar, **R. Majumder**, S. Das, A. Ray and P. P. Parui, *Langmuir*, 2018, **34**, 6271.
6. P. P. Parui, Y. Sarkar, **R. Majumder**, S. Das, H. Yang, K. Yasuhara and S. Hirota, *Chem. Sci*., 2019, **10**, 9140.
7. Y. Sarkar, S. Roy, **R. Majumder**, S. Das, D. V. Bhalani, A. Ray, S. Kumar Jewrajka and P. P. Parui, *Soft Matter*, 2020, **16**, 798.

Analyst

COMMUNICATION

View Article Online
View Journal | View Issue

Published on 04 May 2016. Downloaded by Jadavpur University on 24/05/2016 09:21:52.

Cite this: *Analyst*, 2016, **141**, 3246

Received 10th March 2016,
Accepted 29th April 2016

DOI: 10.1039/c6an00582a

www.rsc.org/analyst

A ratiometric solvent polarity sensing Schiff base molecule for estimating the interfacial polarity of versatile amphiphilic self-assemblies†

Rini Majumder,[a] Yeasmin Sarkar,[a] Sanju Das,[a,b] Suresh K. Jewrajka,[c] Ambarish Ray[b] and Partha Pratim Parui*[a]

A newly synthesised Schiff base molecule (PMP) existing in equilibrium between non-ionic and zwitterionic forms displays solvent polarity induced ratiometric interconversion from one form to another, such novelty being useful to detect the medium polarity. The specific interface localisation of PMP in versatile amphiphilic self-assembled systems has been exploited to monitor their interfacial polarity by evaluating such interconversion equilibrium with simple UV-Vis spectroscopy. In spite of the large differences in pH and/or viscosity between the bulk and interface, the unchanged equilibrium between the two molecular forms on varying the medium pH or viscosity provides a huge advantage for the exclusive detection of interfacial polarity.

The interfacial physicochemical properties, mainly the surface charge density, pH, polarity, viscosity *etc*. for self-aggregated assembly of amphiphilic molecules are of prime importance in a variety of fields, extending from materials science[1–4] to catalysis[4–8] and controlled drug delivery.[9–15] As the interface is considered as the separation between the bulk aqueous phase and the self-assembled interior oil phase, the interfacial polarity is expected to be less polar than that of bulk water. It has been reported that the local polarity across the membrane interface plays a critical role in controlling different biochemical processes like membrane transport,[16] ion transport across the membrane interface,[17–19] insertion of protein/molecules into membranes and their translocation across the membrane.[15,20,21] On the other hand, the dramatic change in the interfacial polarity for drug-loaded polymeric micelles during their interaction with the cellular membrane plays the ultimate role in targeted drug release.[9,22–24] Therefore, the detection of interfacial polarity is indispensable to understand the interface selective biological processes that are controlled by its local polarity.

The polarity induced change in the electronic transition energy parameter (E_T) for small organic chromophoric systems has commonly been utilized to detect the medium polarity.[25–27] However, a similar approach to evaluate the interfacial polarity for different self-assembled systems has yet to be addressed, although numerous studies have indicated a large difference in the polarities between the interface and bulk.[28–31] The detection of interfacial polarity with an optical probe is challenging mainly due to micro-heterogeneous compartmentalization and the uncertainty about its bulk phase contribution. Moreover, the optical signal originating from the interface is often caused by multiple interfacial parameters,[26,32] such as the optical response due to the pH difference between the interface and bulk phase may contribute to the optical responses originating due to the difference in their polarities.[32]

Recently, we have demonstrated simple UV-Vis absorption spectrometry to evaluate the interfacial pH for cationic micelle and vesicle interfaces by utilizing an interface interacting Schiff-base molecule.[32] The simplicity of such a detection methodology encourages us to show it as a simple and powerful technique for monitoring various interfacial physicochemical properties. Herein, for the first time, detection of the interfacial polarity for versatile self-assemblies, such as lipid vesicles and micelles with variable interfacial charge characters and aggregation numbers, is reported. The newly synthesised interface interacting Schiff base molecule, which mainly exists as a non-ionic species in non-polar medium, gradually converts into a zwitterionic form *via* the ground state intra-molecular proton transfer (GSIPT) process with increasing medium polarity (Scheme 1). UV-Vis absorption spectroscopy has been utilized to evaluate the interfacial polarity for vesicles and micelles by estimating the equilibrium between the two molecular forms at the interface.

It has been shown that a phenolic moiety containing a Schiff base molecule with multiple polar O- and N-centres is highly prone to be located at the water/oil interface of

[a]*Department of Chemistry, Jadavpur University, Kolkata 700032, India. E-mail: parthaparui@yahoo.com; Fax: +91-33-24146223; Tel: +91-9433490492*
[b]*Department of Chemistry, Maulana Azad College, Kolkata 700013, India*
[c]*Reverse Osmosis Division, CSIR-Central Salt & Marine Chemicals Research Institute, Gujarat-364002, India*

† Electronic supplementary information (ESI) available: Additional spectroscopic and synthetic information. See DOI: 10.1039/c6an00582a

This journal is © The Royal Society of Chemistry 2016

Published on 04 May 2016. Downloaded by Jadavpur University on 24/05/2016 09:21:52.

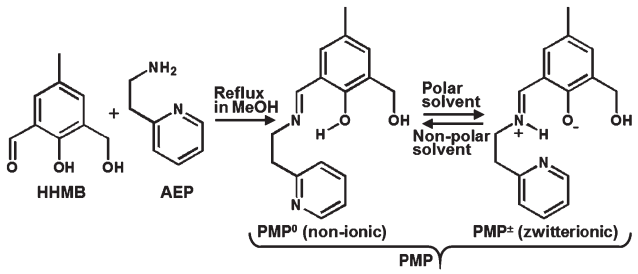

Scheme 1 Synthesis and solvent polarity dependent equilibrium between two molecular forms of the Schiff base molecule (PMP).

self-assemblies.[32] An interface interacting Schiff base molecule, 2-((2-(pyridine-2-yl)ethylimino)methyl)-6-(hydroxymethyl)-4-methylphenol (PMP), was synthesised by the condensation reaction between 2-(2-aminoethyl)pyridine (AEP) and 2-hydroxy-3-(hydroxyl methyl)-5-methyl benzaldehyde (HHMB) (see Experimental and Scheme 1, Fig. S1 and S2, ESI†), showing excellent solvent polarity dependent changes in UV-Vis absorption responses. On increasing the solvent polarity by increasing the amount of water fraction in the mixed THF/water medium, the 330 nm band intensity representing the phenol-conjugated-imine function gradually decreased with a concomitant increase of a visible band centred at ~420 nm with a 360 nm isosbestic point[32,33] (Fig. 1A). An identical spectral changeover was also detected for the comparable variation of medium polarity by using acetone or ethanol as a co-solvent in a mixed medium with water (Fig. S3, ESI†). The results suggest that PMP exists as an equilibrium between the two molecular species and the polarity of the medium preliminary governs their relative concentrations. As the interaction between the solvent and chromophore affects the energy difference between the ground and electronically excited states, a medium polarity/refractive index dependent absorption wavelength shift is often observed owing to the change in the dipole moment during electronic excitation. However, the relatively small slope values for the Stokes shift ($\nu_A - \nu_F$) *vs.* orientation polarizability (Δf) linear plot according to the Lippert equation[34] for different solvent mixtures indicate a negligible change of the dipole moment during excitation, and thus the influence of the solvent polarization on the large absorption shift (~85 nm or 6200 cm^{-1}) can be ignored (Fig. S4, ESI†). Since the absorbance changes with increasing solvent polarity were similar to that of the previously observed base induced conversion of phenol (neutral) to the phenolate (anion) form,[32,33] the 420 nm intensity may be originated for the formation of the phenolate moiety. However, the unperturbed 420 nm intensity with a decrease in the pH of buffer from 11.0 to 6.0 indicates that the medium pH is not responsible for the phenol-to-phenolate interconversion (Fig. S5, ESI†), since the pK_a for such phenolic-OH is close to 8.7.[32] Moreover, in 1 : 1 THF/H_2O medium, the identical absorbances without any increase in the 420 nm intensity for the phenolate between the pH higher and lower than 8.7 in 6.0–11.0 were observed possibly due to the increasing pK_a with decreasing solvent polarity[35] (Fig. S6, ESI†). Also, the unaltered absorption spectra on changing the solvent composition without changing its polarity, such as changing non-protonic acetonitrile (ACN) to protonic water containing a THF/water mixture with the same polarity (Fig. S7, ESI†), show that the H-bonding property of the solvent does not affect the interconversion between the two molecular forms of PMP. All these results support exclusive solvent polarity induced phenol-to-phenolate interconversion at pH 6.0–11.0. A zwitterionic species ($PMP^{\pm}$) containing the phenolate moiety with an absorption maximum at ~420 nm is observed presumably by gradual transfer of protons from the phenolic-OH to the imine-N through the GSIPT reaction on increasing the medium polarity resulting in an enhanced solvent–solute electrostatic stabilisation (Scheme 1 and 2A). Probably, the intra-molecular H-bonding between the pyridine-N and the proton of the imine-NH in the DFT-optimized structure is considered to play the most crucial role in the charge separation in $PMP^{\pm}$ (Scheme 2A). To explain the experimental absorption parameters, TD-DFT calculations on the DFT-optimized geometries in various dielectric media were performed.[36] The calculated vertical electronic transition wavelengths for both neutral (PMP^0) (~320 nm) and $PMP^{\pm}$ (~390 nm) were close to the observed absorption maxima ~330 and 420 nm of the

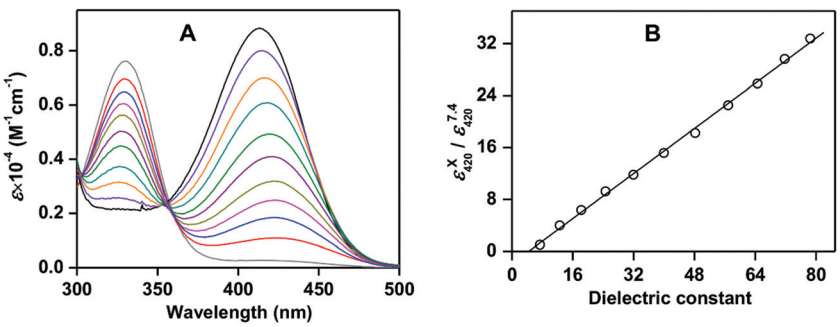

Fig. 1 (A) UV-Vis absorption spectra of the Schiff-base molecule PMP (5 μM) at different dielectric constants (κ) (7.4–78.5) in water/THF mixed medium at 25 °C (wt% of THF in the mixtures are depicted in bracket): gray, 7.4 (1.0); red, 12.6 (0.9); blue, 18.3 (0.8); pink, 24.6 (0.7); dark yellow, 32.0 (0.6); purple, 40.0 (0.5); green, 48.2 (0.4); cyan, 56.6 (0.3); orange, 64.6 (0.2); violet, 71.7 (0.1) and black, 78.5 (0.0). (B) Normalised molar extinction coefficients at 420 nm (ε^{X}_{420}) (normalised by dividing the molar extinction coefficient at 420 nm for the κ = 7.4 of THF ($\varepsilon^{7.4}_{420}$)) are plotted with κ.

Published on 04 May 2016. Downloaded by Jadavpur University on 24/05/2016 09:21:52.

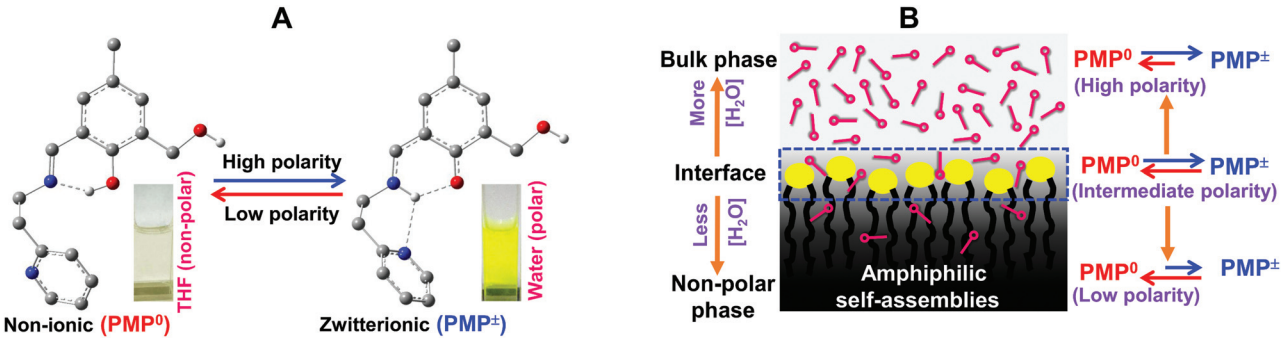

Scheme 2 (A) The equilibrium between two molecular forms of PMP (PMP^0 and $PMP^{\pm}$) with visible colorimetric response (PMP ~30 μM). In the DFT-optimized structure, all H's except those bonded with N (blue) and O (red) are removed for clarity (single broken lines denote H-bond). (B) Schematic representation for the distribution of water (pink) in the presence of amphiphilic self-assemblies. The equilibrium between two forms of PMP at various micro-environments is indicated in the right.

respective species without showing any significant solvation polarizability induced spectral shift (Table S1†). The results strongly support the hypothesis on not only the formation of $PMP^{\pm}$, but also the negligible effect of the solvent polarity on the observed large spectral shift.

As the relative concentration between non-ionic PMP^0 and zwitterionic $PMP^{\pm}$ was found to remain unchanged with the change of solvent viscosity or the pH 6.0–11.0 without changing the polarity (Fig. S8 and S9, ESI†), the solvent polarity, *i.e.*, the dielectric constant (κ) can be estimated from the normalized 420 nm extinction coefficient ($\varepsilon^{X}_{420}/\varepsilon^{7.4}_{420}$) *vs.* κ ratiometric linear correlation according to Fig. 1B as follows.

$$\kappa = 0.44 \times (\varepsilon^{X}_{420}/\varepsilon^{7.4}_{420}) \quad (1)$$

where the extinction coefficient of measuring solution (ε^{X}_{420}) is normalized by the 420 nm ε for solvent THF ($\varepsilon^{7.4}_{420}$) and 0.44 represents the slope value of the linear plot. Although the relative interconversion between fluorescent $PMP^{\pm}$ and non-fluorescent PMP^0 with medium κ shows linear correlation according to the absorption studies, no correlation between the fluorescence intensity and κ was identified probably because the fluorescence quantum yield of $PMP^{\pm}$ depended on the medium polarity (Fig. S10, ESI†). The identical absorbance in pure methanol ($\kappa \sim 33.0$) to that of the same κ achieved by increasing the κ value from 33.0 to 55.0 and subsequently reversing to 33.0 by consecutive addition of water and THF, respectively, suggests the polarity induced reversible interconversion between PMP^0 and $PMP^{\pm}$ (Fig. S11, ESI†). The generation of the visible absorption intensity at ~420 nm due to the conversion from PMP^0 to $PMP^{\pm}$ and the subsequent change of colour from colourless to bright yellow with increasing polarity are also useful for estimating the medium polarity calorimetrically (Scheme 2A). All these observations suggest that the PMP can be utilized as a novel polarity indicator.

For detection of the interfacial polarity, a series of amphiphilic self-assembled systems of different structural and interfacial charge characteristics from one to another, such as anionic sodium dodecyl sulphate (SDS) and sodium taurocholate (STA), cationic cetrimonium bromide (CTAB) and tri-block co-polymer (TBP),[37] neutral triton X-100 (TX-100), and anionic 1,2-dimyristoyl-*sn*-glycero-3-phosphoryl-glycerol (DMPG) phospholipid have been included to show specific interface independent generality for their polarity detection (Fig. 2A). All amphiphilic molecules generate micelles in aqueous medium, whereas DMPG produces vesicles containing bilayer membrane structures (see Experimental in the ESI†). In the UV-Vis absorption spectra, irrespective of the self-assemblies, a gradual decrease in intensity at 420 nm with a concomitant increase at 330 nm was detected for PMP (5.0 μM) when increasing the concentration of any amphiphilic molecule until a saturation was observed at a particular concentration (SDS: 15.0, CTAB: 7.0, TX-100: 9.0, STA: 10.0, TBP: 0.5 and DMPG: 5.0 mM) (Fig. 2B and S12, ESI†). Such a gradual change of intensities with the increasing concentration of amphiphilic molecules indicates that an increasing amount of PMP (PMP^0 and $PMP^{\pm}$) is located at the interface and the intensity saturation justifies the absence of any residual PMP in the bulk medium. In the fluorometric studies, a gradual increase in the steady state fluorescence anisotropy values for the 500 nm band of $PMP^{\pm}$ was observed by increasing the concentration of an amphiphilic molecule until a saturation was observed, at which an identical concentration was obtained for the absorption intensity saturation, suggesting also that almost all PMP molecules were located at the interface (Fig. S13, ESI†). Probably, electrostatic interactions of self-assembled systems possessing variable interfacial charge (positive or negative) characters with $PMP^{\pm}$ possessing the opposite polarity site existed in a considerable amount, which resulted in the interface location of PMP. On the other hand, the non-ionic PMP^0 containing multiple O and N polar-centres is also intent to stay at the interface with intermediate polarity rather than at the highly polar bulk or highly non-polar interior phase (Scheme 2A),[32] although the precise depth for probe (PMP) localisation within the interface is not entirely clear.

As any absorption intensity changes due to variation of [$PMP^{\pm}$] or [PMP^0] are only dictated by the medium polarity,

 This journal is © The Royal Society of Chemistry 2016

Published on 04 May 2016. Downloaded by Jadavpur University on 24/05/2016 09:21:52.

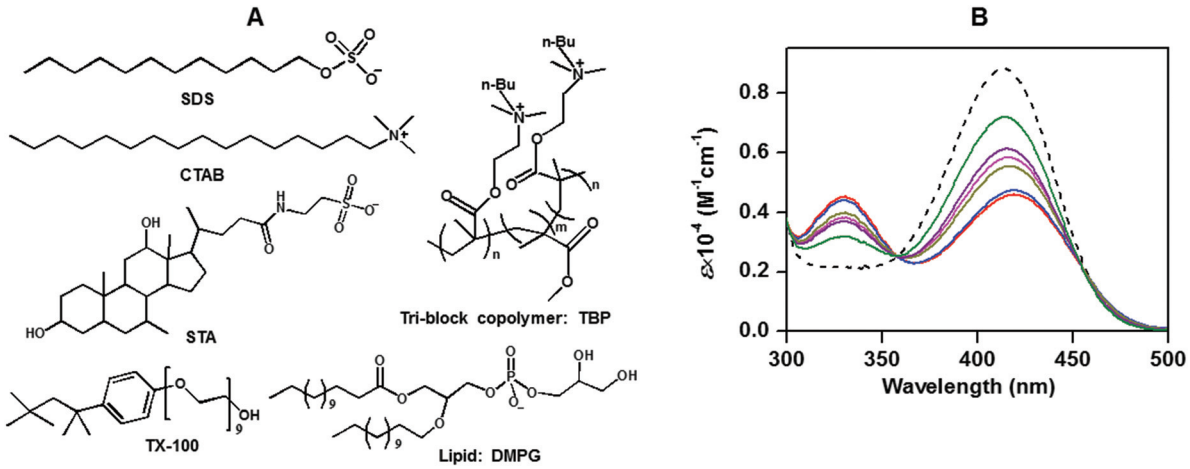

Fig. 2 (A) Different amphiphilic molecules. (B) UV-Vis absorption spectra of Schiff base PMP (5 μM) in the presence of intensity-saturated concentrations of different amphiphilic molecules in 20 mM HEPES buffer, pH 7.3, 25 °C: red, SDS (15.0 mM); blue, CTAB (7.0 mM); pink, TX-100 (9.0 mM); green, STA (10.0 mM); purple, TBP (0.5 mM); dark yellow, DMPG (5.0 mM). The spectrum in the absence of any amphiphilic molecule is depicted by black.

the difference in pH or viscosity between the interface and bulk as reported previously[32,38] may not contribute to the self-assembly induced absorbance changes. Therefore, the change of normalised ε_{420} owing to the relocation of PMP from the bulk to interface can be directly correlated with the interfacial polarity. The κ value corresponding to the deviation-saturated normalized ε_{420} according to eqn (1) represents the interfacial κ (Fig. 1B and 2B, Table 1). It is worth mentioning that the bulk polarity remains the same as that of pure buffer in the presence of self assemblies, since the overall volume occupied by the interface is extremely smaller compared to the total effective volume occupied by the bulk phase. A highly reduced interfacial κ compared to that of the bulk aqueous phase was detected for both SDS and CTAB micelles, where the interfacial κ for the anionic SDS micelle ~43.5 is close to the cationic CTAB micelle ~44.5 (Table 1). It suggests that the interface polarity does not depend on interfacial charge properties. As the interface is the separation between the highly polar aqueous phase and nonpolar micellar core, a considerable decrease of water concentration at the interface compared to the bulk phase may be responsible for such observed similar intermediate polarity between the micellar core and bulk water (Scheme 2B). However, a significant increase in polarity was detected for the TX-100 micellar interface (~53.8) compared to the polarity of the SDS or CTAB micellar interface (Scheme 2B, Table 1). It indicates that the presence of polymeric oxo-ethylene residues in TX-100 induces a greater extent of water penetration by H-bonding interaction directed towards the hydrophobic core resulting in an increase of water concentration at the interface (Scheme 2B and Fig. 2). Also, the presence of multiple polar residues besides ionic residues in both the tri-block copolymer (TBP) and lipid DMPG may be responsible for relatively higher $\kappa \sim 56.0$ and 51.2 for respective self-assemblies, similar to that of TX-100 micelles (Fig. 2, Table 1). Although both SDS and STA contain the same anionic sulphate moiety, a large increase of interfacial κ was identified for the STA micelle ~65.0 (Fig. 2, Table 1), presumably because the interface of the STA micelle with a low aggregation number (a) ~ 4–5 was more hydrated and solvent exposed compared to that of the SDS micelle with high $a \sim 80$.

Table 1 The saturation deviated normalised ε^{X}_{420} ($\varepsilon^{X}_{420}/\varepsilon^{7.4}_{420}$) for PMP in the presence of different self-assemblies in 20 mM HEPES buffer, pH 7.3, 25 °C. The interfacial dielectric constants (κ) are deduced from eqn (1)

Amphiphilic molecule	$\varepsilon^{X}_{420}/\varepsilon^{7.4}_{420}$	κ
Buffer[a]	32.3	78.7
SDS	16.9	43.5
CTAB	17.3	44.5
TX-100	21.5	53.8
STA	26.3	65.0
TBP	22.5	56.0
DMPG	20.3	51.2

[a] Pure aqueous buffer medium without any amphiphilic molecule.

In conclusion, a highly interface selective Schiff base molecule (PMP) showing polarity dependent interconversion from its non-ionic (PMP^0) to zwitterionic ($PMP^{\pm}$) form has been synthesised to evaluate the interfacial polarity for versatile self-assembled systems of different structural and interfacial charge characteristics from one another. The GSIPT leading to switchover from PMP^0 to $PMP^{\pm}$ as evident in the UV-Vis absorption studies and DFT-based theoretical calculations follows a linear correlation with κ of the medium. Although interfacial pH or viscosity is appreciably different from that of the bulk, the unchanged [$PMP^{\pm}$] or [PMP^0] with the change of pH 6.0–11.0 and/or viscosity is highly useful for detection of interfacial κ (SDS: 43.5, CTAB: 44.5, TX-100: 53.8, STA: 65.0,

Published on 04 May 2016. Downloaded by Jadavpur University on 24/05/2016 09:21:52.

tri-block-polymer TBP: 56.0 and lipid DMPG: 51.2) by utilizing the linear relationship between normalised ε_{420} (or $[PMP^{\pm}]$) and κ.

Acknowledgements

The authors gratefully acknowledge Prof. Shun Hirota of NAIST, Japan for scientific discussion. This work was supported by the Research Projects (SB/FT/CS-089/2013) (PPP), UGC (ERO) MRP (PSW-196/13-14) (AR), and UGC (ERO) MRP (PSW-197/13-14) (SD). RM and YS acknowledge UGC for the JRF fellowship.

Notes and references

1 V. Uskokovic and M. Drofenik, *Surf. Rev. Lett.*, 2005, **12**, 239.
2 M. V. Tirrell and A. Katz, *MRS Bulletin*, 2005, **30**, 700.
3 M. F. Ottaviani, A. Moscatelli, D. Desplantier-Giscard, F. Di Renzo, P. J. Kooyman, B. Alonso and A. Galarneau, *J. Phys. Chem. B*, 2004, **108**, 12123.
4 S. Forster and M. Antonietti, *Adv. Mater.*, 1998, **10**, 195.
5 G. L. Sorella, G. Strukul and A. Scarso, *Green Chem.*, 2015, **17**, 644.
6 Z. Nairoukh, D. Avnir and J. Blum, *ChemSusChem*, 2013, **6**, 430.
7 G. Stavber, M. Zupan and S. Stavber, *Synlett*, 2009, 589.
8 D. R. M. Arenas, C. A. M. Bonilla and V. V. Kouznetsov, *Org. Biomol. Chem.*, 2013, **11**, 3655.
9 C. J. F. Rijcken, O. Soga, W. E. Hennink and C. F. V. Nostrum, *J. Controlled Release*, 2007, **120**, 131.
10 N. Nishiyama, Y. Kato, Y. Sugiyama and K. Kataoka, *Pharm. Res.*, 2001, **18**, 1035.
11 P. Couvreur, F. Puisieux and N. Ano, *Adv. Drug Delivery Rev.*, 1995, **10**, 141.
12 D. D. Lasic, *Nature*, 1996, **380**, 561.
13 A. Krishnadas, I. Rubinstein and H. Onyuksel, *Pharm. Res.*, 2003, **20**, 297.
14 M. Yokoyama and M. Novel, *Biorelated Polymers and Gels*, Academic Press, San Diego, CA, 1998, p. 193.
15 J. Cladera and P. Oshea, *Biophys. J.*, 1998, **74**, 2434.
16 G. Apodaca, L. I. Gallo and D. M. Bryant, *Nat Cell Biol.*, 2012, **14**, 1235.
17 S. Kim, K. No and S. Hong, *Chem. Commun.*, 2016, **52**, 831.
18 J. Kim, J. H. Jeon, H. J. Kim, H. Lim and I. K. Oh, *ACS Nano*, 2014, **8**, 2986.
19 S. Liu, Y. Liu, H. Cebeci, R. G. Villoria, J. H. Lin, B. L. Wardle and Q. M. Zhang, *Adv. Funct. Mater.*, 2010, **20**, 3266.
20 M. Barberon, G. Dubeaux, C. Kolb, E. Isono, E. Zelazny and G. Vert, *Proc. Natl. Acad. Sci. U. S. A.*, 2014, **111**, 8293.
21 L. Voglino, T. J. McIntosh and S. A. Simon, *Biochemistry*, 1998, **37**, 12241.
22 D. Neradovic, W. L. J. Hinrichs, J. J. K. Bosch, C. F. V. Nostrum and W. E. Hennink, *Macromol. Rapid Commun.*, 1999, **20**, 577.
23 D. Neradovic, C. F. V. Nostrum and W. E. Hennink, *Macromolecules*, 2001, **34**, 7589.
24 O. Soga, C. F. V. Nostrum, A. Ramzi, T. Visser, F. Soulimani, P. M. Frederik, P. H. H. Bomans and W. E. Hennink, *Langmuir*, 2004, **20**, 9388.
25 M. S. Tunuli, M. A. Rauf and Farhataziz, *J. Photochem.*, 1984, **24**, 411.
26 C. Reichardt, *Chem. Rev.*, 1994, **94**, 2319.
27 P. Jose, C. Carrasco, D. Jacquemin, C. Laurence, A. Planchat, C. Reichardt and K. Sraidi, *J. Phys. Org. Chem.*, 2014, **27**, 512.
28 M. S. Fernandez and P. Fromherz, *J. Phys. Chem.*, 1997, **81**, 1755.
29 R. Epand and R. Kraayenhof, *Chem. Phys. Lipids*, 1999, **101**, 57.
30 P. L. Novaki and O. A. E. Seoud, *Langmuir*, 2000, **16**, 35.
31 A. S. Klymchenko, Y. Mely, A. P. Demchenko and G. Duportail, *Biochim. Biophys. Acta*, 2004, **1665**, 6.
32 Y. Sarkar, S. Das, A. Ray, S. K. Jewrajka, S. Hirota and P. P. Parui, *Analyst*, 2016, **141**, 2030.
33 S. Das, S. Biswas, S. Mukherjee, J. Bandyopadhyay, S. Samanta, I. Bhowmick, D. K. Hazra, A. Ray and P. P. Parui, *RSC Adv.*, 2014, **4**, 9656.
34 J. R. Lakowicz, in *Principles of Fluorescence Spectroscopy*, Springer, 3rd edn, 2006, ch. 6.
35 A. Kütt, I. Leito, I. Kaljurand, L. Sooväli, V. M. Vlasov, L. M. Yagupolskii and I. A. Koppel, *J. Org. Chem.*, 2006, **71**, 2829.
36 D. Robinson, N. A. Besley, P. O'Shea and J. D. Hirst, *J. Phys. Chem. B*, 2011, **115**, 4160.
37 U. Chatterjee, S. K. Jewrajka and B. Mandal, *Polymer*, 2005, **46**, 1575.
38 S. Yamaguchi, K. Bhattacharyya and T. Tahara, *J. Phys. Chem. C*, 2011, **115**, 4168.

 This journal is © The Royal Society of Chemistry 2016

NJC

PAPER

View Article Online
View Journal | View Issue

Check for updates

Cite this: *New J. Chem.*, 2017, **41**, 8536

Interfacial pH and polarity detection of amphiphilic self-assemblies using a single Schiff-base molecule†

Rini Majumder,[a] Yeasmin Sarkar,[a] Sanju Das,[ab] Ambarish Ray[b] and Partha Pratim Parui*[a]

The interfacial pH and polarity are two highly interrelated parameters in amphiphilic self-assembled systems. The hydronium ion (H_3O^+) concentration and/or the pH value near the water/oil separating interface may change significantly due to large polarity gradients between water- and oil-exposed surfaces within the interface. Therefore, for precise detection of these two properties (pH and polarity) at a specific interfacial depth, a similar interfacial location of the same probe is a prerequisite. In this regard, we have synthesized a new interface-interacting Schiff-base (SBOH-Z-SBOH) molecule to detect both the interfacial pH and polarity of various amphiphilic self-assembled micelles and vesicles at a similar interfacial location. SBOH-Z-SBOH, existing mostly as a non-ionic species ($SBOH^0$-Z-$SBOH^0$) in nonpolar solvents, exhibits an exclusive solvent polarity-dependent linear interconversion equilibrium with its partially charge separated zwitterionic form ($SBOH^0$-Z-$SBOH^{\pm}$) as the polarity of the medium increases, which makes it useful to detect the polarity. Additionally, the solvent pH-dependent conversion of both $SBOH^0$-Z-$SBOH^0$ and $SBOH^0$-Z-$SBOH^{\pm}$ into the deprotonated di-anionic species (SBO^--Z-SBO^-) allows it to monitor the pH. We found that the interfacial dielectric constant (~44.0–54.0) differs substantially from that of the bulk aqueous medium depending on the amphiphilic system. On the other hand, unlike the neutral interface of titron X-100 (TX-100) micelles or 1,2-dioleoyl-*sn*-*glycero*-3-phosphocholine (DOPC) unilamellar vesicles (ULVs), a large positive pH-deviation of ~1.8 and 2.2 units from the bulk to the interface was identified for cationic cetrimonium bromide (CTAB) micelles and dimethyldioctadecylammonium bromide (DDAB) ULVs, respectively. The present study provides a unique and simple Schiff-base molecule to monitor the pH and polarity at similar interfacial depths for amphiphilic self-assembled systems.

Received 12th April 2017,
Accepted 1st July 2017

DOI: 10.1039/c7nj01222e

rsc.li/njc

Published on 04 July 2017. Downloaded by Jadavpur University on 18/08/2017 14:10:31.

Introduction

The cellular membrane interface organizes an enormous number of complex biological reactions, which play various essential roles in our life processes. Most of these biochemical reactions at the membrane interface, such as membrane transport,[1] ion transport across the membrane,[2–4] insertion of proteins/molecules into the membrane and their translocation across the membrane,[5,6] are highly interrelated with the membrane subdomain structural identity. However, in most cases, the mechanisms for the membrane's structure-dependent reactivities are not completely understood. The major difficulties appear primarily for the highly complicated structure of the cellular membrane interface. Such structural complexity is often generated due to the micro-heterogeneous distribution of different kinds of lipids and protein molecules.[7–10] Nevertheless, it has also been identified that these membrane reactivities are profusely affected by changes in intercellular physiochemical parameters, such as pH and polarity.[11–15] In this context, we strongly believe that distinct membrane reactivities originate from the membrane structure-dependent manipulation of the interfacial pH and polarity values. Therefore, the accurate detection of the interfacial pH as well as the polarity is essential to identify various biochemical events controlled by the interfacial pH and/or polarity of cellular membranes.

It has frequently been observed that amphiphilic self-assembled micelles and bilayer lipid vesicles can be exploited as a model of a cellular membrane to explain various interfacial biological processes.[16–19] However, the monitoring of the interfacial properties themselves for self-assemblies is extremely

[a] *Department of Chemistry, Jadavpur University, Kolkata 700032, India. E-mail: parthaparui@yahoo.com; Fax: +91-33-24146223; Tel: +91-9433490492*
[b] *Department of Chemistry, Maulana Azad College, Kolkata 700013, India*

† Electronic supplementary information (ESI) available: Additional spectroscopic and analytical information. See DOI: 10.1039/c7nj01222e

 This journal is © The Royal Society of Chemistry and the Centre National de la Recherche Scientifique 2017

Published on 04 July 2017. Downloaded by Jadavpur University on 18/08/2017 14:10:31.

difficult due to the highly complex micro-heterogeneous compartmentalization, including uncertainty regarding the bulk phase contribution. A number of studies have indicated a discrepancy in the interfacial properties from the bulk value in amphiphilic self-assembled systems,[20–22] although their precise estimation has rarely been addressed. Recently, Tahara and co-workers designed a heterodyne-detected electronic sum frequency generation spectroscopic method to estimate the acid/base interconversion properties at ionic micelles and vesicles, and monitored the interfacial pH values.[23,24] These studies showed that the interfacial pH differs adequately from the bulk pH.

Strategically designed Schiff-base molecules, due to their enormous applicability,[25–28] could be utilized to evaluate the interfacial pH/polarity for amphiphilic self-assembled systems. We have recently introduced a new interfacial pH/polarity monitoring method for biologically important micelles and vesicles by utilizing interface-interacting Schiff-base molecular probes.[29,30] We showed that the pH/polarity substantially changes at the interface from that of the bulk phase. The inherent simplicity of this detection technique may be highly effective for complicated biological interfaces. However, the pH and polarity are two highly interrelated physiochemical parameters at the interface. A minute change in the interfacial polarity may affect the pH value to a considerable extent, probably due to the difference in the H^+ ion conducting ability of the H_3O^+ ion.[31–34] As the interface separates hydrocarbons (hydrophobic) from the polar aqueous medium, the interfacial polarity may be expected to change substantially with a small alteration of the depth along the interfacial cross-section.[35,36] Therefore, the detection of pH and polarity at a similar interfacial depth is essential. To eliminate discrepancies arising due to the difference in probe location depth for the pH and polarity, we propose a single optical probe for dual detection purposes. Herein, a simple interface-interacting Schiff-base molecule containing two identical phenol-conjugated-imine functional groups is synthesized for the detection of interfacial pH and polarity. The deviation in the pH/polarity-induced interconversion equilibrium among various molecular forms of the Schiff-base molecule from the bulk to the interface is exploited to monitor the interfacial pH and polarity for various self-assembled micelles and vesicles. Under acidic-to-neutral bulk pH conditions, the polarity-dependent interconversion equilibrium between the non-ionic and the zwitterionic forms for the probe molecule can be utilized to estimate the interfacial polarity. On the other hand, the interfacial pH value and its deviation from the bulk pH value are detected from the pH-dependent interconversion from the non-ionic/zwitterionic species to the deprotonated anionic species for the probe molecule.

Experimental

General experimental methods

The lipids dimethyldioctadecylammonium bromide (DDAB) and 1,2-dioleoyl-*sn-glycero*-3-phosphocholine (DOPC) were purchased from Avanti Polar Lipids (USA). The organic solvents, methanol, ethanol and tetrahydrofuran (THF), from Sigma-Aldrich (USA) were purified by standard methods. Milli-Q Millipore® 18.2 MΩ cm water was used to prepare the buffer solutions as well as the mixed aqueous buffer for spectroscopic measurements. To achieve specific pH values within pH 5.5–12.5, different 20 mM buffer compositions were used for the UV-vis absorption and fluorescence samples: citric acid/Na_2HPO_4 buffer for pH 5.5–7.0, Tris–HCl for pH 7.0–9.0 and carbonate/bicarbonate for pH 9.0–12.0. The pH of the buffer was tuned by adding the required amount of either ~1.0 M NaOH or 1.0 M HCl solution, and checked using a Systronics digital pH meter (Model No. 335). For spectroscopic studies, the Schiff-base probe was mixed with a definite amount of different analytes in 20 mM of specific buffer, with adjustment of the final pH value with addition of either 0.1 M NaOH or 0.1 M HCl if required. The medium dielectric constant and refractive indices for various solvent mixtures were estimated as reported previously.[37,38] The ^{1}H NMR spectra were acquired in $CDCl_3$ (Sigma-Aldrich, USA) with a Bruker 300 MHz NMR spectrophotometer using tetramethylsilane (δ = 0) as an internal standard. However, the ^{13}C NMR spectra were acquired in DMSO-d_6 (Sigma-Aldrich, USA) and recorded on the same instrument operating at 75 MHz. The ESI-MS$^+$ experiment was performed on a Waters Qtof Micro YA263 mass spectrometer in positive mode.

Synthesis of the Schiff-base molecule

For synthesis of the Schiff-base molecular probe, *p*-cresol and 1,2-diaminopropane (DAP) of analytical grade were procured from Sigma-Aldrich (USA) and were used without further purification. The phenolic aldehyde molecule, 2-hydroxy-3-(hydroxymethyl)-5-methylbenzaldehyde (HHMB), was prepared with a yield of 62% with respect to *p*-cresol as the staring material following a standard literature procedure as reported earlier.[39] A pure product was obtained from the crude product by column chromatography followed by rotary evaporation, and further recrystallized from toluene–chloroform mixed solvents (8 : 2, v/v) resulting in light yellow colored solid HHMB. For the synthesis of the Schiff-base molecule (SBOH-Z-SBOH), DAP (0.085 mL, 1 mmol) was added drop-wise with constant stirring to a methanolic solution of HHMB (0.322 g, 2.0 mmol), and a few drops of acetic acid were further added to the reaction mixture. The mixture was refluxed for 2 h at 40 °C and then filtered. The filtrate was then evaporated under reduced pressure to obtain the crude product. This was purified by column chromatography followed by rotary evaporation to obtain the deep yellow solid product, which was dried over $CaCl_2$ under vacuum. Structural analyses were performed by ^{1}H-NMR measurement. ^{1}H NMR ($CDCl_3$, 300 MHz): δ = 1.41 (d, J = 5.7 Hz, 3H, –$\underline{CH_3}$), 2.26 (s, 6H, 2Ar–$\underline{CH_3}$), 2.33 (s, 1H, N–$\underline{CH}$), 3.66–3.71 (br d, 1H, N–C$\underline{H_a}$H), 3.84–3.86 (br d, 1H, N–CH$\underline{H_b}$), 4.72 (d, J = 4.2 Hz, 4H, 2$\underline{CH_2}$–OH), 6.87 (s, 1H, Ar–H_f), 6.97 (s, 1H, Ar–H_c), 7.25 (s, 2H, Ar– (H_d, H_d')), 8.27 (s, 1H, imine-$\underline{H}$), 8.31 (s, 1H, imine-$\underline{H}$), 11.18 (s, 2H, 2Ar–O$\underline{H}$) ppm. ^{13}C-NMR (DMSO-d_6, 75 MHz): 20.3, 57.9, 64.2, 65.1, 117.7, 126.8, 129.9, 130.2, 131.5, 155.8, 156.0, 165.7, 167.6 ppm (see details in ESI,† Fig. S1). ESI-MS+ in water: m/z calcd for SBOH-ZSBOH: 371.4485, found: 371.4112 (see details in ESI,† Fig. S2).

Published on 04 July 2017. Downloaded by Jadavpur University on 18/08/2017 14:10:31.

Unilamellar vesicle (ULV) preparation

The required amount of dimethyldioctadecylammonium bromide (DDAB) or 1,2-dioleoyl-*sn-glycero*-3-phosphocholine (DOPC) was dissolved in 1.0 mL of chloroform. The solvent chloroform was removed with a rotary evaporator at room temperature to obtain a thin lipid film on the wall of a round-bottom flask. Any residual chloroform in the thin lipid film was completely removed *in vacuo* for 3 h. The appropriate 20 mM buffer solution was added to the lipid film at 40 °C for hydration of the film. The solution was vortexed for 2 min to complete dissolution of the lipids. Seven cycles of freeze-and-thaw were performed between −196 and 50 °C to produce giant multilamellar vesicles. To obtain large unilamellar vesicles (ULVs), the liposome dispersion was extruded 15 times through two stacked polycarbonate membrane filters (Whatman) of pore size 100 nm equipped in a Liposo Fast mini extruder (Avanti, USA). For spectroscopic measurements, the resultant ULV solution was diluted with an appropriate amount of buffer to a definite lipid concentration.

UV-vis absorption and fluorescence studies

The UV-vis optical absorption and fluorescence measurements were performed with a UV-2450 spectrophotometer (Shimadzu, Japan) and a PerkinElmer LS-55 spectro-fluorimeter (PerkinElmer, USA), respectively. Quartz cells with 1 cm path lengths were used for the absorption and fluorescence measurements. The fluorescence quantum yield (ϕ_F) of the different molecular species of SBOH-Z-SBOH were estimated by the standard method using eqn (1), where 9,10-diphenylanthracene in ethanol was used as a ref. 40, and $\phi_F^r = 0.95$.

$$\phi_F^s = [A_r F_s n_s^2 / A_s F_r n_r^2]\phi_F^r \quad (1)$$

where A is the absorbance at a particular excitation wavelength, F represents the integrated fluorescence area and n is the refraction index of the solvent. The subscripts refer to the reference (r) or sample (s) compound. By using the above eqn (1), the ϕ_F values for SBOH-Z-SBOH in the presence and absence of amphiphilic systems were estimated as follows: ~0.002 at pH 7.0 and 0.11 at pH 11.5 without amphiphilic molecules; ~0.25 at pH 10.0 in the presence of CTAB/DDAB; ~0.21–0.24 at pH 12.5 in the presence of TX-100/DOPC. Time-resolved fluorescence studies were carried out by using time correlated-single photon-counting (TCSPC) techniques. A nanosecond diode (nano-LED; IBH, U.K.) as the light source at 450 nm was used as the excitation source and a TBX4 detection module (IBH, U.K.) coupled with a special Hamamastu photomultiplier tube (PMT) was used for the detection of the fluorescence decays. The time resolution achievable with the present setup following deconvolution analysis of the fluorescence decays was ~100 ps. The fluorescence decays were recorded with a vertically polarized excitation beam and fluorescence was collected at the magic angle of 54.7°. The solutions were filtered through a Millipore membrane filter (0.22 μm) before spectroscopic measurements. All measurements were repeated at least three times to check the reproducibility.

Binding studies

The ULVs of the DDAB or DOPC lipids (3.0 or 4.0 mM, final concentration) in 20 mM buffer solution were mixed with 5.0 μM SBOH-Z-SBOH. A 100 K MW cut-off centrifugal mini-filter (Amicon Ultra-0.5 mL Centrifugal Filters, Millipore) was used to collect the unbound SBOH-Z-SBOH in the bulk phase. About 200 μL of the filtrate was collected from the initial 400 μL liposome solution after centrifugation for about 2 min at 5000*g*. The amount of residual SBOH-Z-SBOH in the filtrate was estimated using the UV-vis absorption spectra, and the amount of unbound SBOH-Z-SBOH was calculated (see the ESI† for details).

Theoretical calculations

Density functional theory (DFT) and time-dependent DFT (TD-DFT) calculations were performed using the Gaussian 09 program.[41] Geometry optimization based on the most probable structure for various molecular forms of SBOH-Z-SBOH was performed using the B3LYP exchange–correlation functional. The 6-31G++(d,p) basis set was used for the atoms and the geometries were optimized in the gas phase. The global minima of all the species were confirmed by the positive vibrational frequencies. To investigate the electronic properties of the singlet excited state in water, TD-DFT calculations were applied using the optimized geometries of the ground states (S_0) for the respective species in aqueous solution by adapting the conductor polarized continuum model (CPCM). The excitation energies, respective oscillator strengths and extension coefficients (ε) of the optical absorption for the respective species were evaluated.

Results and discussion

SBOH-Z-SBOH acid/base equilibrium in buffer to measure pH

The SBOH-Z-SBOH acid/base equilibrium was utilized to measure the pH. The phenolic-OH deprotonation reaction for the newly synthesized Schiff-base molecule (SBOH-Z-SBOH) containing two identical phenol-conjugated-imine moieties was investigated by pH-metric titration (Scheme 1). Recently, we have observed that the 320 nm UV-vis absorption band for a similar phenol-conjugated-imine moiety gradually depletes with increasing pH of the medium, along with the appearance of a 400 nm band, due to deprotonation of the phenol moiety ($pK_a \sim 8.7$).[29] Although SBOH-Z-SBOH contains two closely related phenol moieties, the co-existence of the ~420 and 320 nm absorption intensities even at an acidic pH of ~5.5 indicates a substantial fraction of both the phenol and phenolate moieties (Fig. 1A). However, the unchanged 420 to 320 nm intensity ratio within pH 5.5 to 8.0 also shows that the phenol-to-phenolate ratio did not vary in this pH range (Fig. 1). This result suggests that any one of the two closely related phenol moieties in SBOH-Z-SBOH is probably susceptible to conversion into its phenolate form to generate 420 nm absorbances in the pH ~ 5.5–8.0 range (Scheme 1A). According to our DFT-based theoretical calculation (*vide infra*), it has been proposed that the large polarity of the aqueous medium induces an intramolecular ground state proton transfer reaction (IGSPT) from the phenolic-OH to its adjacent imine-N in SBOH-Z-SBOH. However, the other

 This journal is © The Royal Society of Chemistry and the Centre National de la Recherche Scientifique 2017

Published on 04 July 2017. Downloaded by Jadavpur University on 18/08/2017 14:10:31.

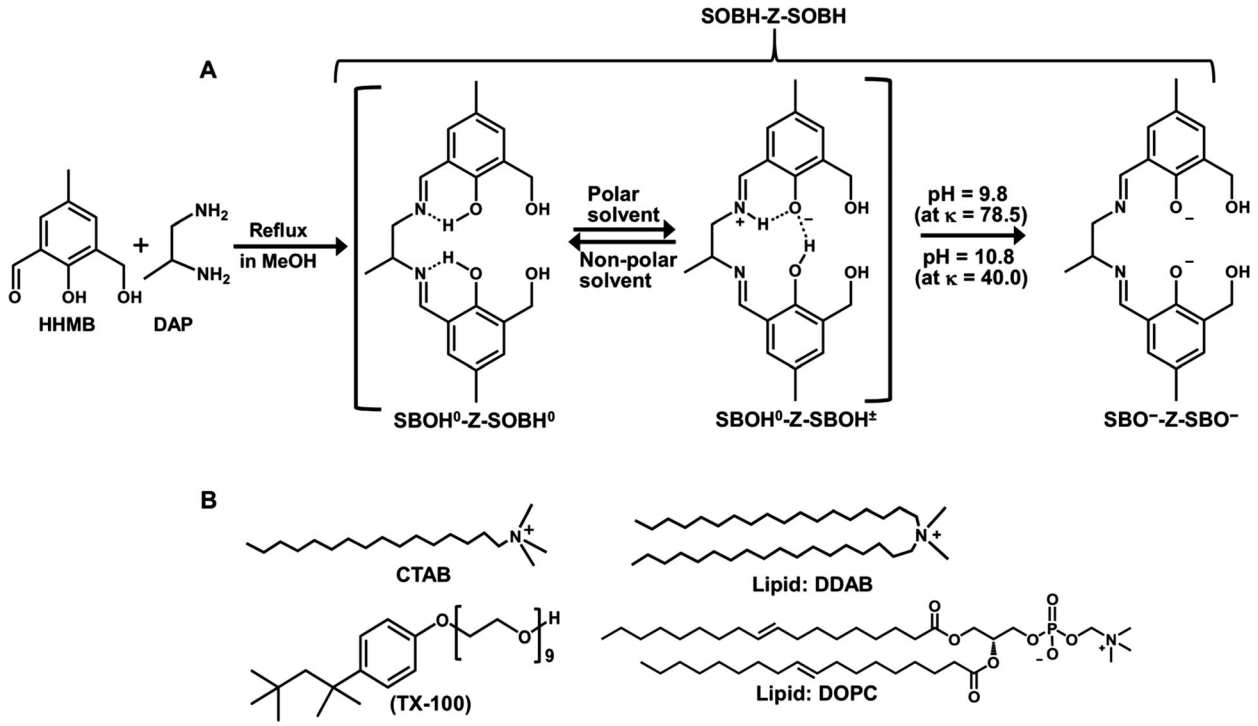

Scheme 1 (A) Synthesis and solvent polarity/pH-dependent different molecular forms of the Schiff base molecule (SBOH-Z-SBOH). (B) Different amphiphilic molecules.

–SBOH moiety exists in its protonated form to produce a partially charge separated zwitterionic species ($SBOH^0$-Z-$SBOH^{\pm}$) (Scheme 1A). This partial zwitterion form most probably predominates in an aqueous medium as a result of the large solute–solvent electrostatic stabilization effect.[30]

On further increasing the buffer pH (>8.5), the 420 nm absorption band was gradually blue shifted maximally up to 395 nm with an increase in its intensity and subsequent depilation of the 320 nm band, until intensity saturation was observed at pH ~ 11.0 (Fig. 1A). The absorption changeover with two different isosbestic points at ~345 and 425 nm indicates that the di-anionic (SBO^--Z-SBO^-) species with two identical anionic phenolate-conjugated-imine moieties (–SBO^-) was generated due to simultaneous deprotonation reactions from both the non-ionic –$SBOH^0$ and zwitterionic –$SBOH^{\pm}$ moieties in SBOH-Z-$SBOH^{\pm}$ (Fig. 1A and Scheme 1A). Unlike phenolic-OH deprotonation from a single phenol-conjugated-imine moiety-containing similar Schiff-base molecule,[29] the multiple proton dissociation reactions from $SBOH^0$-Z-$SBOH^{\pm}$ to form SBO^--Z-SBO^- require more basic pH (pK_a ~ 9.7)[42,43] (Fig. 1B). Nevertheless, the identical absorption spectrum at pH ~ 8.5 to that at the same pH achieved by decreasing the SBOH-Z-SBOH (5.0 μM)-containing buffer pH from 12.0 to 8.5 by addition of dilute HCl suggests a medium pH-induced reversible interconversion between the $SBOH^0$-Z-$SBOH^{\pm}$ and SBO^--Z-SBO^- species (Fig. S3, ESI†).

Fluorometric pH-titration for SBOH-Z-SBOH was also performed in buffer medium (Fig. 2). The weak fluorescence intensity at ~500 nm (ϕ_F ~ 0.002) due to excitation of the zwitterionic

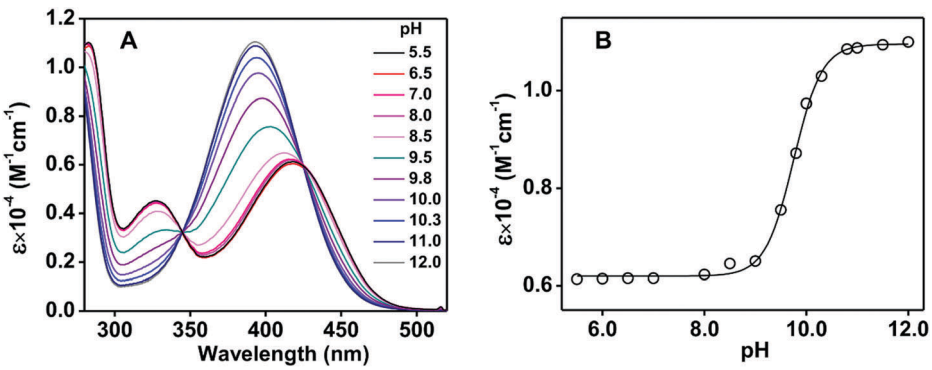

Fig. 1 (A) UV-vis absorption spectra of the Schiff-base molecule SBOH-Z-SBOH (5.0 μM) at different pH (5.5–12.0) values in different 20 mM buffers: sodium citrate/sodium phosphate, pH 5.5–7.5; Tris–HCl, pH 8.0–9.0; and sodium carbonate/bi-carbonate, pH 9.0–12.0. (B) Molar extinction coefficient at the absorption intensity maxima (395–420 nm) (ε) at different pH values.

Published on 04 July 2017. Downloaded by Jadavpur University on 18/08/2017 14:10:31.

moiety (–SBOH$^{\pm}$) by 420 nm light remains invariant with a change in buffer pH from 5.5 to 8.0. Meanwhile, the non-ionic –SBOH^{0} moiety is non-emissive in nature ($\phi_F \sim 0.0$), since not even a trace amount of fluorescence intensity was identified with 320 nm excitation (Fig. 2A). However, the generation of SBO^{-}-Z-SBO^{-} at a highly basic pH of ~11.0 results in a large increase in intensity ($\phi_F \sim 0.11$). In the fluorescence transient decay studies, the excited state fluorescence lifetime (τ_F) value of ~0.5 ns for the –SBOH$^{\pm}$ moiety at a low pH of ~7.0 was enhanced by an order of magnitude to ~4.8 ns due to its conversion into an –SBO^{-} moiety at pH ~ 11.0 (Fig. 2B and Table S1, ESI†). On the other hand, the bi-exponential transient decay nature at a pH close to the acid/base interconversion pK_a of ~9.7 suggests the co-existence of both the SBOH^{0}-Z-SBOH$^{\pm}$ and the SBO^{-}-Z-SBO^{-} species. The fluorescence studies also suggest that the SBOH-Z-SBOH molecules mostly exist as SBOH^{0}-Z-SBOH$^{\pm}$ at pH 5.5–8.0, and convert gradually into the SBO^{-}-Z-SBO^{-} species with increasing pH of the medium.

As fluorescence properties are highly influenced by different environmentally controlled physicochemical parameters (polarity, viscosity),[44,45] the pH-dependent interconversion equilibrium among various molecular forms of SBOH-Z-SBOH was monitored by UV-vis absorption spectroscopy to determine the pH (Fig. 1B). However, to estimate the interfacial pH for different amphiphilic self-assembled systems, the measurement of the interfacial polarity and subsequently the change in the acid/base interconversion pK_a for SBOH-Z-SBOH due to the difference in polarity from the bulk to the interface is essential. To estimate the polarity/dielectric constant at a similar interfacial location/depth to that of the pH sensing molecule (SBOH-Z-SBOH), the investigations were performed by utilizing the same probe molecule (SBOH-Z-SBOH).

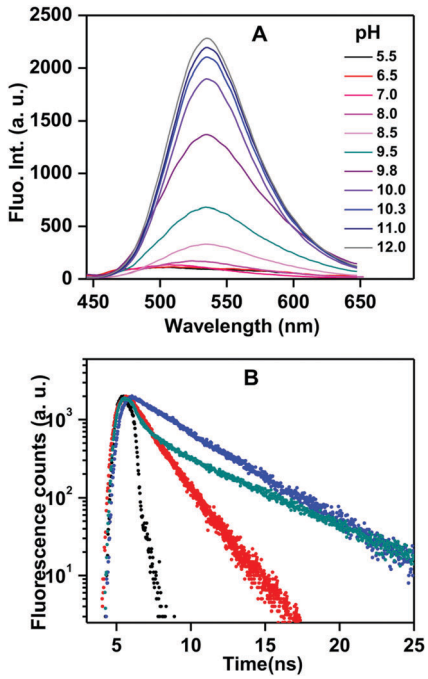

Fig. 2 (A) Steady state fluorescence spectra of SBOH-Z-SBOH (5.0 μM) at different pH (5.5–12.0) values for 400 nm excitation. (B) Time resolved emission decay curves at different pH values: pH 7.0 (red); pH 9.8 (dark cyan); pH 11.0 (blue). The excitation and emission wavelengths were 450 and 530 nm, respectively. The scattering profile is represented in black.

Polarity-dependent different molecular forms of SBOH-Z-SBOH: estimation of dielectric constant

The dielectric constant (κ) or polarity can be estimated from the solvent polarity-dependent changes in the absorption profile of the SBOH-Z-SBOH in mixed THF/buffer medium at pH 5.5–8.0. The 420 nm UV-vis absorption intensity for the zwitterionic moiety (–SBOH$^{\pm}$) in SBOH^{0}-Z-SBOH$^{\pm}$ was found to decrease gradually with increasing solvent κ. The equivalent increase in the 320 nm intensity while maintaining the 365 nm isosbestic absorption suggests conversion from the –SBOH$^{\pm}$ to –SBOH^{0} form (Fig. 3A). Most probably, inadequate solute–solvent electrostatic stabilization is responsible for converting –SBOH$^{\pm}$ into its non-ionic –SBOH^{0} form *via* reverse-IGSPT reaction to form the SBOH^{0}-Z-SBOH^{0} species at a decreased medium polarity. In the fluorometric studies, the 500 nm fluorescence band for the –SBOH$^{\pm}$ moiety in SBOH^{0}-Z-SBOH$^{\pm}$ was also observed to decrease gradually with the decrease of the solvent κ (Fig. S4, ESI†). This result supports the proposed formation of SBOH^{0}-Z-SBOH^{0} containing two non-fluorescent –SBOH^{0} moieties. It is worth mentioning that the extent of spectral changeover at a particular THF/buffer ratio in the mixed medium did not depend on the medium pH in the range of 5.5–8.0 (Fig. S5, ESI†). Moreover, the relative 420 to 320 nm band intensity did not vary with a change in solvent composition, H-bonding character or viscosity without varying the κ value (Fig. S6 and S7, ESI†). Also, the unchanged UV-vis spectra in methanol solvent ($\kappa \sim 33.0$) to that at the same κ achieved by increasing the κ value from 33.0 to 55.0 and subsequently reversing it back to 33.0 by consecutive addition of water and THF, respectively, also suggests the polarity-induced reversible interconversion between SBOH^{0}-Z-SBOH$^{\pm}$ and SBOH^{0}-Z-SBOH^{0} (Fig. S8, ESI†). All of these results strongly suggest that the interconversion equilibrium between SBOH^{0}-Z-SBOH^{0} and SBOH-Z-SBOH$^{\pm}$ depends exclusively on the polarity of the medium. Therefore, the probe (SBOH-Z-SBOH) is highly effective for the detection of interfacial polarity for various amphiphilic self-assembled systems, in spite of the large differences in pH and/or viscosity between the bulk and the interface. Importantly, we identified a linear correlation between the normalized ε at 420 nm (ε_{420}) and the medium κ (Fig. 3B).

$$\varepsilon^{X}_{420}/\varepsilon^{8.0}_{420} = 0.42 \times \kappa - 1.8 \quad (2)$$

where the extinction coefficient of the measuring solution (ε^{X}_{420}) is normalized relative to the 420 nm ε for the solvent THF ($\varepsilon^{8.0}_{420}$). The 0.42 and −1.8 represent the slope and intercept, respectively, for the linear plot. The unknown κ can be estimated using the linear correlation according to eqn (2).

DFT-based theoretical calculation

Structural elucidation for the different molecular forms of the Schiff-base molecule (SBOH-Z-SBOH) identified in the spectroscopic studies was performed by DFT-based theoretical calculation with Gaussian 09.[41] The most probable ground state geometries

 This journal is © The Royal Society of Chemistry and the Centre National de la Recherche Scientifique 2017

Published on 04 July 2017. Downloaded by Jadavpur University on 18/08/2017 14:10:31.

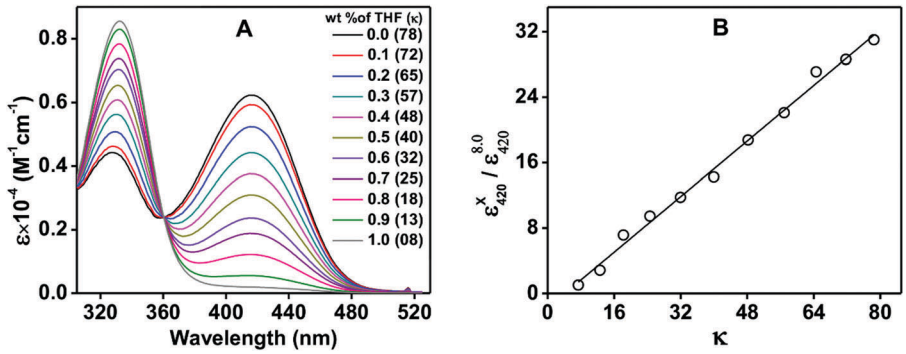

Fig. 3 (A) UV-vis absorption spectra of the Schiff-base molecule SBOH-Z-SBOH (5.0 μM) at different dielectric constants (κ) (8.0–78.5) in buffer/THF mixed medium at pH 7.0. (B) Normalized molar extinction coefficients at 420 nm (ε^{X}_{420}) (normalized by dividing the molar extinction coefficient at 420 nm for the κ of THF ($\varepsilon^{8.0}_{420}$)) plotted against κ.

for the non-ionic ($SBOH^0$-Z-$SBOH^0$), partially zwitterionic ($SBOH^0$-Z-$SBOH^{\pm}$) and di-anionic (SBO^--Z-SBO^-) species were optimized (Fig. 4A). The TD-DFT calculation of the optimized geometry for each species was performed to obtain different UV-vis absorption parameters due to ground singlet (S_0) to excited singlet (S_1) state electronic transition. The excitation energies, oscillator strengths (f), and calculated molar extinction coefficients (ε_C) for the different molecular species are shown in Table S2, ESI.† On changing $SBOH^0$-Z-$SBOH^0$ to $SBOH^0$-Z-$SBOH^{\pm}$, the calculated ε (ε_C = 9.5 × 10^3 M^{-1} cm^{-1}) for the 315 nm vertical electronic transition was decreased to about 40% (~5.8 × 10^3 M^{-1} cm^{-1}) along with the appearance of a new low energy transition at ~385 nm (ε_C ~ 6.6 × 10^3 M^{-1} cm^{-1}). Such spectral changeover is nicely correlated with the experimental 420 nm intensity generation by reducing the 330 nm band intensity (~50%) due to change of the solvent polarity from a highly polar aqueous medium to a non-polar THF medium (Fig. 4B and Table S2, ESI†). The results justify our proposed structural assignment for the $SBOH^0$-Z-$SBOH^0$ and $SBOH^0$-Z-$SBOH^{\pm}$ molecular forms of SBOH-Z-SBOH (*vide supra*). On the other hand, the experimental UV-vis spectral shift from 420 to 395 nm by increasing the aqueous buffer pH from 8.0 to 11.0 was also nicely correlated with the calculated imine deprotonation-induced ~20 nm blue shift (390 to 370 nm) for the phenolate moiety from $SBOH^0$-Z-$SBOH^{\pm}$ to SBO^--Z-SBO^- (Fig. 4B). Similar to the pH-metric studies, about twice the calculated ε_C enlargement is observed for the 370 nm transition of $SBOH^0$-Z-$SBOH^{\pm}$ compared to the 390 nm intensity for SBO^--Z-SBO^-, which indicates the similar magnitude of the ε_C value between the –$SBOH^{\pm}$ and –SBO^- moiety (Table S2, ESI†). All of these results support our structural consideration of various molecular forms of SBOH-Z-SBOH.

Interaction of SBOH-Z-SBOH with amphiphilic self-assemblies

The UV-vis absorption spectroscopic method was utilized to monitor the interaction of SBOH-Z-SBOH with various amphiphilic micelles (CTAB, SDS, TX-100) and unilamellar vesicles (ULVs) (DDAB, DOPC) containing various interfacial charges in an aqueous buffer medium (Fig. 5). The 420 nm absorption intensity of SBOH-Z-SBOH decreases gradually with a concomitant

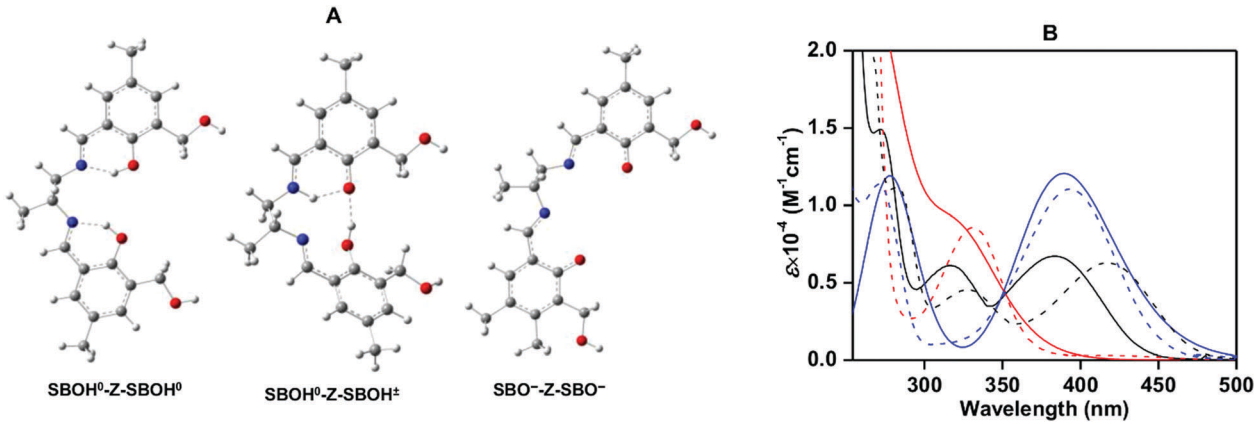

Fig. 4 (A) Optimized geometries for different molecular forms of the Schiff-base molecule ($SBOH^0$-Z-$SBOH^0$, $SBOH^0$-Z-$SBOH^{\pm}$ and SBO^--Z-SBO^-) obtained from DFT calculations (color code: white, H; gray, C; blue, N; and red, O). H-bonding is denoted by a single broken line. (B) Theoretically calculated UV-vis absorption spectra for the different molecular species of the Schiff-base (SBOH-Z-SBOH): $SBOH^0$-Z-$SBOH^0$, red; $SBOH^0$-Z-$SBOH^{\pm}$, black; SBO^--Z-SBO^-, blue. The pH/polarity-dependent experimental UV-vis spectra (broken) are depicted for comparison: red, in THF solvent; black, pH 9.8; and blue, pH 12.0.

Published on 04 July 2017. Downloaded by Jadavpur University on 18/08/2017 14:10:31.

increase in the 320 nm intensity following the addition of increasing concentrations of different amphiphilic systems at pH 7.0 until saturation of the intensity was identified (CTAB: 5.0, DDAB: 3.0, TX-100: 5.0 and DOPC: 4.0 mM) (Fig. S9, ESI†). For different amphiphilic molecules, the identical 365 nm isosbestic wavelength indicates that the partially zwitterionic $SBOH^0$-Z-$SBOH^{\pm}$ form changes into the corresponding non-ionic $SBOH^0$-Z-$SBOH^0$ form with the change of the probe location from the bulk to the interface (Fig. S9, ESI†). The intensity saturation in the presence of a definite concentration of amphiphilic molecules indicates that almost all of the SBOH-Z-SBOH molecules are involved in interactions with the self-assembled system.[29,30] To identify the precise probe location environment within the w/o interface, time-dependent fluorescence anisotropic measurements were performed (Fig. S10, ESI†).[46,47] The cationic CTAB micelles and DDAB ULVs induced a large increase in the correlation time (τ_c) from ~0.5 to 2.0 ns at pH 10.5, which suggests that SBOH-Z-SBOH localizes in the ULV/micellar environment with restricted molecular motion (Table S3, ESI†). Presumably, SBOH-Z-SBOH in its ionic molecular form interacted strongly with the cationic polar head-groups of the amphiphilic systems to locate at the interfacial Stern layer. However, the neutral TX-100/DOPC self-assembled system induced a comparatively small increase in the τ_c value from ~0.5 to 1.0 ns. Most probably, the probe is involved in weak electrostatic interaction with the non-ionic micellar/ULV interfaces (Table S3, ESI†). In fact, the binding of SBOH-Z-SBOH with DDAB vesicles was investigated by determining the residual SBOH-Z-SBOH fraction in the bulk phase in the presence of vesicles. About 90–95% of the SBOH-Z-SBOH molecules were attached to the ULVs in the solution containing 5.0 μM SBOH-Z-SBOH and 3.0 mM DDAB or DOPC ULVs (Fig. S11, ESI†). These results suggest that most of the SBOH-Z-SBOH molecules were bound/located specifically at the Stern layer for the different self-assembled systems.

To observe the effect of interfacial SBOH-Z-SBOH binding on its pH-induced proton dissociation interconversion equilibrium, pH-metric titrations with SBOH-Z-SBOH (5.0 μM) were performed in the presence of absorption saturated concentrations of different self-assembled systems. The CTAB/DDAB-induced intensity change from 320 and 420 nm to 390 nm shows that more SBO^--Z-SBO^- is formed by the simultaneous deprotonation of $-SBOH^{\pm}$ and $-SBOH^0$ moieties in $SBOH^0$-Z-$SBOH^{\pm}$ and/or $SBOH^0$-Z-$SBOH^0$ (pK_a ~ 8.9 for CTAB and ~8.6 for DDAB) (Fig. 6). On the other hand, in comparison with buffer solution, a relatively higher interconversion pK_a (~11.5) was detected for neutral TX-100/DOPC (Fig. 6). However, similar studies with anionic self-assembled systems (SDS micelles) exhibit an unchanged absorption spectrum for almost the entire pH region (5.5–12.0), except for a small change at pH 12.5 (Fig. S12, ESI†). All the results clearly suggest that interfacial charge character plays an essential role in the SBOH-Z-SBOH proton dissociation equilibrium.

Determination of the interfacial pH and polarity at similar interfacial depths for different self-assembled systems

Our studies have revealed that SBOH-Z-SBOH exists mostly in the partially zwitterionic ($SBOH^0$-Z-$SBOH^{\pm}$) form in aqueous medium (pH 5.5–8.0), but gradually converts into non-ionic $SBOH^0$-Z-$SBOH^0$ by maintaining linearity with a decrease in solvent polarity or an increase in the ratio of nonpolar solvent in the mixed aqueous medium (Fig. 3A). Notably, the highest pH value to observe such a solvent polarity-dependent exclusive $SBOH^0$-Z-$SBOH^{\pm}$ to $SBOH^0$-Z-$SBOH^0$ equilibrium increases from ~8.0 to 9.5 with a decrease in solvent κ from 78.5 (aqueous medium) to ~40.0 (ethanol/water mixture) (Fig. S13, ESI†). With a further increase in pH from the above value, the di-anionic SBO^--Z-SBO^- species was produced gradually by deprotonation from $SBOH^0$-Z-$SBOH^0$ and/or $SBOH^0$-Z-$SBOH^{\pm}$ (Fig. 1A and Fig. S13, S14, ESI†). The unaffected ε value and isosbestic wavelengths for the various molecular forms of SBOH-Z-SBOH between the presence and absence of self-assembled systems

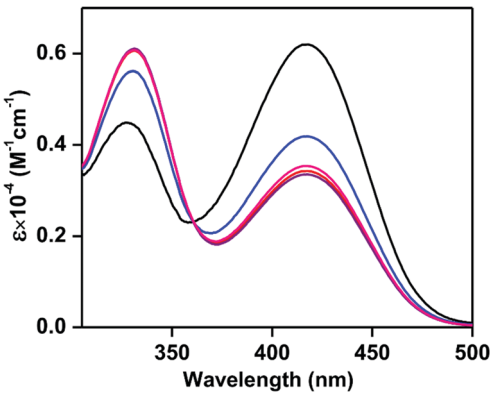

Fig. 5 UV-vis absorption spectra of the Schiff base SBOH-Z-SBOH (5 μM) in the presence of intensity-saturated concentrations of different amphiphilic molecules in 20 mM buffer, pH 7.0: blue, TX-100 (6.0 mM); pink, DOPC (4.0 mM); red, CTAB (5.0 mM); purple, DDAB (3.0 mM). The spectrum in the absence of any amphiphilic molecule is depicted in black.

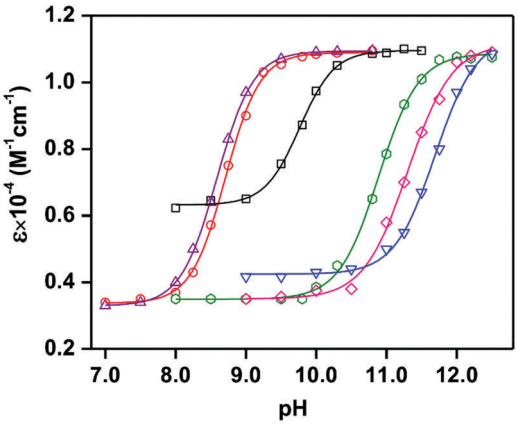

Fig. 6 Plots of molar extinction coefficient (ε) at the absorption intensity maxima (395–420 nm) against the bulk pH in the presence of saturated concentrations of different self-assembled molecules in 20 mM buffer: black, buffer solution without any amphiphilic molecules; purple, DDAB (3.0 mM); red, CTAB (5.0 mM); green, 53% (w/w) ethanol-containing buffer; pink, DOPC (4.0 mM); blue, TX-100 (5.0 mM).

 This journal is © The Royal Society of Chemistry and the Centre National de la Recherche Scientifique 2017

Published on 04 July 2017. Downloaded by Jadavpur University on 18/08/2017 14:10:31.

indicates that there is no structural deformation due to the change in the SBOH-Z-SBOH location between the bulk and the interface (Fig. 1A, 3A and Fig. S9, ESI†). Therefore, the deviation of the interfacial pH/κ from the bulk value can be directly correlated with the self-assembled system-induced change in the interconversion equilibria.

To obtain the interfacial κ for different self-assembled systems, the exclusive $SBOH^0$-Z-$SBOH^0$ to $SBOH^0$-Z-$SBOH^{\pm}$ equilibrium in the presence of an absorption saturated concentration of the self-assembled system was evaluated by monitoring the relative intensity between the 320 and 420 nm bands at a bulk pH of ~7.0. The self-assembled system induced a gradual intensity changeover from 420 to 320 nm without changing the 420 nm intensity maximum (λ_{max}) at a bulk pH of ~7.0, which confirms that the observed intensity change occurs due to the generation of $SBOH^0$-Z-$SBOH^0$ from $SBOH^0$-Z-$SBOH^{\pm}$ species following the change in probe location from the bulk to the interface (Fig. 5). The interfacial κ is evaluated from the linear $\varepsilon_{420}/\varepsilon_{420}^{8.0}$ *vs.* κ relation according to eqn (2) (Fig. 3B). Irrespective of the different amphiphilic systems and their interfacial charge characters, a highly reduced interfacial κ of ~44.0–54.0 compared to that of the bulk aqueous phase was identified (Table 1). As the interface of a self-assembled system of amphiphilic molecules is the separation between the highly polar aqueous phase and the nonpolar hydrocarbon phase, a considerable decrease in water concentration plays a pertinent role in the decrease of $\kappa(i)$ compared to its value in the bulk phase (Scheme 2). It has also been reported that the extensive H-bonding network identified in the bulk water structure is greatly distressed as the molecules move towards the interface from bulk water, which may also contribute to the lower interfacial polarity than the aqueous bulk phase value.[48,49] Most likely, the interfacial water concentration is not affected by the difference in self-assembly charge character, and thereby the interfacial κ does not differ widely among the various self-assembled systems with different interfacial charge characters.

On the other hand, the pH deviation from the bulk to the interface is highly interrelated with the interfacial charge character for amphiphilic self-assemblies.[29] It has been suggested that the distribution between H^+/H_3O^+ and OH^- ions around the charged interface at any bulk pH value can vary from the bulk phase distribution. For the cationic interface of the CTAB/DDAB self-assembled system, its attractive electrostatic interaction with the oppositely charged OH^- ions and simultaneously the repulsive interaction with the H^+/H_3O^+ ions may result in a higher OH^- ion concentration at the interface compared to the bulk phase (Scheme 2). Therefore, the pH at the interface is expected to be higher with respect to the bulk phase pH at any bulk pH value. However, the H^+/OH^- ion distribution within the bulk solvent and the corresponding bulk phase pH value are not affected by the interfacial charge in the H^+/OH^- ion distribution, since the overall volume occupied by the interface is extremely small compared to the total effective volume occupied by the bulk phase. To determine the interfacial pH and its deviation from the bulk value for different amphiphilic systems, the deprotonation equilibrium from $SBOH^0$-Z-$SBOH^0$ and/or $SBOH^0$-Z-$SBOH^{\pm}$ to SBO^--Z-SBO^- at different bulk pH values was estimated in the presence of an absorption intensity saturated concentration of self-assembled systems (Fig. 6). The cationic amphiphilic system induced a greater amount of deprotonation (pK_a: CTAB ~ 8.9; DDAB ~ 8.6) with respect to the bulk phase value (pK_a ~ 9.7), which suggests that the cationic interfaces are more basic than the bulk pH (Fig. 6 and Scheme 2). To estimate the precise interfacial pH-deviation between the bulk and the interface, the change in the proton dissociation pK_a due to the difference in κ from the aqueous bulk to the medium with identical κ to that of the interface is essential. The pH-metric titration with SBOH-Z-SBOH in ethanol/buffer mixed medium by maintaining an identical κ (42.0–54.0) to the interfacial κ has identified an

Table 1 The pH deviation from the bulk to the interface (ΔpH) and the interfacial κ for various self-assembled systems

Amphiphilic molecule	ΔpH	κ
Buffer[a]	—	78.7
CTAB	1.84	43.5
DDAB	2.20	44.5
TX-100	−0.21	53.8
DOPC	−0.32	45.0

[a] Pure aqueous buffer medium without any amphiphilic molecules.

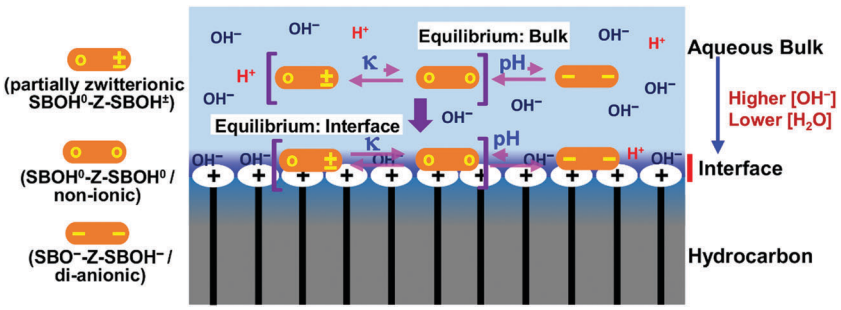

Scheme 2 Schematic view of the distribution between H^+/H_3O^+ and OH^- ions at the interface for cationic amphiphilic self-assembled systems. Pictorial representations of the different molecular forms are provided on the left. The changes in the various interconversion equilibria (pink) from the bulk to the interface among the molecular forms of SBOH-Z-SBOH are also depicted.

Published on 04 July 2017. Downloaded by Jadavpur University on 18/08/2017 14:10:31.

~0.9–1.0 unit increase in pK_a with respect to its value in the pure buffer medium (Fig. 6 and Fig. S13, ESI†). For the correlation of the pH deviation from the bulk to the interface with the self-assembled system-induced change in pK_a (ΔpK_a), the difference in pK_a owing to the polarity difference between the bulk and the interface (δ) needs to be added to the obtained ΔpK_a. The interfacial pH would be greater than ΔpK_a by δ units, by considering the increase of the deprotonated SBO^--Z-SBO^- fraction due to the decrease in the interfacial κ compared to the aqueous bulk value. Therefore, the difference between the interfacial and bulk pH may be expressed as follows:

$$pH_{intf} - pH_{bulk} = \Delta pK_a + \delta \quad (3)$$

$$pH_{intf} = pH_{bulk} + \Delta pK_a + \delta \quad (4)$$

By using eqn (3) or (4), the interfacial pH values for the CTAB micelles and DDAB ULVs are more basic by 1.8 and 2.2 units, respectively, compared to the corresponding bulk phase pH (Table 1). Notably, the estimated pH-deviations from the bulk to the interface for these cationic self-assembled systems are nearly the same as the values reported previously.[23,29] However, the polarity factor (δ ~ 0.9–1.0) contributed the most to the self-assembled system-induced increased value of ΔpK_a of ~1.1 and 1.3 for the neutral TX-100 micelles and DOPC vesicles, respectively. According to eqn (1) or (2), the interface is slightly more acidic by an amount of −0.2 and −0.3 units than the corresponding bulk pH value for TX-100 and DOPC systems, respectively (Table 1).

Conclusions

A new interface-interacting Schiff-base molecule (SBOH-Z-SBOH) with two similar phenol-conjugated-imine moieties was synthesized for the detection of pH and polarity at a similar depth in the water/oil separating interface for various self-assembled micelles and unilamellar vesicles. To detect the interfacial dielectric constant, the difference in the polarity-dependent interconversion equilibrium from the non-ionic ($SBOH^0$-Z-$SBOH^0$) to the partially zwitterionic ($SBOH^0$-Z-$SBOH^\pm$) form of the probe (SBOH-Z-SBOH) between the interface and the bulk phase was investigated. On the other hand, the self-assembled system-induced change in the deprotonation equilibrium from $SBOH^0$-Z-$SBOH^0$ and/or $SBOH^0$-Z-$SBOH^\pm$ to the anionic species (SBO^--Z-SBO^-) was evaluated to obtain the interfacial pH at a similar interfacial depth. In comparison with the small negative pH-deviation of ~−0.2 or −0.3 units from the bulk to the interface for the neutral micelles/vesicles, a large positive pH-deviation of ~1.8–2.2 was identified for the cationic micelles/vesicles. It is our proposition that the interfacial cationic charge properties are primarily responsible for the greater interfacial pH compared to the corresponding bulk pH value. On the other hand, the almost similar interfacial dielectric constants (44.0–53.0) irrespective of the different interfacial charges also indicate that the interfacial polarity does not depend on the specific charge properties.

Conflict of interest

There are no conflicts to declare.

Acknowledgements

This work was supported by Research Projects (SB/FT/CS-089/2013) (PPP) and UGC (ERO) MRP (PSW-196/13-14) (AR). SD acknowledges UGC (ERO) MRP for the research grant (PSW-197/13-14). RM and YS acknowledge UGC for JRF fellowships. The authors gratefully acknowledge Prof. Shun Hirota of NAIST, Japan for scientific discussion.

Notes and references

1 G. Apodaca, L. I. Gallo and D. M. Bryant, *Nat. Cell Biol.*, 2012, **14**, 1235.
2 S. Kim, K. No and S. Hong, *Chem. Commun.*, 2016, **52**, 831.
3 J. Kim, J. H. Jeon, H. J. Kim, H. Lim and I. K. Oh, *ACS Nano*, 2014, **8**, 2986.
4 S. Liu, Y. Liu, H. Cebeci, R. G. Villoria, J. H. Lin, B. L. Wardle and Q. M. Zhang, *Adv. Funct. Mater.*, 2010, **20**, 3266.
5 M. Barberon, G. Dubeaux, C. Kolb, E. Isono, E. Zelazny and G. Vert, *Proc. Natl. Acad. Sci. U. S. A.*, 2014, **111**, 8293.
6 L. Voglino, T. J. McIntosh and S. A. Simon, *Biochemistry*, 1998, **37**, 12241.
7 A. Spector and M. A. Yorek, *J. Lipid Res.*, 1985, **26**, 1015.
8 M. P. Sarria, J. Soares, M. N. Vieira, L. F. C. Castro, M. M. Santos and N. M. Monteiro, *Chemosphere*, 2011, **85**, 1543.
9 M. G. Swetha, V. Sriram, K. S. Krishnan, V. M. J. Oorschot, C. T. Brink, J. Klumperman and S. Mayor, *Traffic*, 2011, **12**, 1037.
10 D. Lee, J. R. Brender, M. F. M. Sciacca, J. Krishnamoorthy, C. Yu and A. Ramamoorthy, *Biochemistry*, 2013, **52**, 3254.
11 A. Mugs, J. M. Gonzalez-ManasllII, J. H. Lakeyll, F. Pattusy and W. K. Surewicz, *J. Biol. Chem.*, 1993, **268**, 1553.
12 A. D. Petelska and Z. A. Figaszewski, *Biophys. J.*, 2000, **78**, 812.
13 D. Marsh, *Proc. Natl. Acad. Sci. U. S. A.*, 2001, **98**, 7777.
14 M. Naumowicz and Z. A. Figaszewski, *J. Membr. Biol.*, 2014, **247**, 361.
15 M. K. Singh, H. Shweta, M. F. Khan and S. Sen, *Phys. Chem. Chem. Phys.*, 2016, **18**, 24185.
16 S. J. Singer and G. L. Nicolson, *Science*, 1972, **175**, 720.
17 Y. M. Chan and S. G. Boxer, *Curr. Opin. Chem. Biol.*, 2007, **11**, 581.
18 G. J. Hardya, R. Nayaka and S. Zauschera, *Curr. Opin. Colloid Interface Sci.*, 2013, **18**, 448.
19 F. M. Goni, *Biochim. Biophys. Acta*, 2014, **1838**, 1467.
20 C. G. Knight and T. Stephens, *Biochem. J.*, 1989, **15**(258), 683.
21 F. R. Beierlein, A. M. Krause, C. M. Jager, P. Fita, E. Vauthey and T. Clark, *Langmuir*, 2013, **29**, 11898.
22 M. A. Voinov, I. A. Kirilyuk and A. I. Smirnov, *J. Phys. Chem. B*, 2009, **113**, 3453.
23 S. Yamaguchi, K. Bhattacharyya and T. Tahara, *J. Phys. Chem. C*, 2011, **115**, 4168.
24 A. Kundu, S. Yamaguchi and T. Tahara, *J. Phys. Chem. Lett.*, 2014, **5**, 762.

 This journal is © The Royal Society of Chemistry and the Centre National de la Recherche Scientifique 2017

Published on 04 July 2017. Downloaded by Jadavpur University on 18/08/2017 14:10:31.

25 M. F. Yin, T. F. Jiao and M. H. Liu, *Chin. Chem. Lett.*, 2007, **18**, 30.
26 T. Jiao, X. Li, Q. Zhang, P. Duan, L. Zhang, M. Liu, X. Luo, Q. Li and F. Gao, *Colloids Surf., A*, 2012, **407**, 108.
27 X. Zhao, K. Ma, T. Jiao, R. Xing, X. Ma, J. Hu, H. Huang, L. Zhang and X. Yan, *Sci. Rep.*, 2017, **7**, 44076.
28 J. T. Feng, L. X. Hui, Z. Q. Rui, L. Q. Rong, Z. J. Xin and G. F. Ming, *Sci. China: Technol. Sci.*, 2013, **56**, 20.
29 Y. Sarkar, S. Das, A. Ray, S. K. Jewrajka, S. Hirota and P. P. Parui, *Analyst*, 2016, **141**, 2030.
30 R. Majumder, Y. Sarkar, S. Das, S. K. Jewrajka, A. Ray and P. P. Parui, *Analyst*, 2016, **141**, 3246.
31 K. Naa, K. H. Leea and Y. H. Baea, *J. Controlled Release*, 2004, **97**, 513.
32 E. S. Lee, K. T. Oh, D. Kim, Y. S. Youn and Y. H. Bae, *J. Controlled Release*, 2007, **123**, 19.
33 D. M. Mitchell, J. P. Shapleigh, A. M. Archer, J. O. Alben and R. B. Gennis, *Biochemistry*, 1996, **35**, 9446.
34 W. Chen, D. A. Tomalia and J. L. Thomas, *Macromolecules*, 2000, **33**, 9169.
35 E. Gaidamauskas, D. P. Cleaver, P. B. Chatterjee and D. C. Crans, *Langmuir*, 2010, **26**, 13153.
36 B. B. Lorenz, D. C. Crans and M. D. Johnson, *Eur. J. Inorg. Chem.*, 2014, 4537.
37 G. Akerlof, *J. Am. Chem. Soc.*, 1932, **54**, 4125.
38 F. E. Critchfield, J. A. Gibson and J. L. Hall, *J. Am. Chem. Soc.*, 1953, **75**, 6044.
39 E. Lambert, B. Chabut, S. C. Noblat, A. Deronzier, G. Chottard, A. Bousseksou, J. P. Tuchagues, J. Laugier, M. Bardet and J. M. Latour, *J. Am. Chem. Soc.*, 1997, **119**, 9424.
40 J. V. Morris, M. A. Mahaney and J. R. Huber, *J. Phys. Chem.*, 1976, **80**, 969.
41 M. J. Frisch, *et al.*, *Gaussian 09 Rev. A.1*, Gaussian Inc., Wallingford, CT, 2009.
42 I. D. Cunningham and M. Woolfall, *J. Org. Chem.*, 2005, **70**, 9248.
43 R. Álvarez-Diduk, M. T. Ramírez-Silva, A. Galano and A. MerkoçI, *J. Phys. Chem. B*, 2013, **117**, 12347.
44 S. Y. Kim, A. N. Semyonov, R. J. Twieg, A. L. Horwich, J. Frydman and W. E. Moerner, *J. Phys. Chem. B*, 2005, **109**, 24517.
45 J. Hu, H. Zhu, Y. Li, X. Wang, R. Ma, Q. Guo and A. Xi, *Phys. Chem. Chem. Phys.*, 2016, **18**, 18750.
46 J. R. Lakowicz, *Principles of Fluorescence Spectroscopy*, Springer, 3rd edn, 2006, ch. 11.
47 Sonu, S. Kumari and S. K. Saha, *Phys. Chem. Chem. Phys.*, 2016, **18**, 1551.
48 D. E. Moilanen, E. E. Fenn, D. Wong and D. M. Fayer, *J. Chem. Phys.*, 2009, **131**, 014704.
49 N. Nandi, K. Bhattacharyya and B. Bagchi, *Chem. Rev.*, 2000, **100**, 2013.

LANGMUIR Article
Cite This: Langmuir 2020, 36, 426−434
pubs.acs.org/Langmuir

Porphyrin-Based Probe for Simultaneous Detection of Interface Acidity and Polarity during Lipid-Phase Transition of Vesicles

Rini Majumder,[†] Snigdha Roy,[†] Kentaro Okamoto,[‡] Satoshi Nagao,[‡] Takashi Matsuo,*[,‡] and Partha Pratim Parui*[,†]

[†]Department of Chemistry, Jadavpur University, Kolkata 700032, India
[‡]Division of Materials Science, Graduate School of Science and Technology, Nara Institute of Science and Technology (NAIST), 8916-5 Takayama-cho, Ikoma, Nara 630-0192, Japan

Supporting Information

ABSTRACT: Biochemical activities at a membrane interface are affected by local pH/polarity related to membrane lipid properties including lipid dynamics. pH and polarity at the interface are two highly interdependent parameters, depending on various locations from the water-exposed outer surface to the less polar inner surface. The optical response of common pH or polarity probes is affected by both the local pH and polarity; therefore, estimation of these values using two separate probes localized at different interface depths can be erroneous. To estimate interface pH and polarity at an identical interface depth, we synthesized a glucose-pendant porphyrin (GPP) molecule for simultaneous pH and polarity detection by a *single* optical probe. pH-induced protonation equilibrium and polarity-dependent $\pi-\pi$ stacking aggregation for GPP are exploited to measure pH and polarity changes at the 1,2-dimyristoyl-*sn*-glycero-3-phospho-(1′-*rac*-glycerol) (DMPG) membrane interface during DMPG phase transition. An NMR study confirmed that GPP is located at the interface Stern layer of DMPG large unilamellar vesicle (LUV). Using UV−vis absorption studies with an adapted analysis protocol, we estimated interface pH, or its deviation from the bulk phase value (ΔpH), and the interface polarity simultaneously using the same spectra for sodium dodecyl sulfate micelle and DMPG LUV. During temperature-dependent gel to liquid-crystalline phase transition of DMPG, there was ∼0.5 unit increase in ΔpH from approximately −0.6 to −1.1, with a small increase in the interface dielectric constant from ∼60 to 63. A series of spectroscopic data indicate the utility of GPP for evaluation of local pH/polarity change during lipid phase transition of vesicles.

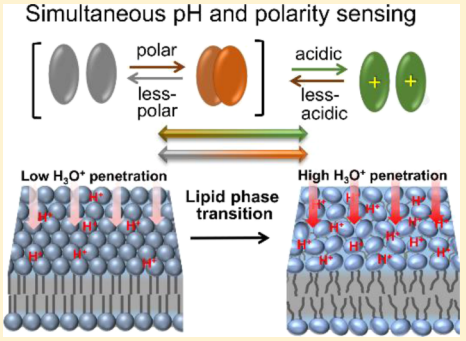

INTRODUCTION

Cellular events at phospholipid membrane interfaces are associated with the structural dynamics of the membrane, for example, the lipid phase transition from tightly packed gel to the flexible liquid-crystalline state at room temperature.[1,2] Because the membrane becomes softer in the liquid-crystalline state, endocytosis and exocytosis reactivity are accelerated above the lipid melting temperature.[3,4] Mechanical signal propagation phenomenon such as nerve pulses transmittance is strongly associated with lipid phase transition.[5] However, several other independent investigations have revealed that these membrane biochemical activities are highly sensitive to local pH and polarity surrounding the membrane.[6−8] In this context, we believe that any changes in these physicochemical properties at the membrane interface during lipid phase transition may have profound roles to affect aforementioned membrane reactivity.

Self-assembly occurs at the interface whereby charged/uncharged polar headgroups separate from the nonpolar (lipid/surfactant acryl chain) phase and assemble at the polar (aqueous) phases. Thus, pH and polarity at the interface are different from that of the bulk medium. We have recently developed a new interface pH and polarity monitoring method for micelles and vesicles using two *separate* pH and polarity sensitive chromophore probes that interact with the interface.[9,10] However, interface pH and polarity are highly interrelated physicochemical parameters along various interface locations. For example, a decrease of polarity with increasing interface depth toward the hydrophobic phase may decrease interface acidity because of a lack of H_3O^+ conduction ability.[11] pH-induced optical changes for a pH probe are frequently affected by solvent polarity[9,10] and vice versa. Thus, the precise measurement of pH and polarity using two separate probes localized at different interface depths can be problematic. The simultaneous detection of pH and polarity at an identical interface depth using a *single* optical probe is proposed here to evaluate either of these two parameters. This is particularly useful for temperature-dependent studies because polarity is intrinsically related to temperature.

Porphyrin derivatives have characteristic absorption bands around 400 nm (Soret band) and 550 nm (Q band). A large extinction coefficient (∼10^4 to 10^5 M^{-1} cm^{-1}) at the Soret

Received: September 4, 2019
Revised: November 13, 2019
Published: December 10, 2019

Downloaded via JADAVPUR UNIV on January 20, 2020 at 13:23:36 (UTC).
See https://pubs.acs.org/sharingguidelines for options on how to legitimately share published articles.

© 2019 American Chemical Society

DOI: 10.1021/acs.langmuir.9b02781
Langmuir 2020, 36, 426−434

band is useful as an indicator reagent.[12] Porphyrin derivatives work as pH indicators because of the significant UV−vis spectral changes during protonation at inner nitrogen atoms in the ring. For example, Liu and co-workers reported that tetraphenylporphyrin (TPP)-type compound **1** (Chart 1)

Chart 1. Chemical Structures of TPP-Type Porphyrins and Lipid Surfactants

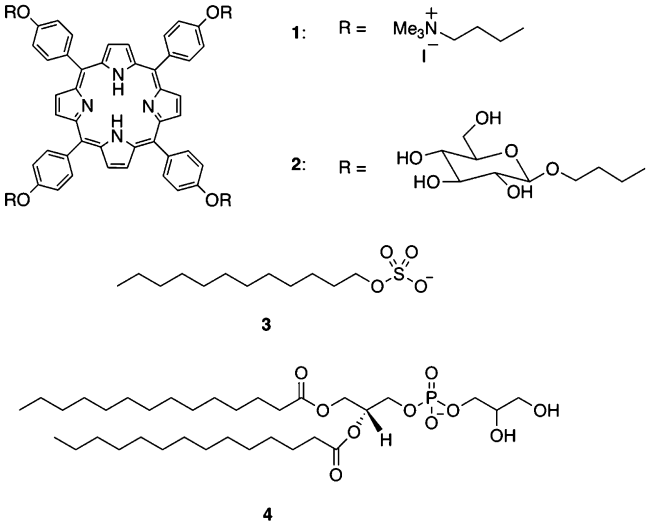

works as a pH indicator in the range of pH 4−5, where the electron-donating phenoxy moiety is a key structural factor of pH detection in this range.[13] Furthermore, deprotonated porphyrin compounds (i.e., nonprotonated state at the inner nitrogen atoms) readily form molecular aggregation states (known as J-aggregation or H-aggregation) through intermolecular hydrophobic π-stacking under polar environments, whereas the porphyrin compounds exist as a monomer state in non-polar solvents.[14,15] The aggregation behavior is also reflected in the shape of UV−vis spectra of porphyrins. Therefore, the UV−vis spectra of porphyrin derivatives reflect both environmental pH and polarity. According to these characteristics, we expected that TPP-type porphyrins are suitable for simultaneously elucidating the local pH and polarity at a membrane interface.

In this study, we demonstrate the utility of moderately water-soluble glucose-pendant porphyrin GPP (**2**) for monitoring pH and polarity simultaneously at the membrane interface. GPP (**2**) adopts both a neutrally charged (basic form) and cationic forms (acidic form) depending upon the surrounding pH. This assures: (1) binding of GPP (**2**) to the Stern layer of the anionic interface assisted by the cationic charge in the acidic-form porphyrin unit and/or by the dual characteristics of GPP (**2**) with the *polar* glucose residues and the *nonpolar* basic-form porphyrin unit; and (2) polarity-induced aggregation behavior of GPP (**2**) without affecting the intrinsic protonation property at the porphyrin core. First, we demonstrate the protocol for synchronized evaluation of pH and polarity in homogeneous solvents. Next, we applied this protocol for the simultaneous evaluation of local pH and polarity at the interface of self-assembled sodium dodecyl sulfate (SDS) (**3**) micelles and 1,2-dimyristoyl-*sn*-glycero-3-phospho-(1′-*rac*-glycerol) sodium salt (DMPG) (**4**) vesicles. In addition, we succeeded in the quantitative measurement of interface pH and polarity changes during temperature-induced DMPG phase transition in vesicles.

EXPERIMENTAL SECTION

Materials and Instruments. Porphyrin 1 was prepared according to a previously reported method.[13] GPP (**2**) and its related intermediate species were synthesized as described in the Supporting Information. SDS (**3**) and DMPG (**4**) were purchased from Sigma-Aldrich Chemicals (USA) and used without further purification. DMPG LUV was prepared as described below. For preparation of buffers and other analytical measurements, Milli-Q Millipore 18.2 MΩ·cm water was used. Medium pH was measured with a Systronics digital pH meter (model no. 335). Other chemicals were obtained from conventional vendors. UV−vis spectral changes were followed using a Shimadzu UV-2550 double beam spectrophotometer with a thermostated cell holder. The average particle size for lipid vesicles was evaluated by dynamic light scattering (DLS) measurement with Malvern Instruments, DLS-nano ZS, Zetasizer, Nanoseries. Cryo-transmitted electron microscopy (TEM) experiments were performed with an FEI Tecnai F20 electron microscope equipped with Gatan K2 summit direct detection device. ^{1}H NMR spectra were collected using JEOL NM-ECA600 or JNM-ECX400 spectrometers. Differential scanning calorimetry (DSC) measurements were carried out using a Malvern MicroCal VP-DSC calorimeter. Electron ionization mass (EI-MS) measurements were conducted using a JEOL JMS-700 mass spectrophotometer. Matrix-assisted laser desorption ionization mass (MALDI-TOF-MS) spectra were measured using a JEOL JMS-S3000 mass spectrophotometer, where *trans*-2-[3-(4-*tert*-butylphenyl)-2-methyl-2-propenylidene]malononitrile (DCTB) was used as a matrix reagent.

Preparation of DMPG LUV.[9,16] DMPG was dissolved in 1.0 mL chloroform/methanol (5:1) mixed solvent in a 5 mL round bottom flask. The organic solvents were removed using a rotary evaporator at 35 °C to prepare thin lipid film. Any residual amount of organic solvent was completely removed in vacuo for 3 h. For hydration of prepared thin film, appropriate buffer solution at desired pH was added at 45 °C. The solution was vortexed for 2.0 min for complete dissolution of the lipids to form multilamellar vesicles. Seven cycles of freeze-and-thaw were performed between −196 and 50 °C to produce giant multilamellar vesicles. To obtain unilamellar vesicles (LUVs) of diameter ∼100 nm, the liposome dispersion was extruded 15 times through two stacked polycarbonate membrane filters (Whatman) of 100 nm pore sizes equipped in a Mini-Extruder system (Avanti Polar Lipid, USA). The temperature throughout the LUV preparation process before and after lipid film hydration was maintained above 30 °C.

UV−vis absorption studies: A Quartz cell with 1 cm path length was used for absorption measurements. All solutions were filtered through a Millipore membrane filter (0.22 μm) before spectroscopic measurements. For temperature variation measurement, the measuring solutions were equilibrated at the particular temperature for 5 min. All measurements were carried out at least three times to check the reproducibility. Different buffer compositions were used to attain a particular medium pH: sodium citrate/sodium phosphate for pH 3.0−5.0; sodium cacodylate−HCl for pH 5.0−6.0; and HEPES−NaOH for pH 6.0−7.0. The required amount of GPP (**2**) was added to a buffer solution in the presence and absence of amphiphilic systems, with an addition of either 0.1 M NaOH or 0.1 M HCl to adjust the desired pH, if required. The dielectric constants of mixed solvent medium were determined according to a previous report.[17]

RESULTS AND DISCUSSION

Synthesis of GPP 2. The synthetic route of GPP (**2**) is shown in Scheme 1. The detailed synthetic procedure is described in the Supporting Information.

A popular method for the synthesis of compound **8**, a key building block in the synthesis of GPP (**2**), is the reflux of a propionic acid solution of 4-hydroxybenzaldehyde (**5**) and

DOI: 10.1021/acs.langmuir.9b02781
Langmuir 2020, 36, 426−434

Scheme 1. Synthetic Route of GPP (2)

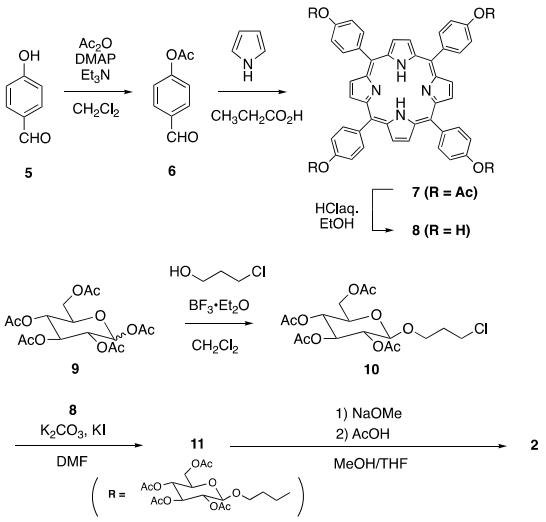

pyrrole[13] (the so-called Adler-Longo method[18]). However, the hydrophilic property of **8** (insoluble in CH_2Cl_2 or $CHCl_3$) caused difficulty in separation from turbid and gummy byproducts. The low solubility of **5** in CH_2Cl_2 prevented Lindsay porphyrin synthesis[19] using a Lewis acid catalyst. In contrast, the synthetic route shown in Scheme 1 proved that column purification is not required for obtaining porphyrin **8**. To attach sugar moieties to the periphery of the porphyrin ring, peracetylated glucose with a chloroethyl linker (**10**) was reacted with the phenolic moiety of **8** by Williamson synthesis to yield compound **11**. The in-site replacement of the chlorine atom in **10** with iodine using potassium iodide (KI) was essential to increase the yield of **11**. Finally, the acetyl groups in **11** were removed under basic conditions to obtain GPP (**2**).

GPP Monomer/Aggregate Equilibrium: Estimation of Polarity. First, we attempted to evaluate medium polarity [dielectric constant (κ)] by the observation of UV−vis spectral changes in buffer/acetone mixed medium (Figure 1).

In buffer (pH > 6.0) at 25 °C, GPP (**2**, 2.5 μM) exhibited broad absorbances consisting of weak overlapping intensities spreading from ∼400 to 440 nm (Figure 1A). This spectrum shape is often observed for H-type aggregated porphyrins with a small contribution of J-type aggregation in aqueous media,[14] where the inner nitrogen atoms in GPP (**2**) are deprotonated. With an increasing amount of acetone in the buffer, a sharp absorption band around 420 nm appeared with concomitant depletion of these broad bands (Figure 1A). The absorption band around 420 nm is a typical feature of TPP-type porphyrins observed in organic solvents.[20] Although the absorbance changes were not systematic up to 10% (w/w) of acetone with dielectric constant (κ) ≈ 73 [due to change in aggregation fashion[14,21] (Figure S1)], the absorbance increased from ∼0.17 to 0.44 upon the addition of acetone from ∼16 to 60% (w/w) with maintaining isosbestic points at ∼407 and 430 nm (Figure 1A). The quantity of intensity changes at ∼420 nm was very similar in other organic solvents than acetone (e.g., methanol and ethanol, protic solvents) (Figures 1A and S2), suggesting that the observed UV−vis spectral change is interpretable as not specific solvent effect but as polarity effect in the range of solvent κ from approximately 41−69. The series of observed spectral changes indicate that the deprotonated GPP undergoes an interconversion equilibrium between the aggregated form (denoted as d_A-GPP) and the monomer form (d_M-GPP), where "d", "A", and "M" stand for "deprotonated", "aggregated", and "monomer", respectively.

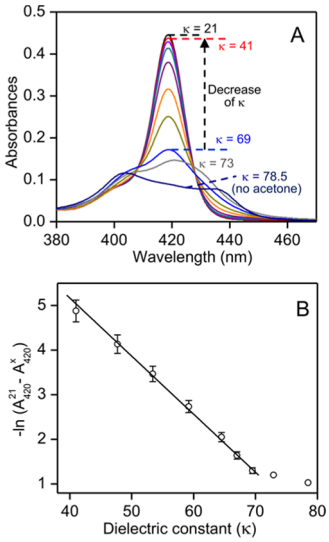

Figure 1. (A) UV−vis absorption spectra of GPP (**2**; 2.5 μM) in 10.0 mM sodium citrate/sodium phosphate buffer containing various amounts of acetone % (w/w), pH 6.0 at 25 °C: red, 60% (κ = 41.5); violet, 51% (κ = 47.7); dark cyan, 42% (κ = 53.4); purple, 33% (κ = 59.2); orange, 24% (κ = 64.5); light green, 20% (κ = 67.0); blue, 16% (κ = 69.5) and gray, 73% (κ = 72.9). The spectra in pure buffer (κ = 78.5) and acetone (κ = 21.0) medium are shown by dark blue and black, respectively. The change in dielectric constant (κ) is depicted by the arrow. (B) Negative logarithmic values of intensity difference at 420 nm from pure acetone with $\kappa \approx 21$ (A_{420}^{21}) of other various acetone/buffer mixed media with $\kappa \approx 41.5$−69.5 (A_{420}^{x}) are plotted against κ. The values of dielectric constants were quoted from a previous paper.[17]

In contrast to GPP (**2**), porphyrin **1** showed a distinct absorption band at ∼420 nm in aqueous medium with comparable intensity to that observed for GPP (**2**) in the presence of organic solvents (Figure S3). The absorption pattern and intensity increased a little (<10%) in the presence of methanol or acetone in buffer at pH 7.0. These results demonstrate that the UV−vis spectra of porphyrin **1** are less sensitive on solvent polarity compared to GPP (**2**). The spectral changes indicate that porphyrin **1** predominantly exists as a monomer form in the buffer solution because of cationic ammonium moieties. Therefore, GPP (**2**) is superior to **1** as a polarity indicator.

The d_A-GPP to d_M-GPP interconversion equilibrium was found to depend on medium temperature as well. For the mixed medium containing different acetone ratios (24−50%) in buffer, the intensity at ∼420 nm for GPP (**2**; 2.5 μM) increased gradually with rising temperature from 20 to 45 °C (Figure S4). Both the increase in temperature and in acetone ratio displayed a similar decrease in solvent κ ∼5.5−6.0 units (Figures 1A and S4A).[17] Namely, the temperature-induced absorbance change at ∼420 nm is regarded as the temperature affected change in medium κ.[17] Therefore, κ of GPP (**2**) localized environment can be estimated by monitoring d_A-GPP to d_M-GPP interconversion based on the absorbance change at ∼420 nm. Accordingly, we empirically correlate the absorbance change at ∼420 nm and medium κ. The negative logarithmic value for the amount of intensity decrease at ∼420 nm from the saturated intensity at κ < 35 under complete conversion to d_M-GPP exhibited a linear correlation with

DOI: 10.1021/acs.langmuir.9b02781
Langmuir 2020, 36, 426−434

solvent κ in the range from $\kappa \approx 40$ to 70 (Figure 1B) and thus κ can be estimated by using the eq 1

$$-\ln({A_{420}}^{21} - {A_{420}}^{x}) = -0.13 \times \kappa + 10.3 \quad (40 \leq \kappa \leq 70) \tag{1}$$

where ${A_{420}}^{21}$ and ${A_{420}}^{x}$ represent the absorbance value at ~420 nm in acetone medium ($\kappa = 21$) and the observed absorbance for a solution at unknown polarity (i.e., an observation target), respectively. The intercept and slope values are represented by 10.3 and −0.13, respectively.

GPP Acid/Base Equilibrium: Estimation of pH. Next, we attempted to develop the protocol for evaluation of pH at various polarity conditions based on the UV−vis spectra of GPP (**2**). In pH-dependent UV−vis absorption studies for GPP (2.5 μM) in a buffer solution, a new absorption band at ~446 nm appeared with the decrease in the broad band of d_A-GPP on decreasing pH from 5.2 (Figure 2A). The spectral

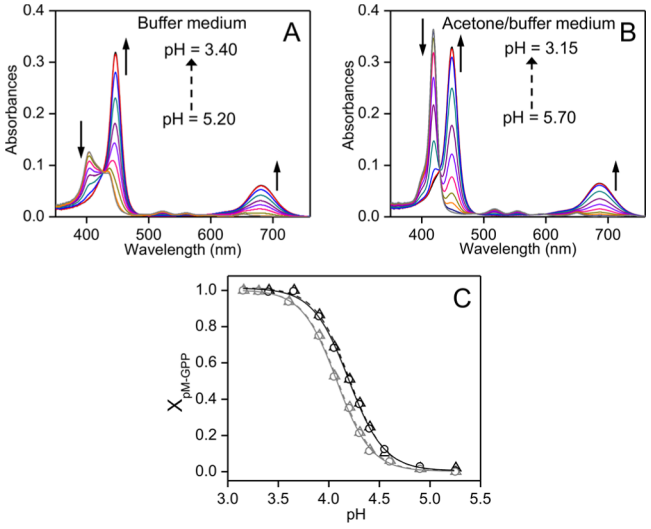

Figure 2. pH-dependent UV−vis analyses of GPP (**2**; 2.5 μM) at 25 °C; (A) spectral changes observed in 10 mM sodium citrate/sodium phosphate buffer, pH 3.40, 3.70, 3.90, 4.05, 4.20, 4.30, 4.40, 4.55, 4.90, and 5.20; (B) spectral changes observed in the buffer containing 31% (w/w) acetone, pH 3.15, 3.40, 3.60, 3.90, 4.05, 4.20, 4.30, 4.40, 4.60, 4.90, 5.25, and 5.7. The change in intensities with decreasing pH is shown in arrows. (C) pM-GPP mole ratio ($X_{pM\text{-}GPP}$) analyzed from the intensity at ~450 nm (circle, solid lines) and ~685 nm (triangle, broken lines) are plotted against pH: black, 10 mM sodium citrate/sodium phosphate buffer; gray, 31% (w/w) acetone containing buffer.

change is because of the protonation at inner nitrogen atoms in the porphyrin ring. The absorbance increase saturated at pH below 3.5, suggesting a complete protonation at inner nitrogen atoms in GPP.[12] A much sharper Soret band of the protonated GPP compared to d_A-GPP (Figure 2A) indicates that the protonated GPP exists in the monomeric state. Namely, the protonated GPP is denoted as "p_M-GPP", where "p" stands for "protonated" form. In the presence of buffer containing different acetone ratios, the single isosbestic point in the pH-dependent spectral changes indicates the apparent one-step interconversion of two deprotonated forms (d_A-GPP and d_M-GPP) (at high pH, $\lambda_{abs} \approx 420$ nm) into protonated p_M-GPP (at low pH, $\lambda_{abs} \approx 450$ and 685 nm) (Figures 2B and S5). The whole porphyrin interconversion reflected in Figure 2A,B is summarized in Scheme 2.

Scheme 2. pH and Dielectric Constant (κ)-Dependent Interconversion Equilibrium Among Aggregated-Deprotonated (d_A-GPP), Monomeric-Deprotonated (d_M-GPP) and Monomeric-Protonated (p_M-GPP) Forms of GPP

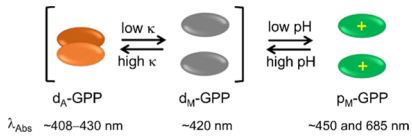

Electrostatic repulsion between positively charged porphyrins with protonated inner nitrogen atoms prevent the hydrophobic π-stacking interaction, resulting in the existence of the monomeric state, even in pure aqueous buffer. By following a similar trend, another relatively weak absorption intensity at ~685 nm also increased systematically with decreasing pH, suggesting that both intensities at ~446 and ~685 nm are associated with the p_M-GPP form (Figure 2A). Therefore, the equilibrium mole ratio of p_M-GPP ($X_{pM\text{-}GPP}$) can be determined by analyzing the absorption intensities at ~446 and ~685 nm as follows

$$X_{pM\text{-}GPP} = (A_\lambda^{pH} - {A_\lambda}^{6.0})/({A_\lambda}^{3.5} - {A_\lambda}^{6.0}) \tag{2}$$

where A_λ^{pH} and ${A_\lambda}^{3.5}$ represent the pH-dependent absorbance and the saturated intensities below pH 3.5 at wavelength (λ) ~446 or ~685 nm, respectively. ${A_\lambda}^{6.0}$ denotes the absorption intensity at ~446 or ~685 nm when GPP exists as the deprotonated state (d_M-GPP and/or d_A-GPP) at pH above 6.0. The mole ratios of p_M-GPP ($X_{pM\text{-}GPP}$) were plotted with pH (Figure 2C), and the acid/base pK_a for GPP was estimated to be ~4.2 by fitting data points with a sigmoidal-Boltzmann equation (the data of first raw in Table S1). The unknown pH of an aqueous medium can be estimated from the pH versus p_M-GPP mole ratio calibration curve.

The pH versus p_M-GPP mole ratio calibration curve in acetone/buffer solutions shifted to the direction of lower pH compared to the pure buffer solution (cf. black and gray lines in Figure 2C). The deviation reflects the polarity effect on the protonation/deprotonation equilibrium. This indicates that the contributions of solvent κ and pH should be separated in the observed UV−vis spectral changes in order to develop the protocol to estimate pH under variable polarity conditions.

Accordingly, we performed the pH-metric titration of GPP under various polarity conditions to monitor the interconversion from d_A-GPP and/or d_M-GPP to p_M-GPP (Figure S5A–E). Similar to the spectral change observed in buffer solutions, a sharp band around ~450 nm for p_M-GPP forms gradually appeared with decreasing pH from 6.0 to 2.5. The apparent acid/base pK_a decreased from ~4.10 to 3.35 with decreasing solvent κ from ~62.0 to ~42.0 at 25 °C (Table S1, Figure S5). The lack in solvation of cationic p_M-GPP at low κ results in the decrease in apparent pK_a. Because the magnitude of ${A_\lambda}^{6.0}$ (in eq 2) is independent of medium polarity ($\kappa \leq 70$), the pH-dependent p_M-GPP/GPP ratio ($X_{pM\text{-}GPP}$) can be estimated independently without knowing the κ of mixed solvents.

For the acetone/buffer mixed medium, temperature-dependent pK_a values are estimated and listed in Table S1. Interestingly, a certain decrease in solvent κ by either an increase in acetone ratio or increase in temperature in the buffer/acetone mixed medium exhibited a similar extent in acid/base pK_a shift (Table S1, Figures S5 and S6). These

DOI: 10.1021/acs.langmuir.9b02781
Langmuir 2020, 36, 426−434

results suggest that the temperature-dependent pK_a shift for GPP is mostly associated with the variation of solvent κ (Figures S5 and S6). Therefore, maintaining an identical temperature condition of the measuring and calibrating solutions is a prerequisite to determine the GPP environmental pH by utilizing pH-metric titration curves.

Simultaneous Estimation of pH and Polarity in Homogeneous Solutions. Under complete protonation of GPP, the identical absorption intensity at various solvent κ (Figure 2 for buffer solutions, Figure S5 for acetone-containing buffer solutions, and in Figure S6 for solutions at different temperatures) indicates molar extinction coefficients (ε) at all wavelengths does not depend upon medium κ. However, when GPP becomes partially protonated, the intensity change at ~420 nm is to be affected not only by the κ-induced change in d_A-GPP to d_M-GPP ratio for the deprotonated GPP but also their protonation to form p_M-GPP. By evaluating $X_{p_M\text{-GPP}}$ from eq 2, the intensity because of the p_M-GPP form at ~420 nm is calculated as $A^p_{420} \times X_{p_M\text{-GPP}}$, where A^p_{420} denotes the intensity for the fully protonated GPP ($X_{p_M\text{-GPP}} = 1$). Therefore, the actual intensity of deprotonated GPP (d_A-GPP and/or d_M-GPP) at ~420 nm can be obtained by subtracting $A^p_{420} \times X_{p_M\text{-GPP}}$ from the observed intensity (A^{obs}_{420}). Furthermore, ($A^{obs}_{420} - A^p_{420} \times X_{p_M\text{-GPP}}$) was normalized by dividing it with the mole ratio of deprotonated GPP ($1 - X_{p_M\text{-GPP}}$) to use eq 1 for the estimation of κ

$$A^N_{420} = {A_{420}}^{x} = (A^{obs}_{420} - A^p_{420} \times X_{pM\text{-GPP}})/(1 - X_{pM\text{-GPP}}) \quad (3)$$

$$\begin{aligned} &-\ln({A_{420}}^{21} - {A_{420}}^{x}) \\ &= -\ln[{A_{420}}^{21} - (A^{obs}_{420} - A^p_{420} \times X_{pM\text{-GPP}}) \\ &\quad /(1 - X_{pM\text{-GPP}})] \\ &= 0.13 \times \kappa + 10.3 \end{aligned} \quad (4)$$

Using eq 4, an unknown κ can be estimated by evaluating $X_{p_M\text{-GPP}}$ and A^N_{420} from the intensities at ~450 or 685 and 420 nm, respectively. Notably, the more general eq 4 than eq 1 can be used to estimate κ under the conditions of various extents of GPP protonation in a wide range of bulk pHs. Once the medium κ is known, pH of the medium can also be simultaneously estimated from the same absorption spectrum by correlating $X_{p_M\text{-GPP}}$ with the pH-metric calibration curve obtained under same medium κ.

A series of test of the above procedure above demonstrated that GPP (**2**) is highly effective for simultaneous detection of environmental pH and κ using a single absorption spectrum.

Interaction of GPP with Self-Assembly Interfaces. Encouraged by the proved utility of GPP (**2**) for simultaneous determination of the local polarity and pH around the molecule, we investigated the availability of GPP (**2**) for probing the local environment at the interface of lipid emulsions. First, we attempted to elucidate interaction fashions between GPP (**2**) and DMPG LUV by ^{1}H NMR spectroscopy. The full 1D ^{1}H NMR spectrum of the mixture of GPP (**2**) and DMPG LUV observed at 40 °C is shown in Figure 3A. Figure 3B shows the temperature dependency on the 1D ^{1}H NMR spectrum in the range from 7.0 to 10.0 ppm. The diameter of DMPG LUV at ~100 nm was controlled by the lipid extrusion

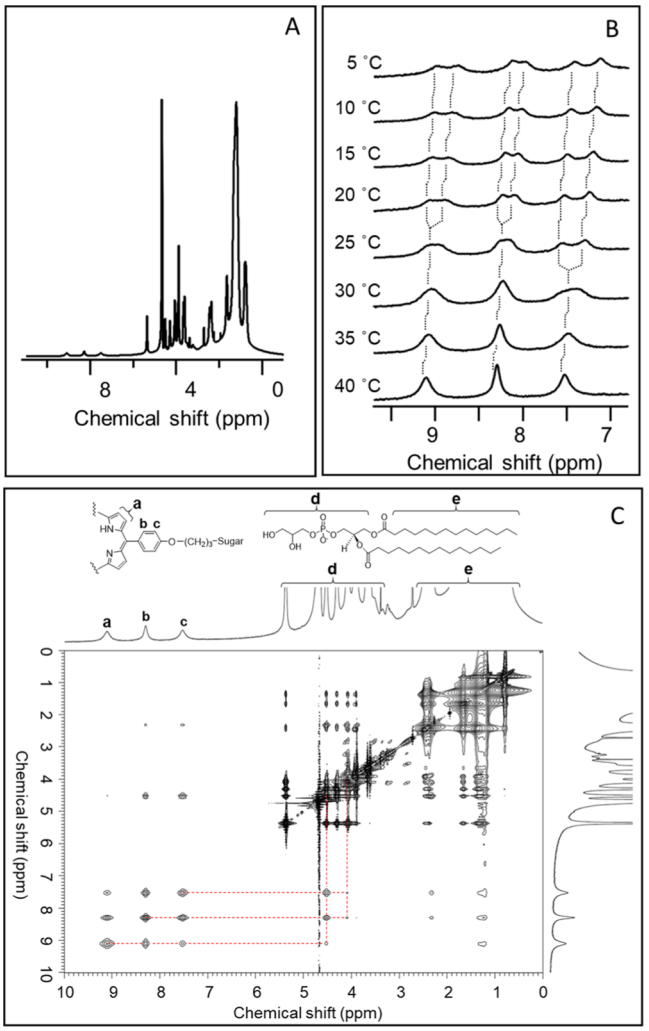

Figure 3. 600 MHz-^{1}H NMR spectroscopic analysis for the mixture of GPP (**2**) and DMPG LUV; (A) whole 1D NMR spectrum at 40 °C; (B) 1D NMR spectra at various temperatures in the range from 7.0 to 10.0 ppm; (C) NOESY spectrum at 40 °C; conditions: [**2**] = 1 mM, [DMPG LUV ($d \approx 100$ nm)] = 8 mM in D_2O-containing DMSO-d_6 (5% v/v)). The dotted lines marked in Figure 3B indicate the signal shifts of the protons during change in temperature. Red broken lines in Figure 3C indicate the correlations between the protons in GPP (**2**) and those in the head moiety of DMPG.

(see Experimental Section), and the size distribution and morphology were further confirmed by DLS and cryo-TEM analysis, respectively (Figures S7 and S8).

The signals at 7.5, 8.3, and 9.1 ppm are assigned as protons of *m*-phenyl, *o*-phenyl, and porphyrin β-positions, respectively (Supporting Information). The signal broadening is wholly because of the existence of LUV macromolecular substance. At lower temperatures, each signal tends to split into two peaks (Figure 3B). The splitting occurs around 25−30 °C, which is close to the phase-transition temperature of DMPG LUV (vide infra).[22,23] Consequently, this finding indicates that GPP (**2**) interacts with DMPG LUV. The signal splitting at low temperatures is caused by the decrease in exchange rate between several interaction fashions. We also collected the NOESY spectrum of the mixture of GPP (**2**) and DMPG LUV at 40 °C in order to address the location of GPP (**2**) in DMPG LUV (Figure 3C). The proton signals at 7.5, 8.3, and 9.1 ppm of **2** displayed correlation signals with proton peaks at 4.1 and

DOI: 10.1021/acs.langmuir.9b02781
Langmuir 2020, 36, 426−434

4.5 ppm, corresponding to the protons at the head moiety of DMPG. Similar cross peaks were also observed in the measurement at 20 °C (Figure S9). The results of 2D NMR spectral analysis strongly indicate that GPP (**2**) locates on the interface Stern layer of DMPG LUV regardless of temperature change. Therefore, GPP (**2**) is suitable to measure pH and polarity at a similar Stern layer location for DMPG LUV during the temperature-induced lipid phase transition.

Next, we measured UV−vis spectra of GPP in the presence of amphiphilic systems. The absorbances at ∼450 or ∼685 nm for GPP (2.5 μM) in 10 mM citrate/phosphate buffer (pH 4.2) increased gradually with increasing concentration of SDS micelles or DMPG LUV (Figure S10). This is indicative of the interaction between GPP and the interface of these self-assemblies. The increase in absorbances shown in Figure S10 is very similar to the spectral change observed for the pH titration in a buffer solution (Figure 2A), suggesting that GPP in the amphiphilic systems undergoes the acid/base equilibrium to generate the p_M-GPP form. No significant changes in LUV morphology is confirmed by the observation of almost identical distribution in the DMPG LUV diameter (Figure S7). The intensities saturated in the presence of 8 mM SDS or 1.1 mM DMPG, and the intensity saturation justifies that all the GPP molecules interacted with the interface. The red-shift of absorption band from ∼446 to 450 nm for the p_M-GPP form in the self-assembled system suggests that GPP interacted with the self-assembly interface with κ lower than the bulk phase. Therefore, we performed further measurement under these micelle or LUV-interacting intensity saturation conditions to monitor d_A-GPP and/or d_M-GPP to p_M-GPP interconversion for GPP at the self-assembly interfaces.

Simultaneous Estimation of pH and Polarity at the Self-Assembly Interfaces. pH-metric titrations for GPP (**2**) were performed with a interaction saturated high concentration of DMPG LUV (lipid, 1.1 mM, Figure 4A) and SDS micelles (8 mM, Figure S11B) at 25 °C. As described above, the extinction coefficient of p_M-GPP form does not depend on κ. The pH-dependent equilibrium p_M-GPP mole ratio ($X_{p_M\text{-GPP}}$) at the DMPG LUV interface was estimated by monitoring absorption intensity at ∼450 or ∼685 nm at the full interaction of GPP with self-assembled systems, according to eq 2. On the other hand, for the determination of $X_{p_M\text{-GPP}}$ value at the SDS micelle interface, only absorbance change at ∼685 nm can be used for the analysis. The higher energy absorption band around 450 nm tended to gradually blue-shift with decreasing pH from 5.3 to 4.3 and overlapped considerably with that of d_A-GPP and/or d_M-GPP (Figure S11B). When using $X_{p_M\text{-GPP}}$ under different bulk pH conditions, the interface κ was estimated by calculating the corresponding A^N_{419} from the observed intensity at ∼420 nm, according to eqs 3 and 4. The interface κ was determined to be similar at ∼61.5 and 60.5 for SDS micelle and DMPG LUV, respectively, at 25 °C using eqs 3 and 4 (Table 1).

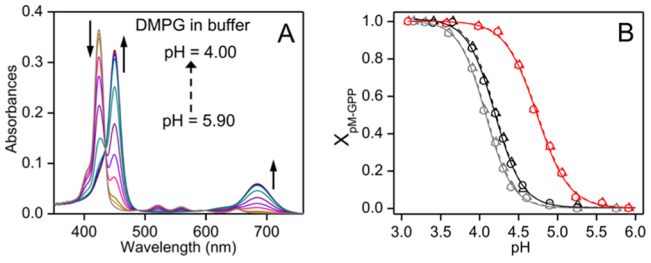

Figure 4. pH-dependent UV−vis analysis of GPP (**2**; 2.5 μM) at 25 °C in 10 mM sodium citrate/sodium phosphate buffer containing DMPG LUV (lipid, 1.1 mM); (A) spectra measured at pH 4.0, 4.25, 4.50, 4.70, 4.90, 5.05, 5.25, 5.55, and 5.90. The change in intensities with decreasing pH is shown in arrows; (B) p_M-GPP mole ratio ($X_{p_M\text{-GPP}}$) analyzed from the intensity at ∼450 nm (circle, solid lines) and ∼685 nm (triangle, broken lines) is plotted against bulk pH (red). The plots for pure buffer solutions (black) and buffer containing 31% (w/w) acetone (gray) in Figure 2 are shown for comparison.

Table 1. Temperature- and Bulk pH- Dependent pH Deviation from the Bulk to the Interface (ΔpH) and Interface Dielectric Constant ($\kappa(i)$) for SDS Micelle and DMPG LUV

	T (°C)	bulk pH	interface κ	ΔpH
SDS micelle	20	4.3−5.3	63.0 ± 0.2	−0.72 ± 0.03
	25	4.3−5.3	61.5 ± 0.2	−0.70 ± 0.03
	35	4.2−5.2	59.4 ± 0.2	−0.69 ± 0.03
	40	4.1−5.1	57.6 ± 0.2	−0.67 ± 0.03
DMPG LUV	20	4.5	61.6 ± 0.4	−0.62 ± 0.03
		4.9−5.3	61.5 ± 0.2	−0.62 ± 0.03
	25	4.5	60.6 ± 0.4	−0.67 ± 0.03
		4.9−5.3	60.3 ± 0.2	−0.67 ± 0.03
	30	4.5	59.6 ± 0.4	−0.85 ± 0.03
		4.9−5.3	61.9 ± 0.2	−1.01 ± 0.03
	35	4.5	62.1 ± 0.4	−1.05 ± 0.03
		4.9−5.6	63.0 ± 0.2	−1.09 ± 0.03
	40	4.5	62.6 ± 0.4	−1.10 ± 0.03
		4.9−5.6	61.4 ± 0.2	−1.11 ± 0.03

The interface pH can be evaluated by monitoring the bulk pH-dependent p_M-GPP mole ratio between the interface and the bulk. The increase in the amount of p_M-GPP mole ratios observed in self-assembled systems indicates that the interfaces of these self-assemblies provide more acidic environments than the bulk phase does (DMPG LUV: Figure 4; SDS: Figure S11B). For quantitative measurement of pH at the interface, the p_M-GPP mole ratio in the absence and presence of interaction saturated high concentration of SDS or DMPG LUV is compared with that of bulk pH (Figures 4B and S11E). The apparent pH shift between the interface and the bulk pH (Δ) can be estimated from the difference in p_M-GPP ratio between the interface and the bulk at 25 °C, where Δ should be negative because the interface is more acidic compared to the bulk. Irrespective of a different bulk pH, the Δ value was estimated to be approximately −0.54 and −0.59 for DMPG LUV and SDS micelles, respectively (Figures 4 and S11). Because the pH-induced interconversion between p_M-GPP and d_A-GPP and/or d_M-GPP is also affected by medium κ, Δ can also be affected by the difference in κ between the interface and the bulk. The polarity contribution (δ) to Δ is estimated by the apparent pH shift caused by the difference in κ between the interface and the bulk. The pH deviation (ΔpH) from the bulk to the interface pH (pH_{inf}) and subsequently pH_{inf} is obtained from the bulk pH (pH_{bulk}), Δ, and δ

$$\Delta pH = \Delta - \delta \quad (5)$$

$$pH_{inf} = pH_{bulk} + \Delta - \delta \quad (6)$$

DOI: 10.1021/acs.langmuir.9b02781
Langmuir 2020, 36, 426−434

Δ is the function of combined interface pH and κ, whereas δ is related to interface κ. Conventionally, two separate pH and polarity-responsive probe molecules are used to evaluate Δ and δ, respectively.[9,10] However, the change in the locations of these pH and polarity probes at various interface depths makes the determination of δ erroneous because the interface polarity can decrease drastically with increasing interface depth from the water-exposed outer surface. In contrast, the simultaneous estimation of Δ and δ parameters using a *single* GPP probe at an *identical* interface depth not only enables us to compute the correct value of δ for measuring interface pH but also provides simultaneous values of interface pH and κ.

The value of κ in acetone/buffer mixed solution was adjusted same as the interface κ for SDS micelles and DMPG LUV at 25 °C (Table 1), and δ was found to be ∼0.11 for SDS micelles and ∼0.13 DMPG LUV, respectively, under different pH conditions at 25 °C (Figure S5B,F,G). With the variation of bulk pH, the estimated pH deviation from the bulk to the interface (ΔpH) for SDS micelles and DMPG LUV was found to be similar ∼0.70 and ∼0.67, respectively, at 25 °C (Table 1, Figures 4B, and S5B,FG). For anionic self-assemblies, the negatively charged headgroup at the interface may involve attractive electrostatic interaction with H^+ but it repels OH^-. In comparison to the bulk phase, $[H^+]$ and $[OH^-]$ may increase and decrease, respectively, at the interface. However, $[H^+]$ and $[OH^-]$ remain unchanged in the bulk owing to the larger volume of the bulk phase than the interface. Therefore, higher $[H^+]$ at the anionic SDS micelle or DMPG LUV interface than the corresponding bulk phase makes the interface more acidic compared to the bulk pH.

Temperature Effect on SDS Micelle Interface pH and Polarity. The general temperature effect on interface pH and κ was examined for SDS micelle. Upon increasing the temperature from 20 to 40 °C, the acid/base pK_a at the SDS micelle interface decreased from ∼4.8 to 4.6 (Table S2 and Figure S11). At first, the dependency of interface κ on temperature was estimated by analyzing the intensity contribution of d_M-GPP from absorption spectra under various pH conditions according to eq 1 (for complete deprotonation of GPP, pH > 7.0) or eq 4 (for a mixture of protonated and deprotonated GPP, pH < 7.0). Irrespective of different bulk pH values, the observed intensity (for pH ≥ 7.0) or normalized intensity (A^N_{420} for pH < 7.0) at 420 nm increased from ∼0.34 to 0.39 with an increase of temperature from 25 to 40 °C (Figure S11), which corresponds to a decrease of interface κ from ∼61.5 to 57.6 (Table 1 and Figure S5). Interestingly, the identical decrease of κ from 25 to 40 °C was observed for 31% acetone-containing buffer medium (Table S1, Figures S4 and S5), suggesting that the typical temperature versus κ correlations are also maintained at the SDS micelle interface. In addition, a similar amount of pK_a decreases ∼0.2 for GPP between SDS micelle and acetone/buffer medium with κ similar to that of the SDS interface was detected by the increase of temperature from 25 to 40 °C (Tables S1 and S2, Figures S6 and S11). The results show that the interface pH for SDS micelle remains unchanged, and the acid/base pK_a change for GPP is caused by the temperature-induced variation of interface κ.

Interface pH/Polarity Changes during Temperature-Induced Phase Transition for DMPG LUV. The gel to liquid-crystalline phase transition process of lipids in LUV membrane is not only affected by temperature but also dependent on environmental pH conditions.[24] DMPG is known to exhibit weakly energetic pretransition peaks at low temperatures (∼11−15 °C) and highly cooperative strongly energetic gel to liquid-crystalline phase transitions (∼23−25 °C).[25] The phase transition temperatures (T_m) of DMPG in its LUV were measured by DSC in 10 mM citrate/phosphate buffer solution at various pH 4.5−5.5 (Figure 5). The weak

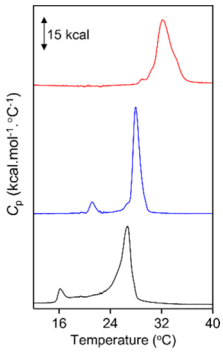

Figure 5. DSC thermograms of DMPG LUV (lipids, 1 mM) in 10 mM citrate/phosphate buffer, pH 4.5 (red), pH 4.9 (blue), and pH 5.5 (black).

pretransition peak at ∼16 and 21 °C was observed at pH 5.5 and 5.0, respectively, although no such peak appeared at pH 4.5. However, the main phase-transition temperature, T_m,[26] was found to increase from 28.0 to 32.3 °C by decreasing pH from 4.9 to 4.5, whereas T_m increased to a relatively lower extent from 26.6 to 28.0 °C with increasing pH to 5.5.

Temperature- and pH-dependent acid/base equilibrium for GPP (2.5 μM) were monitored at the DMPG LUV interface to monitor the effect of phase transition from the DMPG gel state to its liquid-crystalline state on the interface pH and κ (Figure S12). In contrast to SDS micelles, an increase in absorption intensity at ∼450 and ∼685 nm was observed for DMPG LUV by increasing temperature from 20 to 40 °C (Figures 6 and

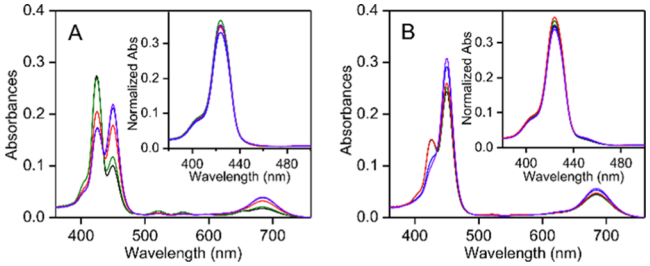

Figure 6. Temperature-dependent UV−vis absorption spectra of GPP (**2**; 2.5 μM) and (inset) corresponding normalized absorption spectrum in 10 mM sodium citrate/sodium phosphate buffer containing DMPG LUV (1.1 mM) at (A) pH 4.9 and (B) pH 4.5: black, 20 °C; green, 25 °C; red, 30 °C; blue, 35 °C; and violet, 40 °C. Each spectrum in the inset is normalized according to the similar procedure to obtain normalized intensity (A^N_{420}) using eq 3.

S12) under a different but constant pH. However, major increases in absorption intensity at ∼450 nm from ∼0.12 to 0.21 and at ∼685 nm (from ∼0.02 to 0.04) were detected between 25 and 35 °C at bulk pH 4.9. No further intensity increase was observed at above 35 °C (Figure 6 and Table 1). Under a decreased bulk pH condition of 4.5, a major increase in intensity was noticed at above 30 °C up to 40 °C (Figure 6B). The increase in T_m for DMPG LUV from 28.0 to 32.3 °C

DOI: 10.1021/acs.langmuir.9b02781
Langmuir 2020, 36, 426−434

with decreasing pH from 4.9 to 4.5 also clearly correlates with the increasing temperature required to obtain the major increase in p_M-GPP mole ratio from 4.9 to 4.5 (Figure 6). The temperature-induced increase in the p_M-GPP mole ratio indicating an increase in interface acidity can be correlated with the phase transition process of the DMPG gel state to liquid-crystalline state (Figure 6 and Table 1).

According to our analysis protocol, we first estimated interface κ by normalizing each spectrum in Figures 6 and S12. For example, normalized spectra at pH 4.9 and 4.5, according to eq 3, are represented in the inset of Figure 6. Interface κ for DMPG LUV at different temperatures and pH values was determined from the value of normalized intensity (A^N_{420}) using eq 4 (Figures 6, S12 and Table 1). When DMPG involves a phase transition process from ~25 to 35 °C at pH 4.9 and ~30 to 40 °C at pH 4.5, the interface κ increased from 60.3 to 63.0 and 59.6 to 62.6, respectively (Figures 5, 6 and Table 1). For other temperatures when DMPG did not involve a phase transition significantly according to DSC measurements (Figure 5), a decrease in interface κ with increasing temperature was also observed in similar to SDS micelles (Figure S11, and Tables 1 and S). Because the acid/base equilibrium for GPP is affected substantially by environmental κ (Figure S5 and Table S1), various polarity correction factors ($\delta \approx 0.09-0.13$ depending on different interface $\kappa \approx 60.3-63.0$) are considered to estimate interface pH and its deviation from the bulk pH (ΔpH) using eqs 5 and 6. Bulk pH and temperature-dependent interface pH and ΔpH are listed in Table 1. A similar increase of $\Delta pH \approx -0.5$ was mostly observed upon increasing temperature from 20 to 40 °C at bulk pH 4.9 and 4.4, respectively, although the major increase of ΔpH was observed around the DMPG phase transition temperature (Figures 5 and 6, Table 1). As we observed that pH at the typical self-assembly interface (SDS micelle) does not depend on temperature, the temperature-dependent increase of Stern layer interface acidity for DMPG LUV should be associated with the DMPG gel to liquid-crystalline phase transition.

It has been reported that interface pH and κ for a charged amphiphilic self-assembled system are highly controlled by the packing arrangement of ionic headgroups at the interface Stern layer.[9,27] A tight headgroup packing arrangement with their low solvent accessible surface area restricts the electrostatic penetration of H_3O^+ (for an anionic headgroup) or OH^- (for a cationic headgroup) and H_2O (for solvation) into the interface stern layer.[9] However, the penetrating ability is gradually improved with increasing interheadgroup separation distance (loose headgroups packing) during gel to liquid-crystalline phase transition. The packing flexibility may allow the anionic headgroup to have more access to the bulk water phase for solvation and penetration of H_3O^+ into the interface (Scheme 3).

The higher H_3O^+ penetration at the DMPG LUV interface makes the interface more acidic by ~0.5 pH unit for the liquid-crystalline phase compared to the gel phase. Notably, no significant change of pH at the SDS micelle interface was observed in the range of 20–40 °C (Table 1), which surely eliminates any role of intrinsic temperature-induced pH change at the LUV interface. On the other hand, only a small increase of interface κ from ~60 to 63 was detected for the transition from the gel to liquid-crystalline phase (*inset* of Figure 6 and Table 1). Presumably, the lipid-phase transition-induced increase of interface κ may be partially compensated by increasing temperature-dependent decrease in κ (Table 1), resulting in the affection to the small change of interface κ.

Scheme 3. Schematic Representation of Lipid Headgroup Packing Arrangement in DMPG LUV in Gel (Left) and Liquid-Crystalline (Right) Phases

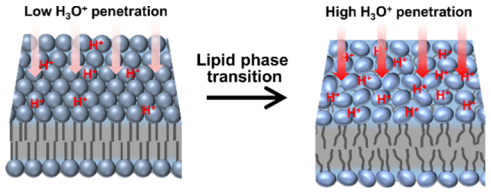

CONCLUSIONS

A series of UV–vis spectral changes shown by GPP (**2**) prove the utility of GPP (**2**) as a probe for the simultaneous evaluation of interface pH and polarity for amphiphilic self-assemblies. Throughout the UV–vis spectral changes during the protonation/deprotonation at inner nitrogen atoms in the porphyrin ring and aggregation character, GPP (**2**) is able to reflect the local pH and polarity in media around GPP (**2**). Furthermore, the delicately balanced structure composed of a porphyrin moiety (hydrophobic deprotonated or cationic protonated) and hydrophilic glucose parts in GPP (**2**) enables the compound to stay at the Stern layer of anionic phospholipid self-assemblies. The evaluation of physicochemical properties based on the spectral changes of GPP (**2**) in the presence of DMPG LUV is possible during the phase transition of the lipid self-assembly. The difference in pK_a between the bulk and the lipid membrane surface is interpretable in terms of structural dynamics of phospholipid self-assemblies that affect the interface ion penetration abilities. Designed chromophore probes, such as GPP (**2**), will be useful to understand chemical events on the membrane surface.

ASSOCIATED CONTENT

Supporting Information

The Supporting Information is available free of charge at https://pubs.acs.org/doi/10.1021/acs.langmuir.9b02781.

Synthesis protocol and characterization for GPP (**2**), several UV–vis spectra, NOESY spectrum, and DLS measurement results and a cryo-TEM image (PDF)

AUTHOR INFORMATION

Corresponding Authors

*E-mail: tmatsuo@ms.naist.jp (T.M.).
*E-mail: parthaparui@yahoo.com (P.P.P.).

ORCID

Satoshi Nagao: 0000-0003-1674-7697
Takashi Matsuo: 0000-0002-5646-6251
Partha Pratim Parui: 0000-0002-2674-7458

Notes

The authors declare no competing financial interest.

ACKNOWLEDGMENTS

T.M. thanks a Grant-in Aid for Scientific Research on Innovative Areas "Molecular Engine" (JSPS KAKENHI grant number JP19H05395). S.N. also thanks a Grant-in Aid for Scientific Research (C) (JSPS KAKENHI grant number JP19K05695). P.P.P. acknowledges UGC and government of

DOI: 10.1021/acs.langmuir.9b02781
Langmuir 2020, 36, 426–434

West Bengal for financial support under RUSA 2.0 scheme (no: 5400-F(Y)). R.M. and S.R. acknowledges UGC for SRF fellowship. We thank Yoshiko Nishikawa for mass spectral analyses. We also acknowledge Prof. Shun Hirota for his kind help in usage of some experimental facilities.

REFERENCES

(1) Heimburg, T. *Thermal biophysics of membranes*; Wiley-VCH Verlag GmbH & Co. KGaA: Weinheim, 2007.
(2) Heimburg, T.; Jackson, A. D. On soliton propagation in biomembranes and nerves. *Proc. Natl. Acad. Sci. U.S.A.* **2005**, *102*, 9790−9795.
(3) Ben-Dov, N.; Korenstein, R. Proton-induced endocytosis is dependent on cell membrane fluidity, lipid-phase order and the membrane resting potential. *Biochim. Biophys. Acta* **2013**, *1828*, 2672−2681.
(4) Nambiar, R.; McConnell, R. E.; Tyska, M. J. Control of cell membrane tension by myosin-I. *Proc. Natl. Acad. Sci. U.S.A.* **2009**, *106*, 11972−11977.
(5) Pérez-Camacho, M. I.; Ruiz-Suárez, J. C. Propagation of a thermo-mechanical perturbation on a lipid membrane. *Soft Matter* **2017**, *13*, 6555−6561.
(6) Freedman, S. D.; Kern, H. F.; Scheele, G. A. Acinar lumen pH regulates endocytosis, but not exocytosis, at the apical plasma membrane of pancreatic acinar cells. *Eur. J. Cell Biol.* **1998**, *75*, 153−162.
(7) Zhang, Z.; Nguyen, K. T.; Barrett, E. F.; David, G. Vesicular atpase inserted into the plasma membrane of motor terminals by exocytosis alkalinizes cytosolic pH and facilitates endocytosis. *Neuron* **2010**, *68*, 1097−1108.
(8) Neuhoff, S.; Ungell, A.-L.; Zamora, I.; Artursson, P. pH-dependent passive and active transport of acidic drugs across caco-2 cell monolayers. *Eur. J. Pharm. Sci.* **2005**, *25*, 211−220.
(9) Sarkar, Y.; Majumder, R.; Das, S.; Ray, A.; Parui, P. P. Detection of curvature-radius-dependent interfacial pH/polarity for amphiphilic self-assemblies: Positive versus negative curvature. *Langmuir* **2018**, *34*, 6271−6284.
(10) Parui, P. P.; Sarakar, Y.; Majumder, R.; Das, S.; Yang, H.; Yasuhara, K.; Hirota, S. Determination of proton concentration at cardiolipin-containing membrane interfaces and its relation with the peroxidase activity of cytochrome *c*. *Chem. Sci.* **2019**, *10*, 9140−9151.
(11) Singh, M. K.; Shweta, H.; Khan, M. F.; Sen, S. New insight into probe-location dependent polarity and hydration at lipid/water interfaces: Comparison between gel- and fluid-phases of lipid bilayers. *Phys. Chem. Chem. Phys.* **2016**, *18*, 24185−24197.
(12) Rudine, A. B.; DelFatti, B. D.; Wamser, C. C. Spectroscopy of protonated tetraphenylporphyrins with amino/carbomethoxy substituents: Hyperporphyrin effects and evidence for a monoprotonated porphyrin. *J. Org. Chem.* **2013**, *78*, 6040−6049.
(13) Liu, Y.-Y.; Wu, M.; Zhu, L.-N.; Feng, X.-Z.; Kong, D.-M. Colorimetric and fluorescent bimodal ratiometric probes for pH sensing of living cells. *Chem.−Asian J.* **2015**, *10*, 1304−1310.
(14) Villari, V.; Mineo, P.; Scamporrino, E.; Micali, N. Role of the hydrogen-bond in porphyrin *J*-aggregates. *RSC Adv.* **2012**, *2*, 12989−12998.
(15) Verma, S.; Ghosh, A.; Das, A.; Ghosh, H. N. Ultrafast exciton dynamics of *J*- and *H*-aggregates of the porphyrin-catechol in aqueous solution. *J. Phys. Chem. B* **2010**, *114*, 8327−8334.
(16) Meister, A.; Finger, S.; Hause, G.; Blume, A. Morphological changes of bacterial model membrane vesicles. *Eur. J. Lipid Sci. Technol.* **2014**, *116*, 1228−1233.
(17) Akerlof, G. Dielectric constants of some organic solvent-water mixtures at various temperatures. *J. Am. Chem. Soc.* **1932**, *54*, 4125−4139.
(18) Adler, A. D.; Longo, F. R.; Finarelli, J. D.; Goldmacher, J.; Assour, J.; Korsakoff, L. A simplified synthesis for meso-tetraphenylporphine. *J. Org. Chem.* **1967**, *32*, 476.
(19) Lindsey, J. S.; Schreiman, I. C.; Hsu, H. C.; Kearney, P. C.; Marguerettaz, A. M. Rothemund and Adler-Longo reactions revisited: synthesis of tetraphenylporphyrins under equilibrium conditions. *J. Org. Chem.* **1987**, *52*, 827−836.
(20) Matile, S.; Berova, N.; Nakanishi, K.; Fleischhauer, J.; Woody, R. W. Structural studies by exciton coupled circular dichroism over a large distance: Porphyrin derivatives of steroids, dimeric steroids, and brevetoxin b. *J. Am. Chem. Soc.* **1996**, *118*, 5198−5206.
(21) Maiti, N. C.; Mazumdar, S.; Periasamy, N. *J*- and *H*-aggregates of porphyrin-surfactant complexes: Time-resolved fluorescence and other spectroscopic studies. *J. Phys. Chem. B* **1998**, *102*, 1528−1538.
(22) Riske, K. A.; Amaral, L. Q.; Lamy-Freund, M. T. Thermal transitions of dmpg bilayers in aqueous solution: SAXS structural studies. *Biochim. Biophys. Acta, Biomembr.* **2001**, *1511*, 297−308.
(23) Riske, K. A.; Fernandez, R. M.; Nascimento, O. R.; Bales, B. L.; Lamy-Freund, M. T. DMPG gel-fluid thermal transition monitored by a phospholipid spin labeled at the acyl chain end. *Chem. Phys. Lipids* **2003**, *124*, 69−80.
(24) Cevc, G.; Watts, A.; Marsh, D. Titration of the phase transition of phosphatidylserine bilayer membranes. Effects of pH, surface electrostatics, ion binding, and head-group hydration. *Biochemistry* **1981**, *20*, 4955−4965.
(25) Lamy-Freund, M. T.; Riske, K. A. The peculiar thermo-structural behavior of the anionic lipid dmpg. *Chem. Phys. Lipids* **2003**, *122*, 19−32.
(26) Watts, A.; Harlos, K.; Maschke, W.; Marsh, D. Control of the structure and fluidity of phosphatidylglycerol bilayers by ph titration. *Biochim. Biophys. Acta* **1978**, *510*, 63−74.
(27) Nagarajan, R. Molecular packing parameter and surfactant self-assembly: The neglected role of the surfactant tail. *Langmuir* **2002**, *18*, 31−38.

DOI: 10.1021/acs.langmuir.9b02781
Langmuir 2020, 36, 426−434